Advancement of a Forward Solution Mathematical Model of the Human Knee Joint

A Dissertation Presented for the
Doctor of Philosophy
Degree
The University of Tennessee, Knoxville

Milad Khasian
December 2020

Copyright © 2020 by Milad Khasian
All rights reserved.

DEDICATION

This dissertation is dedicated to my wife, Dr. Nooshin Hamidian, for always believing in me and making life more enjoyable. Your unconditional love and support have been invaluable throughout this journey. This dissertation is also dedicated to my family. To my mother, Narges, for supporting me in all stages of my life. To my late father, Mohammadkarim, from whom I inherited the love for engineering. And to my sisters, Nooshin and Mehrnoush, for encouraging me to pursue my academic goals.

ACKNOWLEDGEMENTS

First and foremost, I would like to express my gratitude to my advisor, Dr. Richard Komistek, for giving me the opportunity to work as a research assistant in the Center for Musculoskeletal Research. Your knowledge, support, and guidance have been incredible for me and have guided me in developing my problem-solving skills.

Thank you, Dr. LaCour, for all your support and help during the past year. I have learned a lot from you during our collaboration in publishing journal articles.

Thank you, Dr. Meccia, for all your technical help throughout the course of this dissertation.

I would also like to thank my colleagues at the CMR lab, Dr. Ian Zeller, Dr. Duc-Manh Ta, Garett Dessinger, Jarrod Nachtrab, Seth Coomer, Lauren Smith, and Thang Nguyen for your assistance along the way.

ABSTRACT

Sometimes called degenerative joint disease, osteoarthritis most often affects the knee, which is a leading cause of pain and reduced mobility. While early treatment is ideal, it is not always successful in combating osteoarthritis and improving joint function, therefore creating the need for total knee arthroplasty (TKA), which is a late-stage treatment where damaged bone and cartilage are replaced by artificial cartilage. Joint arthroplasty is a common and successful procedure for end-stage osteoarthritis. Unfortunately, TKA patient satisfaction rates lag behind those of total hip arthroplasty [1,2], which remains an impetus to create new designs.

Due to ethical issues, time requirements, and prohibitive expenses of testing new designs in vivo, mathematical modeling may be an alternative tool to efficiently assess the kinetics and kinematics of new TKA designs. In general, the knee is one of the most complicated joints in the human body, including multiple articulating surfaces and the complexity of soft tissues encompassing the knee joint. Therefore, mathematically modeling the knee is a challenging and complex process. With increasing computational power and advanced knowledge and techniques, advanced mathematical models of the knee joint can be created utilizing various modeling techniques [3].

Furthermore, mathematical modeling can advance our knowledge related to knee biomechanics, especially those parameters that are otherwise challenging to obtain, such as soft tissue properties and effects pertaining to knee mechanics. Mathematical modeling allows the user to evaluate multiple designs and surgical approaches quickly and cost-efficiently without having to conduct lengthy clinical studies. Mathematical models can also provide insight into topics of clinical significance and can efficiently analyze outcome

contributions that cannot be controlled in fluoroscopic studies, such as anatomical, mechanical, and kinematic alignment comparisons for the same subject. Furthermore, mathematical models can evaluate the effect of TKA design concerns such as changing conformity of the polyethylene or using femoral components with single or multi radius designs [3].

The objectives of this dissertation are to advance a forward solution model to create a more sophisticated and physiological representation of the knee joint. This is achieved by developing a muscle wrapping algorithm, integrating a validated inverse dynamics model, adding more muscles, incorporating several different TKA types including revision TKA designs, and expanding the model to include other daily activities. All these modifications are incorporated in a graphical user interface. These advancements increase both functionality and accuracy of the model. Several validation methods have been implemented to investigate the accuracy of the predicted kinetics and kinematics of this mathematical model.

TABLE OF CONTENTS

Chapter 1: Introduction 1

1.1 Basic Definitions 1

1.2 The Human Knee 1

1.2.1 The Muscles of the Knee 3

1.2.2 The Ligaments of the Knee 4

1.2.3 The Motion of the Knee 6

1.3 Total Knee Arthroplasty 9

1.4 TKA Complications 14

1.5 TKA Evaluation 15

Chapter 2: Background 18

2.1 Mathematical Modeling 18

Chapter 3: Objectives and Contributions 23

3.1 Objectives 23

3.2 Contributions 24

Chapter 4: Materials and Methods 26

4.1 General Modeling Method 26

4.1.1 Kane's Dynamics 26

4.1.2 General Setup of the Model 28

4.1.3 Graphical User Interface 30

4.1.4 Ligaments 32

4.1.5 Muscles 34

4.1.6 Contact Detection Algorithm 38

4.2 Muscle Wrapping Algorithm 40
4.2.1 Updating the FSM 41
4.3 Integration of an Inverse Solution Model 48
4.3.1 Updating the FSM 50
4.4 Settling Algorithm 58
4.4.1 Updating the FSM 60
4.5 Physiological Knee Simulation 64
4.5.1 Incorporating the Foot 64
4.5.2 Incorporating More Muscles 69
4.5.3 Incorporating Clinically Relevant Simulations 72
4.5.4 Incorporating Various Subjects 78
4.6 Other Activities 81
4.6.1 Squat to Rise 81
4.6.2 Lunge 82
4.6.3 Chair Rise 84
4.6.4 Stair Descent 85
4.6.5 Stair Ascent 89
4.6.6 Gait 90
4.7 Revision TKA 92
4.7.1 Rotating Bearing Hinge System 93
4.7.2 Fixed Bearing Hinge System 101
4.8 Graphical User Interface 105
4.8.1 General 105

4.8.2 Wrapping animation 115
4.8.3 Physiological Knee Mathematical Model 117
4.8.4 Tibia Bone modification 119
4.8.5 Initial Position 119
4.8.6 Multiple Activities 125
Chapter 5: Results and Discussion 128
5.1 Muscle Wrapping 128
5.1.1 Effects of a Larger Femoral Component Size 132
5.2 Inverse Model 136
5.2.1 Effects of AP Translation 139
5.3 Settling Algorithm 145
5.3.1 Settling Algorithm for Various TKA Type 149
5.4 Foot 149
5.5 Multiple Subjects 153
5.5.1 PCR TKA 156
5.5.2 PS TKA 156
5.6 Other Activities 164
5.6.1 Squat to Rise 164
5.6.2 Chair Rise 164
5.6.3 Lunge 170
5.6.4 Stair Descent 176
5.6.5 Stair Ascent 176
5.6.6 Gait 180

5.7 Revision TKA 184
5.7.1 Rotating-bearing Hinge 184
5.7.2 Fixed-bearing Hinge 188
5.8 Sensitivity Analysis 198
5.8.1 Posterior Tibial Slope 198
5.8.2 Initial Placement 208
5.8.3 Patella Baja 209
5.8.4 Bearing Insert Conformity 219
5.8.5 PS TKA Post location 222
5.8.6 Pin Design in Fixed-bearing Hinge 226
Chapter 6: Validation 231
6.1 Kinetics validation 231
6.1.1 Deep Knee Bend 231
6.1.2 Chair Rise 232
6.1.3 Stair Ascent 232
6.2 Kinematics Validation 237
6.2.1 Fixed-bearing PS TKA 237
6.2.2 Mobile-bearing PS TKA 237
6.2.3 Posterior Cruciate Retaining Medial Pivot TKA 238
Chapter 7: Summary 245
7.1 Assumptions and Limitations 248
7.2 Future Works 250
REFERENCES 252

VITA 273

LIST OF TABLES

Table 1-1: The cruciate ligaments are treated differently for each TKA type. 13

Table 4-1: The masses of bodies are defined as a percentage of the total body-weight..... 28

Table 4-2: Ligaments stiffness coefficients implemented in the mathematical model..... 33

Table 4-3: The incorporated muscles and their insertion and origins in the FSM..... 35

Table 4-4: Kinematics parameters measured from fluoroscopy analysis and are used as inputs of the inverse solution model. 51

Table 4-5: Patient demographic for ten subjects included in the updated FSM. 80

Table 5-1: The flexion angles where the wrapping algorithm starts for different quadriceps muscle fibers and different implant types..... 130

Table 5-2: The average femora axial rotation and maximum weight-bearing flexion for subjects with initial internal or external femoral component rotation..... 211

Table 6-1: The lateral and medial AP translation and axial rotation for the average fluoroscopy and the mathematical model as well as root-mean-square errors between model prediction and average fluoroscopy for FB PS group. 240

Table 6-2: The lateral and medial AP translation and axial rotation for the average fluoroscopy and the mathematical model as well as root-mean-square errors between model prediction and average fluoroscopy for MB PS group. 242

Table 6-3: The lateral and medial AP translation and axial rotation for the average fluoroscopy and the mathematical model as well as root-mean-square errors between model prediction and average fluoroscopy for medial pivot TKA. 244

LIST OF FIGURES

Figure 1-1: Anatomic planes of the human bodies and reference axes. Image modified from human-memory.net. 2

Figure 1-2: The major bones of the human knee [14]. 2

Figure 1-3: The muscles of the knee joint are shown here from the anterior (left) and the posterior view (right) (image from anatomynote.com). 5

Figure 1-4: Major ligaments of the human knee joint (image modified from coreem.net)..... 5

Figure 1-5: The knee joint is a six degree of freedom system with three translational and three rotational motion [32]. 7

Figure 1-6: Tibiofemoral knee kinematics are shown here. The femoral lateral condyle moves posteriorly with knee flexion. The medial femoral condyle movement is limited compared to the lateral condyle. The combination of these two movements result in consistent femoral external rotation of the knee during knee flexion [26]. 8

Figure 1-7: Osteoarthritis of the Medial Side of the Knee [39]. 10

Figure 1-8: A conventional TKA consists of at least three components: a femoral component rigidly attached to the femur, a tibial tray rigidly attached to the tibia, and a bearing insert placed between the femoral component and tibial tray. Often, the patella is resurfaced, and a component is placed on resurfaced patella. 10

Figure 1-9: The femoral component can be made with different sagittal curvatures [46]..... 12

Figure 1-10: Different TKA types retain or resect cruciate ligaments. And often replace the functionality of these ligament with a form of physical constraint on the bearing insert. 13

Figure 1-11: the medial compartment in the medial pivot design is similar to a ball and socket joint to restrict the medial motion. The lateral compartment is flatter to allow femoral lateral rollback (image modified from [47]). 14

Figure 2-1: The difference between the inverse dynamics model (left) and forward dynamics model (right)..... 19

Figure 2-2: Free body diagram of the mathematical model. Soft tissue forces (muscles and ligaments) are defined with vectors. 22

Figure 2-3: Graphic user interface of the mathematical model. 22

Figure 4-1: Bones and relative components implemented in the knee model. 29

Figure 4-2: Quadriceps muscle attachments (red) and patellar ligament attachments (blue) are shown. 29

Figure 4-3: Graphical user interface of the forward solution model. 30

Figure 4-4: The forward solution model overall process is shown. 31

Figure 4-5: The ligaments attachments can be defined by the user in the GUI. 34

Figure 4-6: Schematic of the quadriceps muscle controller acting on the knee flexion. 37

Figure 4-7: The contacting surfaces are modeled either as a point cloud or surface polynomial. Patellofemoral articulating surfaces are shown on left, tibiofemoral articulating surfaces are shown in the middle, and cam/post mechanism surfaces are shown in the right. 39

Figure 4-8: Muscle moment arm is defined as the smallest distance from the joint center of rotation to the muscle line of action. 42

Figure 4-9: Muscles wrap around the bone. (Image modified from comportho.com) 42

Figure 4-10: The current wrapping algorithm only accounts for one wrapping algorithm around the femoral component. The muscle line of action passes through the bone and the femoral component rather than wrapping about the bone. 44

Figure 4-11: Five wrapping points are defined around the femoral component to account for the geometry of the femora component. 44

Figure 4-12: If the inferior wrapping points ML location are defined fixed to the femoral component, then the quadriceps tendon cannot move in ML direction with the patella. 47

Figure 4-13: The wrapping algorithm detection is based on the change in the sign of the cross product of two vectors. The cross product is toward the sagittal plane, negative sign, when there is no wrapping (left) and is pointing toward outside the plane, positive sign when there is wrapping (right). 47

Figure 4-14: Simplified schematic diagram of two main widely mathematical solutions in biomechanics. a) Inverse solution models utilize motion to predict the in vivo forces. b) Forward solution models predict the joint kinematics based on the joint forces and torques. 48

Figure 4-15: Validated inverse solution model implemented in the GUI based on the forward solution outcomes. 49

Figure 4-16: Measurement of kinematics data to input into the inverse mathematical model. 51

Figure 4-17: The lateral and medial contact point translations are collected relative to the femoral component (left). The femoral component center of mass translation relative to the bearing insert is obtained throughout the activity range of motion (right). Red points show the contact points/center of mass and green lines show the trajectory of these points during the range of motion... 52

Figure 4-18: Free body diagram of the inverse mathematical model. F_{ground}, ground reaction force; $F_{pat.lig.}$, patellar ligament force; F_{quad}, quadriceps muscle group force; $F_{pat.fem.}$, patellofemoral contact force; F_{hip}, hip joint reaction force; W_{tib}, the weight of the tibia [9]. 53

Figure 4-19: The average soft tissue attachments are obtained as an average of all bundles for each soft tissue (a). Then a string is created between the average insertion and origin to represent the soft tissue (b)..... 55

Figure 4-20: The patellar ligament is projected onto the sagittal view and then the patellar ligament angle is calculated from the projected vector. 56

Figure 4-21: The low point (yellow) and contact point (red) do not always coincide..... 59

Figure 4-22: at each time step there are multiple points that are in contact between each femoral condyle and bearing insert plateau. The average location of lateral contact points (red) and medial contact points (yellow) are considered as the lateral and medial contact points, respectively..... 59

Figure 4-23: Oscillations in early flexion in DKB simulation in previous FSM. These oscillations affect the knee contact forces (a), muscle force prediction (b), and kinematic outcomes (c). 61

Figure 4-24: New variables, forces and torques, are introduced in the inverse solution model to make the system stable at initial condition. 63

Figure 4-25: The movement of the foot during the stance phase of the gait. The foot is not stationary throughout the range of motion of the activity. 66

Figure 4-26: Both gastrocnemius muscle fibers are inserted on the posterior calcaneus on the foot (image from www.healthlinkbc.ca)..... 66

Figure 4-27: The foot and toe are modeled separately to account for different flexion profiles during different activities. 67

Figure 4-28: In the current FSM, the ground reaction forces are applied at the ankle joint and the model starts at the ankle joint (left). The updated model incorporated the foot and toes. The location of the toes and the tibia are defined relative to the foot (right). 68

Figure 4-29: Display of all four fibers of the hamstring muscle group. 71

Figure 4-30: Two fibers of the gastrocnemius muscle group are shown here. 71

Figure 4-31: The default Attune PCR model in the previous GUI. 72

Figure 4-32: Two different alignment techniques. a) Anatomical alignment, b) mechanical alignment. [134] 74

Figure 4-33: In the updated FSM, the components are aligned based on the mechanical alignment (right). 75

Figure 4-34: Tibial posterior slope is shown for the normal knee (left), a PCR TKA (middle), and a PS TKA design (right). 76

Figure 4-35: Different tibial posterior slope are considered for different TKA designs in the updated FSM. 6° for PCR (left), 0° for PS (middle), and 2° for ACL substituting design (right). 76

Figure 4-36: Measurement of the posterior condylar offset preoperatively (left) and postoperatively (right) [124]. 77

Figure 4-37: Posterior condylar offset and other measurements from actual fluoroscopic images are collected (left) and the surgical cuts are performed based on these measurements that are incorporated into the new FSM. 77

Figure 4-38: The CAD models of bone geometries were created from CT scans using segmentation techniques for all ten subjects. 79

Figure 4-39: Ligaments insertion and origin for each of the ten subjects (right) were created from ligaments attachment data available in the literature (left) [148]. 80

Figure 4-40: The squat to rise activity compromises of a DKB activity and knee extension. The blue graph shows the desired knee flexion profile and the red graph shows the actual knee flexion. 83

Figure 4-41: During the turn-around flexion angle, the previous FSM experienced instability. 83

Figure 4-42: The lunge activity (top) is different from the DKB activity (bottom). The distribution of the load on the knee joint is different in these activities. 84

Figure 4-43: The chair rise activity has been incorporated into the new FSM. The user can update the initial condition for this activity using the GUI. 85

Figure 4-44: Gait cycle compromises of two distinct phases; stance and swing phase. During the swing phase the foot remains in contact with the ground. The top image is from [160]. 87

Figure 4-45: Each body's location is defined relative to its distal body/frame using the concept of the coincident point. The black point is the coincident point on the foot, and the red point is the coincident point on the tibia. This coincident point is the tibia center of rotation. 91

Figure 4-46: The center of rotation of the foot changes throughout the gait cycle. 92

Figure 4-47: Incorporated hinge systems into the forward solution model. The rotating bearing hinge system is shown on the left. The femoral component rotates about the ML axis, and the insert rotates about the SI axis. The fixed bearing design is shown on the right. The femoral component rotates about the ML axis, the bearing is fixed, and the pin rotates about the SI axis (right). . 94

Figure 4-48: Assembly view of the rotating bearing hinge implant. 96

Figure 4-49: The assembly of the rotating bearing hinge design. A pin inserted between the bearing insert and the femoral component restrict the AP and SI motion of the femoral component and facilitate the flexion. The surfaces shown with magenta and orange are the articulating surfaces of the cam/post of the hinge design. 97

Figure 4-50: Cam point cloud on the femoral component. This point cloud is used for both anterior and posterior cam/post mechanism. 98

Figure 4-51: The inside surface of the bearing will be used to represent the post surfaces in the cam/post mechanism. Left) the anterior post surface, right) the posterior post surfaces on the bearing insert. 99

Figure 4-52: Moving the ring surfaces anteriorly or posteriorly can be used to simulate different clearance between the pin and the ring. Left) Increasing the clearance between the pin and the ring; right) Decreasing the clearance between the pin and the ring. 99

Figure 4-53: The location of the ML Spring force can be defined in the GUI. 101

Figure 4-54: The rotating bearing hinge has a single radius femoral curvature (left). Therefore, the center of rotation remains the same during the whole range of motion. The fixed bearing hinge incorporates a J-curve sagittal curvature. The center of rotation for J-curve design is different between late flexion and early flexion. 102

Figure 4-55: the femoral component rotates about the ML axis and the SI axis and can translates in the SI direction. 103

Figure 4-56: The bearing insert (white component) is fixed to the tibial tray in the fixed bearing design. The axial rotation occurs with the pin inserted between the tibial tray and the femoral component (blue component). the pin axially rotates inside the tibial tray and the contact between the surfaces between the femoral component and the pin (magenta and orange surfaces) force the femoral component to rotate axially with the pin. 106

Figure 4-57: Adding the fixed bearing hinge into the GUI. 106

Figure 4-58: Modeling cam mechanism for the fixed bearing hinge. Left) The outside surface of the pin created to represent the cam. Right) The cam point cloud. 107

Figure 4-59: New feature for adding the post surfaces on the fixed bearing hinge. 107

Figure 4-60: Post mechanism preparation for the fixed bearing hinge. Left) The anterior and posterior post surfaces on the pin. Right) The post surfaces representation in the GUI. 108

Figure 4-61: The previous user interface with a dark background. 110

Figure 4-62: The new visualization of the user interface featuring a bright background. 110

Figure 4-63: All plotting functions have been updated to allow the user to plot against the activity percentage as well as knee flexion. 111

Figure 4-64: New updates of the FSM GUI. The user can control the number of data points included in the results (top). The GUI is capable of exporting the bone and component geometries, as well as their respective transformation matrices. 111

Figure 4-65: Difference between condylar points clouds by each method. a) Two methods to calculate the condylar point clouds. b) Condylar contact point cloud calculated by the 'AutCompute' feature. c) Condylar contact point cloud calculated by importing surfaces to the GUI. 113

Figure 4-66: Femoral component IE rotation calculations based on the low points..... 114

Figure 4-67: A GUI has been incorporated in the main GUI to visualize the muscle wrapping algorithm. 115

Figure 4-68: The user can select which muscle to visualize. The default camera views are lateral and medial, but the user can select to view the wrapping from the front view..... 116

Figure 4-69: The user can easily select various subjects with different implant type to perform different activities simulations..... 118

Figure 4-70: Different default simulations for different implants have been added to the latest GUI. 120

Figure 4-71: Default models were created and incorporated in the GUI for various TKA design. 120

Figure 4-72: In the most recent version of the FSM user can modify the initial position of the tibia bone. 121

Figure 4-73: In the previous version of the GUI, the user selects the close initial condition (left), components cannot be placed in contacting condition (right). 122

Figure 4-74: The new version of the GUI features the ability to place the components at the close contact condition automatically..... 124

Figure 4-75: To perform different activities, the user needs to select the proper activity. The GUI creates the approximation of the starting position for that activity. 127

Figure 4-76: The current GUI allows the user to select various subjects with different implant type performing different activity. 127

Figure 5-1: The developed muscle wrapping algorithm is capable of accurately muscle wrapping around the femoral component (top) and also around the bones (bottom). 129

Figure 5-2: Comparison of quadriceps forces between the old wrapping method (red) and the new wrapping algorithm (green). 131

Figure 5-3: Comparison of patellofemoral joint forces between the old wrapping method (red) and the new wrapping algorithm (green). 131

Figure 5-4: Comparison of lateral tibiofemoral joint forces between the old wrapping method (red) and the new wrapping algorithm (green). 133

Figure 5-5: Comparison of medial tibiofemoral joint forces between the old wrapping method (red) and the new wrapping algorithm (green). 134

Figure 5-6: Comparison of lateral tibiofemoral AP translation between the old wrapping method (red) and the new wrapping algorithm (green). 134

Figure 5-7: Comparison of medial tibiofemoral AP translation between the old wrapping method (red) and the new wrapping algorithm (green). 135

Figure 5-8: Comparison of tibiofemoral axial rotation between the old wrapping method (red) and the new wrapping algorithm (green). 135

Figure 5-9: Quadriceps tendon wraps further from the center of mass of the femoral component when a larger implant size is used. 137

Figure 5-10: Quadriceps force is lower when the larger femoral component (green) is implanted. 137

Figure 5-11: Patellofemoral joint forces comparison between the default femoral component size (red) and one size larger femoral component (green). 138

Figure 5-12: the quadriceps muscle force for a PCR TKA design using the inverse solution model. 140

Figure 5-13: the patellofemoral contact force for a PCR TKA design using the inverse solution model. 140

Figure 5-14: The total tibiofemoral contact force for a PCR TKA design using the inverse solution model. 141

Figure 5-15: The hip joint force for a PCR TKA design using the inverse solution model. 141

Figure 5-16: The comparison between the lateral A-P translation for a PCR TKA (solid red) and an ACL substituting TKA (Solid blue) and the medial A-P translation for a PCR TKA (dashed red) and an ACL substituting TKA (dashed blue) 143

Figure 5-17: The comparison between the quadriceps muscle forces for a PCR TKA (solid red) and an ACL substituting TKA (Solid blue). 143

Figure 5-18: The comparison between the patellofemoral contact forces for a PCR TKA (solid red) and an ACL substituting TKA (Solid blue). 144

Figure 5-19: The comparison between the tibiofemoral contact forces for a PCR TKA (solid red) and an ACL substituting TKA (Solid blue). 144

Figure 5-20: The developed settling algorithm (red) effectively eliminates the early oscillations observed in the lateral AP translation compared to the previous FSM (green). 145

Figure 5-21: Comparison between the medial AP translation for a PCR TKA using the settling algorithm (red) and without the settling algorithm (green). 146

Figure 5-22: Comparison between the total tibiofemoral contact force for a PCR TKA using the settling algorithm (red) and without the settling algorithm (green). 146

Figure 5-23: Comparison between the quadriceps force for a PCR TKA using the settling algorithm (red) and without the settling algorithm (green). 147

Figure 5-24: Comparison between the ML torque applied to the tibial tray for a PCR TKA using the settling algorithm (red) and without the settling algorithm (green). 147

Figure 5-25: Using the settling algorithm, the effects of the anterior cam and the contact force can be analyzed more accurately in an ACL substituting design. 148

Figure 5-26: The settling algorithm successfully eliminates the early oscillation in the lateral tibiofemoral contact force for all types of TKA. 150

Figure 5-27: The settling algorithm successfully eliminates the early oscillation in the quadriceps muscle force for all types of TKA. 150

Figure 5-28: The settling algorithm successfully eliminates the early oscillation in the patellofemoral contact force for all types of TKA. 151

Figure 5-29: The settling algorithm successfully eliminates the early oscillation in the lateral AP translation for all types of TKA..... 151

Figure 5-30: The settling algorithm successfully eliminates the early oscillation in the medial AP translation for all types of TKA. 152

Figure 5-31: The settling algorithm successfully eliminates the early oscillation in the patella flexion angle for all types of TKA. 152

Figure 5-32: A theoretical patient was created in the FSM, where the patient starts rotating the foot close to the end of the DKB activity. 154

Figure 5-33: Comparison between the quadriceps muscle forces between a simulation with foot rotation (green) and a simulation with the stationary foot (red). 154

Figure 5-34: Comparison between the patellar ligament forces between a simulation with foot rotation (green) and a simulation with the stationary foot (red). 155

Figure 5-35: Comparison between the tibiofemoral contact forces between a simulation with foot rotation (green) and a simulation with the stationary foot (red). 155

Figure 5-36: Comparison of lateral condylar AP translation between ten subjects implanted with Attune CR TKA. 157

Figure 5-37: Comparison of medial condylar AP translation between ten subjects implanted with Attune CR TKA. 157

Figure 5-38: Comparison of femoral axial rotation between ten subjects implanted with Attune CR TKA. 158

Figure 5-39: Comparison of tibiofemoral contact force between ten subjects implanted with Attune CR TKA. 158

Figure 5-40: Comparison of patellofemoral contact force between ten subjects implanted with Attune CR TKA. 159

Figure 5-41: Comparison of quadriceps muscle force between ten subjects implanted with Attune CR TKA. 159

Figure 5-42: Comparison of lateral condylar AP translation between ten subjects implanted with Attune PS TKA. 160

Figure 5-43: Comparison of medial condylar AP translation between ten subjects implanted with Attune PS TKA. 160

Figure 5-44: Comparison of femoral axial rotation between ten subjects implanted with Attune PS TKA 161

Figure 5-45: Comparison of tibiofemoral contact force between ten subjects implanted with Attune PS TKA 161

Figure 5-46: Comparison of patellofemoral contact force between ten subjects implanted with Attune PS TKA 162

Figure 5-47: Comparison of quadriceps muscle force between ten subjects implanted with Attune PS TKA.....162

Figure 5-48: Comparison of cam/post contact force between ten subjects implanted with Attune PS TKA.....163

Figure 5-49: Comparison of the lateral AP translation between the current FSM (green) and the previous FSM (red) for a squat to rise activity. 165

Figure 5-50: Comparison of the medial AP translation between the current FSM (green) and the previous FSM (red) for a squat to rise activity. 165

Figure 5-51: Comparison of the quadriceps muscle between the current FSM (green) and the previous FSM (red) for a squat to rise activity. 166

Figure 5-52: The lateral AP translation for a PCR TKA design during the chair rise activity. 166

Figure 5-53: The medial AP translation for a PCR TKA design during the chair rise activity. 167

Figure 5-54: The femoral axial rotation for a PCR TKA design during the chair rise activity. 167

Figure 5-55: The tibiofemoral contact force for a PCR TKA design during the chair rise activity.....168

Figure 5-56: the quadriceps muscle force for a PCR TKA design during the chair rise activity.....168

Figure 5-57: the patellofemoral contact force for a PCR TKA design during the chair rise activity.....169

Figure 5-58: Comparison between the end position of the lunge activity (left) with the DKB activity (right). The range of motion of the tibia and the upper body is limited in the lunge activity. 171

Figure 5-59: Comparison between the lateral AP translation between the DKB activity (solid red) and the lunge activity (dashed black).....172

Figure 5-60: Comparison between the medial AP translation between the DKB activity (solid red) and the lunge activity (dashed black).....172

Figure 5-61: Comparison between the femoral axial rotation between the DKB activity (solid red) and the lunge activity (dashed black).....173

Figure 5-62: Comparison between the tibiofemoral contact force between the DKB activity (solid red) and the lunge activity (dashed black).....173

Figure 5-63: Comparison between the quadriceps muscle force between the DKB activity (solid red) and the lunge activity (dashed black). 174

Figure 5-64: Comparison between the patellofemoral contact force between the DKB activity (solid red) and the lunge activity (dashed black). 174

Figure 5-65: Comparison between the patellar ligament length between the DKB activity (solid red) and the lunge activity (dashed black). 175

Figure 5-66: Comparison between the patellar ligament force between the DKB activity (solid red) and the lunge activity (dashed black). 175

Figure 5-67: The lateral AP translation for a PCR TKA during the stair descent activity. 177

Figure 5-68: The medial AP translation for a PCR TKA during the stair descent activity. 177

Figure 5-69: The femoral axial rotation for a PCR TKA during the stair descent activity. 178

Figure 5-70: The tibiofemoral contact force for a PCR TKA during the stair descent activity. 178

Figure 5-71: The quadriceps muscle force for a PCR TKA during the stair descent activity. 179

Figure 5-72: The patellofemoral contact force for a PCR TKA during the stair descent activity. 179

Figure 5-73: The lateral AP translation for a PCR TKA during stair ascent activity. 181

Figure 5-74: The medial AP translation for a PCR TKA during stair ascent activity. 181

Figure 5-75: The femoral axial rotation for a PCR TKA during stair ascent activity. 182

Figure 5-76: The tibiofemoral contact force for a PCR TKA during stair ascent activity. 182

Figure 5-77: The quadriceps muscle force for a PCR TKA during stair ascent activity. 183

Figure 5-78: The patellofemoral contact force for a PCR TKA during stair ascent activity. 183

Figure 5-79: The lateral AP translation for a PCR TKA during gait activity. 185

Figure 5-80: The medial AP translation for a PCR TKA during gait activity. 185

Figure 5-81: The femoral axial rotation for a PCR TKA during gait activity. 186

Figure 5-82: The tibiofemoral contact force for a PCR TKA during gait activity. 186

Figure 5-83: The quadriceps muscle force for a PCR TKA during gait activity. 187

Figure 5-84: The patellofemoral contact force for a PCR TKA during gait activity. 187

Figure 5-85: The lateral AP translation for the rotating bearing hinge design during the DKB activity. 189

Figure 5-86: The medial AP translation for the rotating bearing hinge design during the DKB activity. 189

Figure 5-87: The femoral axial rotation for the rotating bearing hinge design during the DKB activity. 190

Figure 5-88: The bearing axial rotation relative to the tibial tray for the rotating bearing hinge design during the DKB activity. 190

Figure 5-89: The tibiofemoral contact force for the rotating bearing hinge design during the DKB activity. 191

Figure 5-90: The quadriceps muscle force for the rotating bearing hinge design during the DKB activity. 191

Figure 5-91: The patellofemoral contact force for the rotating bearing hinge design during the DKB activity. 192

Figure 5-92: Comparison of the lateral AP translation between the rotating-bearing hinge (solid red) and the fixed-bearing hinge (dashed black). 194

Figure 5-93: Comparison of the medial AP translation between the rotating-bearing hinge (solid red) and the fixed-bearing hinge (dashed black). 194

Figure 5-94: Comparison of the femoral axial rotation between the rotating-bearing hinge (solid red) and the fixed-bearing hinge (dashed black). 195

Figure 5-95: Comparison of the bearing axial rotation between the rotating-bearing hinge (solid red) and the fixed-bearing hinge (dashed black). 195

Figure 5-96: Comparison of the tibiofemoral contact force between the rotating-bearing hinge (solid red) and the fixed-bearing hinge (dashed black). 196

Figure 5-97: Comparison of the quadriceps muscle force between the rotating-bearing hinge (solid red) and the fixed-bearing hinge (dashed black). 196

Figure 5-98: Comparison of the patellofemoral contact force between the rotating-bearing hinge (solid red) and the fixed-bearing hinge (dashed black). 197

Figure 5-99: Comparison of the lateral AP translation between different posterior tibial slopes for a PCR TKA. 200

Figure 5-100: Comparison of the medial AP translation between different posterior tibial slopes for a PCR TKA. 200

Figure 5-101: Comparison of the femoral axial rotation between different posterior tibial slopes for a PCR TKA. 201

Figure 5-102: Comparison of the tibiofemoral contact force between different posterior tibial slopes for a PCR TKA. 201

Figure 5-103: Comparison of the quadriceps muscle force between different posterior tibial slopes for a PCR TKA. 202

Figure 5-104: Comparison of the PCL ligament force between different posterior tibial slopes for a PCR TKA. 202

Figure 5-105: Comparison of the anterior cam/post contact force between different posterior tibial slopes for an ACL substituting TKA. 204

Figure 5-106: Comparison of the lateral AP translation between different posterior tibial slopes for an ACL substituting TKA. 204

Figure 5-107: Comparison of the medial AP translation between different posterior tibial slopes for an ACL substituting TKA. 205

Figure 5-108: Comparison of the femoral axial rotation between different posterior tibial slopes for an ACL substituting TKA. 205

Figure 5-109: Comparison of the tibiofemoral contact force between different posterior tibial slopes for an ACL substituting TKA. 206

Figure 5-110: Comparison of the quadriceps muscle force between different posterior tibial slopes for an ACL substituting TKA. 206

Figure 5-111: Comparison of the PCL ligament force between different posterior tibial slopes for an ACL substituting TKA. 207

Figure 5-112: Three theoretical PCR TKA patients were created with different femoral component orientations at the full extension. 210

Figure 5-113: Comparison between the femoral axial rotation between the reference PCR (blue), the externally rotated PCR (green), and the internally rotated PCR (red). 210

Figure 5-114: Comparison between the MCL ligament force between the reference PCR (blue), the externally rotated PCR (green), and the internally rotated PCR (red). 211

Figure 5-115: Comparison between the PCL ligament force between the reference PCR (blue), the externally rotated PCR (green), and the internally rotated PCR (red). 212

Figure 5-116: Comparison between the patellofemoral contact force between the reference PCR (blue), the externally rotated PCR (green), and the internally rotated PCR (red). 212

Figure 5-117: Three simulations were created using the FSM to investigate the effects of patella positioning on TKA outcomes. 214

Figure 5-118: The sensitivity analysis of the patella baja (dashed black), the patella alta (dash-dotted blue), and the reference (solid red). The left graphs show the extensor mechanism forces for the PCR design, and the right graphs are for the PS design. 215

Figure 5-119: Comparison between the quadriceps force (top), tibiofemoral contact force (middle), and the patellofemoral force (bottom) for the PCR (solid red) and the PS (dashed black) designs. 216

Figure 5-120: Comparison in the PCL force in the PCR design (solid red) with the cam-post force in the PS design (dashed black). 217

Figure 5-121: The PCL is almost in the vertical direction in mid to late flexion and therefore the PCL forces is more in the SI direction (top) and cam/post mechanism forces is applied in the AP direction (bottom). 218

Figure 5-122: The user can alter the geometries of TKA components and component alignment using the GUI and perform sensitivity analyses to study the effects of TKA design aspects and surgical conditions as related to knee mechanics. The sagittal conformity of medial plateau was increased (right) to make the medial plateau more conforming and decreased to make the medial plateau flatter (left). 220

Figure 5-123: The sensitivity analysis of the reference (solid red), increased medial conformity (solid green), and decreased medial conformity (dashed green) designs are included for a PS TKA. LAP (top left), MAP (top right), cam-post contact force (bottom left), and tibiofemoral contact force (bottom right) are represented. 221

Figure 5-124: Three different simulations were created for a PS TKA design. One with a normal post position, the reference design (middle), one with the post moved anteriorly, design #1 (left), and one with post moved posteriorly, design #2 (right) 222

Figure 5-125: Comparison of the lateral AP translation between the reference PS (red), the anteriorized post PS (blue), and the posteriorized post PS (green). 223

Figure 5-126: Comparison of the medial AP translation between the reference PS (red), the anteriorized post PS (blue), and the posteriorized post PS (green). 223

Figure 5-127: Comparison of the femoral axial rotation between the reference PS (red), the anteriorized post PS (blue), and the posteriorized post PS (green). 224

Figure 5-128: Comparison of the cam/post contact force between the reference PS (red), the anteriorized post PS (blue), and the posteriorized post PS (green). 225

Figure 5-129: Comparison of the patellofemoral contact between the reference PS (red), the anteriorized post PS (blue), and the posteriorized post PS (green). 225

Figure 5-130: Increasing the clearing of the cam/post mechanism by moving the anterior surface further anterior (left) and the posterior surface more posterior (right). 226

Figure 5-131: Comparison of the lateral AP translation between the default (blue) and the increased clearance design (green). 228

Figure 5-132: Comparison of the medial AP translation between the default (blue) and the increased clearance design (green). 228

Figure 5-133: Comparison of the femoral axial rotation between the default (blue) and the increased clearance design (green). 229

Figure 5-134: Comparison of the patellofemoral contact force between the default (blue) and the increased clearance design (green). 229

Figure 5-135: Comparison of the anterior cam/post contact force between the default (blue) and the increased clearance design (green). 230

Figure 5-136: Comparison of the posterior cam/post contact force between the default (blue) and the increased clearance design (green). 230

Figure 6-1: The lateral contact force comparison between model prediction (dashed black line) and the telemetric device (solid red line) for subject 1. .233

Figure 6-2: The medial contact force comparison between model prediction (dashed black line) and the telemetric device (solid red line) for subject 1. .233

Figure 6-3: The total contact force comparison between model prediction (dashed black line) and the telemetric device (solid red line) for subject 1. .234

Figure 6-4: The lateral contact force comparison between model prediction (dashed black line) and the telemetric device (solid red line) for subject 2. .234

Figure 6-5: The medial contact force comparison between model prediction (dashed black line) and the telemetric device (solid red line) for subject 2. .235

Figure 6-6: The total contact force comparison between model prediction (dashed black line) and the telemetric device (solid red line) for subject 2. .235

Figure 6-7: The contact force comparison between model prediction (dashed black line) and the telemetric device (solid red line) during a chair rise activity. 236

Figure 6-8: The contact force comparison between model prediction (dashed black line) and the telemetric device (solid red line) during a stair ascent activity. 236

Figure 6-9: The predicted lateral rollback is validated against average fluoroscopic data for FB PS. The solid red line shows the average fluoroscopy of subjects (shown with thin grey lines), and the mathematical model predictions are shown with dashed black lines.....239

Figure 6-10: The predicted medial rollback is validated against average fluoroscopic data for FB PS. The solid red line shows the average fluoroscopy of subjects (shown with thin grey lines), and the mathematical model predictions are shown with dashed black lines.....239

Figure 6-11: The predicted axial rotation is validated against average fluoroscopic data for FB PS. The solid red line shows the average fluoroscopy of subjects (shown with thin grey lines), and the mathematical model predictions are shown with dashed black lines.....240

Figure 6-12: The predicted lateral rollback is validated against average fluoroscopic data for MB PS. The solid red line shows the average fluoroscopy of subjects (shown with thin grey lines), and the mathematical model predictions are shown with dashed black lines. 241

Figure 6-13: The predicted medial rollback is validated against average fluoroscopic data for MB PS. The solid red line shows the average fluoroscopy of subjects (shown with thin grey lines), and the mathematical model predictions are shown with dashed black lines. 241

Figure 6-14: The predicted axial rotation is validated against average fluoroscopic data for MB PS. The solid red line shows the average fluoroscopy of subjects (shown with thin grey lines), and the mathematical model predictions are shown with dashed black lines. 242

Figure 6-15: The predicted lateral rollback is validated against average fluoroscopic data for medial pivot design. The solid red line shows the average fluoroscopy of subjects (shown with thin grey lines), and the mathematical model predictions are shown with dashed black lines. 243

Figure 6-16: The predicted medial rollback is validated against average fluoroscopic data for medial pivot design. The solid red line shows the average fluoroscopy of subjects (shown with thin grey lines), and the mathematical model predictions are shown with dashed black lines. 243

Figure 6-17: The predicted axial rotation is validated against average fluoroscopic data for the medial pivot design. The solid red line shows the average fluoroscopy of subjects (shown with thin grey lines), and the mathematical model predictions are shown with dashed black lines. 244

Figure 7-1: The same validation technique with the same patient was used in the previous FSM. The model tibiofemoral joint force prediction (red) was compared to the telemetric forces (green) [98]. 247

ACRONYMS

2D	Two-Dimensional
3D	Three-Dimensional
ACL	Anterior Cruciate Ligament
AP	Anteroposterior
BCS	Bicrucaite Substituting
BF	Bicep Femoris
BFL	Bicep Femoris – Long Head
BFS	Bicep Femoris – Short Head
BW	Body Weight
CAD	Computer-Aided Design
CT	Computed Tomography
DKB	Deep Knee Bend
DOF	Degrees Of Freedom
FB	Fixed-Bearing
FE	Flexion/Extension
FEA	Finite Element Analysis
GL	Gastrocnemius Lateralis
GM	Gastrocnemius Medialis
GRF	Ground Reaction Force
GUI	Graphical User Interface
IE	Internal / External
KOOS	Knee injury and Osteoarthritis Outcome Score
KSS	Knee Society Score
LAP	Lateral Anteroposterior
LCL	Lateral Collateral Ligament
LPFL	Lateral Patellofemoral Ligament

MAP	Medial Anteroposterior
MB	Mobile-Bearing
MCL	Medial Collateral Ligament
ML	Mediolateral
MPFL	Medial Patellofemoral Ligament
MPML	Medial Patellomeniscal Ligament
MRI	Magnetic Resonance Imaging
PCL	Posterior Cruciate Ligament
PCR	Posterior Cruciate Retaining
PFR	Posterior Femoral Rollback
PS	Posterior Stabilized
RF	Rectus Femoris
ROM	Range Of Motion
SI	Superoinferior
SMB	Semimembranosus
SMT	Semitendinosus
TFS	tracking fluoroscope system
TKA	Total Knee Arthroplasty
TKR	Total Knee Replacement
VI	Vastus Intermedius
VL	Vastus Lateralis
VM	Vastus Medialis
VV	Varus/Valgus

Chapter 1: Introduction

1.1 Basic Definitions

Before starting to delve into the knee and mechanics of the knee joint, it would be beneficial to provide some basic definition to describe the human anatomy and movements. The movements of the human joint are often described using three orthogonal planes: the coronal (frontal), the sagittal, and the transverse (horizontal) plane. The movements in these planes are called the medial/lateral (ML), the anterior/posterior (AP), and the superior/inferior (SI), respectively (Figure 1-1).

1.2 The Human Knee

The knee joint is the largest and one of the most complex joints of the human body [4]. The knee joint consists of two separate joints: The tibiofemoral joint (the articulating surface between the femur and the tibia), and the patellofemoral joint (articulating surface between the femur and the patella) (Figure 1-2).

The tibiofemoral joint, which is mainly responsible for carrying the weight of the upper body and absorbing loads through flexing during daily activity, consists of two compartments: one between the lateral condyle of the femur and the lateral plateau of the tibia, and one between medial femoral condyle and the medial tibial plateau.

The patellofemoral joint is mainly responsible for transferring the loads of the extensor mechanism of the knee. Specifically, the main function of the patella is to increase the moment arm of quadriceps muscles on the knee and to change the line of action of quadriceps force during knee flexion/extension [5–8]. Both joints often experience forces multiple times of body weight [9–13].

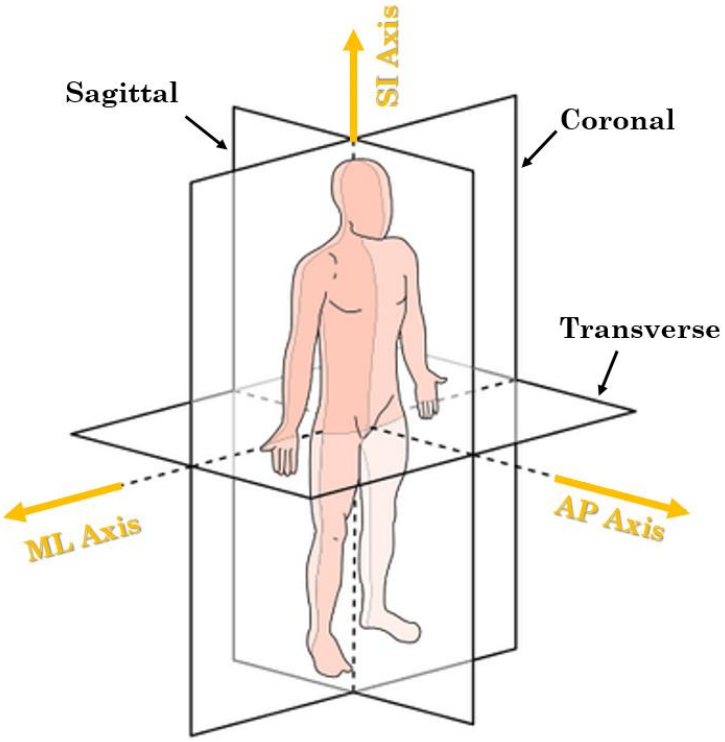


Figure 1-1: Anatomic planes of the human bodies and reference axes. Image modified from human-memory.net.

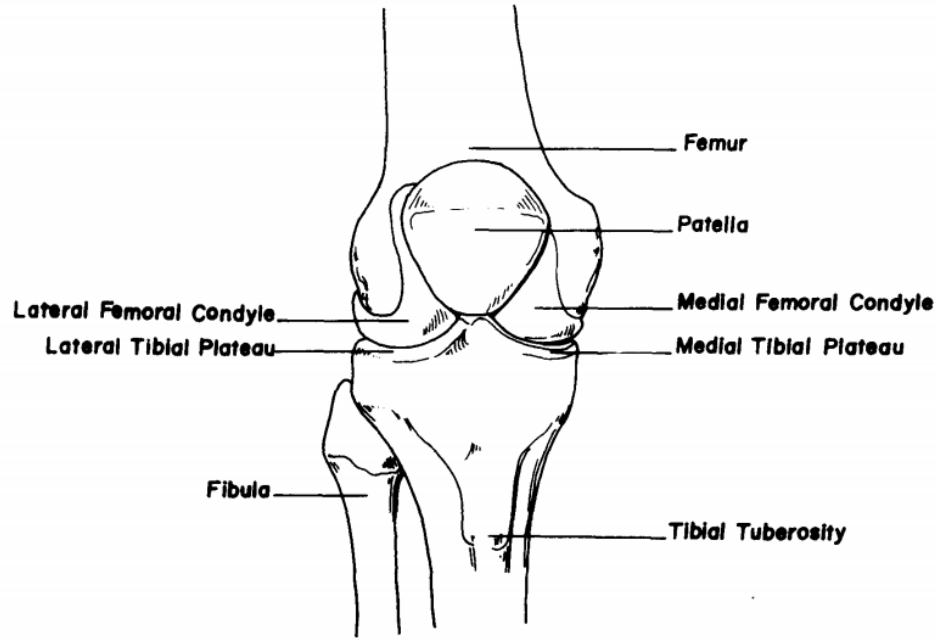


Figure 1-2: The major bones of the human knee [14].

1.2.1 The Muscles of the Knee

The primary muscle groups of the human knee are quadriceps, hamstring, and gastrocnemius (Figure 1-3). The quadriceps muscles are the main extensor muscles of the knee and consist of rectus femoris, vastus medialis, vastus lateralis, and vastus intermedius. All four quadriceps muscles insert on the proximal patella. The vasti muscles originate on the anterior side of the femur, while rectus femoris originates on illium on the pelvis.

The hamstring muscle group is mainly responsible for knee flexion and consists of four fibers: the semitendinosus and semimembranosus, which originate from ischial tuberosity (distal part of the pelvis) and insert on the medial tibial condyle, the bicep femoris – long head, which also originates from ischial tuberosity but inserts on the lateral side of the fibula, and the bicep femoris – short head, which originates from the posterior side of the femur bone and inserts on the fibula. The primary functions of hamstring muscles at the knee joint are to extend the knee.

The gastrocnemius muscles have two fibers: the lateral head originates from the lateral femoral condyle, and the medial head originates from the medial femoral condyle. Both insert on the posterior side of the calcaneus on the back of the foot as Achilles tendon.

In addition to these three main muscle groups, there are several other muscles acting at the knee joint. These muscle groups are mainly act as stabilizers for the knee joint stability. For example, the sartorius is a thin muscle originates from the pelvis and inserts on the tibia. The sartorius plays a minor role in knee and hip joint movements, such as medially rotating the tibial while the knee is flexed. The popliteus muscle originates from lateral femur and obliquely cross the posterior knee and inserts to the medial tibia. The popliteus muscle plays a role in “screw-home mechanism” of the knee. It helps lock the

femur through internal rotation at full extension relative to the tibia. Iliotibial tract or iliotibial band is another muscle crossing both the knee and hip joints. At the knee joint iliotibial tract provides lateral knee stabilization.

1.2.2 The Ligaments of the Knee

The main four ligaments of the knee between the femur and the tibia are the anterior cruciate ligament (ACL), the posterior cruciate ligament (PCL), the lateral collateral ligament (LCL), and the medial collateral ligament (MCL) (Figure 1-4).

Unlike muscle, the ligaments do not generate forces, but act as constraints resisting in tension. They act as passive forces to provide stability for the knee joint and to restrain abnormal motion [15–17].

The cruciate ligaments are often described as a four-bar linkage system [18,19] and facilitate the screw-home mechanism and consistent rollback and external rotation of the femur relative to the tibia [20,21]. The collateral ligaments are parallel ligaments on the medial and lateral sides of the knee and are primarily responsible for resisting the varus/valgus rotation of the femur relative to the tibia [17,22].

Another major ligament at the human knee is the patellar ligament. The patellar ligament, sometimes called the patellar tendon, originates from distal patella and inserts on tibia tuberosity [23]. The patellar ligament is an essential part of the extensor mechanism of the knee, transferring the quadriceps muscle forces to the tibia [24].

Additionally, there are other minor ligaments around the patella, providing stability to the patella during knee flexion, such as the lateral patellofemoral ligament (LPFL), medial patellofemoral ligament (MPFL), and patellomeniscal ligament.

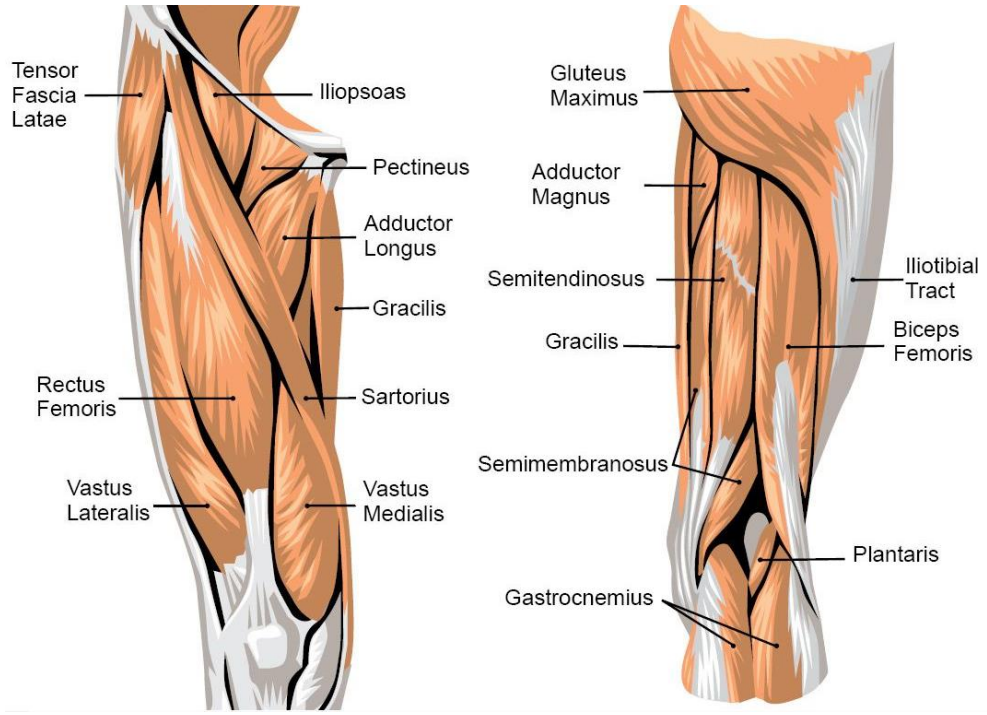


Figure 1-3: The muscles of the knee joint are shown here from the anterior (left) and the posterior view (right) (image from anatomynote.com).

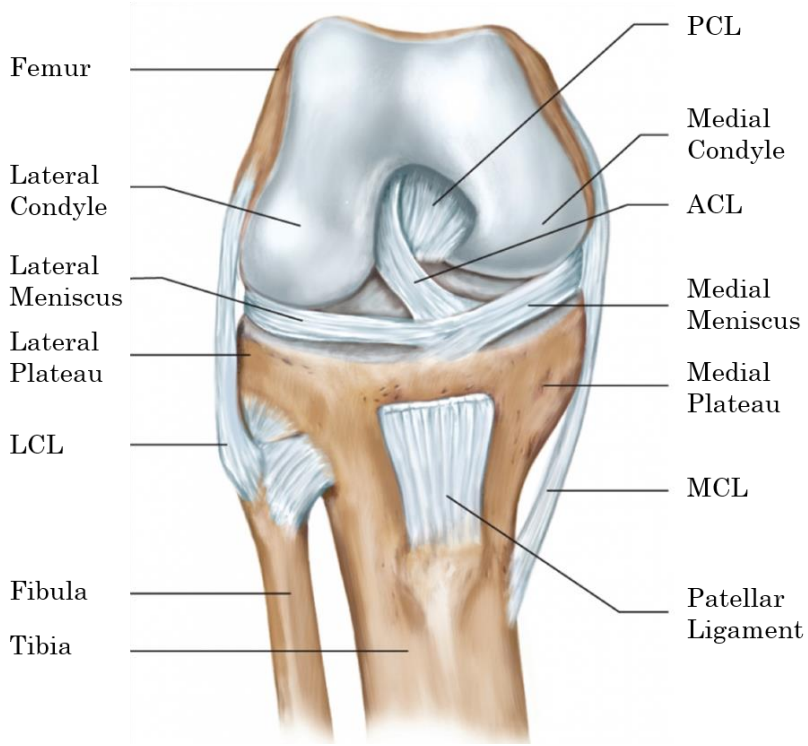


Figure 1-4: Major ligaments of the human knee joint (image modified from coreem.net).

1.2.3 The Motion of the Knee

In essence, the human knee joint can be defined as a one-degree of freedom joint, which is flexion. With properly functioning ligaments working in unison with geometry, the other two rotations and three translations are constrained and defined by flexion and constraints. In contrast, if the ligaments have laxity and are not providing proper constraints, the human knee can be considered as a six degree of freedom system, with three translational and three rotational components. The translations include AP, ML, and SI translations alongside those axes. And the rotations are called flexion/extension (FE), varus/valgus (VV), and internal/external (IE) (axial) rotation about the ML, AP, and SI axes, respectively (Figure 1-5).

The kinematics of the normal knee is well established during the weight-bearing flexion activities [25–29]. At full extension, the femur internally rotates relative to the tibia exhibiting the "screw home" mechanism. During dynamic knee flexion, the femur rotates externally relative to the tibia, and correspondingly the lateral condyle moves progressively posteriorly as knee flexes (Figure 1-6).

Fluoroscopic studies have reported lateral condylar rollback values up to 21.0 mm throughout a deep knee bend activity [30]. The medial condyle, on the other hand, generally does not exhibit such as much rollback throughout the flexion, with average rollback of 1.9 mm [30]. In fact, previous studies have revealed that the medial condyle may actually experience an anterior motion pattern between 90° to 120° of knee flexion. It has been reported that the medial condyle for the normal knee has moved up to 2.2 mm in the anterior direction with increasing knee flexion [31]. Cadaveric studies have shown similar patterns for the normal knee during active knee flexion. A study by Iwaki et al. documented 18 mm of lateral rollback and 1.5 mm of medial

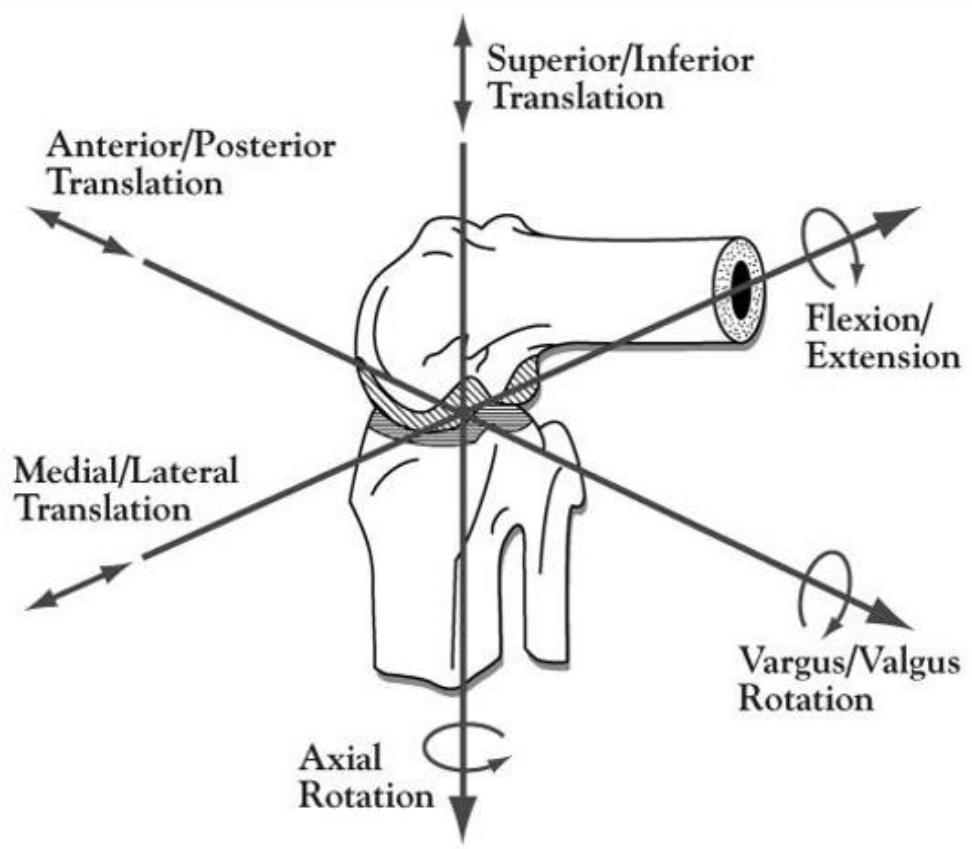


Figure 1-5: The knee joint is a six degree of freedom system with three translational and three rotational motion [32].

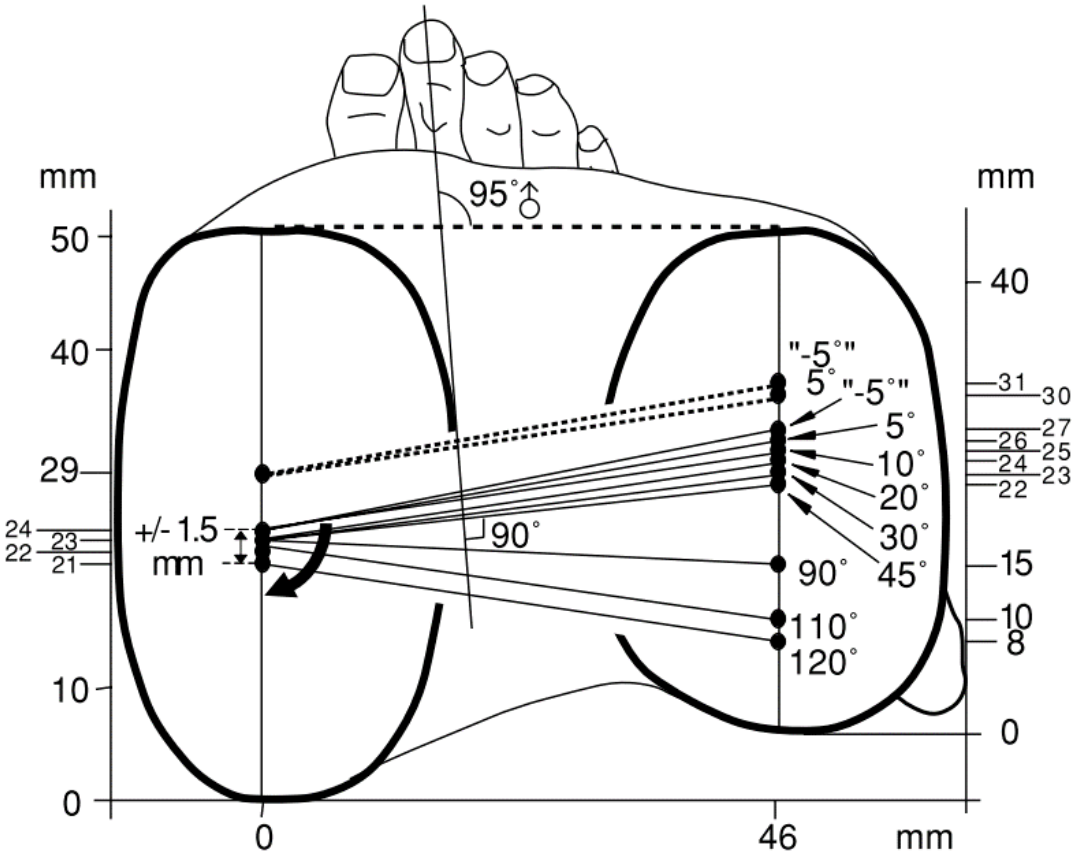


Figure 1-6: Tibiofemoral knee kinematics are shown here. The femoral lateral condyle moves posteriorly with knee flexion. The medial femoral condyle movement is limited compared to the lateral condyle. The combination of these two movements result in consistent femoral external rotation of the knee during knee flexion [26].

rollback in a cadaveric study [26]. The difference in the magnitudes of the lateral and medial condylar translation results in consistent external rotation of the femur relative to the tibia.

1.3 Total Knee Arthroplasty

Osteoarthritis, the most common joint disorder, signified by the excessive wear of joint cartilage, is most common in knee, hip, and spinal joints (Figure 1-7). Osteoarthritis of the knee is the most common cause of the pain and reduced mobility [33]. Knee arthroplasty is the late-stage treatment when other medical treatments are unable to improve the affected knee. Knee arthroplasty is a successful treatment at relieving pain and improving osteoarthritis patients' quality of life.

There are several types of knee arthroplasty, including total knee arthroplasty (TKA), unicompartmental knee arthroplasty (UKA), and bicompartmental knee arthroplasty (BKA). TKA is the most common. In a TKA procedure, the degenerative articulating surfaces are replaced with prostheses. The distal end of the femur and proximal end of tibia removed and replaced with metallic components, generally titanium or cobalt chrome.

Polyethylene bearing components are inserted in between these two components to provide a smooth articulating surface. Sometimes, the patella is resurfaced, and a polymer component is placed on the posterior patella (Figure 1-8).

The total knee arthroplasty has become a highly successful procedure to improve the mobility and pain relief in late-stage arthritic joints [34–38]. Since TKA surgery has proven to be very successful at relieving pain and improving osteoarthritis patients' quality of life, the number of total knee arthroplasty

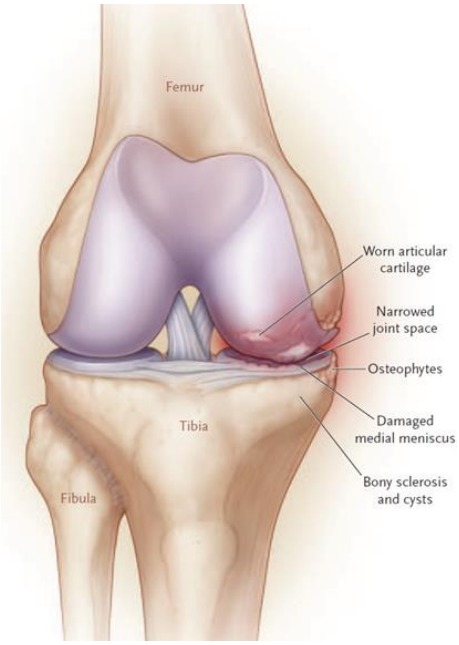


Figure 1-7: Osteoarthritis of the Medial Side of the Knee [39]**.**



Figure 1-8: A conventional TKA consists of at least three components: a femoral component rigidly attached to the femur, a tibial tray rigidly attached to the tibia, and a bearing insert placed between the femoral component and tibial tray. Often, the patella is resurfaced, and a component is placed on resurfaced patella.

(TKA) procedures has been increased over the past decades [40,41] and is projected to continue to grow [42]. It is estimated that the number of TKAs will grow by 673%, accounting for 3.48 million primary TKA procedures, by 2030 [43].

Additionally, the TKA design can be categorized based on the shape of the contacting surfaces, either femoral component condylar shapes or bearing insert plateau surfaces. There are three major types of femoral component shapes based on the sagittal curvature: single radius, multiple radii (J-curve), and gradually reducing radii (G-curve) (Figure 1-9).

The most commonly used femoral component shape is the J-curve design, which incorporates a large radius anteriorly and a smaller radius distally, to replicate the anatomical shape of the natural knee [44]. The instantaneous shift in the radius is believed to be a cause for mid-flexion abnormal kinematics [45], and therefore single radius designs were introduced featuring a uniform radius.

Additionally, gradually reducing radii (G-curve) femoral condylar designs, which incorporate a gradually reducing radius curvature, have been developed to improve the anteroposterior translation of the femoral component.

Furthermore, based on the amount of constraint associated with the bearing insert, as well as the decision to keep or resect certain knee ligaments, there are multiple specific types of TKA: posterior cruciate-retaining (PCR), posterior stabilizing (PS), bi-cruciate retaining (BCR), posterior cruciate sacrificing (PCS), bi-cruciate stabilizing (BCR), and medial pivot (Figure 1-10).

In the PCR design the ACL is resected and the PCL is retained. In the PS design, both cruciate ligaments are resected, but the functionality of the PCL is replaced with cam and post mechanism. In BCS designs, both cruciate ligaments are replaced with cam and post mechanisms.

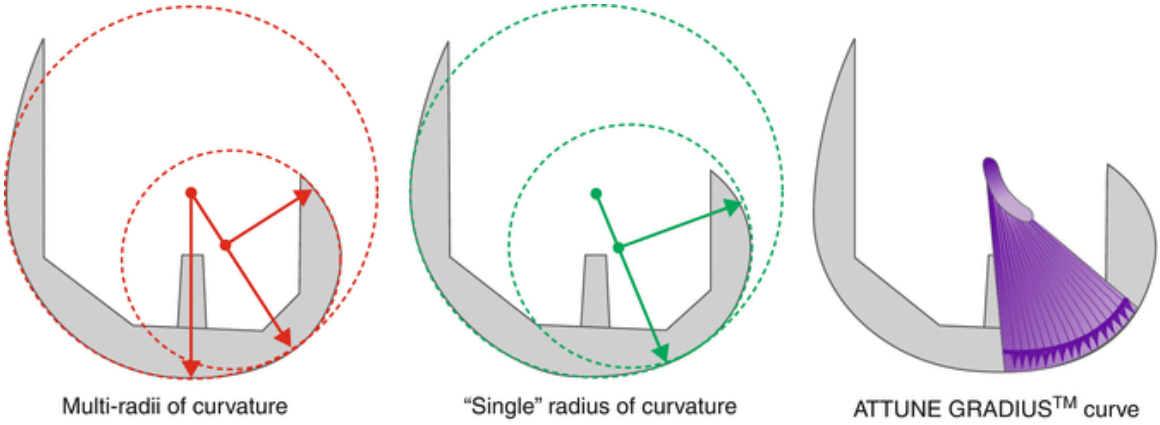


Figure 1-9: The femoral component can be made with different sagittal curvatures [46].

In the PCS design, both cruciate ligaments are resected, but there is no cam and post mechanism. The bearing of these designs is ultra-congruent, in which the anterior lips are raised to provide a physical constraint against anterior sliding of the femur.

In BCR designs both cruciate ligaments are retained. Table 1-1 summarizes theses design and how the cruciate ligaments are treated in these designs. The medial pivot design is similar to the PCS deign.

The idea of medial pivot design comes from the motion of normal knee, where the lateral condyle moves posteriorly while the medial condyle movement is very limited. The medial compartment is designed like a ball and socket joint to only allows for medial rotation without slipping. The lateral compartment is designed flatter to allow for posterior translation (Figure 1-11).

Furthermore, TKAs can be categorized based on the axial rotation of the bearing insert. As the name implies, in the fixed-bearing design the bearing insert is rigidly attached on the tibial tray and therefore there is no relative movement between the tibial tray and the bearing insert.

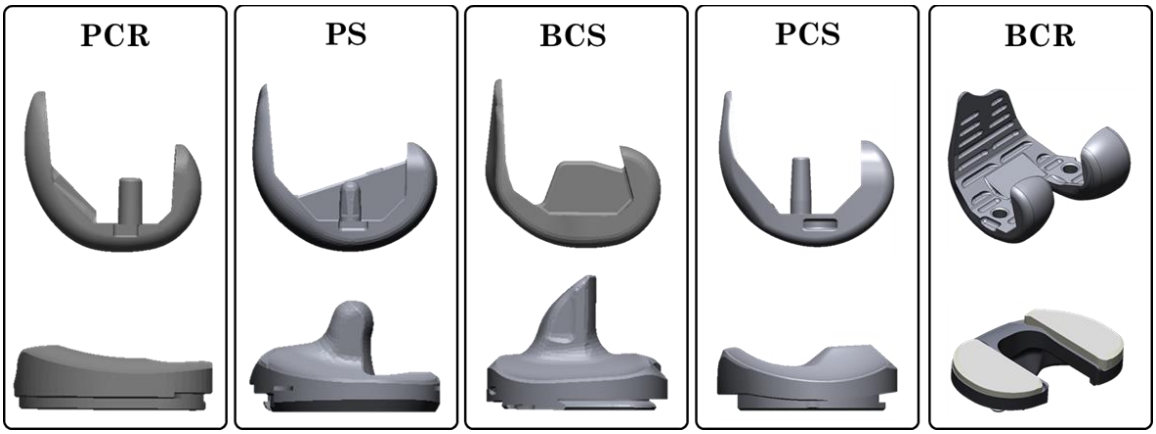


Figure 1-10: Different TKA types retain or resect cruciate ligaments. And often replace the functionality of these ligament with a form of physical constraint on the bearing insert.

Table 1-1: The cruciate ligaments are treated differently for each TKA type.

	ACL	**PCL**
PCR	Resected	Retained
PS	Resected	substituted with cam-post
PCS	Resected	substituted with ultra-congruent bearing
BCS	Substituted with cam-post	Substituted with cam-post
BCR	Retained	Retained



Figure 1-11: the medial compartment in the medial pivot design is similar to a ball and socket joint to restrict the medial motion. The lateral compartment is flatter to allow femoral lateral rollback (image modified from [47]***).***

On the other hand, the bearing in the mobile-bearing design is able to axially rotate relative to the tibial tray. The rationale behind mobile-bearing TKA is that the rotation of the bearing might encourage additional femorotibial rotation, reduce stresses applied on the bearing from the femoral component, and ultimately reduce the component wear.

1.4 TKA Complications

Despite the high rate of survivorship in TKA implants [34–38], there are still considerable numbers of dissatisfied patients having a TKA [2,48–51]. One can assume that there are many reasons associated with patient dissatisfaction after TKA, but most issues are attributed to the patients expecting more out of their implant. Patients are no longer satisfied when pain is simply diminished, as they are desiring better function and the ability to perform a wide range of

activities under normal conditions [49,51–55]. Restoring normal-like knee kinematics can contribute to improving the functional outcome of a TKA and therefore can increased patient satisfaction [56]. An even more pressing need is to restore normal kinematics for younger, more active patients demanding to live a more active lifestyle post TKA [57].

Due to various reasons, such as severe bone damage, altered knee joint geometry, soft tissue deficiency, and surgical procedure [29,58–65], it is not surprising that the TKA kinematics vary more considerably than those observed in normal knees [58,59,63,66,67]. Specifically, cruciate retaining (CR) designs have been shown to exhibit paradoxical anterior slide of the femur with flexion leading to increases patellofemoral pressure and anterior knee pain [45,68–72]. Although the cam-post mechanism in posterior-stabilized (PS) TKA is designed to prevent the anterior sliding of the femur, the mechanism does not engage until late flexion. This makes PS designs vulnerable to similar anterior movement during the mid-flexion, and studies have reported non-progressive rollback of the femur [63,73]. Progressive femoral rollback is one of the key features of the kinematics of a normal healthy knee joint, as it increases the moment arm of the extensor muscles and therefore reduces the amount of muscle forces required to perform daily activity [74]. Thus, it is believed that achieving more progressive rollback and preventing paradoxical anterior sliding can improve TKA functionality.

1.5 TKA Evaluation

With such a multitude of TKA designs, it has become necessary to develop methods to assess and compare each design quantitatively to distinguish the differences and evaluate the potential outcomes. Unfortunately, it has been documented in numerous studies that 20% of TKA patients are dissatisfied with their knee implant [2,48–51]. One of the most common causes of

dissatisfaction is the limited functionality of the implanted knee compared to a non-implanted, normal knee. Therefore, developing new implant designs to mimic the native joint kinematics is a common goal, not only for implant companies but also for the orthopedic surgeons striving to implement the most novel implant designs to achieve the better post-operative functionality for their patients. There are various in vivo and in vitro methods that have been developed to assess both kinematic and kinetic outcomes associated with TKA designs. In addition, many of these devices and tools can provide insight into predicting implant life.

One such TKA evaluation method is to use wear simulators, which place the TKA in a mechanical device that attempts to replicate the in-vivo loading conditions over millions of cycles. Cadaveric simulators are another method to assess TKA outcomes. Cadaveric rigs implant the TKA into a cadaver leg, which is then manipulated, along with the extensor mechanism, to analyze and predict outcomes. These methods provide more "in vivo-like" conditions because they analyze the kinematics of the knee under the soft tissue constraints the ligaments around the knee. The in vivo joint loads also can be determined using telemetry devices. In this case, joint forces are determined using sensors placed within the implant. Finally, the kinematics of TKAs can be assessed using motion tracking using skin markers, roentgen stereophotogrammetric analysis [75,76], quasi- dynamic magnetic resonance imaging (MRI), and fluoroscopic registration techniques [77–83].

While all these methods are valuable, they have several drawbacks. First, all these methods require the physical, manufactured versions of the implants, and in many cases these methods also require the TKA to be implanted into patients. Second, these methods are often costly and time-consuming. Third, some of these methods can be highly invasive.

Mathematical modeling is another tool to evaluate the TKA. During the entire process of developing a new TKA design, a validated mathematical model can be a viable tool to help investigate the effects of the specific new features and/or entire new implants designs.

Chapter 2: Background

2.1 Mathematical Modeling

Using mathematical modeling, the motions and interactive forces between TKA components during various activities are defined with a series of differential equations of motion. There are different methods to derive these equations of motion. For example, Kane's dynamics and Lagrangian methods are two common methods to obtain the dynamic equations of motion. Although different in methods, both are reformulations of the classic Newtonian method, $\boldsymbol{F} = m\boldsymbol{a}$.

There are various types of mathematical models of the human body that currently exist, varying from commercially developed models to institutionally research developed models. The two most commonly used types of mathematical models in the field of biomechanics are inverse dynamics solution and forward dynamics solution models (Figure 2-1). This terminology originates from Newton's second law, $\boldsymbol{F} = m\boldsymbol{a}$, where obtaining the forces as an output from the motions (accelerations) as an input is the inverse solution technique, while calculating the kinematic outputs based on the forces and torques applied to the system is called forward dynamics. The inverse solution technique, which is more widely used, relies on knowing and inputting the motion of bodies into a multi-body system and obtaining the forces that derive the system [9–11,84–87]. In contrast, in the forward solution technique, forces and torques will be used to predict the unknown motion of the system [88–92]. The forward solution models are generally more advanced and complicated compared to inverse models. However, these models can be powerful tools to model the human body since they mimic the way the human body works, specifically by using forces (i.e. muscles) to drive motions (i.e. flexing and

extending). Conversely, the inverse solution models require known motion of human joints, more specifically the knee in our study, as an input to the system, often from fluoroscopic data. However, when evaluating new TKA design, such data is not readily available, and therefore forward solution models may be more powerful for cases such as these.

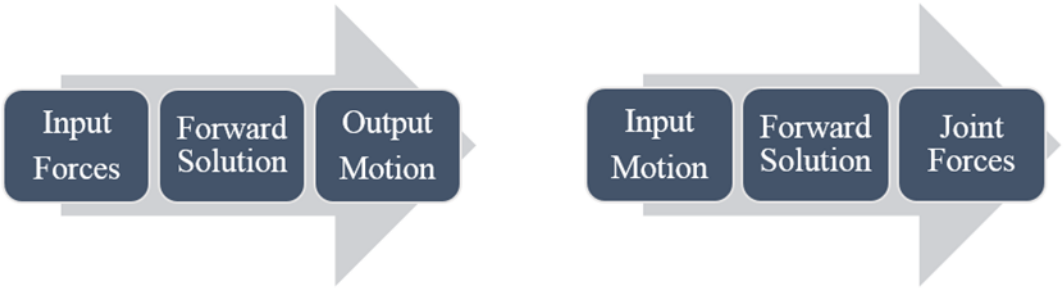


Figure 2-1: The difference between the inverse dynamics model (left) and forward dynamics model (right)

Furthermore, mathematical models can be categorized as optimization techniques or reduction techniques. Since there are many muscles exerting forces at each joint of the human body, there are more unknown than degrees of freedom. Optimization techniques revolve around defining an objective function and try to optimize this function [86,87]. Often the object function in human body mathematical models is to minimize the energy expenditure or to minimize the error between measured and simulation kinematics.

On the other hand, in the reduction techniques, the number of unknowns is reduced [10,93]. For instance, the main driver of the knee extension movement is the quadriceps muscles; hence, the roles of other muscles that are insignificant compared to quadriceps muscles can be neglected. While this technique may not be as anatomically accurate as advanced optimization techniques, the differences are often negligible, and reduction techniques often produce solutions faster [94].

Based on the technique to model the interaction in the human joint, mathematical models can be either rigid body models or finite element models (FEM). FEM models are developed based on the fact that all material, when in contact, will deform no matter how rigid they are [95,96]. Then, based on the properties of the material, the interaction forces and stress distributions on the articulating surfaces are calculated. FEM models are usually very complex and therefore very time-consuming. FEM medals are especially useful in predicting the wear patterns of the TKA components. On the other hand, rigid body models are developed based on the assumption that there is no deformation occurring between contacting surfaces [97]. Rigid body models can be very powerful tools to predict the kinematics of the TKA designs. Rigid body models are often used in biomechanics and aerospace fields where the dynamic system contain several bodies. In contrast to the FEM technique, it is generally assumed that there is no deformation occurs between bodies. Although FEM models are more reliable and accurate at predicting joint kinetics, they are often limited to only the bodies interacting at the joint of interest. With rigid body models, on the other hand, the effects of other bodies on the interactive forces and torques on the joint can be investigated. Rigid body models are generally faster than FEM models.

The mathematical model proposed in this study is based on a forward solution mechanics using a rigid body technique [98]. This model is a mathematical model of the lower extremity of a human body consisting of tibia, femur, patella, and pelvis bones (Figure 2-2). Also, the model incorporates bodies for TKA implants, the femoral component, tibial tray, bearing insert, and patella component. Ligaments are modeled as non-linear springs, and a PID controller was utilized to predict the quadriceps muscle forces. A contact detection algorithm was used to calculate the interactive forces at the tibiofemoral and patellofemoral joints.

The model is based on Kane's dynamics equation of motion, developed using the symbolic manipulation algorithm, Autolev. A graphic user interface (GUI) was developed that allows the user to create different TKA conditions, such as implant placement and component geometry manipulation to simulate different in vivo conditions (Figure 2-3). A more detailed description of this model is given in section 4.1.

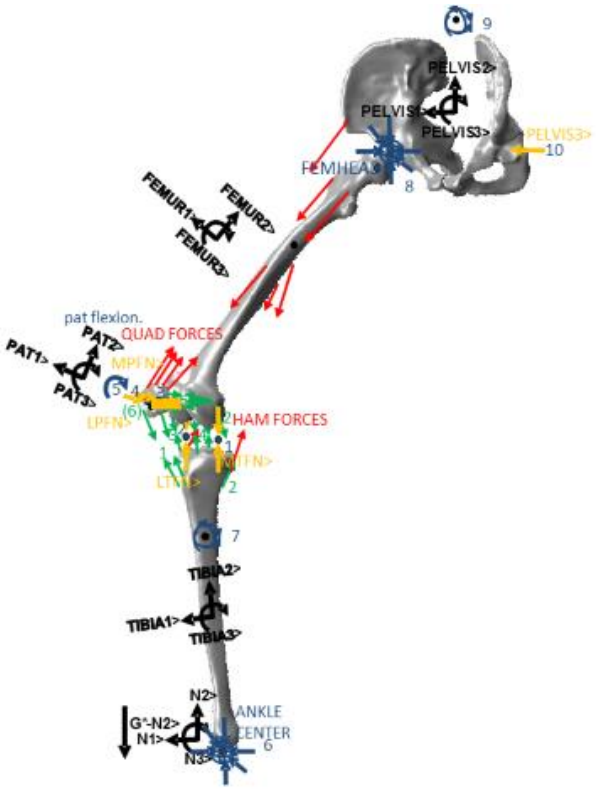


Figure 2-2: Free body diagram of the mathematical model. Soft tissue forces (muscles and ligaments) are defined with vectors.

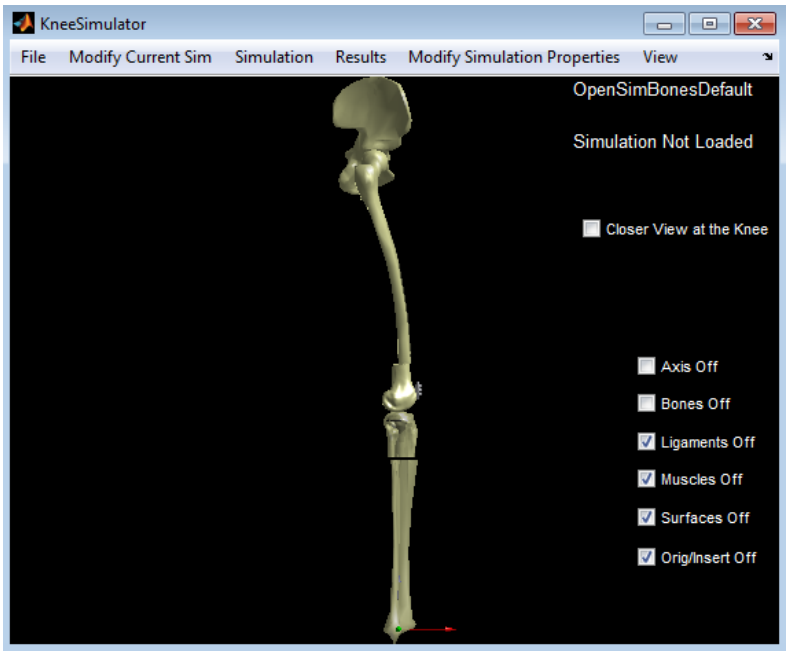


Figure 2-3: Graphic user interface of the mathematical model.

Chapter 3: Objectives and Contributions

3.1 Objectives

Surgical conditions such as component placement and soft tissue balancing, as well as TKA design features such as the conformity of the articulating surfaces or position of the post on a PS design, are all shown to play significant roles in TKA outcomes [99–102]. There are several methods to assess the outcomes of TKA, such as fluoroscopic studies, wear simulators, cadaveric rigs, etc. [67,103,104]. While these methods are effective at predicting TKA mechanics and providing insight into TKA outcomes, they are usually invasive, expensive, and not feasible to utilize during the early stages of implant development. A theoretical model capable of accurately predicting knee mechanics is of crucial importance to investigating novel implant designs. Additionally, mathematical models provide insight on aspects of the knee that are difficult to measure otherwise, such as soft tissue forces and properties. A validated mathematical model can expand our understanding of the effects of soft tissues and component alignment on the outcomes of TKA.

Therefore, the objective of this dissertation will be to advance the capabilities of an existing mathematical model to represent a more accurate physiological simulation of the human knee joint.

- The model will enhance the physiological aspect of the knee joint by the development of a more accurate muscle wrapping algorithm.
- More muscles will be added to the model.
- the two additional rigid bodies, comprising of the foot (toes and talus/calcaneus) will be added into the model.
- The model will allow the user to more thoroughly investigate the in vivo forces and kinetics of the knee joint by incorporating an inverse solution

model that can utilize kinematic motion from the forward solution model.

- The model will expand its functionality by incorporating more subjects of various deformity and conditions.
- Develop the capability to analyze mobile and fixed bearing revision knee arthroplasty designs, including hinged designs.
- More daily activities will be incorporated into the model.
- The accuracy of the model will advance through incorporating more clinically relevant simulations, as well as incorporating a settling algorithm to better model the early flexion simulations.
- The GUI will be advanced to incorporate new analysis features.
- The quadriceps mechanism has been advanced in the model to more accurately determine knee mechanics.

3.2 Contributions

As previously mentioned, there are several types of mathematical models in the field of biomechanics, especially at the knee joint, contributing to our knowledge of the biomechanics of the human knee. One such model is the one described herein, developed at the University of Tennessee, which utilizes a ridged body reduction principle using Kane's system of dynamics to evaluate both tibiofemoral and patellofemoral mechanics under simulated in vivo conditions. These results can then be used to assess prospective TKA designs and develop a better understanding of the interrelationship between design features, with the ultimate goal of restoring "normal" functionality. While previous versions of this model are incredibly sophisticated, the analyses are limited to a single theoretical patient performing a single activity. Like any other mathematical model, this model has its unique capabilities, assumptions, and limitation built into it.

The major contributions of this dissertation revolve around expanding the functionalities of this model, as well as addressing some of the limitations and assumptions of the existing model. Specifically, this dissertation brings the following contributions:

1) Develop a novel muscle wrapping algorithm and wrapping detection to accurately calculate the muscle forces and changes in the lines of action of muscle forces.
2) Expand the forward solution model to incorporate a validated inverse model to extend the tools to assess in vivo knee loads.
3) Develop a settling algorithm to better evaluate knee kinematics and kinetics at the beginning of each activity. Additionally, this algorithm will make the model capable of simulating activities that start in deeper flexion where high forces and torques make the system more unstable.
4) Expand the functionality of the model and create a more physiologically accurate representation of the human knee joint by:
    a. Incorporating the two separate bodies representing the foot in the model.
    b. Incorporating more muscles at the knee joint to accurately predict joint forces.
    c. Incorporating various subjects to extend the variability of the knee simulator.
    d. Incorporating relevant TKA outcomes.
5) Expand the mathematical model to be able to simulate other daily activities.
6) Expand the knee simulator to accommodate the simulation of revision TKA as well as primary TKA.
7) Provide a detailed kinematics validation against fluoroscopy data for several TKA types and validate the model kinetic predictions against teletibia data for several activities.
8) Advance the quadriceps mechanism in the model to allow for more accurate determination of knee mechanics.

Chapter 4: Materials and Methods

4.1 General Modeling Method

The mathematical model described in this dissertation is a continuation of an ongoing forward solution model of the knee joint to evaluate existing and future implant designs. This dissertation is an advancement of the previous model by developing new modules and further development of existing computational analyses. The overall goal of this model is to predict and evaluate the biomechanics of the human knee joint, especially kinematics and kinetics of the implanted knee to assess the outcome of various TKA designs and surgical techniques to help advance the current concepts in TKA design. This progression of the mathematical model has been advanced from a 2D inverse mathematical model to a 3D forward solution model [9–11,93,98,105–107].

4.1.1 Kane's Dynamics

There are many dynamics analysis methods available to mathematically model a multi-body dynamics system and formulate the equations of the motion. Three common-used methods are Newton-Euler equations, Lagrange's equations, and Kane's method. While all these methods are equivalent in nature, the applications and efficiencies vary. In the Newton-Euler method, forces and kinematics for all bodies of the system must be calculated. Therefore, this method is not efficient for multibody systems where calculating every reactive force and torque at the joint is not required.

In Lagrange's method, all interactive forces and constraint forces that do not perform work are disregarded. While Lagrange's method is more efficient than the Newton-Euler method, it is not very efficient for a large multibody dynamic system. Kane's method offers the advantages over both of these methods. By

introducing generalized forces, there is no need to solve interactive forces leading to greater efficiency, unless specified by the user [108]. Additionally, there is no need to calculate and differentiate energy equations. The equations of motion in Kane's dynamics are derived from the below equation:

$$F_r + F_r^* = 0 \quad (r = 1,2, \dots, n)$$

Where n is the number of generalized coordinates of the system, F_r is the sum of the generalized active forces on the system, and F_r^* is the sum of generalized inertia forces. The generalized inertia forces are contributing to the inertia forces related to accelerations (either linear or angular) of the bodies. In other words, Kane's equation is just a reformulation of Newton's second law, $F = ma$, where the terms related to the acceleration are transferred to the other side of the equation. Kane's dynamics is a highly systematic method that uses the concept of generalized velocities and generalized speeds. Although these terms are purely mathematical concepts and do not have physical meaning, these concepts are the reason why Kane's method is more appealing to analyze complex multi-body in the field of aerospace and biomechanics.

Autolev is an interactive symbolic manipulation program, developed by a group of engineers, led by David A. Levinson and Thomas R. Kane [109–111], and based on Kane's dynamics method. Autolev allows users to formulate equations of motion in and step by step manner to define the dynamic system structure. In the concept of the current dissertation, the lower extremity of the human body, from toes to torso, is created in the Autolev program as bodies. Then, the relevant points, such as soft tissue attachments and interactive contact points between bodies are defined for bodies. Next, the soft tissue forces and interactive forces at each joint are defined into the system to generate the equations of motion of the system based on Kane's dynamics principals.

Autolev creates a C++ program based on the definition of the bodies and the geometries of the dynamics system. These geometric definitions serve as inputs of the dynamics system. The C++ program will be modified to incorporate muscle controller and contact detection algorithm, to calculate muscle forces and knee joint contact forces. Then, the C++ program solves the differential equations of motion.

4.1.2 General Setup of the Model

A total of five bones are defined in the mathematical model: foot (heel and toes are modeled separately), tibia, femur, patella, and pelvis (pelvis and torso). Additionally, four implant components are defined in the system: tibial tray, femoral component, bearing insert, and patellar component (Figure 4-1). The masses of each body are defined as a percentage of total body weight (Table 4-1). The femoral component, the tibial tray, and the patella component are rigidly attached to the bones and therefore are modeled as frames. The attachment sites of soft tissues, muscles and ligaments, are defined on the relative bones (Figure 4-2).

Table 4-1: The masses of bodies are defined as a percentage of the total body-weight.

Bodies	Body-weight Percentage
Foot	1.4%
Tibia	4.9%
Femur	11%
Patella	0.5%
Torso	32.1%
Bearing Insert	0.05%

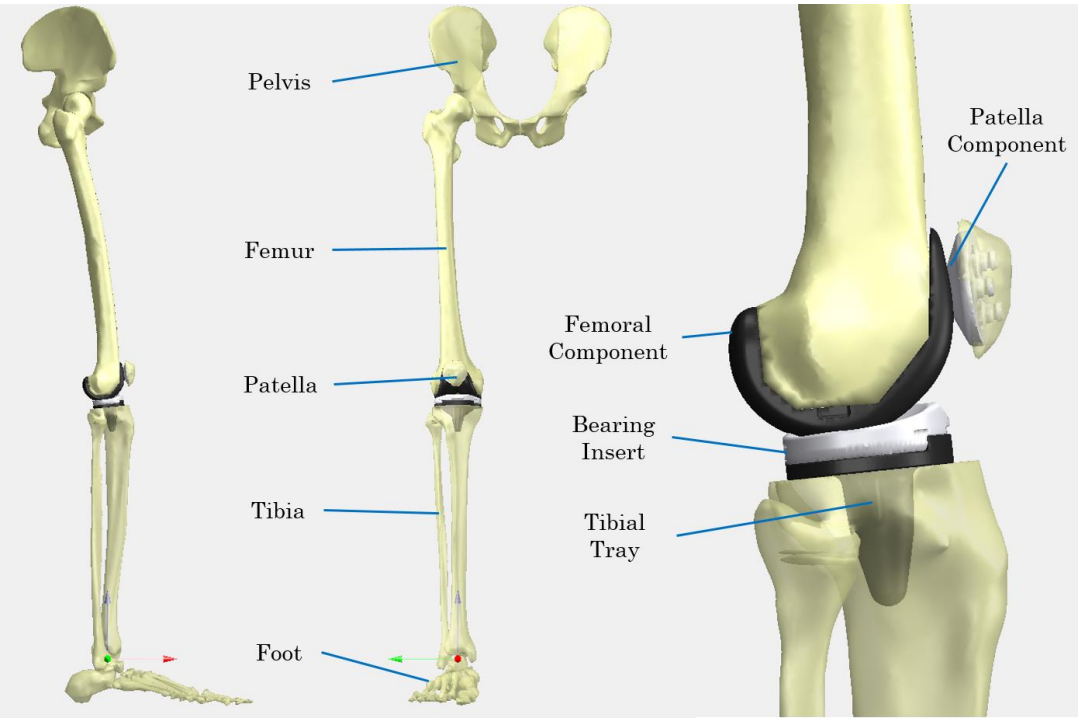


Figure 4-1: Bones and relative components implemented in the knee model.

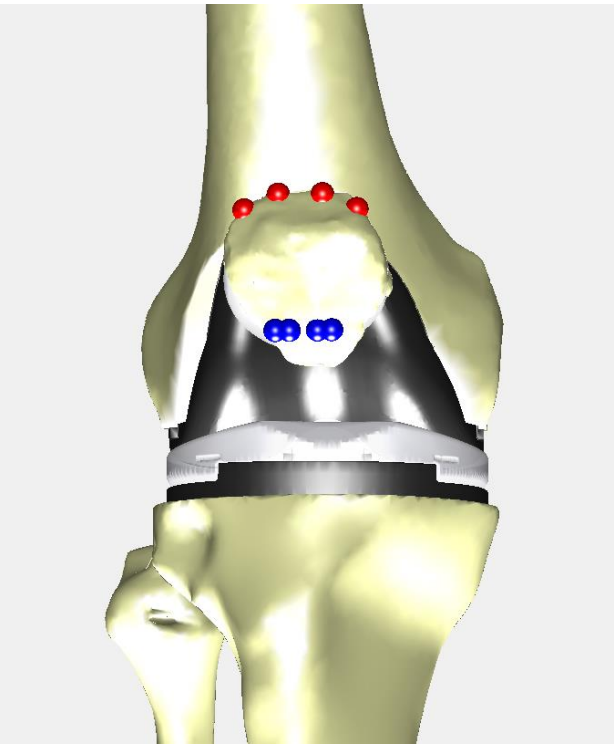


Figure 4-2: Quadriceps muscle attachments (red) and patellar ligament attachments (blue) are shown.

4.1.3 Graphical User Interface

Ultimately, the forward solution model is a computational tool based on the development of differential equations to assess the TKA outcomes in various conditions. Therefore, such a model should allow the user to easily perform simulations for these conditions. The presented forward solution model incorporates a graphical user interface (GUI), which allows the user to visualize the model and perform multiple simulations (Figure 4-3).

Several aspects of the knee model can be controlled by the user through the GUI, including soft tissue properties, the ligaments insertions and origins on the bones, the placement and alignment of the components relative to the bone, geometry of contacting surfaces, specified motion of the system, etc. Finally, the GUI updates the inputs of the system based on these changes. Figure 4-4 indicates the interaction between the GUI, Autolev, and C++ code and how the forward solution model is structured.

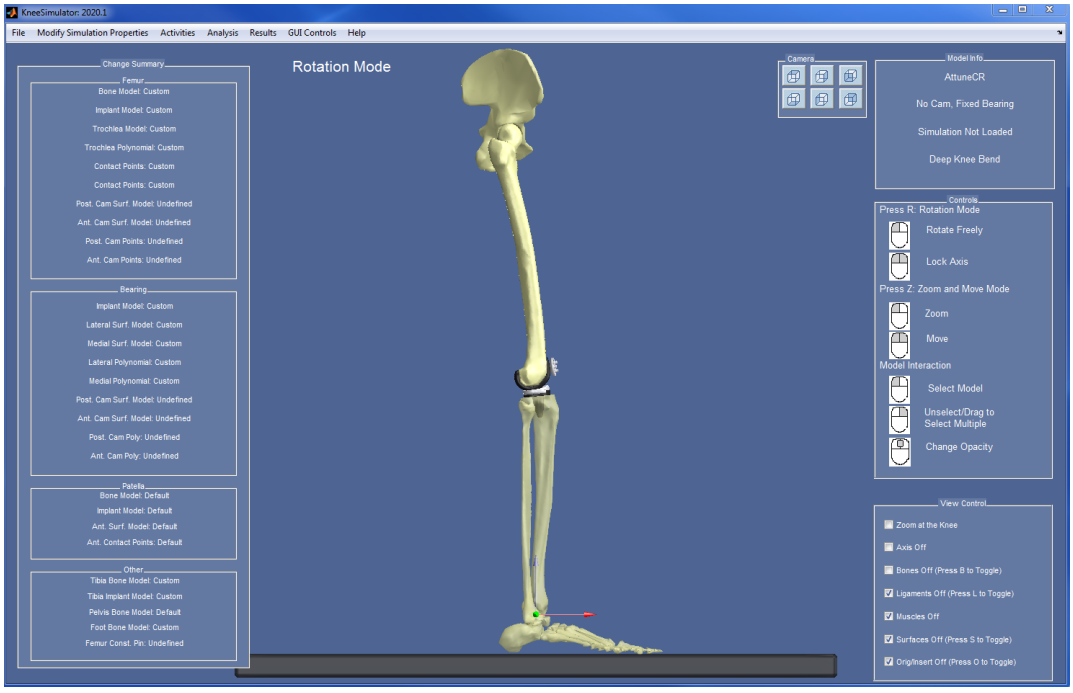


Figure 4-3: Graphical user interface of the forward solution model.

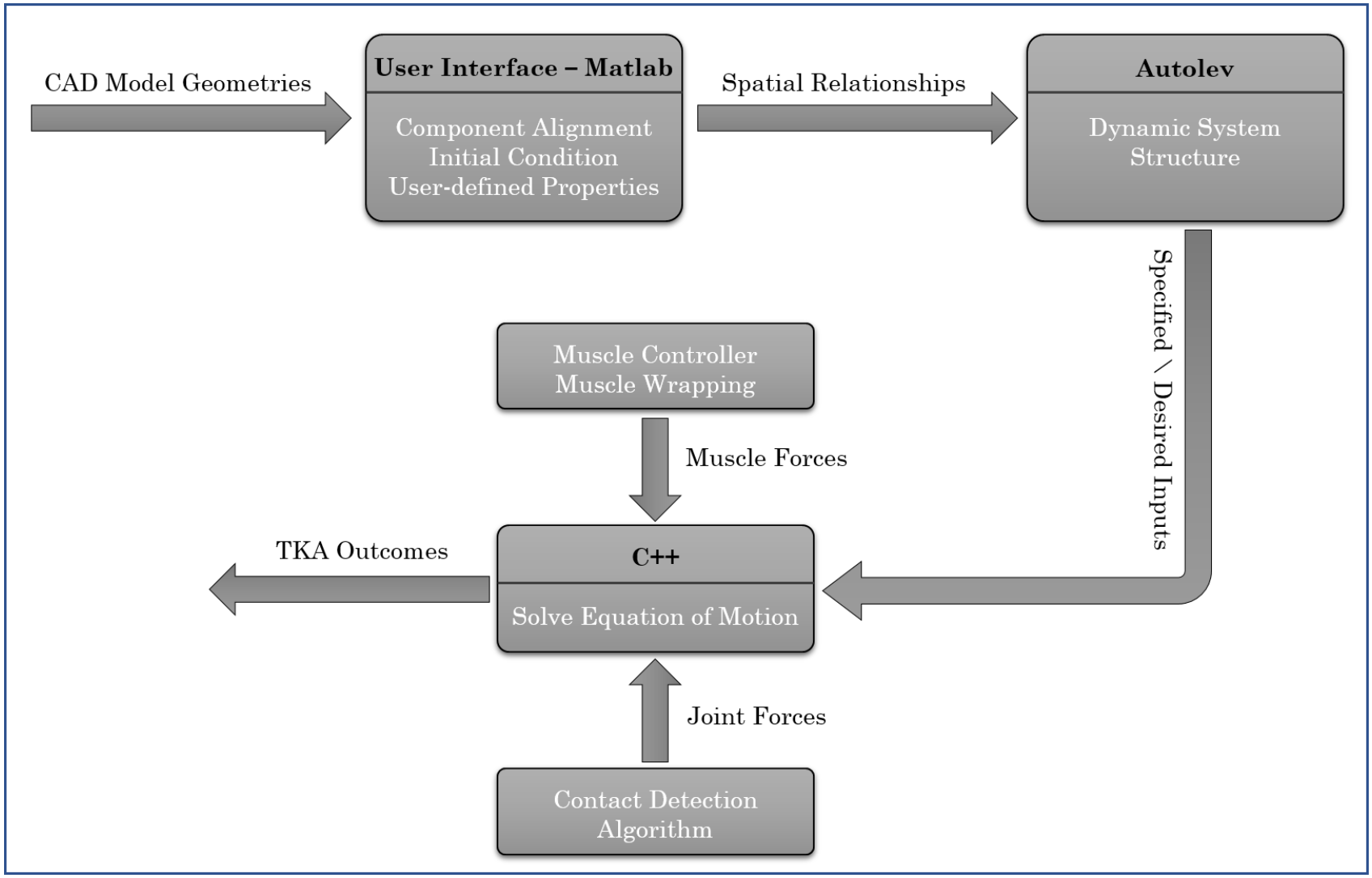


Figure 4-4: The forward solution model overall process is shown.

4.1.4 Ligaments

There are several ligaments included in the mathematical model, including the major knee ligaments (ACL, LCL, MCL, and PCL) and the patella ligaments (LPFL, MPFL, and MPML). The patellar ligament is also modeled in the same fashion as other ligaments.

The ligaments are modeled as a bundle of fibers to account for the thickness of the ligaments. Additionally, some of the ligaments have two or more bundles. The ligaments are defined as non-linear spring [112] between insertion and origin. The ligament force is applied between the insertion and origin and is calculated by the equation

$$F = \begin{cases} 0 & \varepsilon \leq 0 \\ {}^{k}/_{2}\,(L - L_0) & 0 \leq \varepsilon \leq 2\varepsilon_1 \\ k[L - (1 + \varepsilon_1)l_0] & 2\varepsilon_1 \leq \varepsilon \end{cases}$$

where k is the ligament stiffness, adapted from literature [112–115] (Table 4-2), L is the current length of the ligament as each time step, L_0 is the ligament slack length, can be specified by the user or calculated as a percentage of the initial ligament length, ε_1 is the reference ligament strain adapted from literature [89,116], and ε is the ligament strain as each time step calculated by the equation

$$\varepsilon = \frac{L - L_0}{L_0}$$

The GUI allows the user to change the insertion and origins of the ligaments (Figure 4-5). Additionally, the user can update the stiffness of the ligaments to simulate possible damages made on the ligaments during the surgery.

Table 4-2: Ligaments stiffness coefficients implemented in the mathematical model.

Ligament	No. of Bundles	Bundles	Stiffness (N/mm)
ACL	2	Posterolateral (PL)	108
		Anteromedial (AM)	108
LCL	1	-	180
MCL	3	Deep	72.2
		Anterior	27.9
		Oblique	21.1
PCL	2	Anterolateral (AL)	90
		Posteromedial (PM)	50
LPFL	1	-	5.4
MPFL	1	-	20.4
MPML	1	-	20.4
Patellar Ligament	2	Lateral	400
		Medial	400

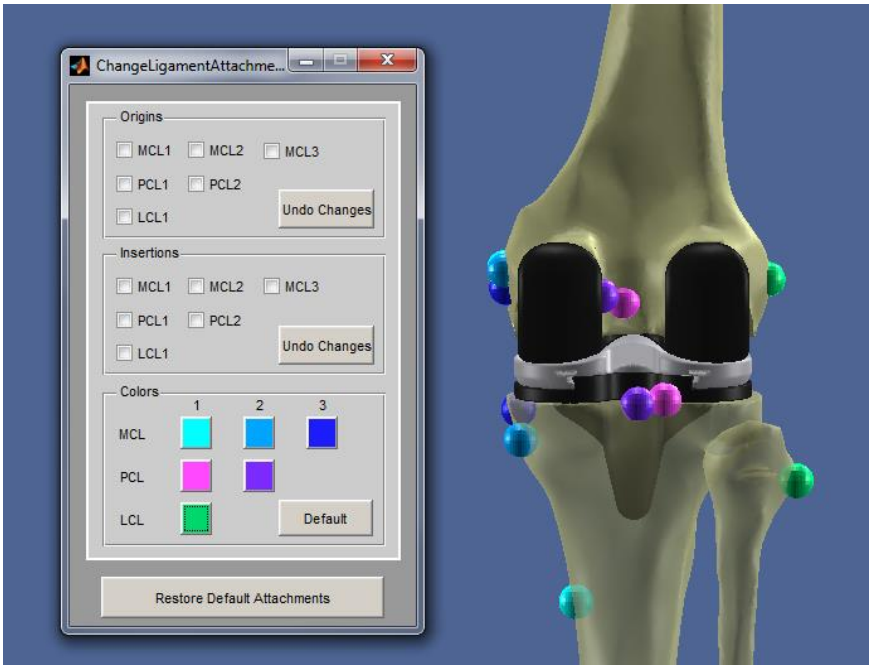


Figure 4-5: The ligaments attachments can be defined by the user in the GUI.

4.1.5 Muscles

The model contains three major muscle groups at the knee joint: quadriceps, hamstring, and gastrocnemius. The quadriceps muscle group includes rectus femoris, vastus lateralis, vastus medialis, and vastus intermedius. The hamstring muscle group has four muscles: bicep femoris – shorts head, bicep femoris – long head, semimembranosus, and semitendinosus. The gastrocnemius muscles include the lateral head and the medial head. Table 4-3 shows these muscles and their insertions and origins.

The muscles in FSM are defined as forces acting alongside the lines of action of the muscles. The line of action of a muscle is the straight line from insertion to origin when there is no wrapping, and the line of action passes through the appropriate wrapping points when muscle wraps around the bone (more on muscle wrapping algorithm on section 4.2). Similar to the ligaments, muscles are defined as bundles of fibers to account for the girth of each muscle. The

origins and insertions of each muscle are defined on the respective bone relative to the center of mass of that bone.

The quadriceps muscle forces are calculated using a muscle controller while the hamstring and gastrocnemius muscle forces are specified forces and can be updated for each activity. The muscle controller is a modified proportional-integral-derivative (PID) controller that acts on the knee flexion to obtain the quadriceps muscle force. The controller adjusts muscle force at each time step based on the difference between the actual flexion rate and the desired flexion rate at the current time step. A schematic of the muscle controller is shown in Figure 4-6. The muscle force is calculated using this equation

$$F_{Quad}(t) = F_{Quad}(t-1) + F_{add}(t)$$

Where $F_{add}(t)$ is the sum of each PID error at the current time step multiplied by the respective gain, and it is given by the below equation

$$F_{add}(t) = K_p * e_p(t) + K_i * e_i(t) + K_d * e_d(t) + K_{acc} * e_{acc}(t)$$

$$e_p(t) = Flexion_{actual}(t) - Flexion_{desired}(t)$$

$$e_i(t) = e_p(t-1) + e_p(t) * TimeStep$$

$$e_d(t) = \frac{e_p(t) - e_p(t-1)}{TimeStep}$$

$$e_{acc}(t) = Acceleration_{actual}(t) - Acceleration_{desired}(t)$$

Table 4-3: The incorporated muscles and their insertion and origins in the FSM.

Muscle Group	Muscle	Insertion	Origin
Quadriceps	RF	Proximal patella	Illium – pelvis
	VL	Proximal patella	Anterior femur
	VM	Proximal patella	Anterior femur
	VI	Proximal patella	Anterior femur
Hamstring	BFS	Lateral tibial condyle	Posterior femur
	BFL	Lateral tibial condyle	Ischial tuberosity – pelvis
	SMB	Medial tibial condyle	Ischial tuberosity – pelvis
	SMT	Medial tibial condyle	Ischial tuberosity – pelvis
Gastrocnemius	GL	Calcaneus on foot	Lateral femoral condyle
	GM	Calcaneus on foot	Medial femoral condyle

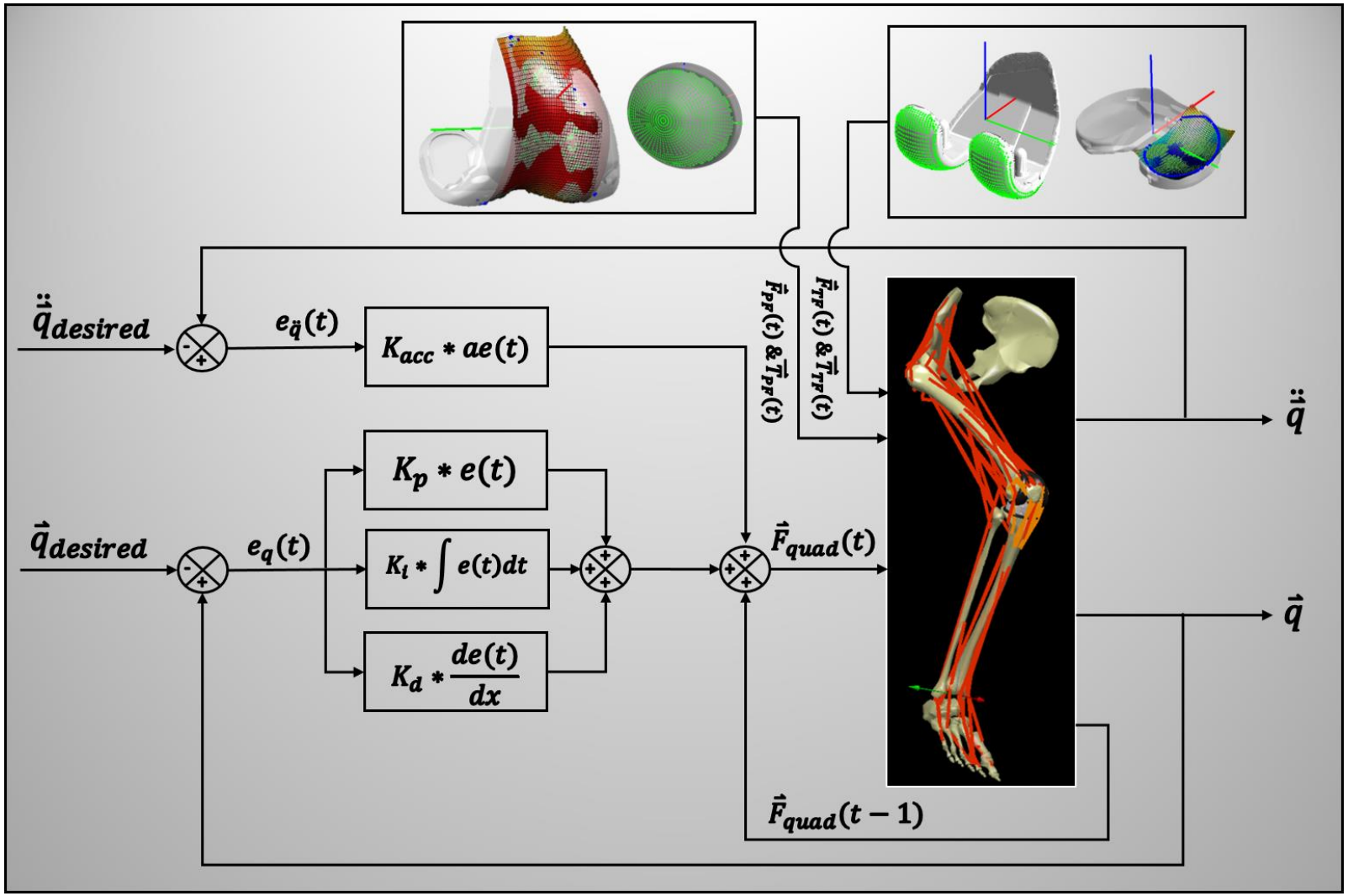


Figure 4-6: Schematic of the quadriceps muscle controller acting on the knee flexion.

4.1.6 Contact Detection Algorithm

A contact detection algorithm is developed to obtain the in vivo kinetics of the knee joint at the bearing surface interfaces, for both tibiofemoral and patellofemoral joints, as well as cam and post mechanism forces. The contact detection algorithm calculates the forces and torques at articulating surfaces. The geometry of one of the articulating components is modeled with a point cloud and the other is modeled as a surface polynomial. For the tibiofemoral joint, the femoral condyles are modeled as point clouds and the tibial plateaus are modeled with surface polynomials. For the patellofemoral joint, the trochlear groove is modeled with surface polynomial and the anterior surface of the patella component is modeled as a point cloud (Figure 4-7). When a cam post mechanism is applicable, the cam is modeled with a point cloud and the post is modeled as a surface polynomial.

In addition, a convex hull defines the boundary of the contacting surface. A convex hull is defined as a set of points that encompasses the perimeter of the contacting surface. The contact forces are calculated based on the amount of penetration that occurs for point clouds on the surface polynomial as well as material properties. The penetration is defined as the difference between the height of the point cloud and the height of the polynomial surface. First, the points on the point cloud are defined in the surface coordinate system using the transformation matrix between two contacting bodies. The polynomial height is also calculated and the difference between these two distances is defined as penetration. Then, using convex hull the program checks whether the contact point is indeed inside the convex hull. If the point is inside the convex hull and the height of point cloud is smaller than the polynomial height, a contact force is applied. The contact forces are obtained using a spring and damper model based on the stiffness of the contacting surfacing and the damping coefficient.

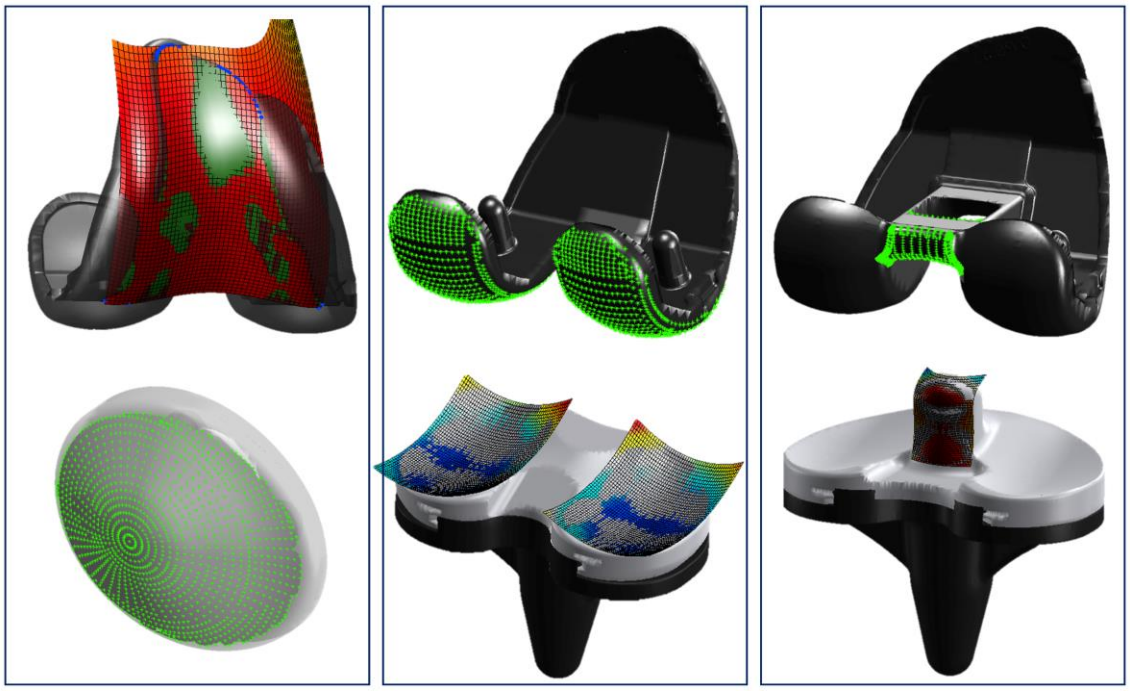


Figure 4-7: The contacting surfaces are modeled either as a point cloud or surface polynomial. Patellofemoral articulating surfaces are shown on left, tibiofemoral articulating surfaces are shown in the middle, and cam/post mechanism surfaces are shown in the right.

4.2 Muscle Wrapping Algorithm

In most mathematical models, muscles are modeled as thin strings commonly referred to as the line of action of the muscle, applying equal and opposite forces at the insertion and origin sites on the respective bones. These linear muscle forces along the line of action can create bone angular rotation through moments [117,118]. The moment created by the muscle force is the cross product of the muscle force and the muscle moment arm. The moment arm of a muscle is the smallest distance from the joint center of rotation to the muscle line of action (Figure 4-8).

However, in reality, the line of action of these muscle forces are not simply a straight line from insertion to origins. In the human body, muscles wrap around the bone and joints (Figure 4-9). Furthermore, the wrapping varies throughout the entire activity, and therefore the muscle line of action can change throughout the activity. For instance, the line of action of the muscle and the muscle moment arm vary during the activity.

The extensor mechanism is an essential part of the human knee joint and it has been shown that TKA designs that increase quadriceps moment arm can reduce the quadriceps muscle force and patellofemoral force [119]. Therefore, it is vital to the FSM to accurately implement a muscle wrapping algorithm to predict the quadriceps muscle line of action and muscle moment arm.

Several studies have investigated the effects of muscle wrapping on the reaction forces in different human and animal joints [120–123]. Kruidhof and Pandy [122] study the effects of muscle wrapping in the cervical spine. They compared two theoretical models with straight-line muscles and wrapped muscle with experimental data and concluded that the muscle wrapping has a significant effect on joint moments and muscle moment arm. Arjmand et al.

[123] showed wrapping of trunk thoracic extensor muscle resulted in lower muscle forces and spinal compression.

4.2.1 Updating the FSM

In the previous knee model, while there was a wrapping algorithm, although very rudimentary and did not accurately define the line of action of muscle forces. There was only one wrapping point around the femoral component, which was a fixed wrapping point. This can result in inaccurate lines of action and reduced moment arms (Figure 4-10).

Additionally, there is no algorithm to check at any flexion rate whether wrapping occurs. It is set to turn on and off at predefined fixed flexion angles. Moreover, the wrapping points are only defined around the femoral component, and there are no wrapping points defined around superior parts of the femur bone or even around the pelvis bone for rectus femoris.

To account for the femoral component geometry, five points are selected as wrapping points (Figure 4-11). These wrapping points are defined for each muscle fiber separately (RF, VL, VM, and VI) to detect the wrapping effect for each fiber separately. These are called inferior wrapping points and are defined to account for wrapping of the muscle at the distal part of the femur around the femoral component.

Additionally, a set of more superior wrapping points are defined to replicate the wrapping of the muscle around the femur bone. For the rectus femoris, which is attached to the pelvis, more superior wrapping points will be considered for wrapping around the pelvis bone thorough flexion.

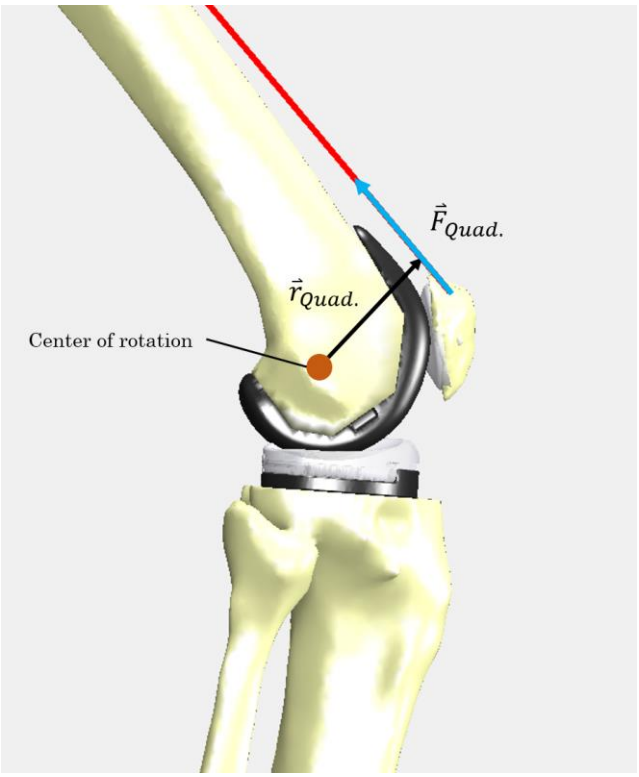


Figure 4-8: Muscle moment arm is defined as the smallest distance from the joint center of rotation to the muscle line of action.

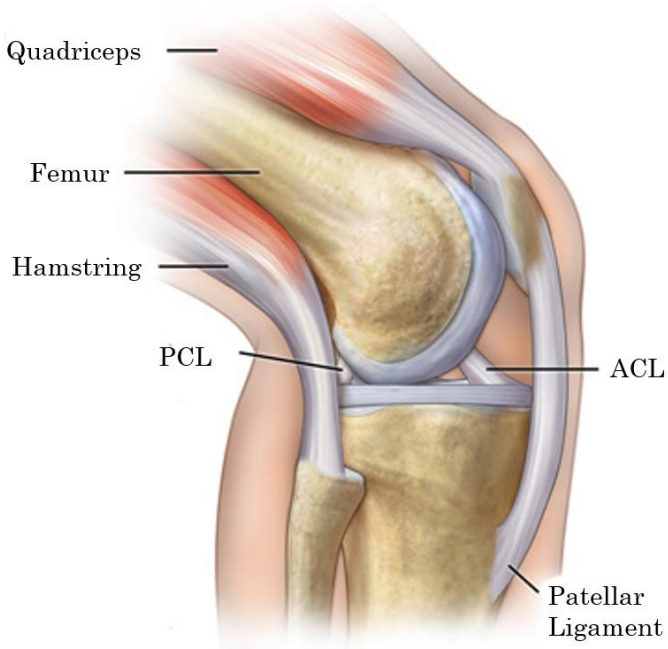


Figure 4-9: Muscles wrap around the bone. (Image modified from comportho.com)

The inferior wrapping points are defined with respect to the femoral component to show the wrapping in the sagittal plane. However, in the coronal plane, the ML location of these points cannot be defined as fixed relative to the femoral component.

During the range of motion of the activity, the patella moves in ML direction with respect to the femoral component, and that means the quadriceps tendon needs to move with the patella in ML direction (Figure 4-12).

To simulate this, the ML positions of the inferior wrapping points are not fixed to the femoral component reference frame and they allow to move with the patella in ML direction. The ML position of the points are defined as follows

$$\vec{P} = x\vec{F}_1 + y\vec{F}_2 + z\vec{F}_3$$

$$z = \vec{P}_{FoPo} \cdot \vec{F}_3$$

Where x, y, and z are the location of the inferior wrapping points in anterior, posterior, and lateral direction, respectively. And $\vec{F}_i$ is the femoral component reference frame unit vectors. $\vec{P}_{FoPo}$ is the position vector from the femoral component center of mass to the patella component center of mass.

The next step is to create a wrapping detection algorithm to detect whether wrapping occurs for each of these wrapping points at any flexion rate. It is based on the idea of the cross product of two vectors, one from origin to insertion and the other from origin to the wrapping point. If the sign of the cross product of these two vectors changes, it means that the wrapping occurs, and the line of action needs to change (Figure 4-13).

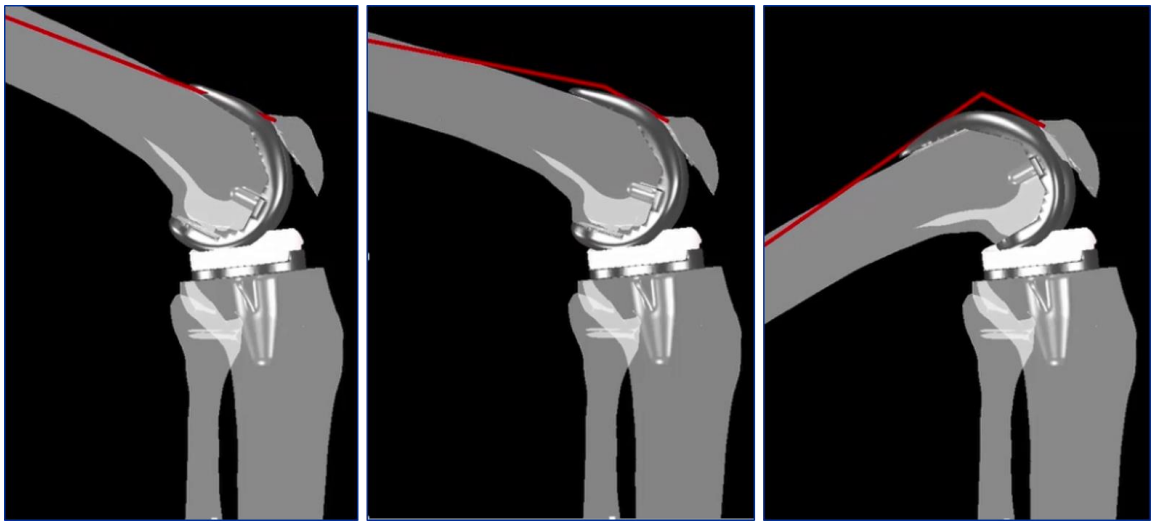


Figure 4-10: The current wrapping algorithm only accounts for one wrapping algorithm around the femoral component. The muscle line of action passes through the bone and the femoral component rather than wrapping about the bone.

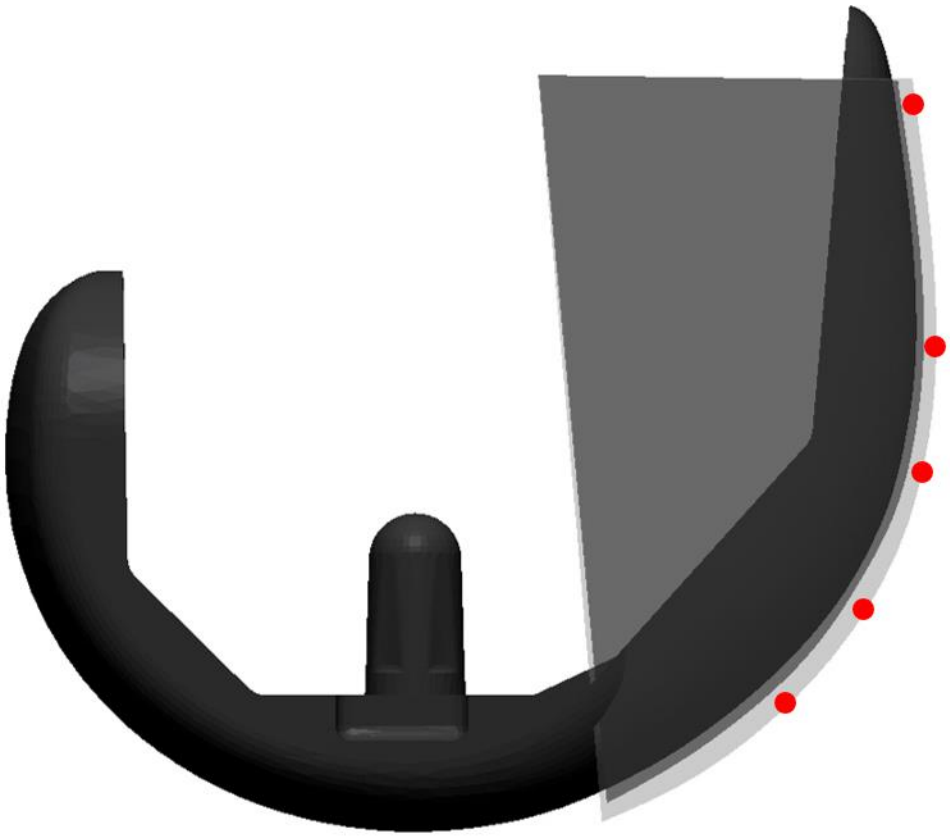


Figure 4-11: Five wrapping points are defined around the femoral component to account for the geometry of the femora component.

Therefore, new "wrapping check" parameters are introduced in the FSM for each fiber and each wrapping point. These wrapping checks are defined as follows

$$WrapCheck_i = \left(\vec{P}_{1i} \times \vec{P}_{2i}\right) \cdot \vec{F}_3 \quad i = 1, 2, \dots, 5$$

where $\vec{P}_{1i}$ is the vector from muscle origin to the i wrapping point and $\vec{P}_{2i}$ is the position vector from the origin to the insertion.

The quadriceps force for each fiber is defined as follows:

$$\vec{F}_{ins.} = F_{Quad} * WrapFactor_{off}\left(\vec{P}_{ins.\rightarrow org.}\right) + \sum_{i=1}^{5} F_{Quad} * WrapFactor_i(\vec{P}_{ins.\rightarrow wrap(i)})$$

$$\vec{F}_{wrap(i)} = F_{Quad} * WrapFactor_i\left(\vec{P}_{wrap(i)\rightarrow ins.}\right) \quad i = 1,2, \dots, 5$$

$$\vec{F}_{org.} = F_{Quad} * WrapFactor_{off}\left(\vec{P}_{org.\rightarrow ins.}\right)$$

$\vec{F}_{ins.}$, $\vec{F}_{org.}$, and $\vec{F}_{wrap(i)}$ are the forces applied to the insertion, origin, and the wrapping point i, respectively. F_{Quad} is the total magnitude of the quadriceps force. $\vec{P}_{A\rightarrow B}$ shows the position vector from point A to point B.

Wrapping factor values change based on the wrapping checks, and they are always between 0 and 1. The summation of all wrapping factors is equal to 1. The wrapping factors are calculated in the C++ code using below pseudo-code.

These wrapping factors gradually change from 0 to 1, which is why a, b, c, d, and e parameters are introduced to make sure not to suddenly jump from 0 to 1 for each wrapping factor. This would cause instability to the system.

```
if ( No wrapping ) {
      woff = 1;
      won1 = 0;   won2 = 0;   won3 = 0;   won4 = 0;
      won5 = 0;
}
else if ( First point wrapping ) {
      woff = a;
      won1 = 1-a;
      won2 = 0;   won3 = 0;   won4 = 0;   won5 = 0;
}
else if ( Second point wrapping ) {
      won1 = b;
      won2 = 1-b;
      woff = 0;   won3 = 0;   won4 = 0;   won5 = 0;
}

else if ( Third point wrapping ) {
      won2 = c;
      won3 = 1-c;
      woff = 0;   won1 = 0;   won4 = 0;   won5 = 0;
}

else if ( Fourth point wrapping ) {
      won3 = d;
      won4 = 1-d;
      woff = 0;   won1 = 0;   won2 = 0;won5 = 0;
}

else if ( Fifth point wrapping ) {
      won4 = e;
      won5 = 1-e;
      woff = 0;   won1 = 0;   won2 = 0;   won3 = 0;
}
```

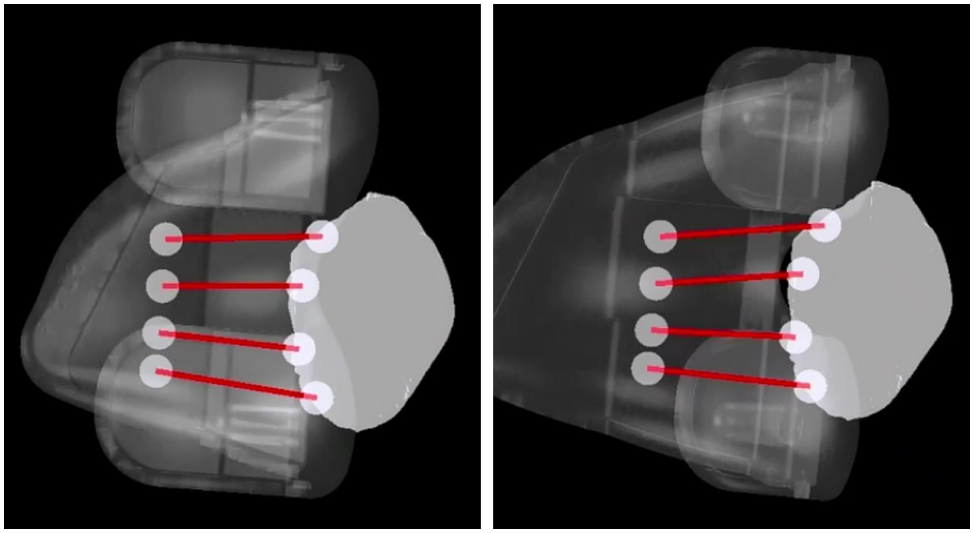


Figure 4-12: If the inferior wrapping points ML location are defined fixed to the femoral component, then the quadriceps tendon cannot move in ML direction with the patella.

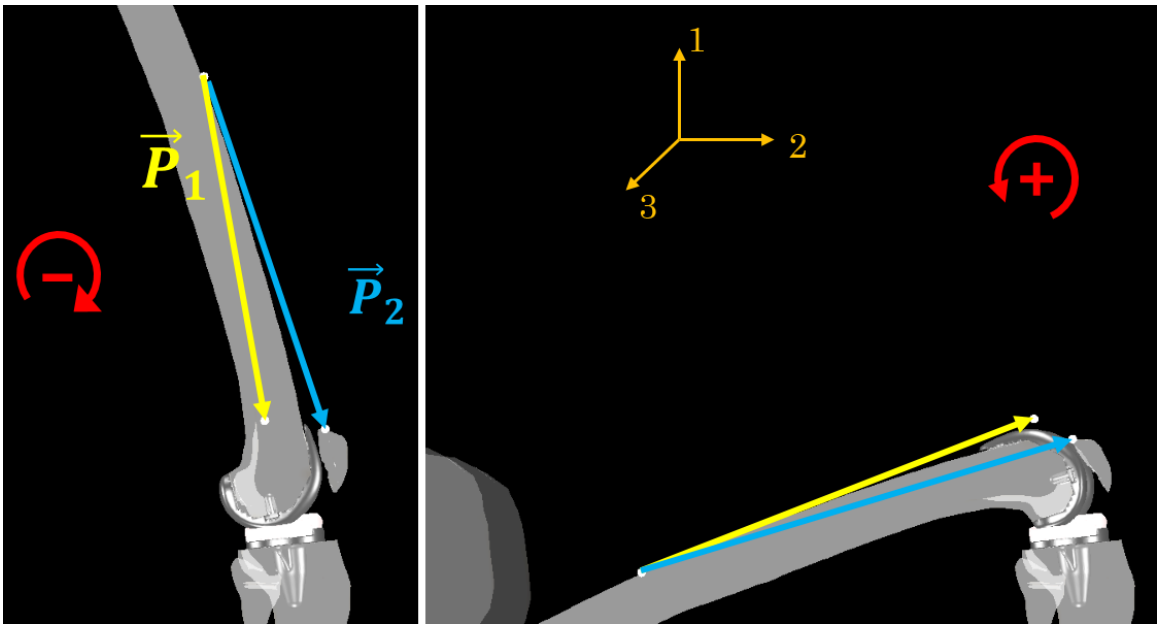


Figure 4-13: The wrapping algorithm detection is based on the change in the sign of the cross product of two vectors. The cross product is toward the sagittal plane, negative sign, when there is no wrapping (left) and is pointing toward outside the plane, positive sign when there is wrapping (right).

4.3 Integration of an Inverse Solution Model

The main two types of mathematical modeling in the field of biomechanics are inverse dynamics solution and forward dynamics solution. The terminology originates from Newton's second law, $F = ma$, where obtaining the forces from motion (acceleration) is an inverse solution, and vice versa (Figure 4-14). The inverse solution, which is more widely used, relies on collecting the motion of bodies inside a multi-body system and obtaining the forces that derive the system. In contrast, in a forward solution, forces and torques are used to predict the motion of the system. The forward solution models are generally more advanced and complicated compared to inverse models, and these models can be powerful tools to model the human body since they mimic the way the human body works by using forces and torques to derive motion. Unfortunately, FSM could become very unstable, leading to difficulty in defining the system.

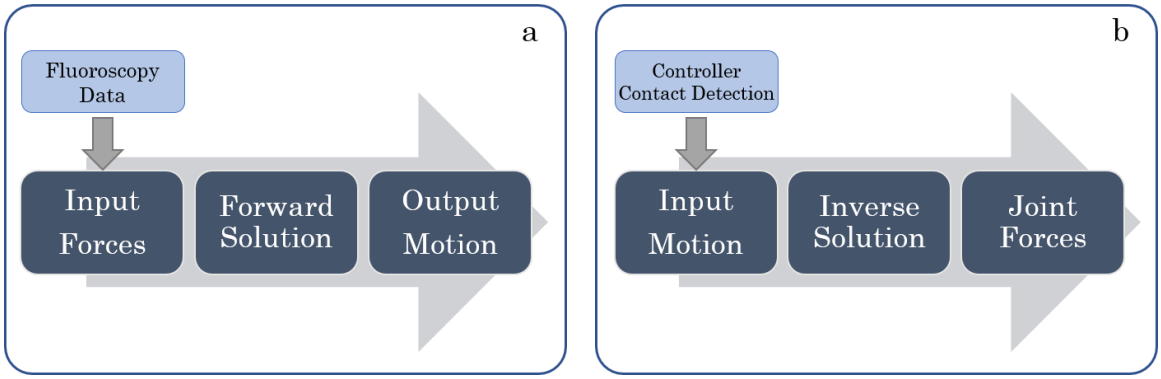


Figure 4-14: Simplified schematic diagram of two main widely mathematical solutions in biomechanics. a) Inverse solution models utilize motion to predict the in vivo forces. b) Forward solution models predict the joint kinematics based on the joint forces and torques.

The current FSM, which is based on Kane's dynamics, implements the aforementioned contact detection algorithm at the tibiofemoral and patellofemoral joints to calculate these joint forces and torques. Moreover, a

muscle controller is used to obtain the muscle forces. Then these forces and torques are fed to the core mathematical equation of motion of the knee joint to predict the kinematics of the knee joint. In order to have more functionality to the GUI, an inverse solution model is linked to the forward solution model, allowing to have more accurate force prediction based on the inverse model. In this method, the FSM model first will be used to predict the knee kinematics; then, these kinematics will be used as the inputs to the inverse solution model to predict the joint forces (Figure 4-15).

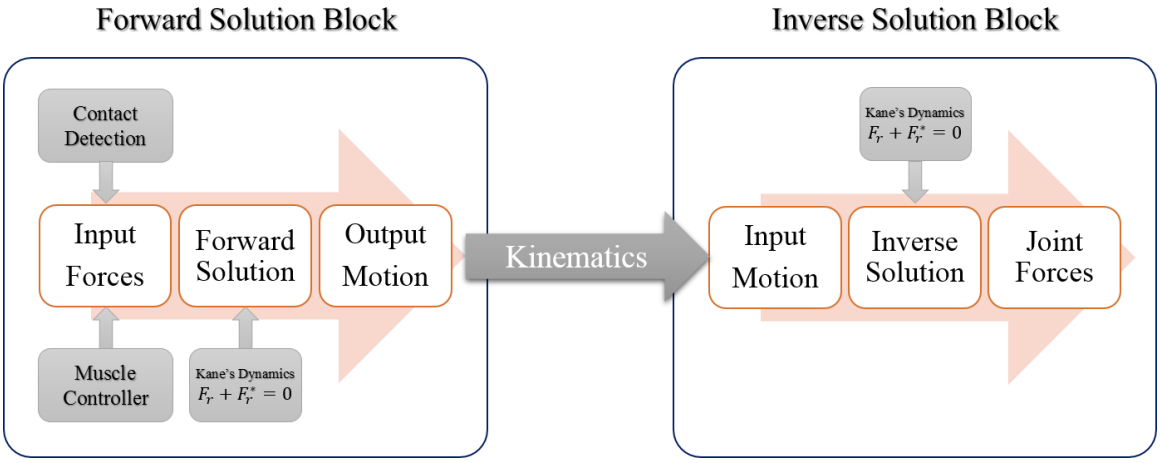


Figure 4-15: Validated inverse solution model implemented in the GUI based on the forward solution outcomes.

The inverse solution model linked to the FSM is a validated mathematical model of an implanted knee joint [9–11]. It was utilized in numerous previous studies, using the data fluoroscopic studies as input to the model to predict the in vivo contact forces, both in tibiofemoral and patellofemoral joints. In fluoroscopic studies, the in vivo kinematics can be gathered from fluoroscopy images.

Two types of kinematic data are used in the inverse solution mode (Table 4-4). First, angle measurements from fluoroscopy images are determined, including

tibia angle, knee flexion angle, quadriceps tendon angle, patella angle, and patella ligament angle. These measurements are in degrees and are obtained in 2D space since the fluoroscopy images are from a sagittal view (Figure 4-16). Second, the translations of lateral and medial contact points relative to the femoral component and also the femoral component center of mass relative to the bearing insert\tibial tray (Figure 4-17).

The model consists of the lower body bones from ankle to hip, modeled as rigid bodies. The ground reaction forces are applied at the ankle and are normalized based on the subject's weight. Lateral and medial tibiofemoral contacts are separately modeled, while the patellofemoral joint is modeled as a single point contact mechanism. All collateral and cruciate (where applicable) are modeled as non-linear elastic springs (Figure 4-18).

To make the inverse solution model work properly, the exact same information must be fed into the model. Therefore, the first step is to make the kinematic outputs of the FSM compatible with these parameters. Hence, new kinematic parameters will be defined in the FSM model based on the inputs of the inverse model. The next step is to add the ability of inverse analysis to the GUI. To this end, once the forward simulation is complete, the user can start the inverse simulation based on the outcomes of the inverse simulation.

4.3.1 Updating the FSM

Some of these kinematics outputs are already defined in the FSM, such as tibia angle, and knee flexion angle. However, for other parameters, the FSM needs to be updated. The first discrepancy comes from the fact that in the inverse solution model, soft tissues are modeled as a single bundle while in FSM, soft tissues are modeled as multiple bundles. Therefore, for quadriceps tendon and

Table 4-4: Kinematics parameters measured from fluoroscopy analysis and are used as inputs of the inverse solution model.

Parameter	Unit	Relative to
Time	Degree	-
Flexion	Degree	Newtonian
Patella angle	Degree	Newtonian
Patellar ligament angle	Degree	Newtonian
Quadriceps tendon angle	Degree	Newtonian
Tibia angle	Degree	Newtonian
Medial contact point	mm	Femoral component
Lateral contact point	mm	Femoral component
Femoral component center of mass	mm	Bearing insert

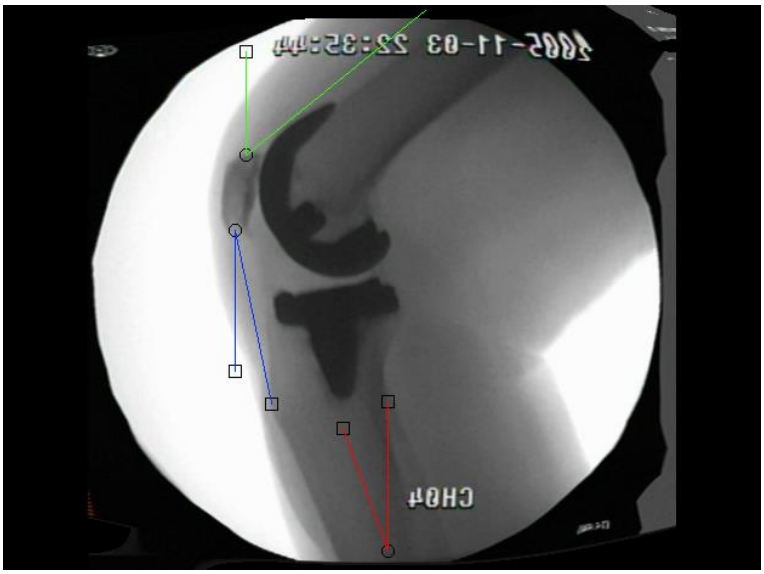


Figure 4-16: Measurement of kinematics data to input into the inverse mathematical model.

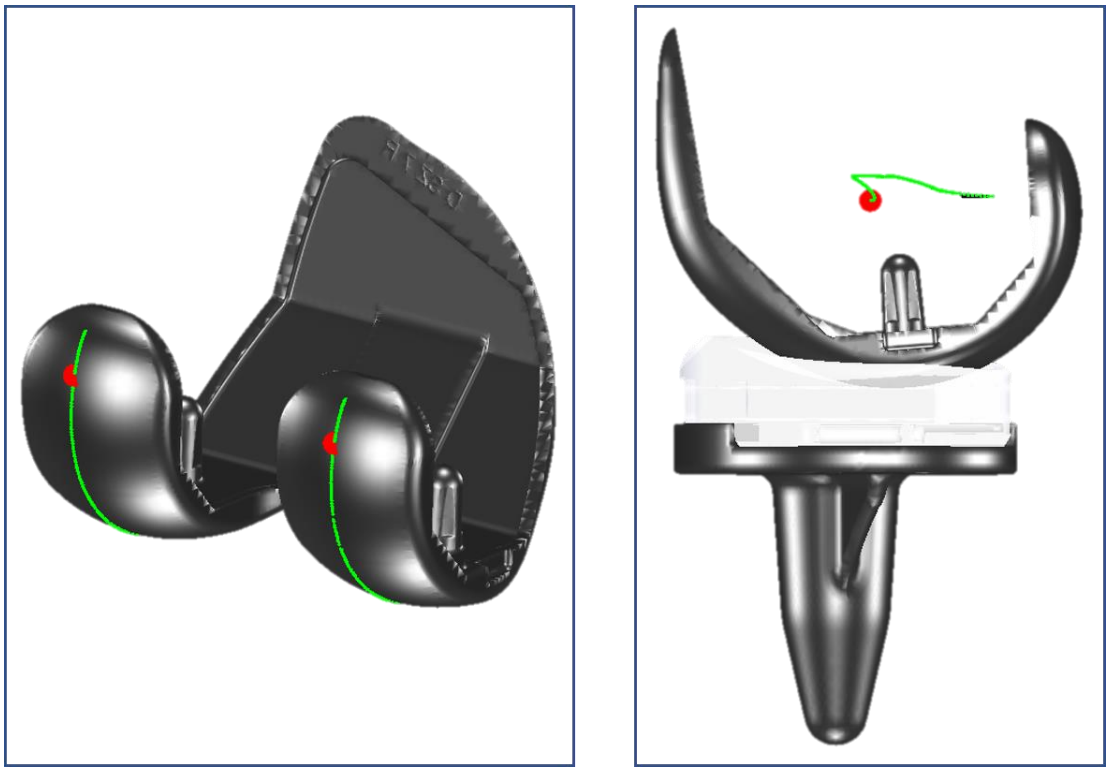


Figure 4-17: The lateral and medial contact point translations are collected relative to the femoral component (left). The femoral component center of mass translation relative to the bearing insert is obtained throughout the activity range of motion (right). Red points show the contact points/center of mass and green lines show the trajectory of these points during the range of motion.

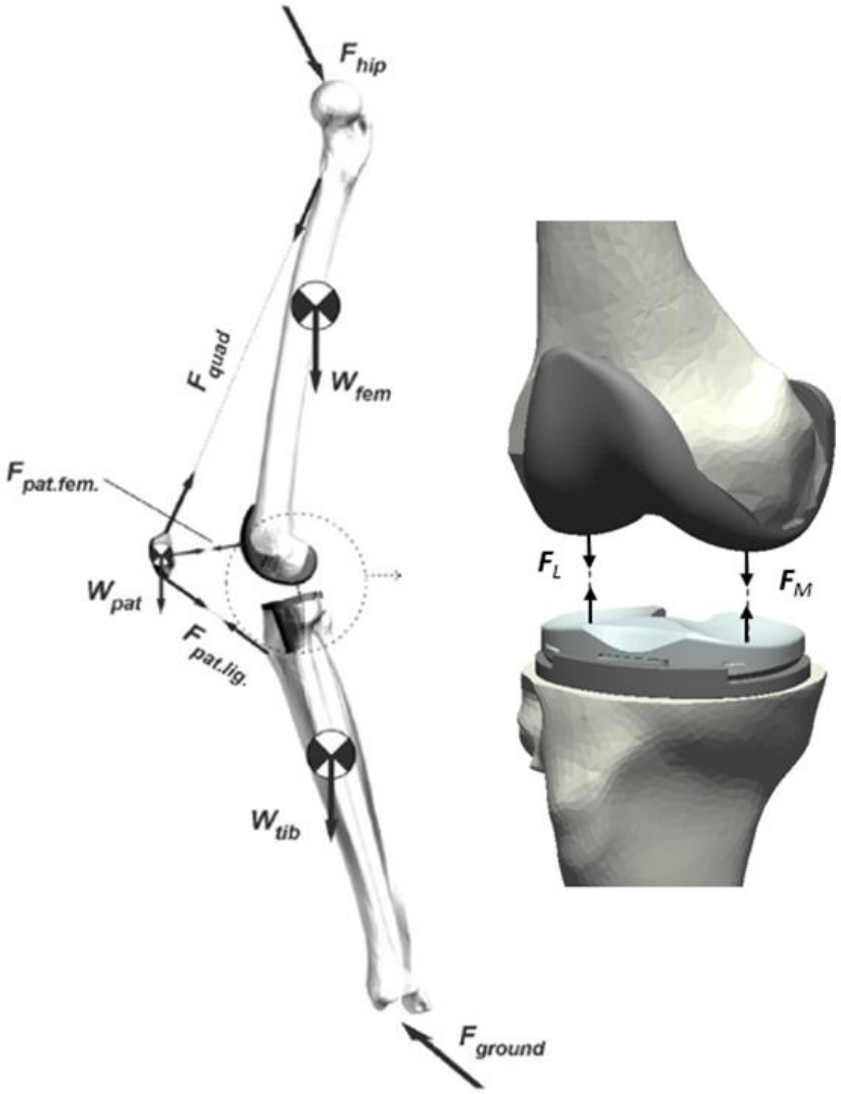


Figure 4-18: Free body diagram of the inverse mathematical model. F_{ground}, ground reaction force; $F_{pat.lig.}$, patellar ligament force; F_{quad}, quadriceps muscle group force; $F_{pat.fem.}$, patellofemoral contact force; F_{hip}, hip joint reaction force; W_{tib}, the weight of the tibia [9].

patellar ligament, another point is defined to act as an average point of insertions and origins of these soft tissues (Figure 4-19). The quadriceps tendon is different in two ways than the patellar ligament angle.

First, unlike the patellar ligament force, the quadriceps force is not distributed evenly between all four fibers.

Second, the quadriceps muscle wraps around the bone/femoral component during activity. To take into account these differences, the quadriceps muscles average attachments are obtained by these equations

$$Quad_{Avg}^{Insertion} = \frac{f_{RF} * Quad_{RF}^{Pat} + f_{VL} * Quad_{VL}^{Pat} + f_{VM} * Quad_{VM}^{Pat} + f_{VI} * Quad_{VI}^{Pat}}{f_{RF} + f_{VL} + f_{VM} + f_{VI}}$$

$$Quad_{Avg}^{Origin} = \begin{cases} \frac{f_{RF} * Quad_{RF}^{fem} + f_{VL} * Quad_{VL}^{fem} + f_{VM} * Quad_{VM}^{fem} + f_{VI} * Quad_{VI}^{fem}}{f_{RF} + f_{VL} + f_{VM} + f_{VI}} & , no\ wrapping \\ \frac{f_{RF} * Quad_{RF}^{wrap} + f_{VL} * Quad_{VL}^{wrap} + f_{VM} * Quad_{VM}^{wrap} + f_{VI} * Quad_{VI}^{wrap}}{f_{RF} + f_{VL} + f_{VM} + f_{VI}} & , wrapping \end{cases}$$

Where

f_i: Muscle i quadriceps force ration

$Quad_i^{Pat}$: Muscle i attachment on the patella

$Quad_i^{Fem}$: Muscle i attachment on the femur (pelvis for RF)

$Quad_{Avg}^{Insertion}$: Average insertion of the quadriceps tendon

$Quad_{Avg}^{Origin}$: Average origin of the quadriceps muscle

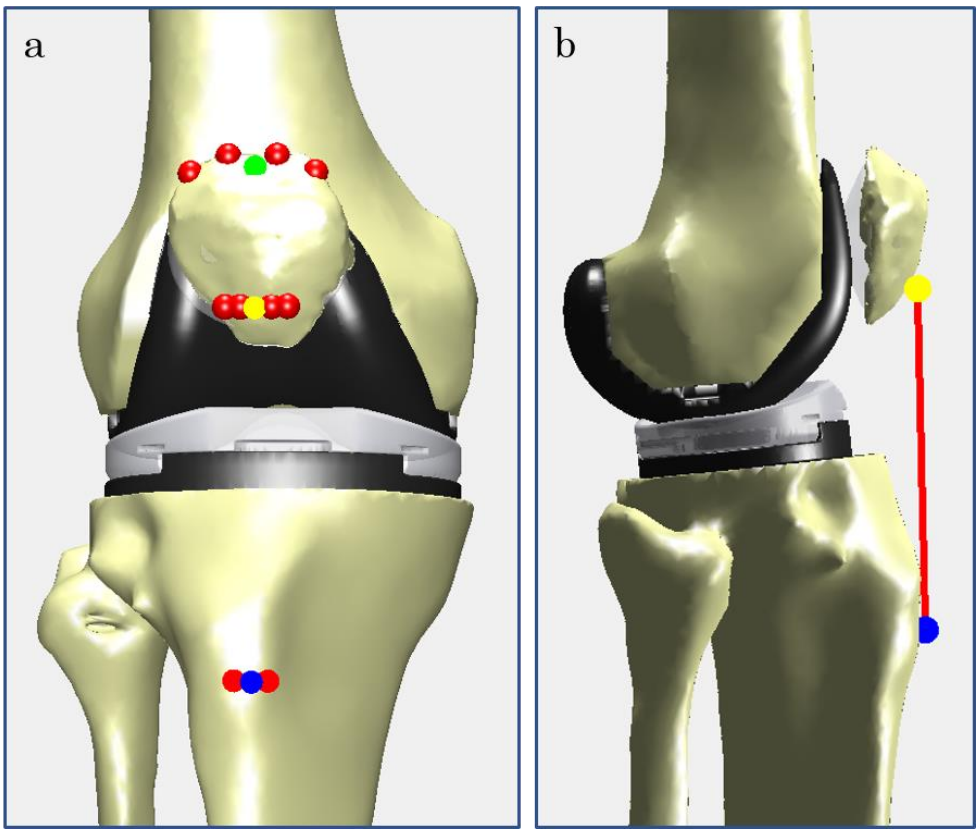


Figure 4-19: The average soft tissue attachments are obtained as an average of all bundles for each soft tissue (a). Then a string is created between the average insertion and origin to represent the soft tissue (b).

Another update that needs to be made in the FSM is that the quadriceps mechanism angle measurements derived from fluoroscopic are images collected from the sagittal view. However, the FSM is a 3D model and therefore these angle measurements must be projected to the sagittal 2D view. The process of obtaining the angle from the projected vector is shown in Figure 4-20.

$$\vec{V}_{proj.} = (\vec{V}_{patlig} \cdot \vec{N}_1)\vec{N}_1 + (\vec{V}_{patlig} \cdot \vec{N}_2)\vec{N}_2$$

$$\theta_{patlig} = \text{acos}\,(\vec{V}_{proj.} \cdot \vec{N}_2)$$

Moreover, the directions of these angles are important for the inverse solution model. Hence, using the sign function, the correct directions of these angles are calculated:

$$\vec{\theta}_{patlig} = (sign(\vec{V}_{proj.} \cdot \vec{N}_1)\theta_{patlig})\vec{N}_3$$

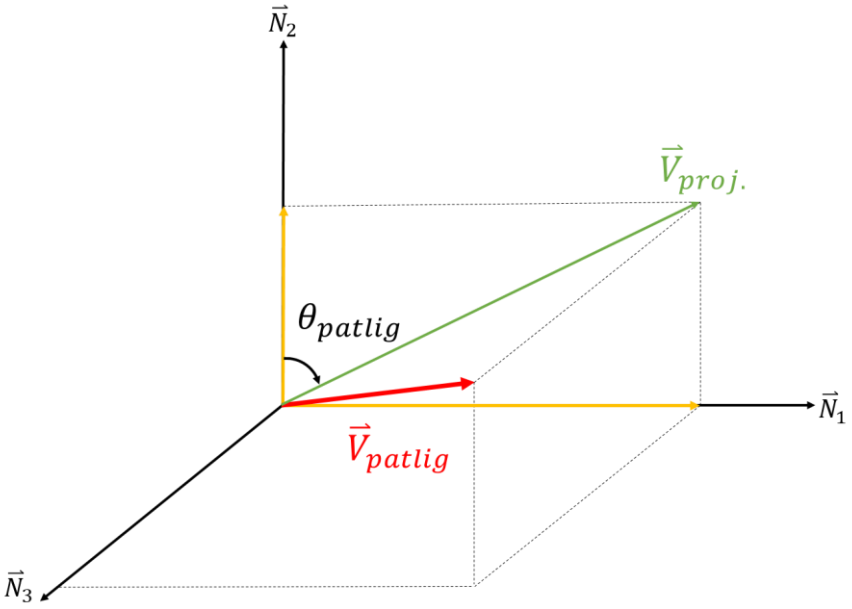


Figure 4-20: The patellar ligament is projected onto the sagittal view and then the patellar ligament angle is calculated from the projected vector.

The next step is to make the translational kinematic data compatible with the inverse solution model in the FSM. The first and easiest parameter is the femoral component center of mass relative to the tibial tray center of mass. The FSM already includes this parameter; however, the position vector is defined in the tibial reference frame. This position vector is defined as follows

$$\vec{V} = v_1\vec{F}_1 + v_2\vec{F}_2 + v_3\vec{F}_3$$

$$v_1 = \vec{P}_{ToFo} \cdot \vec{F}_1 + \vec{P}_{ToFo} \cdot \vec{F}_2 + \vec{P}_{ToFo} \cdot \vec{F}_3$$

where $\vec{F}_1$, $\vec{F}_2$, and $\vec{F}_3$ are the femoral component reference frame unit vectors. And $\vec{P}_{ToFo}$ is the position vector from the tibial tray center of mass to the femoral component center of mass.

The next two parameters are more challenging to define. In the FSM, the low points of the femoral component on lateral and medial condyles are defined to obtain the LAP and MAP of the femoral component with respect to the tibial tray. Although the implementation of the low points is very common in reporting TKA kinematics patterns, the low point and the contact points are not always coincident (Figure 4-21). And the inverse solution model takes the contact point translations, not low point translations. Therefore, the concept of a single contact point needs to be introduced to the FSM.

At any given time, more than one point of the femoral condyles is in contact with the tibial plateaus (Figure 4-22). As it was mentioned in the Contact Detection Algorithm section, the femoral component condyles are modeled as point clouds. Then, the algorithm for each point on the point cloud checks whether it is in contact. The contact detection algorithm is updated to calculate the average location of the points that are in contact at each time step and express that as the single contact point. Pseudo-code below shows how this average location is calculated.

```
Contactpointcount=0;
xsum=0;
ysum=0;
zsum=0;

for (int n=0; n<number of points; n++){
   if (point n is contact){
      contactpointcount=contactpointcount+1;
      xsum = xsum + x[n];
      ysum = ysum + y[n];
      zsum = zsum + z[n];
   }
}

xavg = xsum / contactpointcount;
yavg = ysum / contactpointcount;
zavg = zsum / contactpointcount;
```

In the pseudo-code above, xavg, yavg, ang zavg are the anterior, superior, and lateral location of the average contact point, respectively.

Now that all the required kinematics inputs of the inverse solution model are defined in the FSM, two models can be linked. Once the FSM simulation is complete, the user can run the inverse solution based on the kinematics results of the FSM using the GUI.

4.4 Settling Algorithm

One of the issues that existed in the previous forward solution model was that there were oscillations in force predictions and kinematics output at early flexion (Figure 4-23). These oscillations were seen in the results for about the first 30° of knee flexion. The results after those initial spikes were normal. However, the early flexion results are of critical importance for all TKA design, especially those that either retain the ACL or substitute using an anterior cam and post mechanism which engages in early flexion to replicate the functionality of the ACL.



Figure 4-21: The low point (yellow) and contact point (red) do not always coincide.

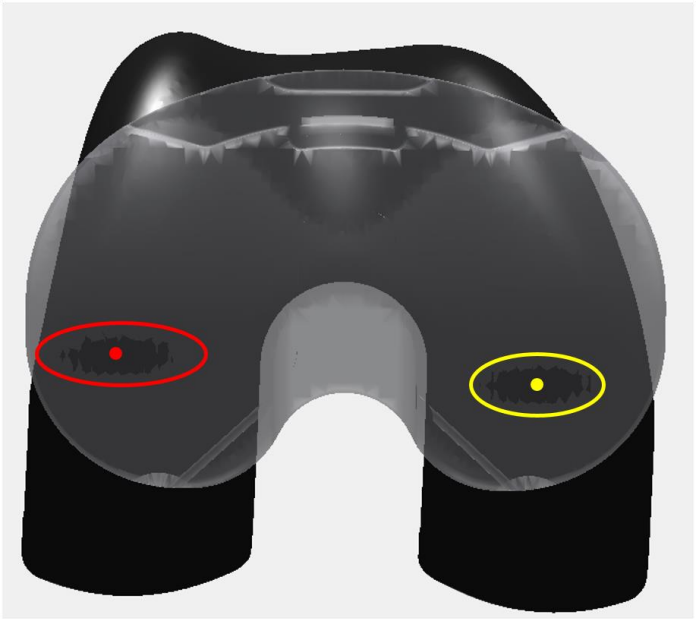


Figure 4-22: at each time step there are multiple points that are in contact between each femoral condyle and bearing insert plateau. The average location of lateral contact points (red) and medial contact points (yellow) are considered as the lateral and medial contact points, respectively.

Additionally, incorporating the settling algorithm is essential for simulating other activities. For DKB, the knee starts at full extension, and since the muscle forces are minimum, even without a settling algorithm, the simulation runs. However, for other activities such as step-up, the forces at the joint are greater, and therefore it is very important to have a settling algorithm to start the simulation in a more stable condition.

The idea to develop a settling algorithm comes from the fact that an inverse solution model can be built on a forward solution model and vice versa. As mentioned before, in an inverse solution model, the motions are specified in the system of equations and the forces are then derived. Therefore, based on these two points, an identical inverse solution is built from the FSM and the motions of the knee joint were specified for the starting position of the activity and then the required forces to make the system stable at the initial condition are calculated.

4.4.1 Updating the FSM

One of the powerful tools of Kane's dynamics is the ability to solve for interaction forces and torques by introducing the concept of auxiliary generalized coordinates and generalized speed. There are three types of generalized speeds in Kane's dynamics.

First are the independent generalized speeds that provide the general characteristics of the motion of the system. Independent generalized speeds are the degrees of freedom of the system. The second type are the dependent generalized speeds, which only facilitate the kinematic analysis. And lastly, auxiliary generalized speeds are introduced to the system in order to solve interactive forces and torques.

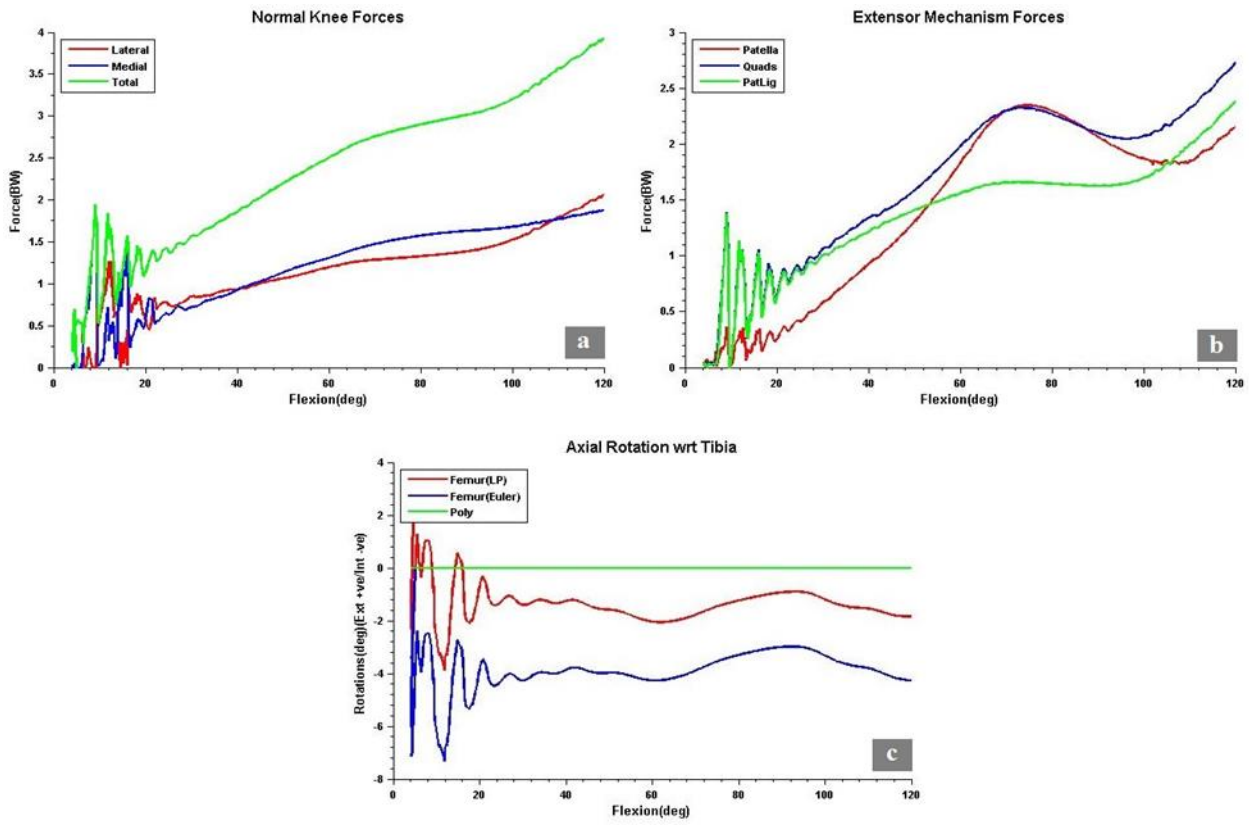


Figure 4-23: Oscillations in early flexion in DKB simulation in previous FSM. These oscillations affect the knee contact forces (a), muscle force prediction (b), and kinematic outcomes (c).

In the FSM model described in this dissertation, 30 generalized speeds are introduced to the system. Of these, 12 are the independent generalized speeds that are used to define the knee joint; 6 for tibiofemoral joint (3 translational and 3 rotational) and 6 for patellofemoral joint (3 translational and 3 rotational).

9 translational generalized speeds are auxiliary generalized speeds to solve interactive force at the hip joint, the interactive force between the tibial tray and the bearing insert, and ground reaction forces. Additionally, 9 rotational auxiliary speeds are used to solve torque on the tibia, torque on the pelvis, and the interactive force between the bearing insert and the tibial tray.

Hence, an identical inverse solution is developed based on the FSM with constraining the degrees of freedom at the knee joint and therefore changing the independent generalized speeds to auxiliary generalized speeds.

Therefore, new variables (interactive forces and torques) are applied at the tibiofemoral joint and the patellofemoral joint (Figure 4-24). By specifying the knee joint motion at the starting of the activity, the inverse model is able to predict the forces and torques required to make the system stable at the initial condition.

The C++ code is further advanced to make the simulations more physiological accurate. Where applicable, some of these forces or torques are replaced with changes in soft tissue forces and tension.

To replace a force or a torque with tension in soft tissue, the soft tissue has to contribute to that force/torque. For instance, the patellofemoral force in the SI direction is replaced by the tension in the patellar ligament. The number of soft tissues present at the knee joint are limited and smaller than the degrees of freedom of the knee.

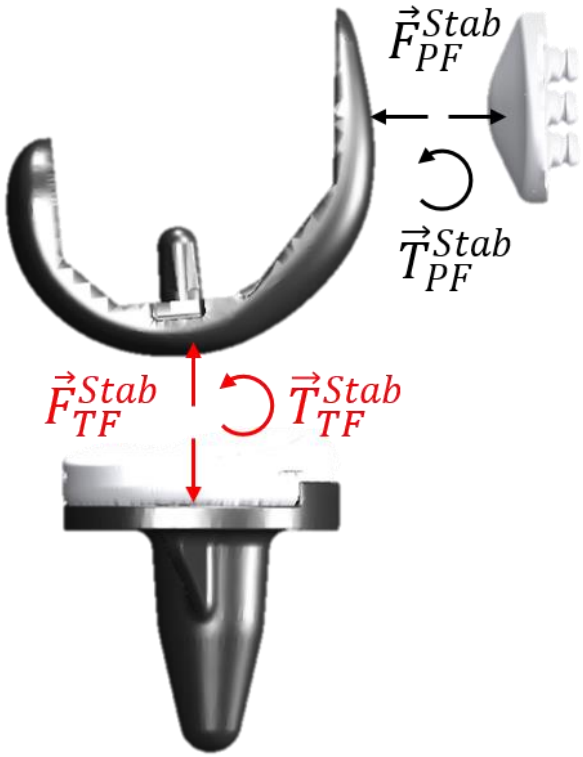


Figure 4-24: New variables, forces and torques, are introduced in the inverse solution model to make the system stable at initial condition.

For example, there is not soft tissue to balance the tibiofemoral stabilizing force in the AP direction. For stabilizing forces in such directions, the positions of the components are altered to replace the respective forces/torques. This process continues until the forces and torques are smaller than 5 N or 0.5 Nm, respectively. This way there would not be a large additional force/torque applied at the knee joint throughout the activity. The pseudo-code below shows how this method is implemented in the C++ code.

```
if (abs(Force)>5) {

    if (Force>0) {
        Position = Position – ChangeAmount;}

    else {
        Position = Position + ChangeAmount;}

    // the next if statement is created to prevent excessive
    // changes when the direction of the force changes.

    if (sign of Force changes) {
        ChangeAmount = ChangeAmount/2;
        Skip the next step;}
}
```

4.5 Physiological Knee Simulation

The current FSM is a very powerful tool to assess kinetics and kinematics of TKA design. To improve the physiological aspects of the FSM, several new additions are introduced into the FSM, such as adding the foot and the toes, incorporating more muscles, creating default simulations for different implant types, and adding multiple subjects to increase the variability of the FSM.

4.5.1 Incorporating the Foot

The previous knee model did not account for the foot into the model. Ground reaction forces are applied at the ankle joint. There are several reasons why

incorporating the foot into the model is off importance. First, the current model only accounts for limited activities, specifically deep knee bend (DKB) and squat to rise. In these activities, the foot is often stationary, and therefore it may not be necessary to include the foot.

However, one goal of this study to further develop the model to include other activities of daily living. Contrary to the DKB, the foot is not stationary on the ground for other activities such as gait, walking downstairs, etc. (Figure 4-25). Additionally, even in the DKB, it is not uncommon to see subjects lift their foot off the ground.

Secondly, one of the essential muscle groups during daily activities, such as walking and climbing the stairs, is the gastrocnemius. Gastrocnemius muscles are inserted on foot (Figure 4-26). Thirdly, the ground reaction forces no longer need to be applied at the ankle. Therefore, there would be a more realistic representation of the actual forces and can be served as another tool for validation of the model.

4.5.1.1 Updating the FSM

Therefore, to include the foot into the model, two more bodies are being included in the model, which are the foot and the toes. The toes will be modeled separately from the foot since they have different rotation profiles during various activities (Figure 4-27).

As mentioned before, the current FSM starts from the ankle joint and the rest of the dynamic chain, bones and components, are defined relative to the inferior body/frame. In the previous FSM, the location of the ankle joint is defined from the global center and then the tibia center of mass is defined relative to the ankle center. Also, the ground reaction forces are applied at the ankle (Figure 4-28).

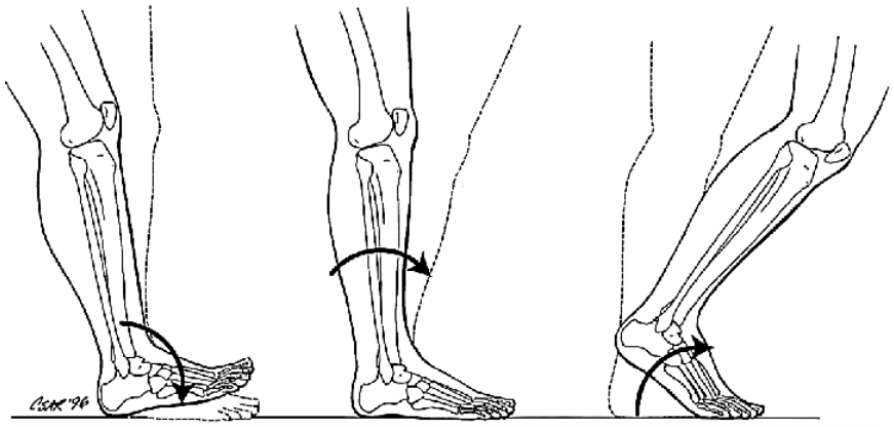


Figure 4-25: The movement of the foot during the stance phase of the gait. The foot is not stationary throughout the range of motion of the activity.

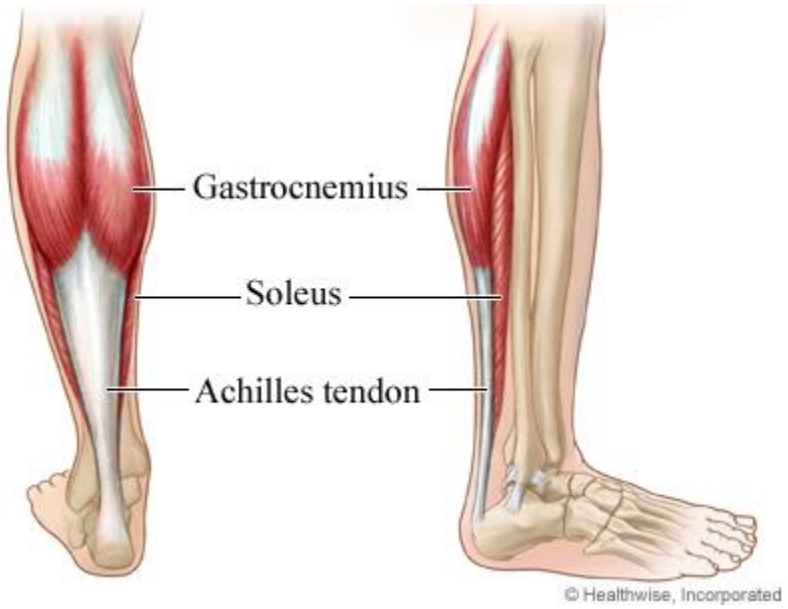


Figure 4-26: Both gastrocnemius muscle fibers are inserted on the posterior calcaneus on the foot (image from www.healthlinkbc.ca).

In the updated FSM, the coincident point between the foot and the ground is defined from the global center. The ground reaction forces are applied at this point. From this point, the foot center of mass is defined. Then, toes center and ankle center are defined from the foot center of mass. Same as before, the tibia center of mass id defined relative to the ankle center (Figure 4-28).

The rotation profile of the foot and toe are defined as specified functions of flexion. The foot flexion profile is defined as follows

$$\theta_i^{Foot} = \sum_{j=0}^{3} f_{ij}(Flexion - Flexion_0) \qquad i = 1,2,3$$

Where $Flexion_0$ is the flexion angle where the foot starts rotating and f_{ij} represents the polynomial coefficients of the foot rotation profile in the i-th direction, which is anterior, superior, and lateral, respectively. The purpose of introducing $Flexion_0$ is to be able to start foot rotation at a certain flexion angle based on the user-specified value. The C++ code will be updated as following pseudo-code.

```
if flexion < flexion0
    Fij = 0;
else
    Fij = user specified values;
end
```



Figure 4-27: The foot and toe are modeled separately to account for different flexion profiles during different activities.

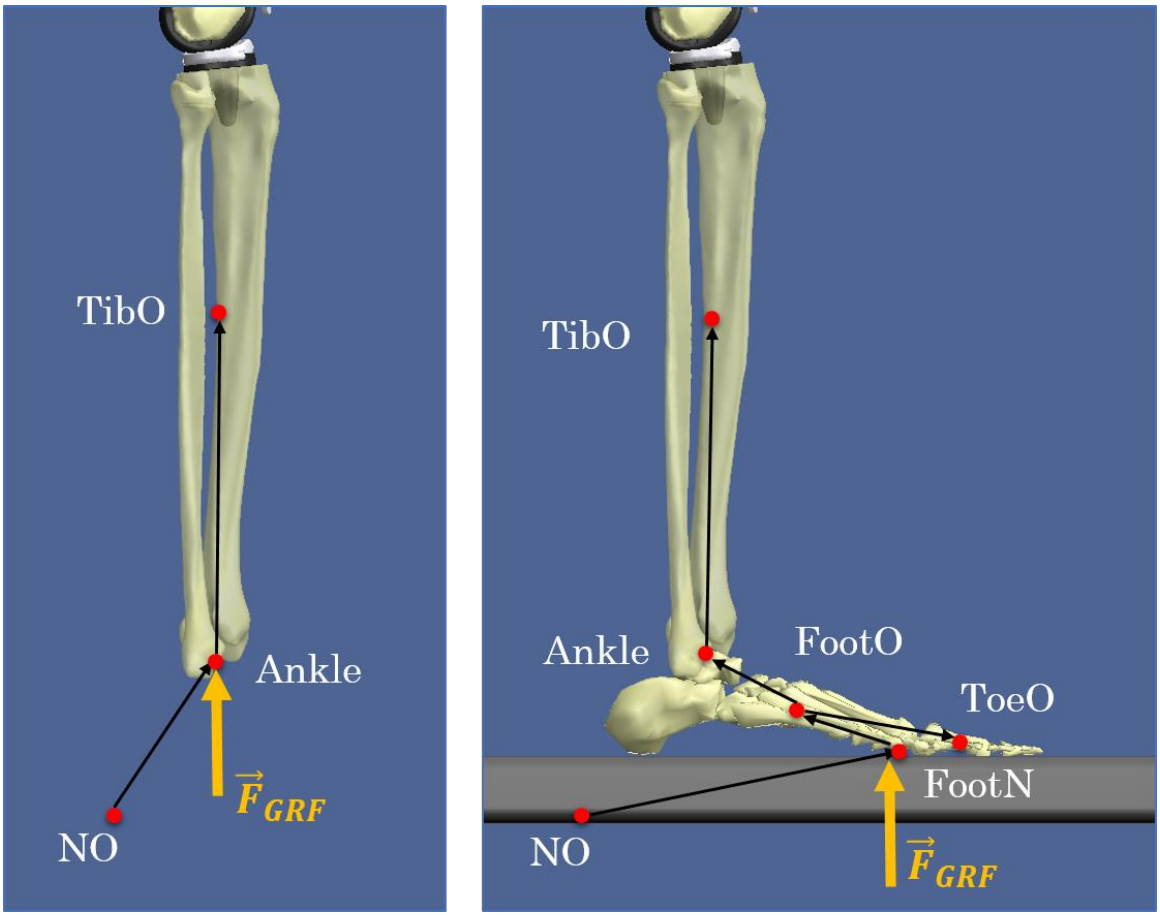


Figure 4-28: In the current FSM, the ground reaction forces are applied at the ankle joint and the model starts at the ankle joint (left). The updated model incorporated the foot and toes. The location of the toes and the tibia are defined relative to the foot (right).

4.5.2 Incorporating More Muscles

There are three major muscle groups at the knee joint. The quadriceps muscles consist of four fibers and are primarily responsible for the knee extension are incorporated into the current model. The hamstring muscle groups consist of four fibers: the semitendinosus and semimembranosus, originate from ischial tuberosity (distal part of the femur) and inserted on the medial tibial condyle, the bicep femoris long head, which also originates from ischial tuberosity but inserts on the lateral side of the fibula, and the bicep femoris short head, which originates from the posterior side of the femur bone and inserts on the fibula (Figure 4-29). The primary function of hamstring muscles at the knee joint is to flex the knee.

The gastrocnemius muscles have two fibers: the lateral head originates from the lateral femoral condyle and the medial head originates from the medial femoral condyle. Both insert on the posterior side of the calcaneus on the back of the foot as Achilles tendon (Figure 4-30). Both hamstring and gastrocnemius muscle groups play a role in daily activities such as walking, running, stair ascent, and stair descent.

4.5.2.1 Updating the FSM

The muscles are modeled as active forces to drive the system and allow for the determination of relative bone motion. Each muscle will be model as a bundle of fibers to account for the girth of the muscles at origin and insertion sites. The forces of the model will be applied as equal but in opposing direction on the insertion and origins. Where applicable, the wrapping points are defined to account for the actual line of action of the muscles. The muscle will be graphically represented as single lines from origins to wrapping points, where applicable, and then to the insertion site. There are four fibers in the hamstring muscle group. The hamstring muscle forces are defined as follows:

$$\vec{F}_{Ins}^{i} = F_{Ham} * Ratio_i * \frac{\vec{P}_{ins(i)\to wrap(i)}}{\left|\vec{P}_{ins(i)\to wrap(i)}\right|} \qquad i = 1, \dots, 4$$

$$\vec{F}_{orig}^{i} = F_{Ham} * Ratio_i * \frac{\vec{P}_{orig(i)\to wrap(i)}}{\left|\vec{P}_{orig(i)\to wrap(i)}\right|} \qquad i = 1, \dots, 4$$

$$\vec{F}_{wrap}^{i} = -(F_{Ham} * Ratio_i * \frac{\vec{P}_{orig(i)\to wrap(i)}}{\left|\vec{P}_{orig(i)\to wrap(i)}\right|} + F_{Ham} * Ratio_i * \frac{\vec{P}_{ins(i)\to wrap(i)}}{\left|\vec{P}_{ins(i)\to wrap(i)}\right|}) \qquad i = 1, \dots, 4$$

Where $\vec{F}_{Ins}^{i}$, $\vec{F}_{orig}^{i}$, $\vec{F}_{wrap}^{i}$ are force applied at insertion, origin, and the wrapping point of each muscle fiber, including BFS, BFL, SMB, and SMT. Also $Ratio_i$ is the percentage of the total hamstring force, F_{Ham}, for the respective fiber. The muscle force is a polynomial function of knee flexion, where the user can update the polynomial coefficients to account force different muscle activations in different activities. These data can be collected from literature or EMG data.

$$F_{Ham} = \sum_{i=0}^{4} HFC_i * Flexion^i$$

The gastrocnemius muscle groups are defined in the same fashion. There are two muscle fibers in gastrocnemius muscle.

$$\vec{F}_{Ins}^{i} = F_{Gast} * Ratio_i * \frac{\vec{P}_{ins(i)\to wrap(i)}}{\left|\vec{P}_{ins(i)\to wrap(i)}\right|} \qquad i = 1, 2$$

$$\vec{F}_{orig}^{i} = F_{Gast} * Ratio_i * \frac{\vec{P}_{orig(i)\to wrap(i)}}{\left|\vec{P}_{orig(i)\to wrap(i)}\right|} \qquad i = 1, 2$$

$$\vec{F}_{wrap}^{i} = -\left(F_{Gast} * Ratio_i * \frac{\vec{P}_{orig(i)\to wrap(i)}}{\left|\vec{P}_{orig(i)\to wrap(i)}\right|} + F_{Ham} * Ratio_i * \frac{\vec{P}_{ins(i)\to wrap(i)}}{\left|\vec{P}_{ins(i)\to wrap(i)}\right|}\right) \qquad i = 1,2$$

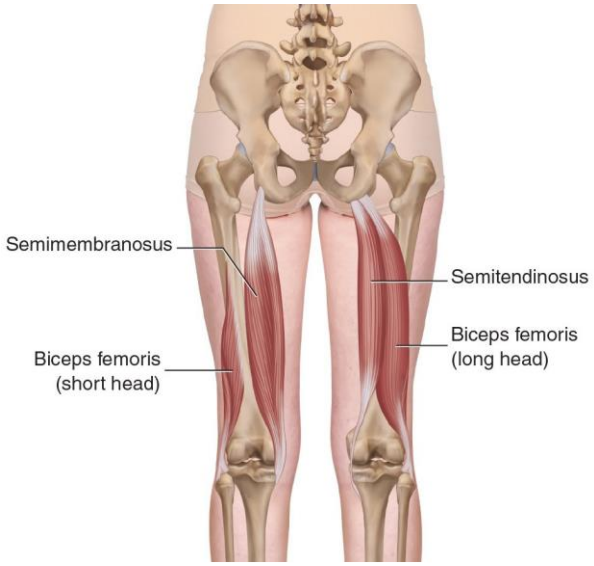


Figure 4-29: Display of all four fibers of the hamstring muscle group.



Figure 4-30: Two fibers of the gastrocnemius muscle group are shown here.

4.5.3 Incorporating Clinically Relevant Simulations

One of the main strengths of the knee mathematical model is that the user can perform several simulations using different surgical conditions and alignments on a specific TKA design in order to investigate the effects of these changes on the TKA outcomes. However, it would be of importance to have a baseline configuration from which other alterations can be created. In the previous GUI, there was only one default simulation, "Attune PCR TKA" (Figure 4-31). Moreover, the alignment and placement of the implant might not be clinically relevant and therefore might not be an excellent baseline default simulation.

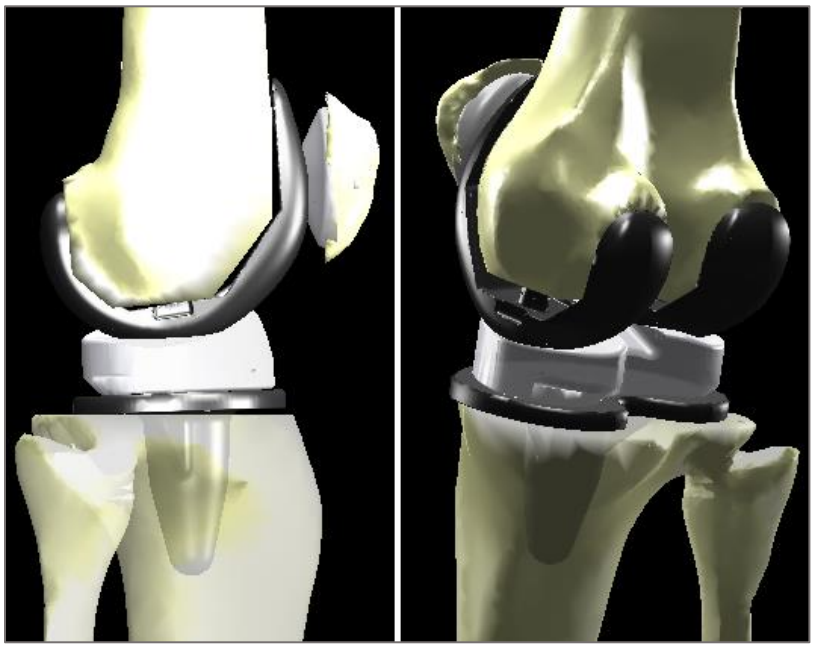


Figure 4-31: The default Attune PCR model in the previous GUI.

Several studies have shown the importance of the surgical techniques, and component alignment on TKA outcomes [64,70,101,124–130]. There are several alignment techniques in total knee replacement [131–134]. Mechanical and anatomical alignments, two of the more popular alignment techniques, revolve around the alignment of the component in the frontal plane to preserve

the mechanical axis or anatomical axis of the leg. In anatomical alignment, the tibia is cut at 3° varus to the mechanical axis of the tibia and the femur is cut distally at 9° valgus to the femur mechanical axis. The tibial cut is perpendicular to the tibial mechanical axis in mechanical alignment and the femur distal cut is at 6° valgus relative to the anatomic axis of the femur (Figure 4-32).

In the updated FSM, the components are placed using mechanical alignment philosophy (Figure 4-33).

Another factor that has been shown to have a significant effect on the TKA outcome is tibial posterior slope [125,135]. The tibial posterior slope is the angle between the tangential line on the tibial plateau and the line perpendicular to the long axis of the tibia (Figure 4-34).

Surgeons often incorporate different tibial posterior slopes for different TKA types, usually 0° of slope for PS design and about 6° for PCR design. To make the FSM a more accurate physiological representation of TKA, different tibial posterior slopes are defined for different TKA designs (Figure 4-35).

Posterior condylar offset, the maximum thickness of posterior condyle, is the distance between the most posterior point of the femoral condyle and the line tangent on the posterior cortex of the femoral shaft (Figure 4-36) [64]. It has been shown that the posterior condylar offset is correlated with TKA outcomes, such as knee flexion [64,125].

To incorporate more accurate posterior condylar offset as well as other sagittal plane cuts, the fluoroscopic images of postoperative TKA patients for different implants were investigated. Based on the average measurements of these fluoroscopic images, the surgical cuts were calculated and incorporated into the updated FSM (Figure 4-37).

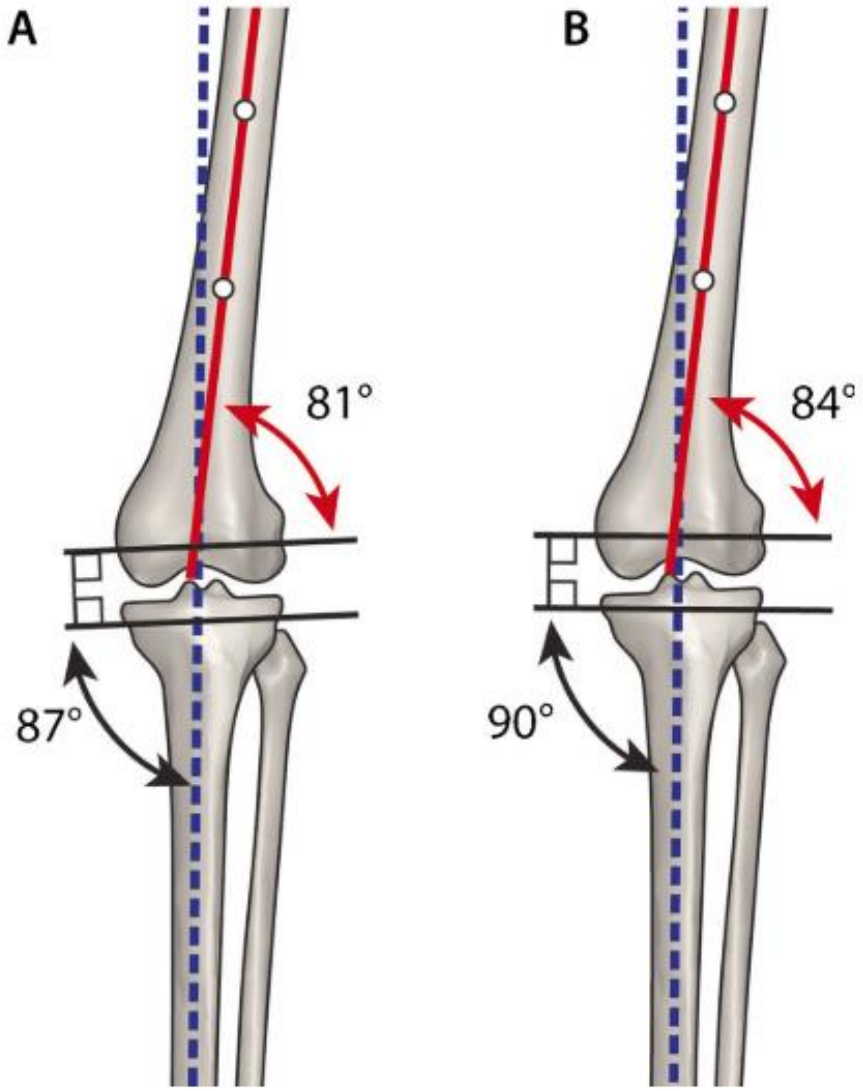


Figure 4-32: Two different alignment techniques. a) Anatomical alignment, b) mechanical alignment. [134]

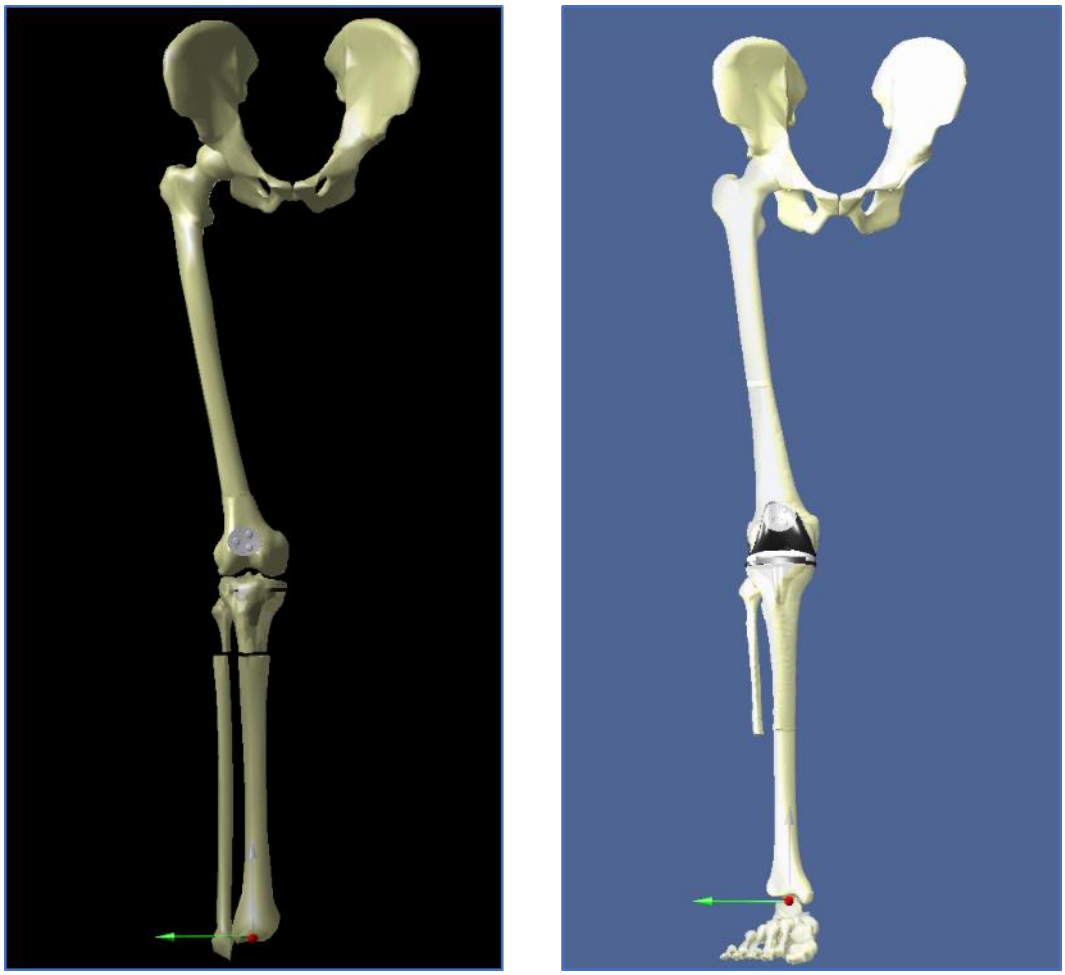


Figure 4-33: In the updated FSM, the components are aligned based on the mechanical alignment (right).

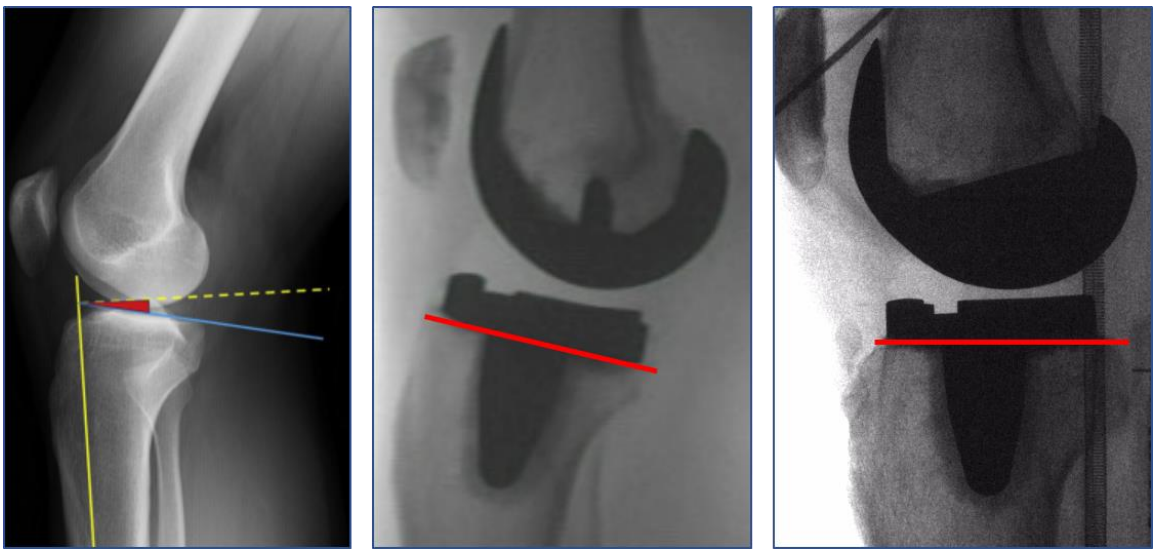


Figure 4-34: Tibial posterior slope is shown for the normal knee (left), a PCR TKA (middle), and a PS TKA design (right).

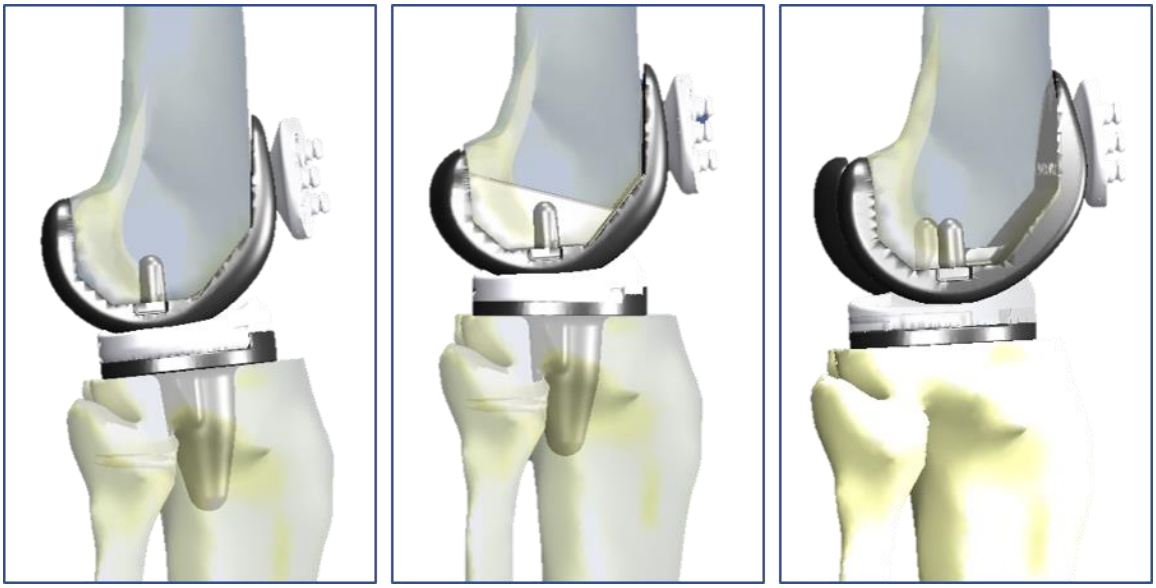


Figure 4-35: Different tibial posterior slope are considered for different TKA designs in the updated FSM. 6° for PCR (left), 0° for PS (middle), and 2° for ACL substituting design (right).

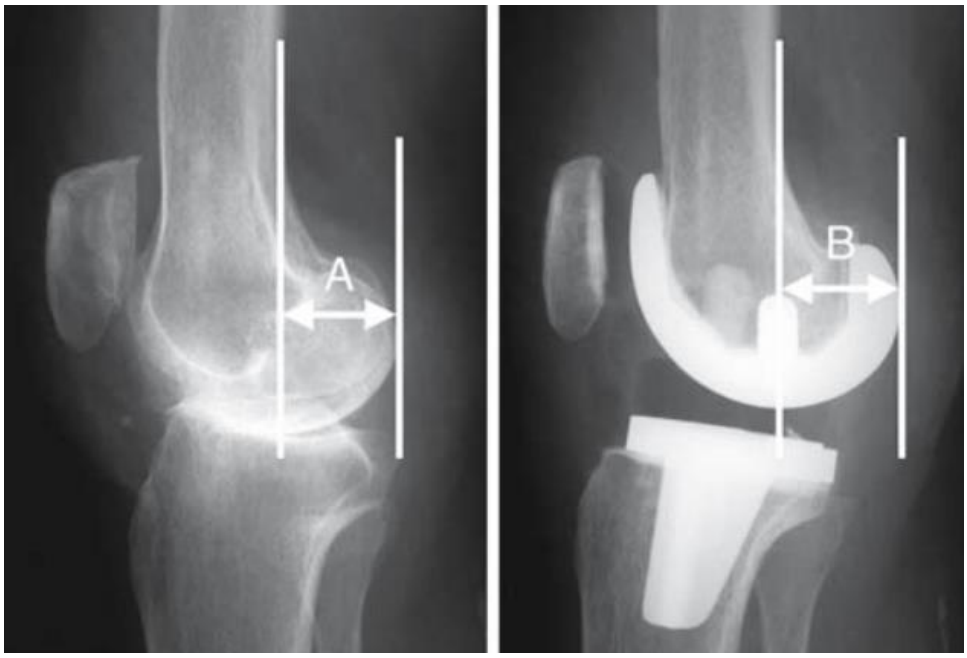


Figure 4-36: Measurement of the posterior condylar offset preoperatively (left) and postoperatively (right) [124].

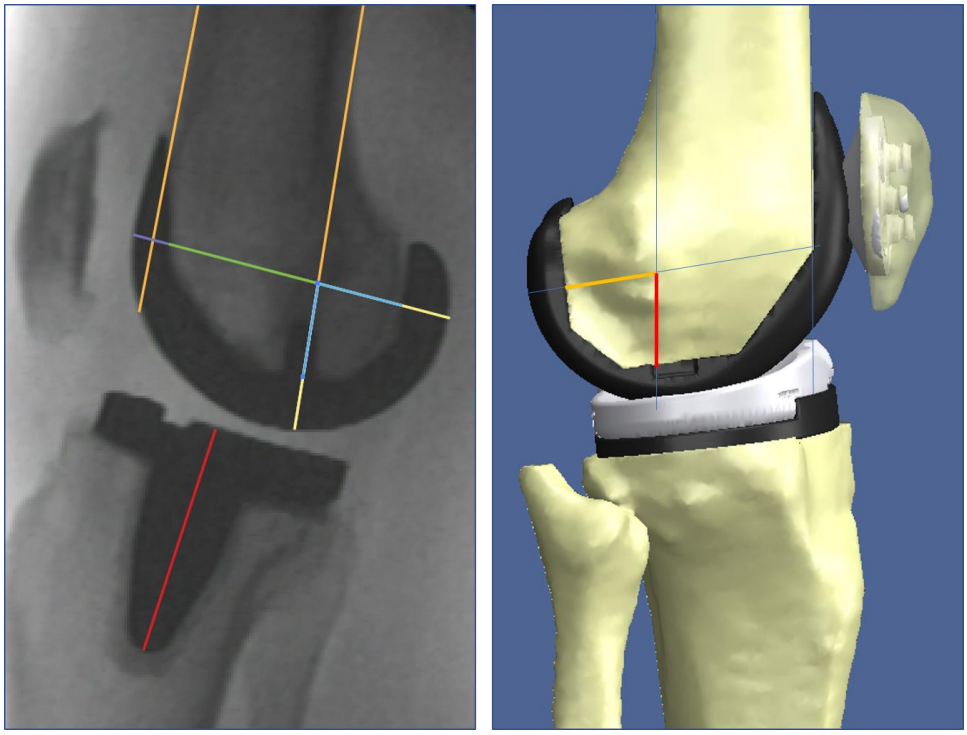


Figure 4-37: Posterior condylar offset and other measurements from actual fluoroscopic images are collected (left) and the surgical cuts are performed based on these measurements that are incorporated into the new FSM.

4.5.4 Incorporating Various Subjects

While the current FSM is a powerful tool in assessing TKA outcomes, one of the limitations is that all simulations were performed only on one subject. However, fluoroscopic studies have documented that there is variability in TKA outcomes between different subjects with similar implants [29,136]. Therefore, one of the goals of the updated FSM is to add more variability to the model by incorporating multiple subjects. To this end, the bone models of 10 subjects have been incorporated into the GUI.

Ten normal subjects had undergone computed tomography (CT) scans. CAD models of tibia, femur, and patella were created from CT data using segmentation techniques (Figure 4-38). These subjects underwent the fluoroscopic process before [137]. Using transformation matrices from the fluoroscopic study, the relative translations and rotations of bones are calculated to set up each subject correct orientation in space.

Patient demographics such as weight and height are crucial for the accuracy of the model (Table 4-5). These data are necessary since the weight of each body segment, such as foreleg, thigh, etc. needs to be applied at the correct location. The relative location of the center of mass of each body segment for each subject was calculated based on average data available in the literature [138–140].

Another important update is to accurately represent the soft tissue insertion and origin sites on each of the bones. Since the geometries of the bones were created using CT scans, no MRI data is available. Hence, the exact locations of the soft tissue attachments are unclear. However, there are several anatomic studies on the anatomy of the human knee soft tissues [15,141–149]. The insertion and origins of knee soft tissues are created based on the data from the literature (Figure 4-39).

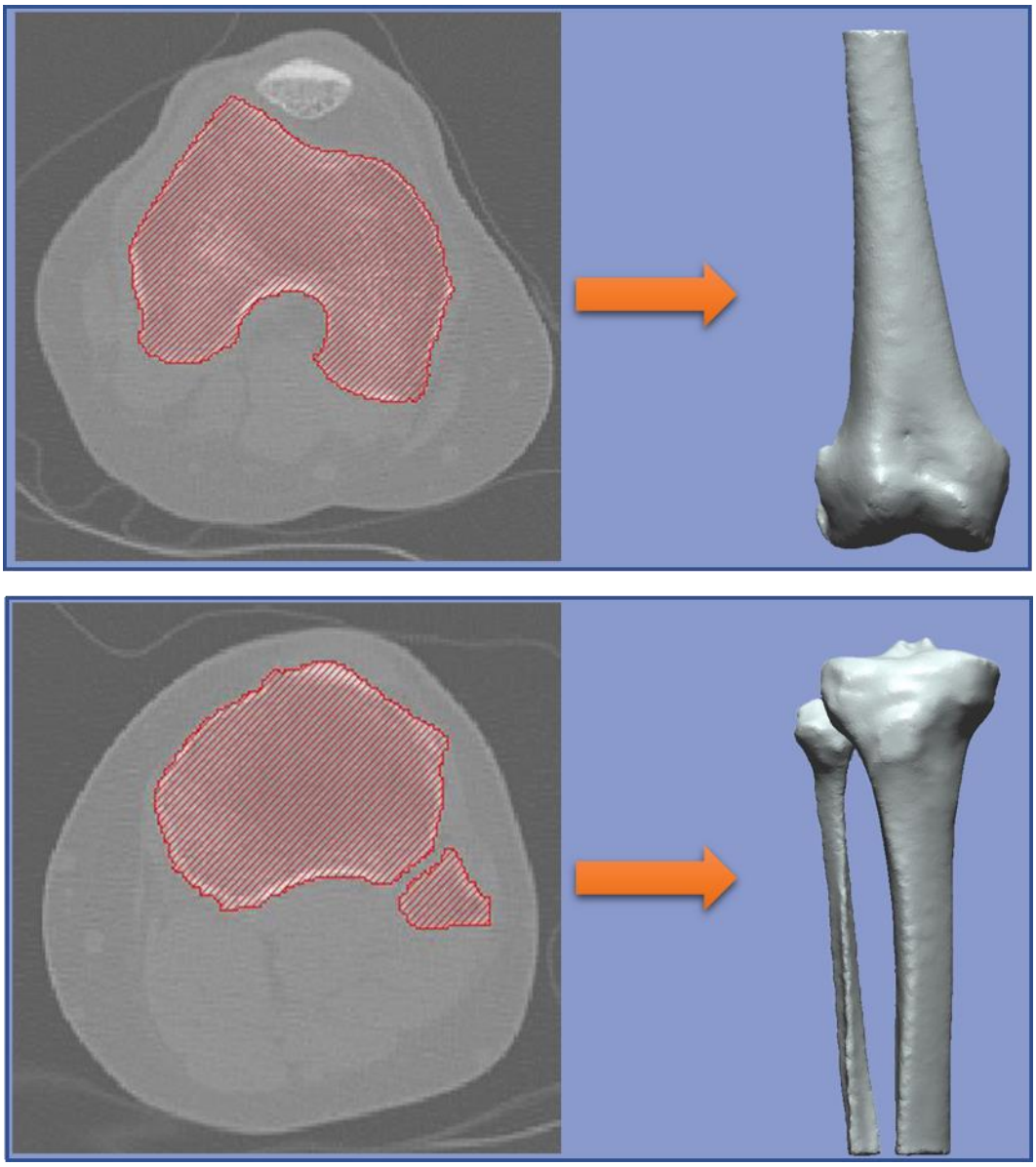


Figure 4-38: The CAD models of bone geometries were created from CT scans using segmentation techniques for all ten subjects.

Table 4-5: Patient demographic for ten subjects included in the updated FSM.

Parameter	Average	Std. Dev.
Age	57.4	7.1
Height (m)	1.7	0.1
Mass (Kg)	79.5	15.2
BMI (kg/m²)	28.7	5.1

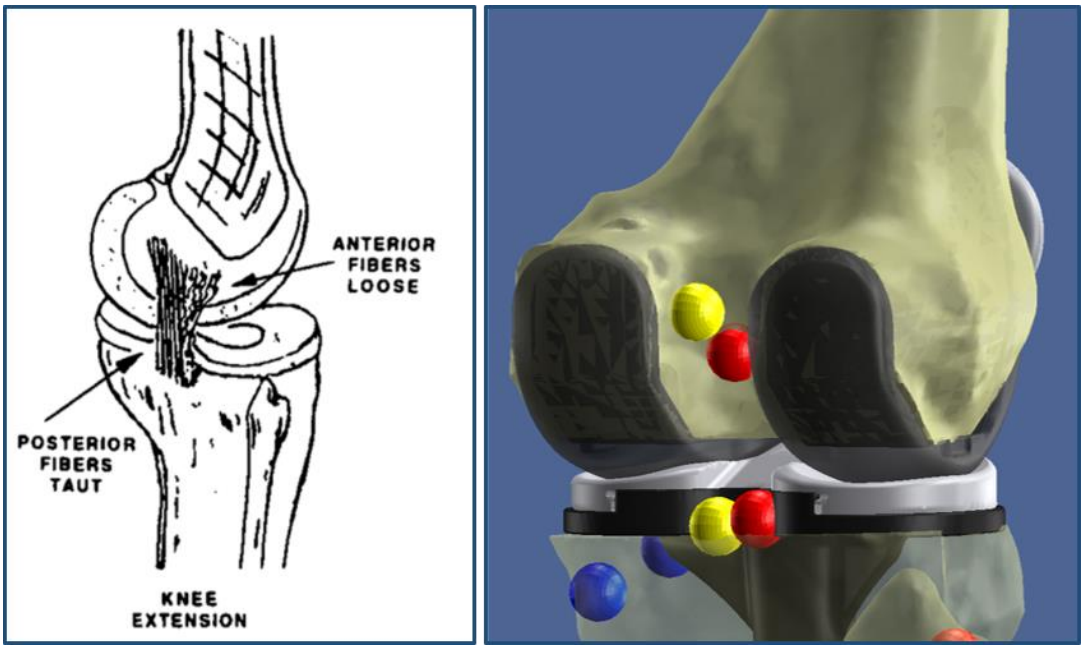


Figure 4-39: Ligaments insertion and origin for each of the ten subjects (right) were created from ligaments attachment data available in the literature (left) [148].

4.6 Other Activities

The current FSM was capable of conducting simulation of flexion-based activities: DKB, and squat to rise activities. Studying these activities is of critical importance since, in these activities, the entire range of motion of the knee is investigated. However, these activities are not as commonly performed as activities such as walking, rising from a chair, etc., following the TKA procedure.

Additionally, other activities such as step up and step down are among the most difficult activities for patients following TKA procedure. Several studies investigated the kinematics and kinetics of TKA during activities such as gait, step down, and step up [74,79,96,150–154]. The kinematics and force profiles seen in these activities are very different than those seen in DKB activity [155–159].

Hence, investigating the kinematics and especially kinetics of TKA designs during these activities is crucial. One of the goals of this study is to further advance the current FSM to account for other activities. Five main activities that will be included in the new mathematical model are: gait, step down, step up, chair rise, and lunge. Also, squat to rise activity has been updated to be more computationally efficient.

4.6.1 Squat to Rise

The squat to rise activity is essentially the opposite movement of the DKB, where the knee starts at a flexed position and starts extending to the maximum knee extension. The way this activity is set up is to start at knee extension and then perform a DKB activity to a pre-defined user-specified flexion angle, and then the desired flexion profile is changed at the specified flexion angle to an extension profile (Figure 4-40).

The problem with the previous squat to rise activity is that it takes about 4 to 5 hours to run (≈ 270 minutes when turn-around flexion angle is set to 120°). Additionally, at turn-around flexion, the activity is unstable for a period of time before it completely starts extending (Figure 4-41).

The muscle controller and desired flexion and extension profiles have been updated in the current FSM to optimize the squat to rise activity. The muscle PID controller gains have also been updated to reduce the instability observed in the turn-around period.

4.6.2 Lunge

The lunge activity is similar to the DKB in nature, with some differences (Figure 4-42). The distribution of the load on the weight-bearing knee, the rotation profile of the bones, and also the foot flexion profile are the major differences between these two activities.

One of the main differences in these two activities is the tibial flexion profile. In lunge activity, the tibia stays relatively upright without any rotation throughout the activity. Limited tibial rotation results in reduced extensor moment arms and consequently increases in quadriceps forces and patellar ligament tension. The flexion profile of the tibia has been updated to match what has been observed for lunge activity.

The next difference between these two activities is the pelvis and upper body flexion profile. The upper body is more upright in the lunge activity. Additionally, in lunge activity, the contralateral leg is placed more posteriorly compared to the ipsilateral leg. Therefore, the rotation profile of the upper body in the FSM needs to be updated with respect to two axes: the ML axis and the SI axis.

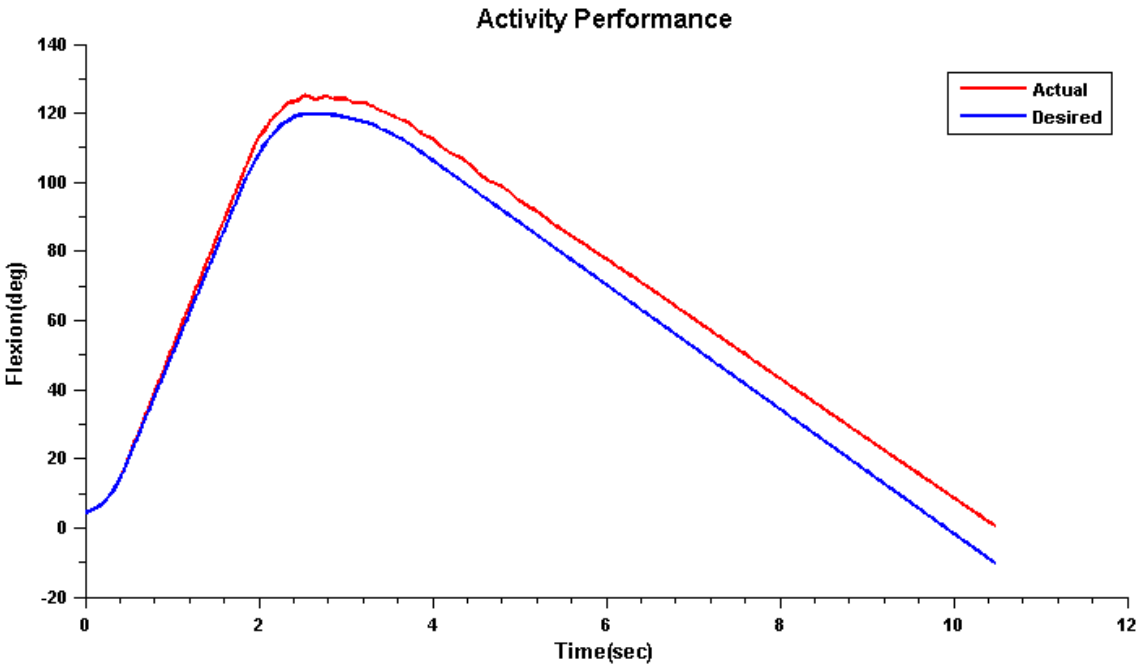


Figure 4-40: The squat to rise activity compromises of a DKB activity and knee extension. The blue graph shows the desired knee flexion profile and the red graph shows the actual knee flexion.

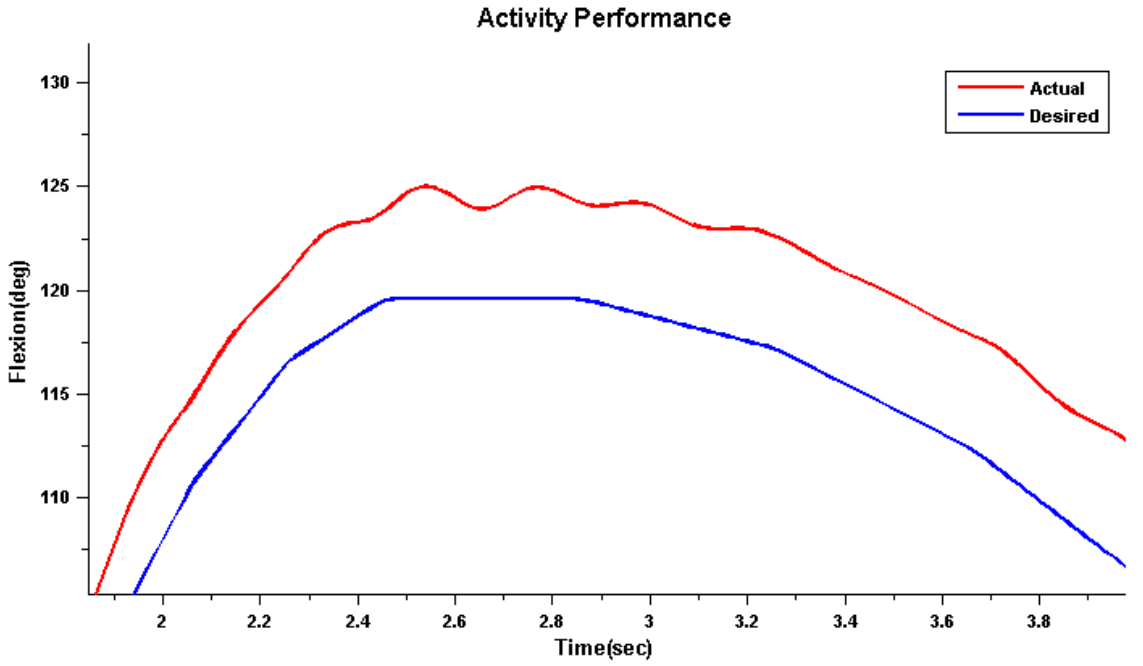


Figure 4-41: During the turn-around flexion angle, the previous FSM experienced instability.

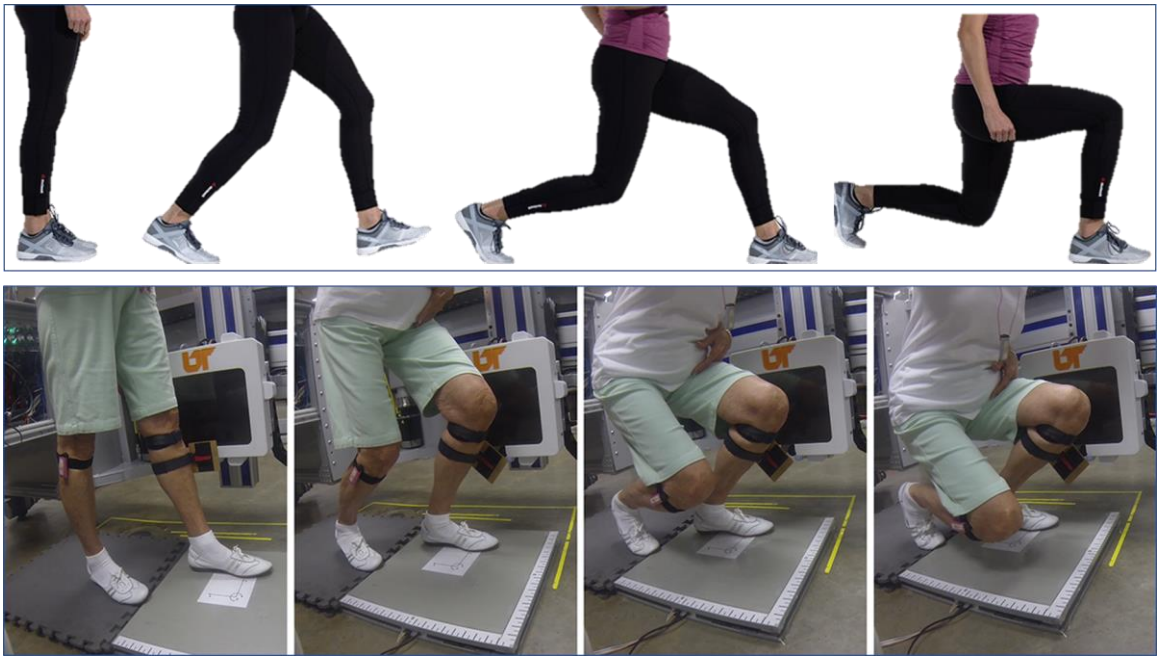


Figure 4-42: The lunge activity (top) is different from the DKB activity (bottom). The distribution of the load on the knee joint is different in these activities.

Finally, sometimes during the lunge activity, near the end of the range of motion, some subjects lift their heel off the ground. This increases the tibial rotation and therefore increases extensor moment arm. Since this phenomenon is not observed for all subjects, the ability to specify the amount of the foot rotation as well as the starting flexion angle has been added to the updated FSM to allow the user to simulate different loading conditions.

4.6.3 Chair Rise

A chair rise activity is inherently similar to a reverse DKB activity or a squat to rise activity. However, the squat to rise activity is just the continuation of a DKB activity, meaning the activity starts at the full extension and goes into the maximum knee flexion and starts extending to full extension again. Although the squat to rise activity can be considered similar to the chair rise activity, however, the user cannot change the component alignment or other

features at the seated position. The FSM has been updated to account for the chair rise activity. The user can change the initial conditions (Figure 4-43) and the desired flexion/extension profile of the femur has been updated. The muscle controller and its gains have been tuned to simulate the correct muscle activation to perform the chair rise activity.

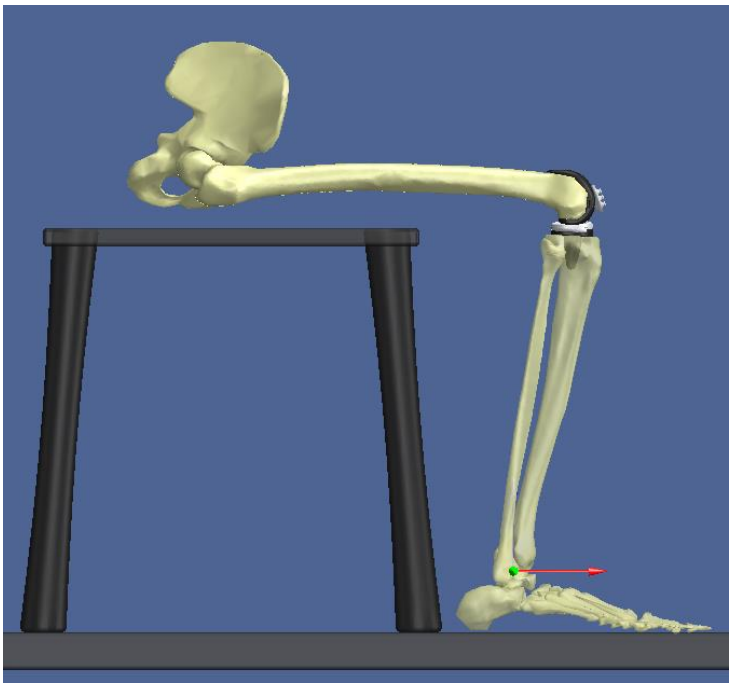


Figure 4-43: The chair rise activity has been incorporated into the new FSM. The user can update the initial condition for this activity using the GUI.

4.6.4 Stair Descent

Thus far, all activities explained are flexion-based activities, with the knee flexion constantly increasing or decreasing over time. The FSM has 12 degrees of freedom at the knee joint. Other bones motion, such as the tibia, or upper body movement, are specified. For flexion-based activities, these specified motions are defined as a function of knee flexion since these motions constantly increase or decrease throughout the knee range of motion.

$$\theta_{tibia} = f(Flexion) \qquad for\ flexion\ based\ activities$$

However, for other activities, these specified motions are not necessarily continuously increasing/decreasing with knee flexion. During different portions of the activity, there are different motion patterns. Therefore, the first step to create these types of activities is to define these motions as a function of time rather than a function of knee flexion.

$$\theta_{tibia} = f(t) \qquad for\ gait\ type\ activities$$

Activities such as stair ascent, stair descent, and walking are considered gait activities. Gait activities compromises of two separate portions: the stance phase and the swing phase (Figure 4-44).

The stance phase of the activity is where the foot is on the ground. Approximately about 60% of the whole activity is the stance phase. When the foot leaves off the ground, the swing phase starts.

The swing phase is the portion of the activity where the foot is not in contact with the ground and swinging in the air.

Knee forces and moments are significantly higher during the stance phase and studying the stance phase is usually of more importance for evaluating TKA designs. For the purpose of this study, only the stance phase is modeled and investigated. The stance phase itself includes two phases.

The initial phase, where foot starts contacting with the ground while the other leg is still in contact with the ground. This part is often called weight acceptance. During this part, the weight is distributed between both legs.

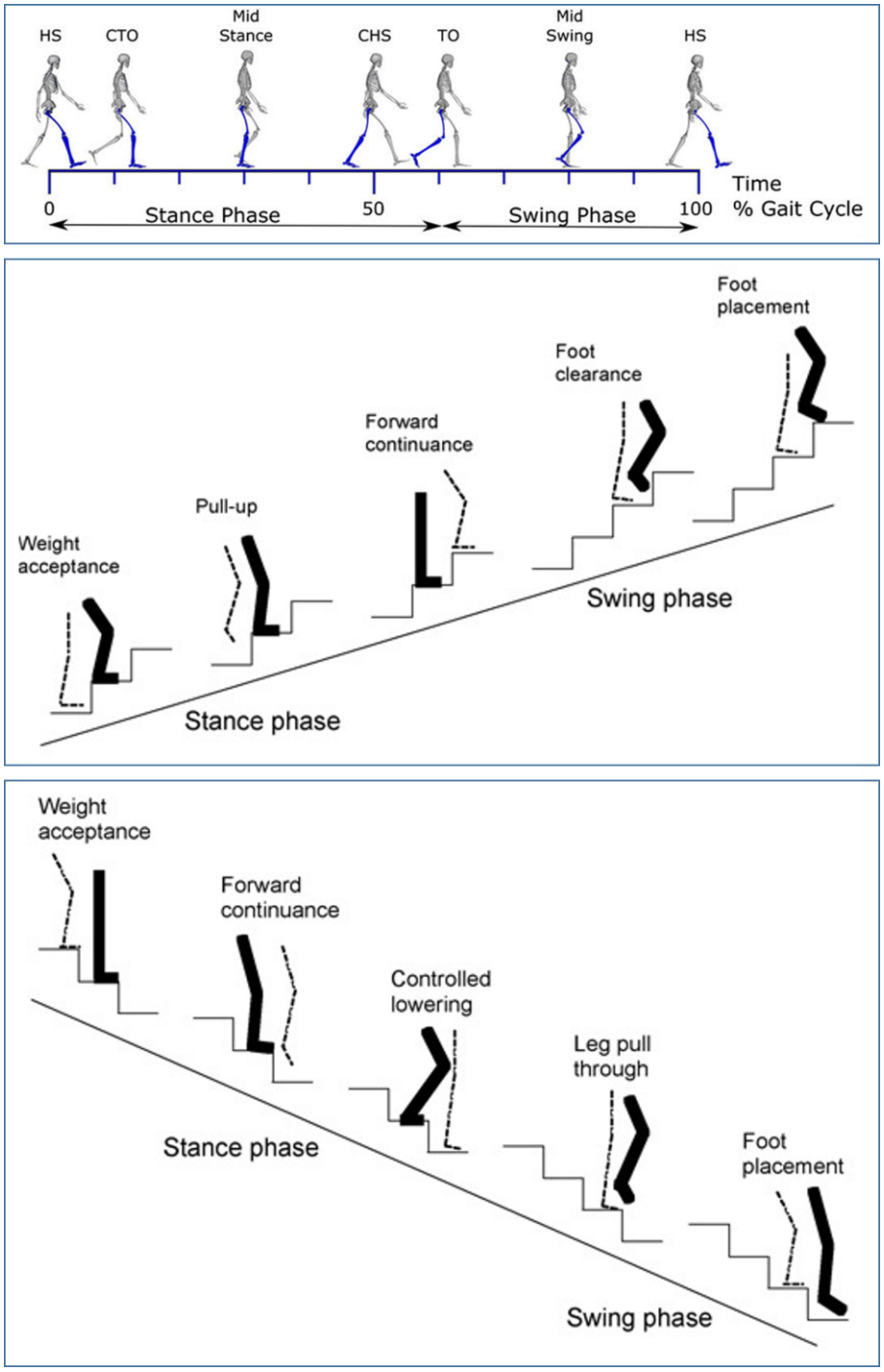


Figure 4-44: Gait cycle compromises of two distinct phases; stance and swing phase. During the swing phase the foot remains in contact with the ground. The top image is from [160]**.**

After the initial weight acceptance phase, the contralateral leg starts swinging and the weight distribution shifts to the ipsilateral leg. During mid-stance, the femur starts extending or flexing to maintain the progression of the gait cycle. The last portion of the stance phase is where the foot starts leaving off the ground. The heel starts rotating while toes remain in contact with the ground. This last part is called toe-off. Although the general gait cycle is similar for all three activities, the movements of different body parts are unique for each activity.

During the stance phase of the stair descent activity, after initial contact, the tibia starts bending forward and the femur starts flexing up to about 50 – 70 degrees relative to the tibia. The foot does not start rotating until close to the end of the stance phase. All the specified motions of the tibia and foot were updated for the stair descent activity. Also, the direction of rotation often changes and is not consistent as in deeper flexion activities.

During KDB, the upper body bends forward. This pelvis flexion is a function of the knee flexion. Also, pelvis rotation about the other two axes, AP and SI, are considered negligible. During the stair descent activity, the pelvis flexion is very limited, while the upper body rotates about the SI axis. The FSM model has been updated to account for these changes. Although the FSM does not include the contralateral leg, there is a force applied at the contralateral hip joint. This force is calculated based on the need to keep the pelvis and upper body stable and prevent the pelvis from moving excessively in ML direction. This force is calculated based on the ML changes in contralateral hip joint via the equation below

$$\vec{F}_{Cont.\ Hip} = \left(k * \left(x_{Hip} - x_0\right) + d * v_{Hip}\right) \hat{N}_3$$

$$x_{Hip} = \vec{P}_{No \rightarrow Hip} \cdot \hat{N}_3$$

$$v_{Hip} = \frac{dx_{Hip}}{dt}$$

Where k is spring stiffness coefficient, d is the damping coefficient, x_{Hip} is the distance of the hip joint from the global center in ML direction, x_0 is x_{Hip} at first time step, and v_{Hip} is the velocity of the hip joint. The stiffness and damping coefficients have been updated for the stair decent activity.

The final step is to simulate the effects of contralateral leg swinging. When the contralateral leg swings, the weight of the upper body is solely distributed on the ipsilateral leg. Therefore, the C++ code will be updated to account for the upper body weight shift

```
TORSOMASSORIG = TORSOMASS; \\ Initializing the upper body mass

if t < t1
   TORSOMASS = TORSOMASSORIG;
else if t < t2
   TORSOMASS = 2*TORSOMASSORIG;
else
   TORSOMASS = TORSOMASSORIG;
```

4.6.5 Stair Ascent

Stair ascent activity, like other gait-type activities, is similar to the stair descent activity, in that it encompasses two separate phases, stance phase, and swing phase. One of the differences between these two activities is the rotation profile of the bones. In the stair descent activity, the tibia and the femur start in a nearly straight, full extension condition, and then both the femur and tibia start bending forward to accommodate the contralateral leg swing phase. In stair ascent activity, however, the knee is moderately flexed. Then, the tibia starts bending forward slightly, and then tibia bends backward to an upright position. During this part, the femur extends to an almost fully extended

position. Close to the end of the activity cycle, the foot also starts bending forward.

The PID controller and rotation profiles for all other bones have been updated from stair descent activity. Similar to stair descent activity, the upper body weight shift is also considered for this activity.

4.6.6 Gait

Walking on level ground is the most common daily activity, and that is why it is one of the most studied activities following the TKA procedure to investigate the mechanics of the knee joint, especially the loads applied on the joint and wear pattern of the bearing insert. Although the forces are not as high as those derived in deeper flexion activities, the incidences of this activities are significantly greater than all other activities combined throughout a normal day. With the progression of knee OA, the kinematics and kinetics of the knee joint, such as knee abduction and flexion moment, are altered during walking [153]. Therefore, it is important to investigate whether TKA treatment can achieve better joint mechanics.

Unlike stair ascent and stair descent, the center of mass is mostly moving horizontally in level walking, hence fewer joint forces and moments are required to move the body. The first difference between level walking and stair climbing is that the heel strike in stair activities is not actually a heel strike. The whole foot is in contact with the ground at the heel strike. In gait, the toes are off the ground, and heel is in contact with the ground. Then the foot starts rotating until both the heel and toes are in contact with the ground. During mid-stance, the whole foot is stationary on the ground. Close to the end of the gait cycle, toe-off part, the heel starts rotating again while toes are in contact.

It is worthwhile to note the difference in the foot rotation regions. This is important because the center of rotation for foot changes throughout the activity. Therefore, it needs to be carefully modeled. As previously mentioned, the FSM is a multibody dynamic chain starting from the ground up, which means that the foot is defined relative to the ground, and each body/frame is defined relative to its distal body/frame.

From the global center, the coincident point between the foot and the ground is defined, and the center of mass of the foot is defined relative to this coincident point. The tibia and other bones are defined in the same fashion; from the distal body/frame to the coincident point and then from that point to the center of mass of the next body. These coincident point between two bodies/frames are the center of rotations for proximal body/frame (Figure 4-45). The position vectors are usually constant but can be defined as functions of other parameters such as time or flexion.

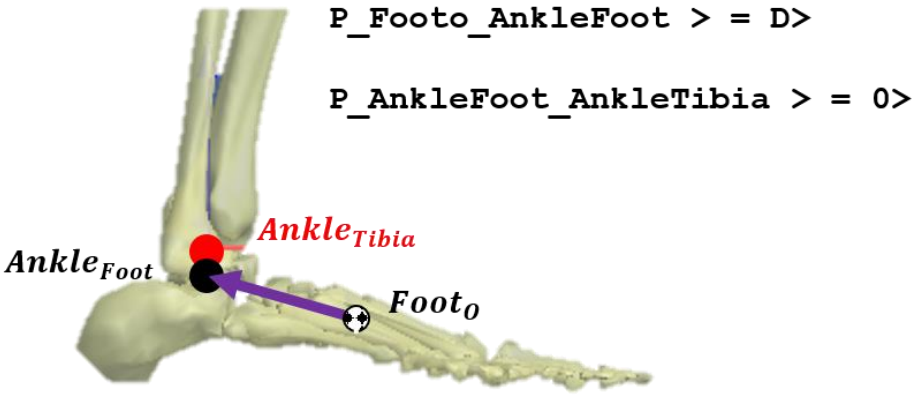


Figure 4-45: Each body's location is defined relative to its distal body/frame using the concept of the coincident point. The black point is the coincident point on the foot, and the red point is the coincident point on the tibia. This coincident point is the tibia center of rotation.

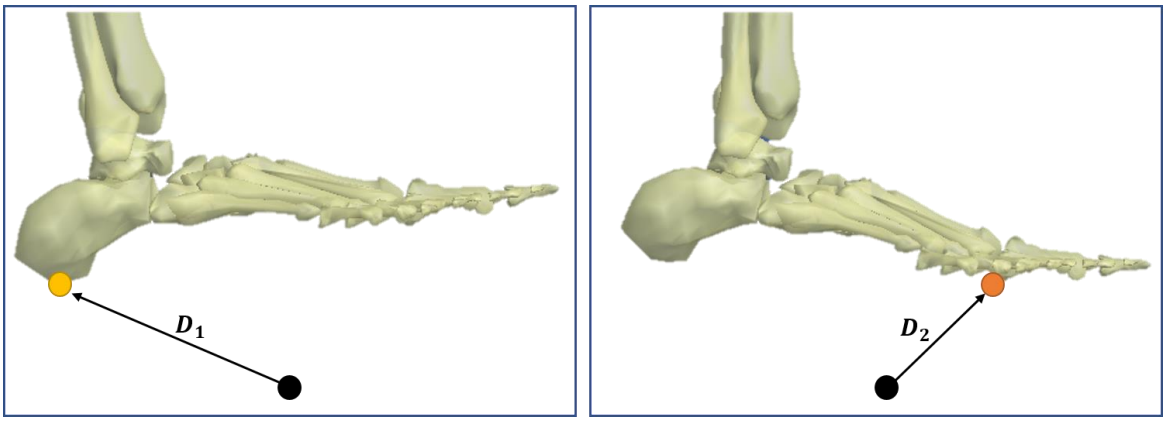


Figure 4-46: The center of rotation of the foot changes throughout the gait cycle.

As mentioned before, the position vectors can be defined as a constant or a specified function of time/flexion. The position vector from the global center to the coincident point between the foot and the ground is defined as constant in other activities. This position vector is initially defined as a specified function of time and is later modified in the C++ code based on below pseudo-code

```
if t < t1
    P_NO_NFoot = D1;
else
    P_NO_NFoot = D2;
```

The muscle controller and gains are updated to account for the different muscle activations.

4.7 Revision TKA

TKA designs can be divided into two main categories: primary and revision. When the primary TKA fails, the patient will have a second surgery where the primary knee implant components are removed and replaced with revision TKA components. Revision TKAs account for 6.9%, 6.4%, and 7.5% of all knee arthroplasties performed in 2016, 2017, and 2018 in the US, respectively [161,162]. There are several reasons associated with TKA failures, with

loosening, infection, instability, and stiffness being the dominant reasons [163]. In general, these revision TKAs are very constraining designs, only allows for limited joint mobility.

The previous forward solution model only accounts for primary TKA. One of the objectives of this project is to further expand the mathematical model to include revision TKA. Two types of revision TKA will be included in the model: rotating bearing hinge system and a fixed bearing hinge design. In both designs, the femoral component only rotates about the ML axis with respect to the tibial component.

The bearing insert can rotate about the SI axis relative to the tibial tray in the rotating bearing design. The bearing is fixed to the tibial tray in the fixed bearing design. However, that does not mean the femoral component cannot axially rotate. The axial rotation in this design is facilitated using another component between the femoral component and the tibial tray. The difference between these two models will be explained later.

The newest version of the forward solution model has the ability to simulate both of these knee hinge systems (Figure 4-47).

In the following sections, these models and the changes to the forward solution model will be explained in more detail.

4.7.1 Rotating Bearing Hinge System

4.7.1.1 Overview

The rotating bearing hinge implant is a highly constrained system in which the femoral component only rotates about the ML axis. A pin between the femoral component and the insert facilitates this rotation. To provide the axial

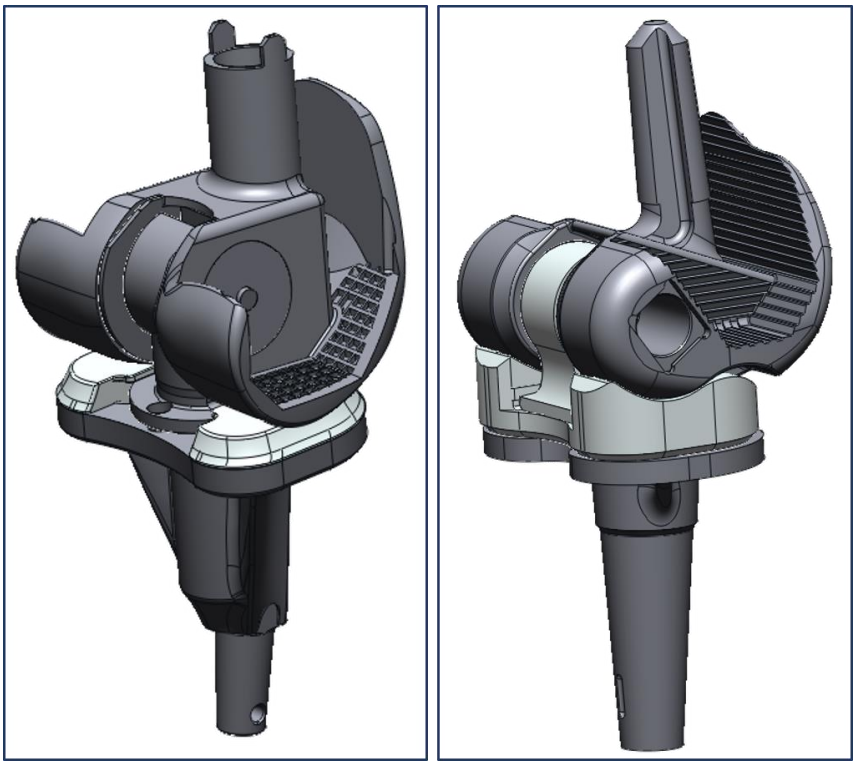


Figure 4-47: Incorporated hinge systems into the forward solution model. The rotating bearing hinge system is shown on the left. The femoral component rotates about the ML axis, and the insert rotates about the SI axis. The fixed bearing design is shown on the right. The femoral component rotates about the ML axis, the bearing is fixed, and the pin rotates about the SI axis (right).

rotation of the knee, the implant is designed to be a mobile bearing implant, i.e. the insert rotates about the SI axis with respect to the tibial tray (Figure 4-48). In order to represent the rotating bearing hinge implant, some modifications have been made to the FSM, which will be explained in the following chapters.

4.7.1.2 Cam/Post Mechanism

The main difference between the rotating bearing hinge and traditional TKA is the constrained rotation and translation of the femoral component with respect to the bearing insert. In this type of implant, this restricted movement is achieved by inserting a pin inside the rings of the femoral component and the insert (Figure 4-49).

In the FSM, the cam/post mechanism is implemented to model the interaction between the femoral component and the insert. Since the contact surfaces are cylindrical, both anterior and posterior cam/post mechanism are used simultaneously. The outside surface of the pin will be modeled as a point cloud and considered as the cam on the femoral component (Figure 4-50). This point cloud will be used for both anterior and posterior cam/post mechanism.

The inside surface of the bearing insert ring will be used for post surfaces in the cam/post mechanism. As shown in Figure 4-51, the cylindrical surface inside the ring is divided into two portions, to represent both the anterior and posterior post surfaces.

Another useful tool for analyzing the rotating hinge implant is to evaluate how the clearance between the pin and ring can affect the outcome of the implant. To this end, the user can quickly simulate moving the post surfaces of the ring anteriorly or posteriorly to assess the effects of clearance and find the optimal solution (Figure 4-52).



Figure 4-48: Assembly view of the rotating bearing hinge implant.

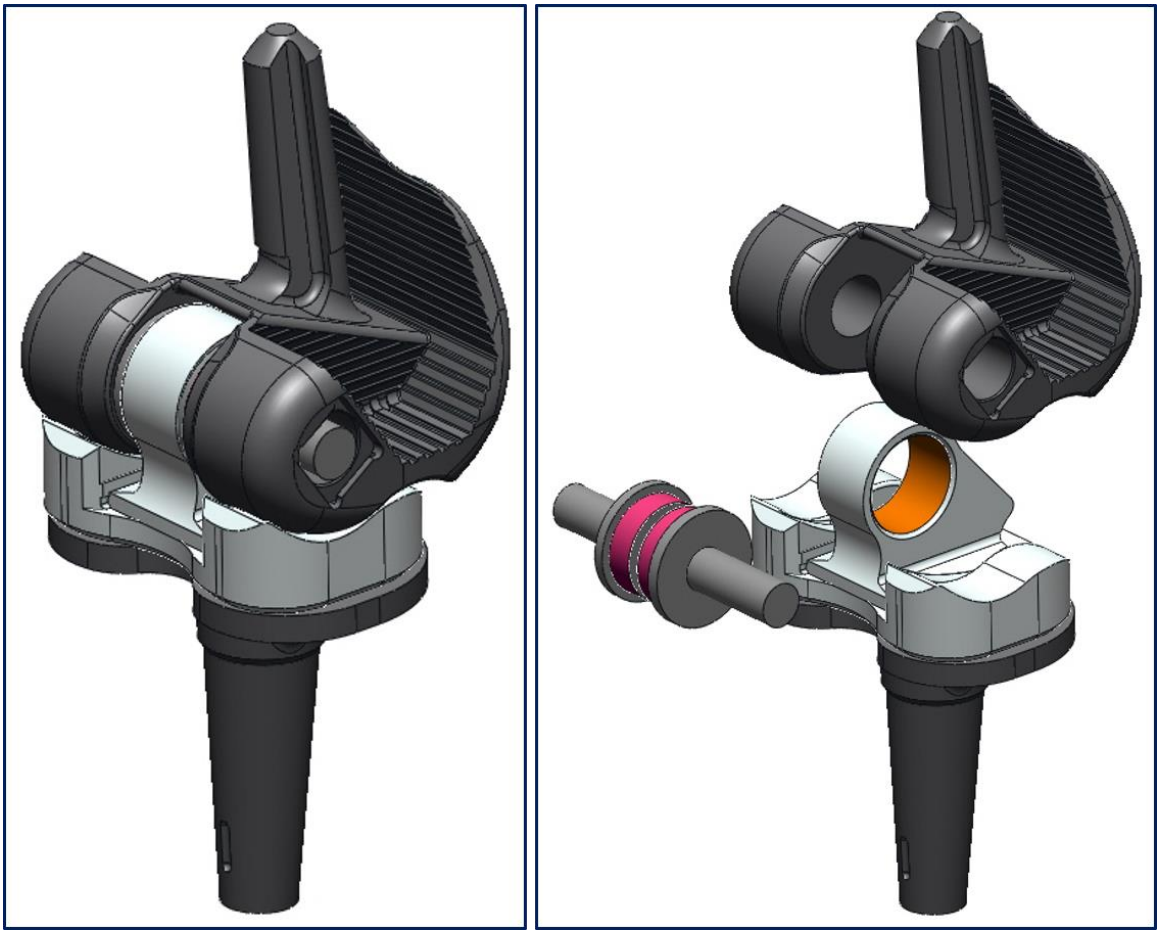


Figure 4-49: The assembly of the rotating bearing hinge design. A pin inserted between the bearing insert and the femoral component restrict the AP and SI motion of the femoral component and facilitate the flexion. The surfaces shown with magenta and orange are the articulating surfaces of the cam/post of the hinge design.

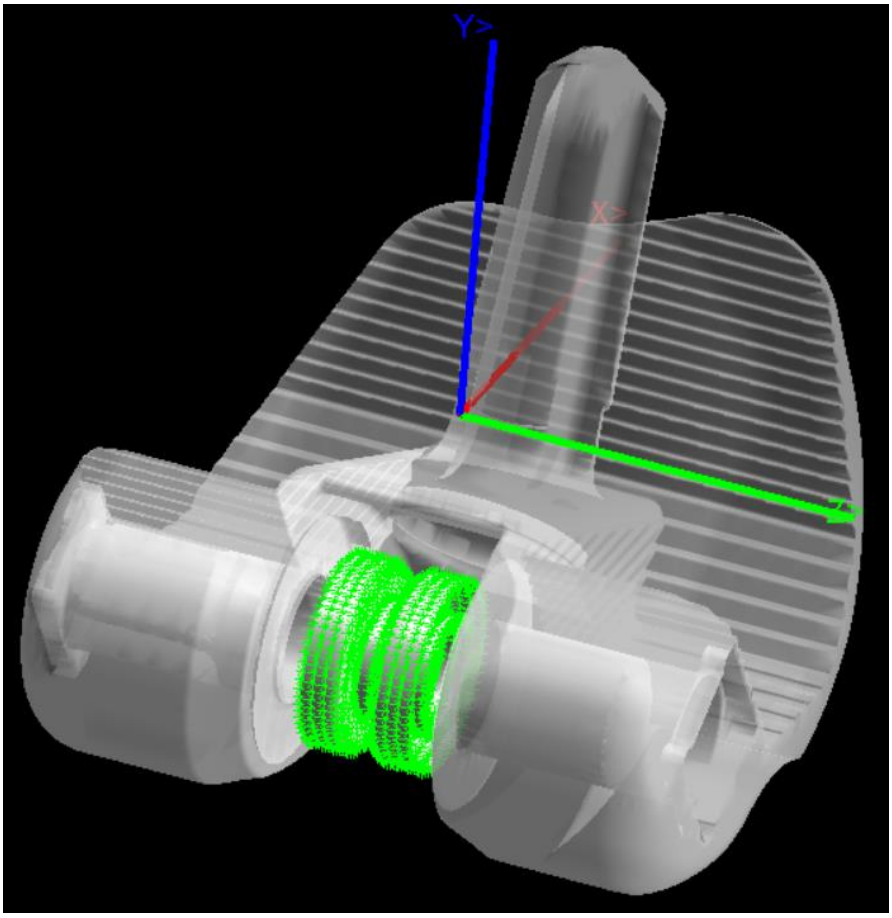


Figure 4-50: Cam point cloud on the femoral component. This point cloud is used for both anterior and posterior cam/post mechanism.

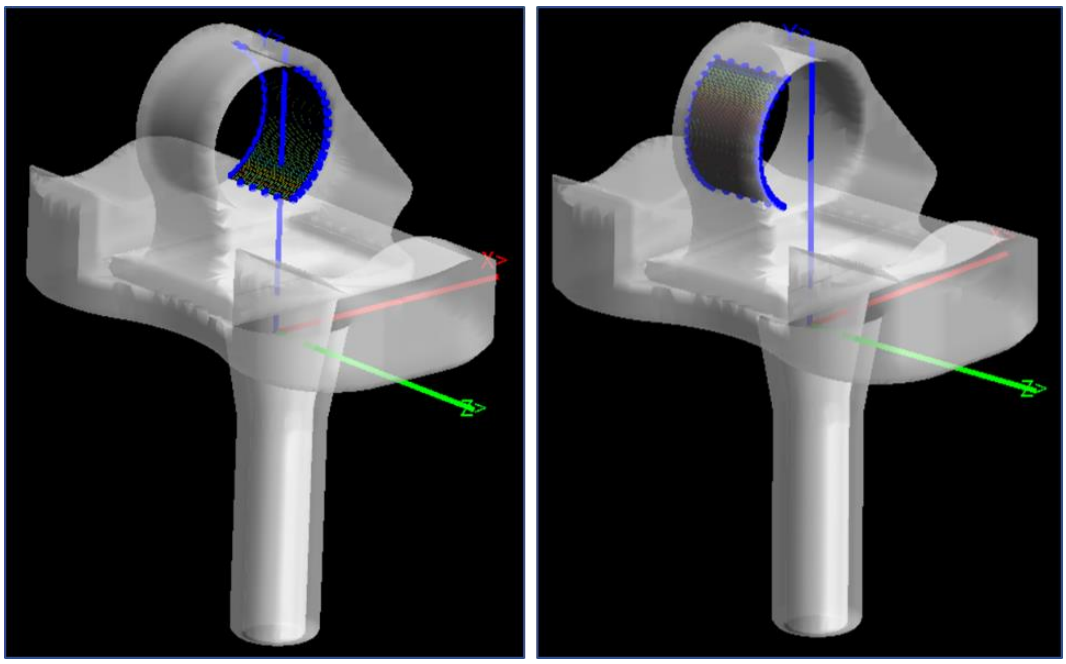


Figure 4-51: The inside surface of the bearing will be used to represent the post surfaces in the cam/post mechanism. Left) the anterior post surface, right) the posterior post surfaces on the bearing insert.

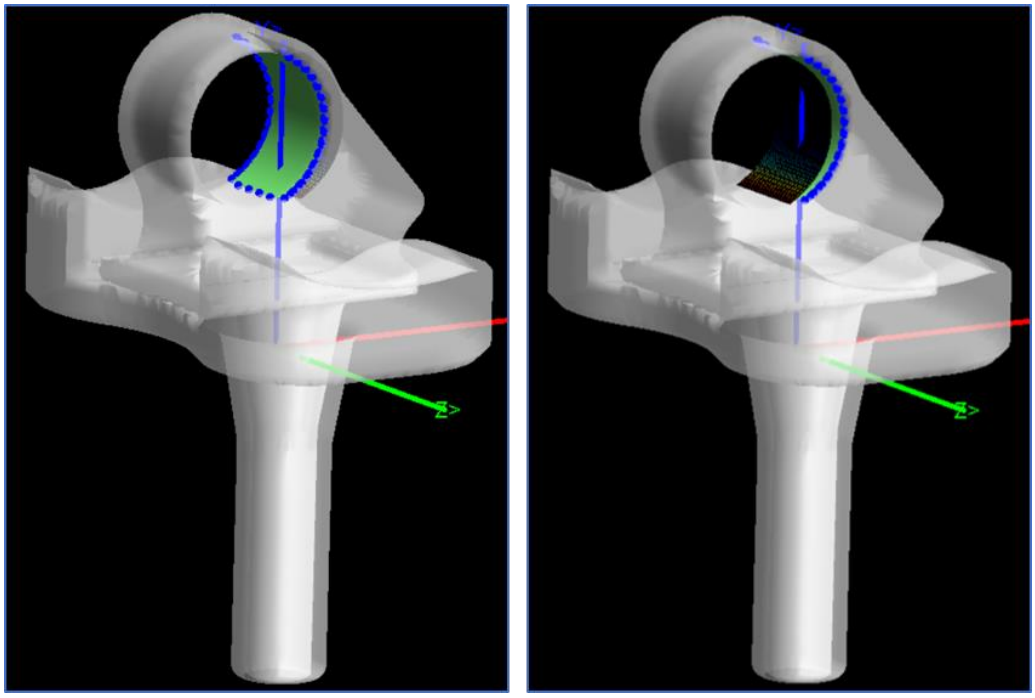


Figure 4-52: Moving the ring surfaces anteriorly or posteriorly can be used to simulate different clearance between the pin and the ring. Left) Increasing the clearance between the pin and the ring; right) Decreasing the clearance between the pin and the ring.

4.7.1.3 ML Spring

As it was mentioned before, the rotating hinge implant is highly constrained. The anterior-posterior translation is constrained by the pin and the ring. Moreover, the medial-lateral translation is constrained by two bushings around the ring, which prevents the femoral component from sliding in ML direction. To model the effects of these bushings, a new feature has been added to the FSM called "ML Spring." The bushings are modeled as spring with high stiffness coefficient.

To simulate the effect of the bushing, two coincident points are defined on the femoral component and bearing insert. An interactive spring force is applied between these two points. The location of the contact point on the femoral component relative to the femoral component center of mass is defined by the user in the GUI. The coincident point on the bearing insert is defined relative to the insert center of mass and calculated by this equation

$$\vec{P} = p_1 * \overrightarrow{Poly_1} + p_2 * \overrightarrow{Poly_2} + p_3 * \overrightarrow{Poly_3}$$

$$p_i = \vec{P}_{Polyo \rightarrow MLSpring}.\overrightarrow{Poly_i} \qquad i = 1,2,3$$

Where $\vec{P}_{Polyo \rightarrow MLSpring}$ is the distance from the bearing insert center of mass to the location of the coincident point on the femoral component. And $\overrightarrow{Poly_i}$ are the unit vectors of the insert coordinate frame.

Then an equal and opposite force is applied between these two points. The spring force is calculated based on the amount of the relative movement of the femoral component relative to the bearing insert, obtained from the below equation

$$\vec{F} = -K_{MLSpring}\left((p_1 - p_1^0) * \overrightarrow{Poly_1} + (p_2 - p_2^0) * \overrightarrow{Poly_2} + (p_3 - p_3^0) * \overrightarrow{Poly_3}\right)$$

p_i are described above and p_i^0 are the p_i at the initial time step. $K_{MLSpring}$ is the spring stiffness coefficient based on the bushing material properties and it can be modified by the user.

In order to have more flexibility in the model, the location of the ML Spring with respect to the femoral component can be defined by the user (Figure 4-53).

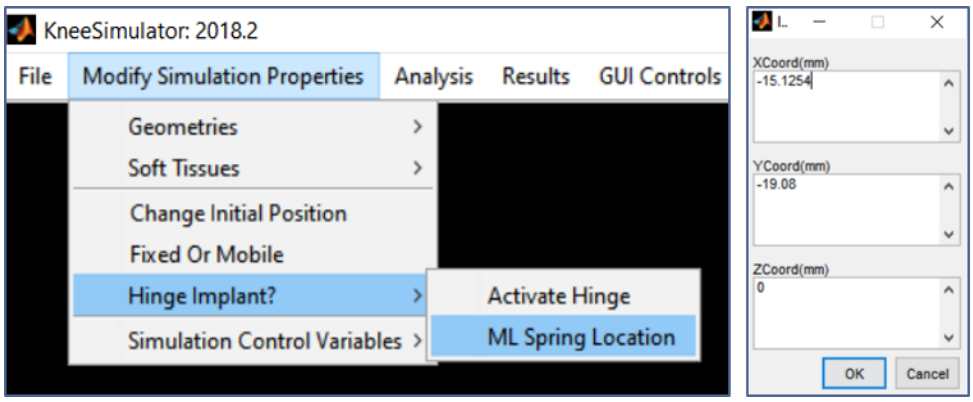


Figure 4-53: The location of the ML Spring force can be defined in the GUI.

4.7.2 Fixed Bearing Hinge System

4.7.2.1 Overview

The fixed bearing hinge system is also a hinge knee system. However, there is a substantial difference between this implant type and the rotating bearing hinge design. The first difference is that the rotating bearing design has single radius femoral component design. This means that during the whole range of flexion the femur rotates about the same axis. On the other hand, the fixed bearing design has J-curve design which means the early flexion femoral curvature and the later flexion femoral curvature are different (Figure 4-54). Different femoral curvature means that the femoral component can translates freely in the SI direction (Figure 4-55) unlike the rotating bearing design which the SI motion is restricted.

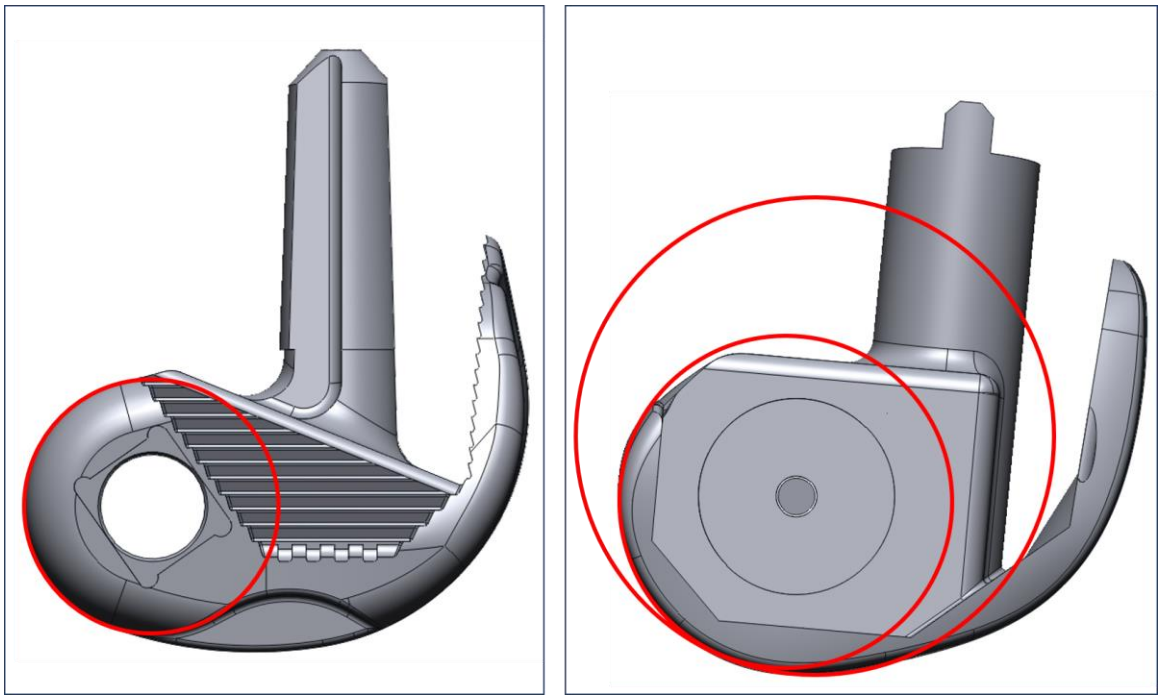


Figure 4-54: The rotating bearing hinge has a single radius femoral curvature (left). Therefore, the center of rotation remains the same during the whole range of motion. The fixed bearing hinge incorporates a J-curve sagittal curvature. The center of rotation for J-curve design is different between late flexion and early flexion.



Figure 4-55: the femoral component rotates about the ML axis and the SI axis and can translates in the SI direction.

The second difference between these two models is the femoral component axial rotation. As the name suggest the bearing is fixed in this design but it does not mean the there is no femoral axial rotation. A pin is designed and inserted between the femoral component and the tibial tray (Figure 4-56). This pin is able to axially rotates inside the tibial tray. The interactive forces happening in the contact forces between the femoral component and the pin (highlighted surfaces in Figure 4-56) force the femoral component to axially rotates with the pin on top of the bearing insert.

4.7.2.2 Pin Modeling

Although the basis of this implant is similar to a rotating bearing implant, the bearing is fixed. In order to solve this dilemma, a new component was introduced into the FSM to represent the pin. Having this component in the FSM is crucial to apply the interactive forces between the femoral component and the pin. Therefore, the IE rotation of the femoral component will be derived using these interactive forces and torques.

Similar to the rotating hinge model, for the fixed bearing hinge type design, the interaction between the femoral component and the pin is modeled using the cam/post mechanism. Same as before, the pin outside surface is considered as cam; however, the post surfaces are parts of the pin, instead of the bearing.

4.7.2.3 The FSM Changes

Few changes have been made to the FSM for modeling the fixed bearing design. It was mentioned that the pin needs to be considered as a new body. Therefore, the first step is to add the pin into the GUI as a separate body. Figure 4-57 shows the required steps to add the pin into the GUI.

Having the pin into the GUI, the next step is to incorporate the contact surfaces between the femoral component and the pin. The outside surface of the pin will be used to create the cam point cloud in the GUI (Figure 4-58).

Since the post surfaces are now part of the pin structure, a new feature has been added to the model to incorporate these surfaces on the pin. Figure 4-59 indicates the steps for adding the cam/post surfaces in the GUI.

Following these steps, the anterior and posterior post surfaces can be introduced into the GUI (Figure 4-60).

4.8 Graphical User Interface

As the FSM is expanded, the ability to simulate various types of implants and multiple activities is increased and therefore, the GUI must be updated to account for these changes. In the new FSM, the GUI has been updated to include all the new updates while maintaining the simplicity of use for non-technical users.

4.8.1 General

The primary purpose of the FSM GUI is to facilitate the process of mathematically evaluating the TKA implants design. To this end, in the latest version of the FSM, the user interface has been updated to be more user-friendly. The first attempt was to modify the overall user interface visualization. In the previous GUI, the background color was dark, which sometimes made it difficult to distinguish the component from the background from various angles (Figure 4-61). The new FSM features a distinct background, aimed at a better representation of the bones and implant (Figure 4-62).

Also, the menu has been updated to make the GUI more-user friendly and avoid confusion with all recent modulus.

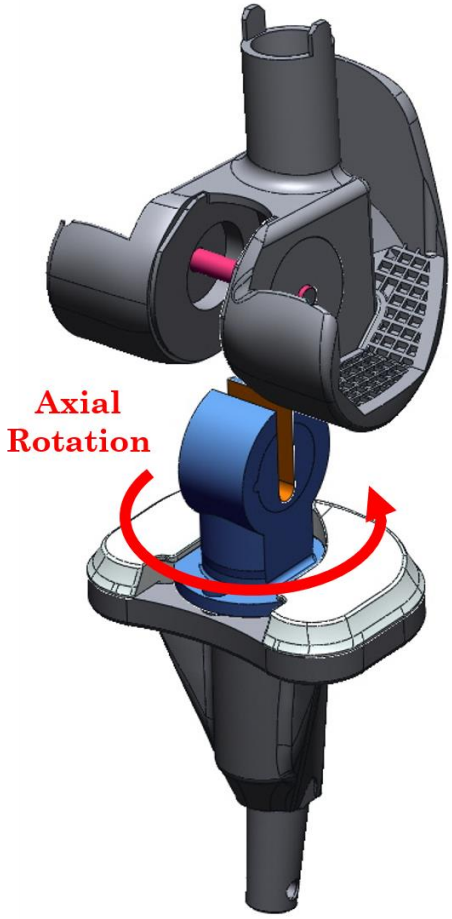


Figure 4-56: The bearing insert (white component) is fixed to the tibial tray in the fixed bearing design. The axial rotation occurs with the pin inserted between the tibial tray and the femoral component (blue component). the pin axially rotates inside the tibial tray and the contact between the surfaces between the femoral component and the pin (magenta and orange surfaces) force the femoral component to rotate axially with the pin.

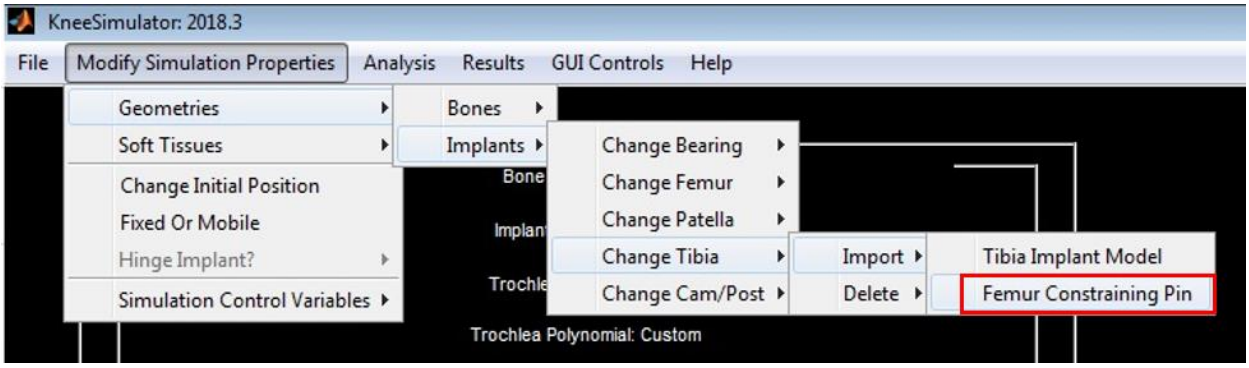


Figure 4-57: Adding the fixed bearing hinge into the GUI.

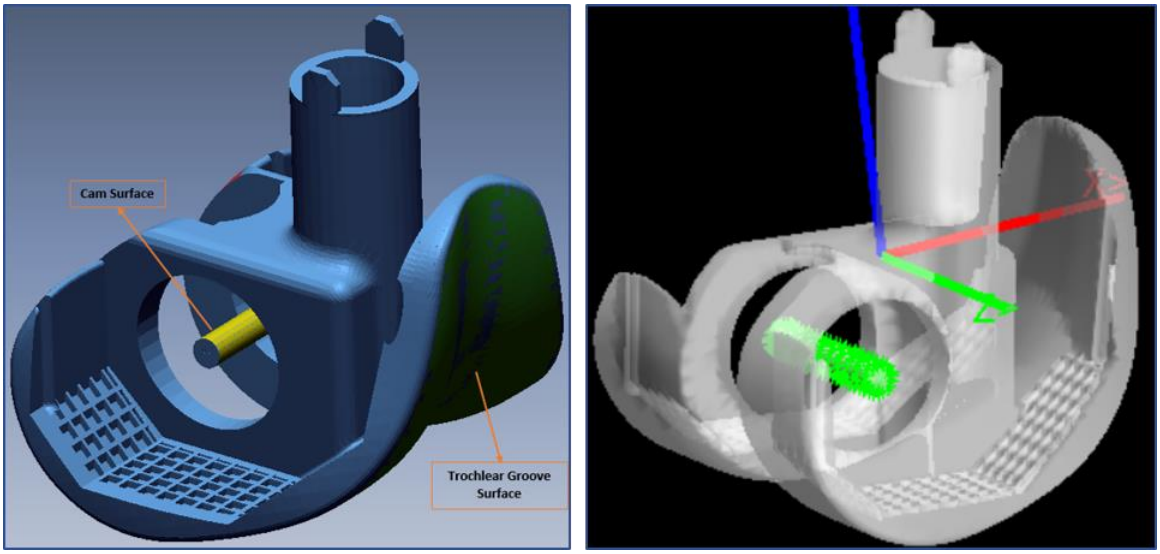


Figure 4-58: Modeling cam mechanism for the fixed bearing hinge. Left) The outside surface of the pin created to represent the cam. Right) The cam point cloud.

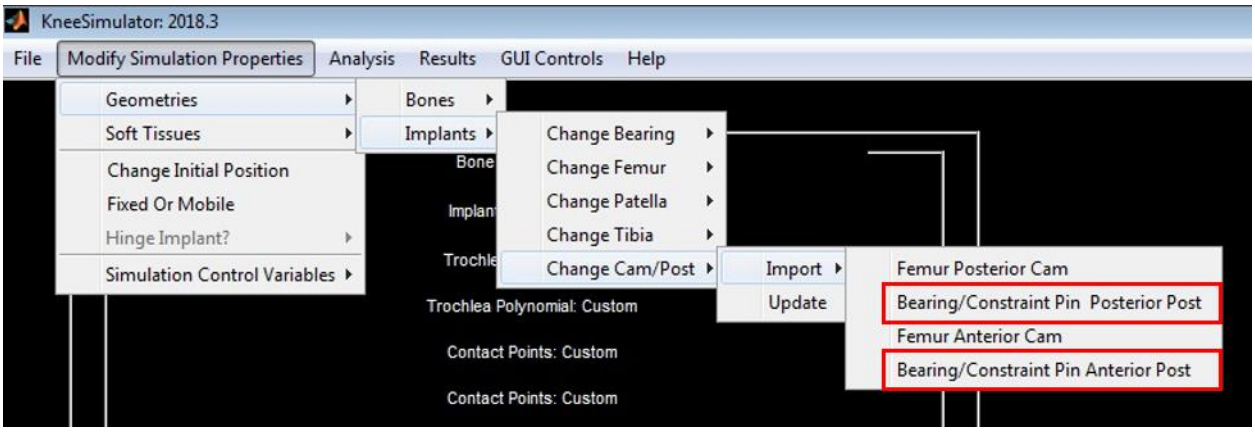


Figure 4-59: New feature for adding the post surfaces on the fixed bearing hinge.

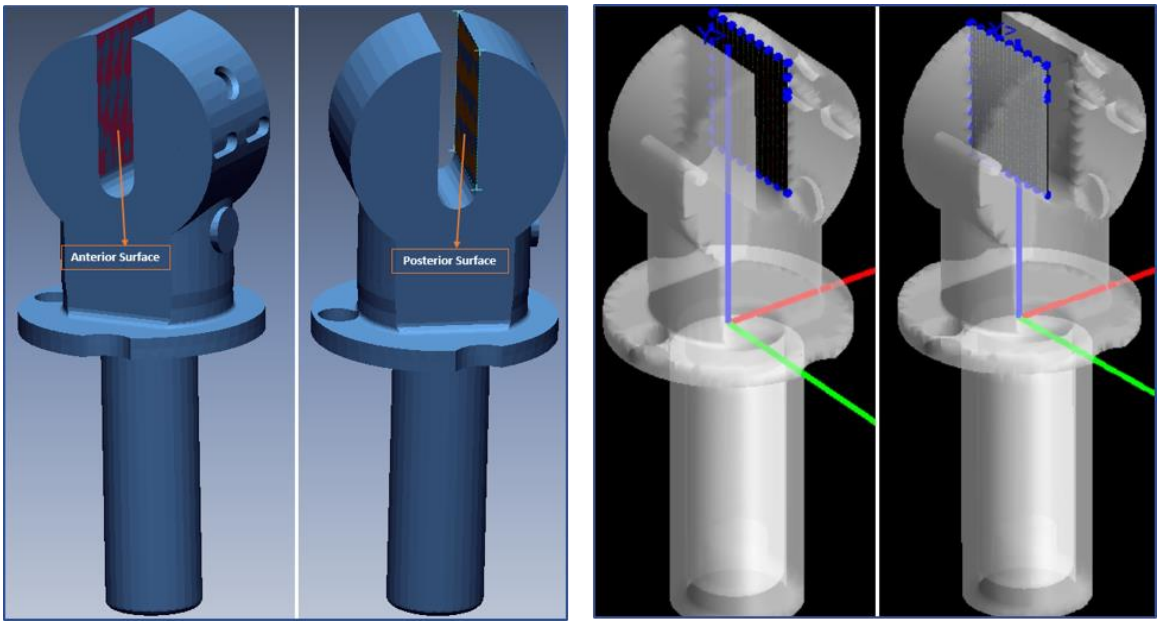


Figure 4-60: Post mechanism preparation for the fixed bearing hinge. Left) The anterior and posterior post surfaces on the pin. Right) The post surfaces representation in the GUI.

4.8.1.1 Activity-based activity plots

Often, when investigating TKAs and reporting the outcomes, the results are plotted with respect to the knee flexion angle. However, as it was mentioned in Section 4.6, flexion is not always increasing/decreasing in all activities and therefore the outcomes cannot be plotted with respect to knee flexion. The outcomes of TKA for gait type activities are usually reported with respect to the percentage of the activity. Therefore, all plotting functions in the GUI are updated to allow the user to plot the results based on the activity percentage as well as knee flexion (Figure 4-63).

4.8.1.2 GUI controls

Two new additions to the GUI are the ability to control the number of data points included in the results and the ability to export the CAD models and their respective transformation matrices.

When a simulation is complete, the results are stored in multiple text files at a location specified by the user. These text files usually contain about 20,000 data point for a DKB activity and can go up to 100,000 data points for squat to rise activity. The loading function in the GUI allows the user to associate results to the GUI. However, including all data points in the results is time-consuming and makes the GUI inefficient. Therefore, the GUI has been updated to allow the user to select the number of data points to include in the GUI (Figure 4-64).

The next functionality allows the user to export the bone and component geometries outside the GUI. The transformation matrices are also exported. By having the components and associated geometries, the user is able to import these geometries and transformations on other CAD software for further investigations.

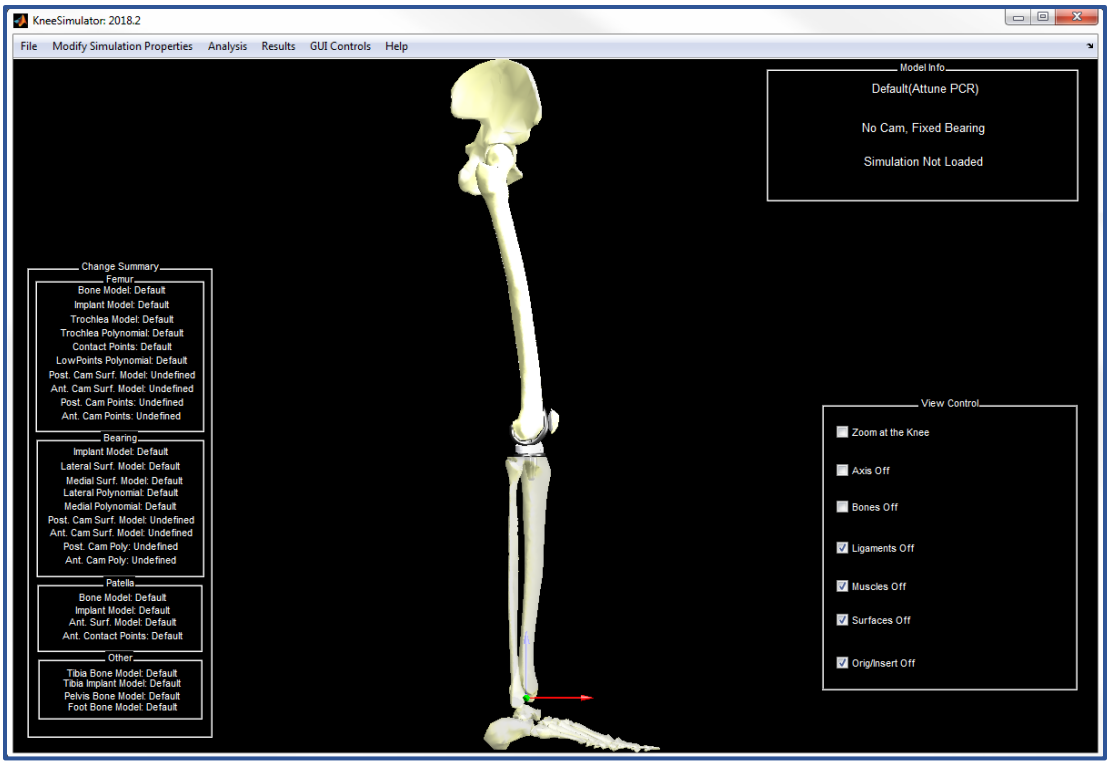


Figure 4-61: The previous user interface with a dark background.

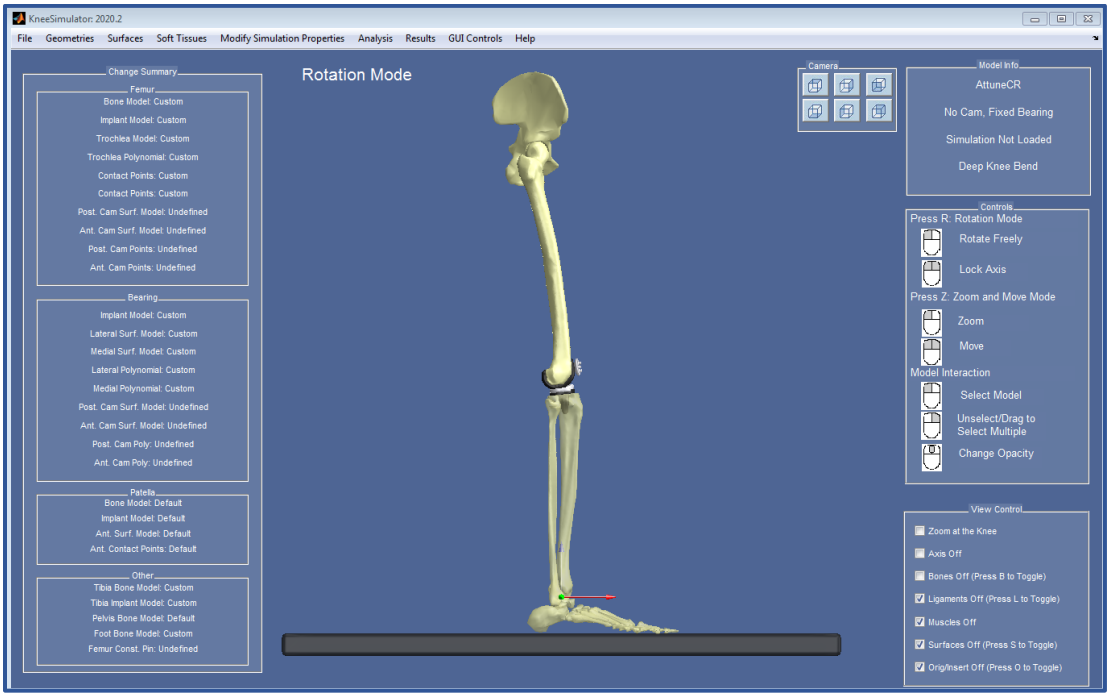


Figure 4-62: The new visualization of the user interface featuring a bright background.

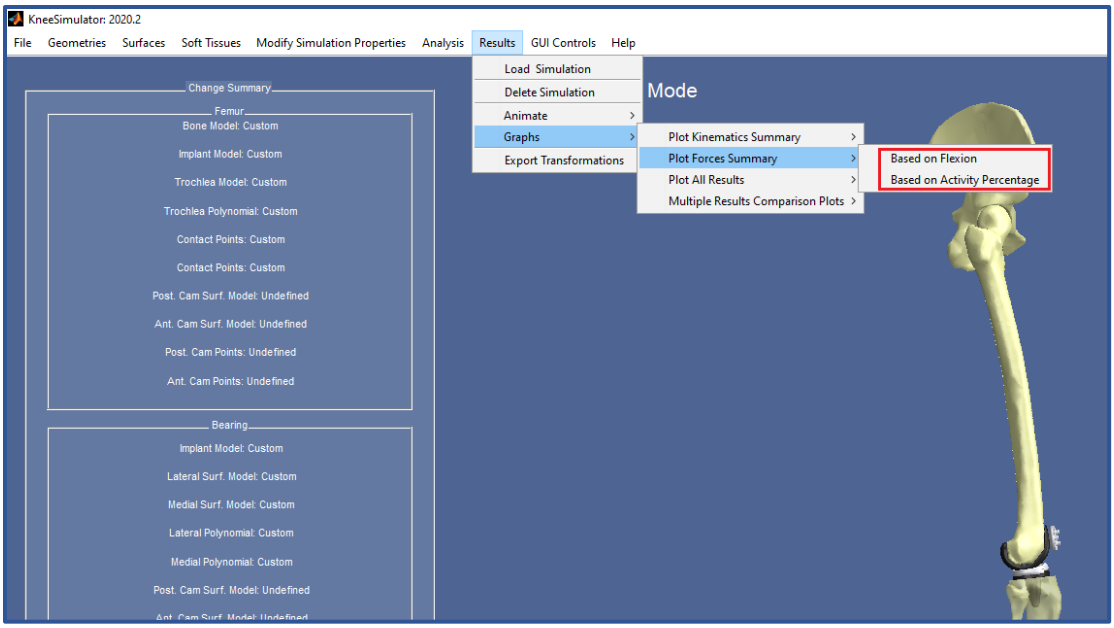


Figure 4-63: All plotting functions have been updated to allow the user to plot against the activity percentage as well as knee flexion.

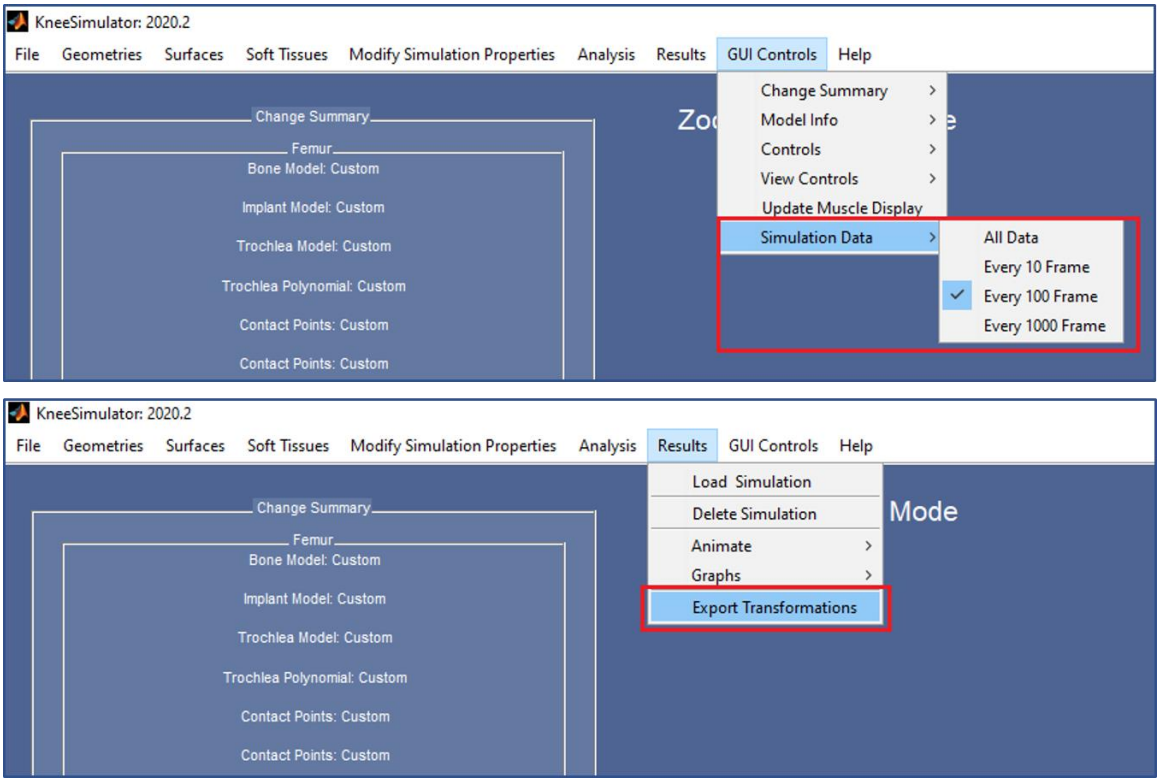


Figure 4-64: New updates of the FSM GUI. The user can control the number of data points included in the results (top). The GUI is capable of exporting the bone and component geometries, as well as their respective transformation matrices.

4.8.1.3 Compatible with newer MATLAB versions

The FSM GUI was developed in MATLAB 2013. Some of the functions used in the GUI are not updated in newer MATLAB versions. Two of the main functionalities of the GUI that are not working with the newer MATLAB versions are the ability to select the soft tissue attachments and modifying the cam post surfaces.

The structure of the GUI and the older functions have been updated to make the GUI compatible with the newer MATLAB version.

4.8.1.4 Import Femoral Component Condylar Surfaces

In the GUI, the femoral component surfaces are modeled with point clouds. Previously, these point clouds were calculated automatically based on the geometry of the femoral component implant. Since this is an automatic process, the point clouds are not true representatives of the contact surfaces.

A new feature has been introduced in the latest version of the GUI, by which the condylar surfaces can be directly imported to the GUI as one of these file types: iv, stl, or wrl. The point clouds calculated using this new feature better represent the actual contact surfaces (Figure 4-65).

4.8.1.5 Femoral Component Axial Rotation

Another feature has been added to the GUI for the kinematics plot. Previously, the internal/external rotation of the femoral component solely derived based on the Euler angles.

The new feature calculates the femoral component IE rotation based on the lowest point calculation. Figure 4-66 indicates the calculation for the new feature.

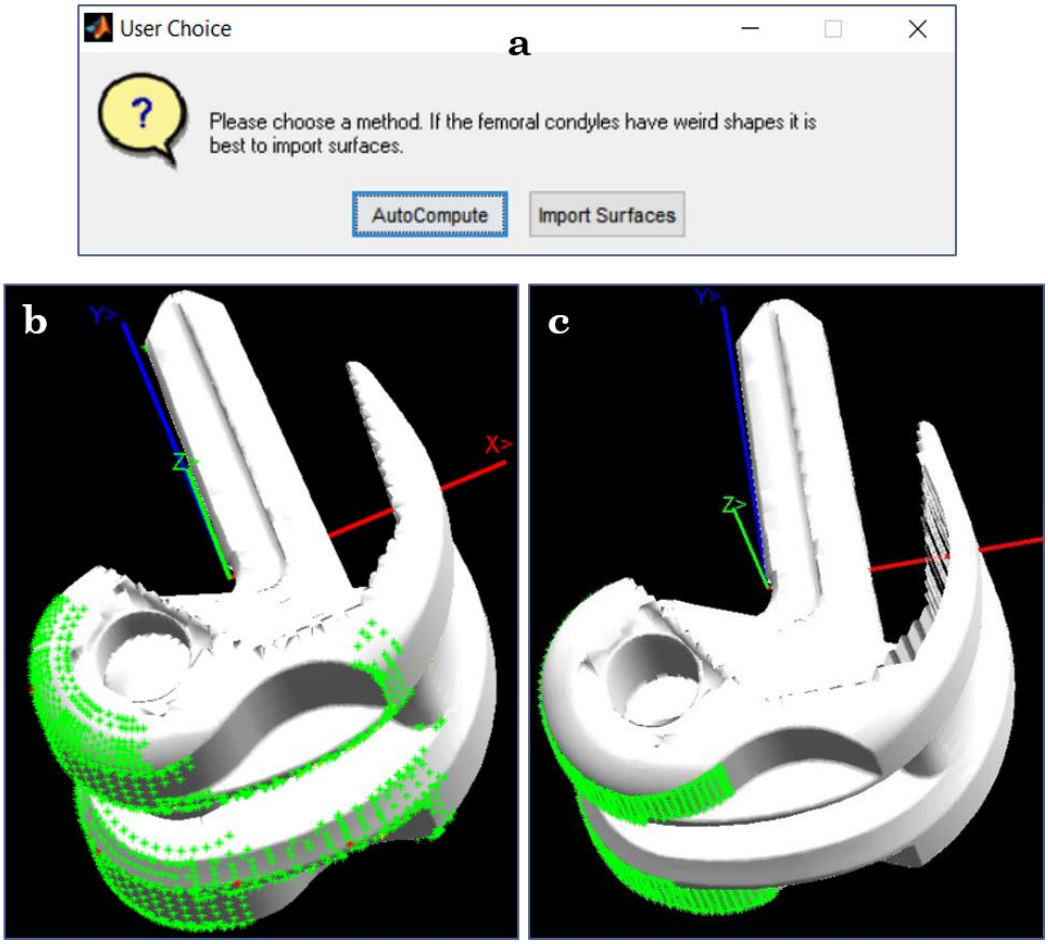


Figure 4-65: Difference between condylar points clouds by each method. a) Two methods to calculate the condylar point clouds. b) Condylar contact point cloud calculated by the 'AutCompute' feature. c) Condylar contact point cloud calculated by importing surfaces to the GUI.

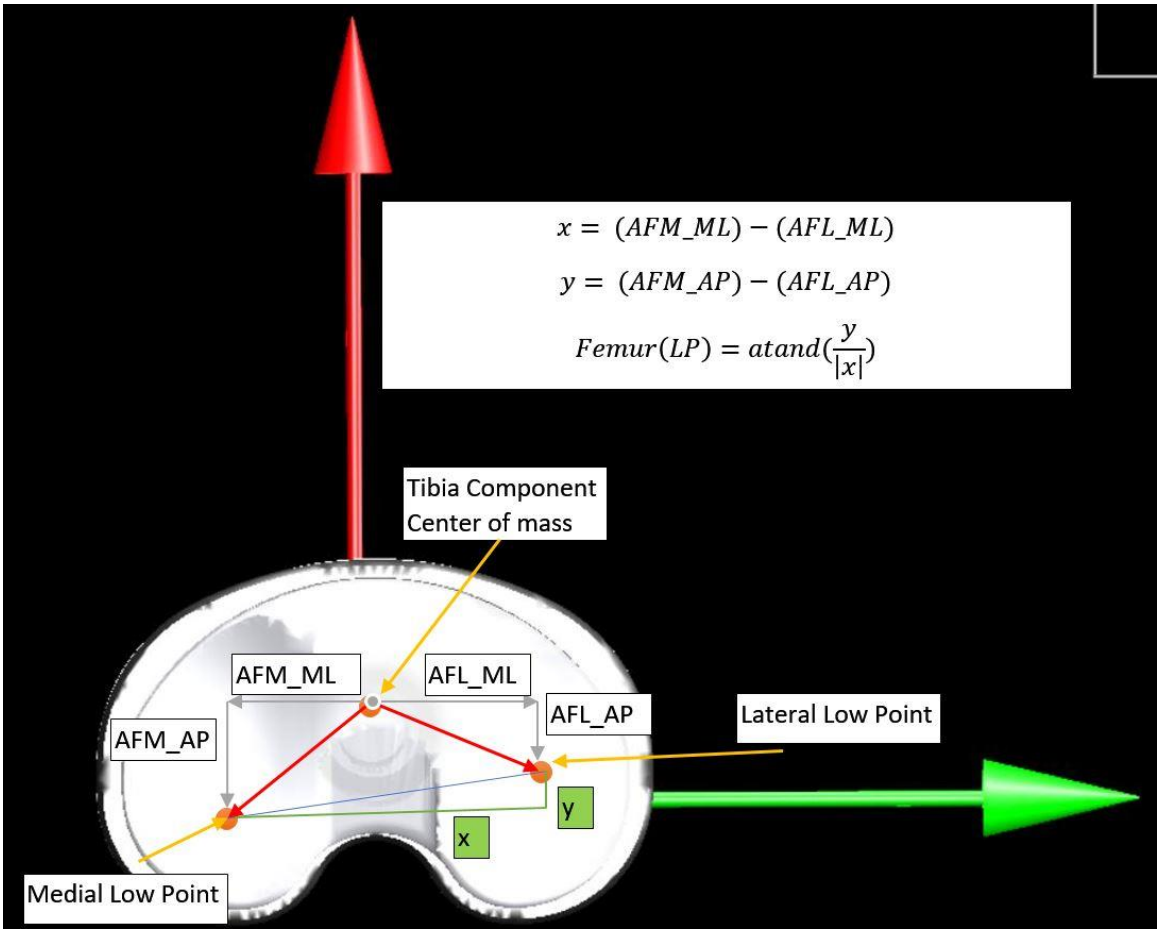


Figure 4-66: Femoral component IE rotation calculations based on the low points.

4.8.2 Wrapping animation

To visualize the muscle wrapping algorithm and how muscles wrap around bones and components, another module inside the main GUI has been developed to allow the user to investigate the wrapping of the muscles (Figure 4-67). Independent from the main GUI, the user can load and associate new results from simulations using the Load Data function. This function reads the output files from the simulation and updates the location of the muscle insertions and origins, as well as wrapping points. Additionally, information about the wrapping checks for each individual muscle is stored. Based on the information about wrapping checks, the flexion angle where wrapping occurs is calculated and the correct muscle wrapping is shown.

The wrapping module has two camera views from the left and right perspectives, allowing the user to view the knee from the lateral and medial sides, respectively. The user can change each of these views to a front view to visualize the muscle wrapping from the front view (Figure 4-68). The user can also select which muscle to visualize throughout the activity.

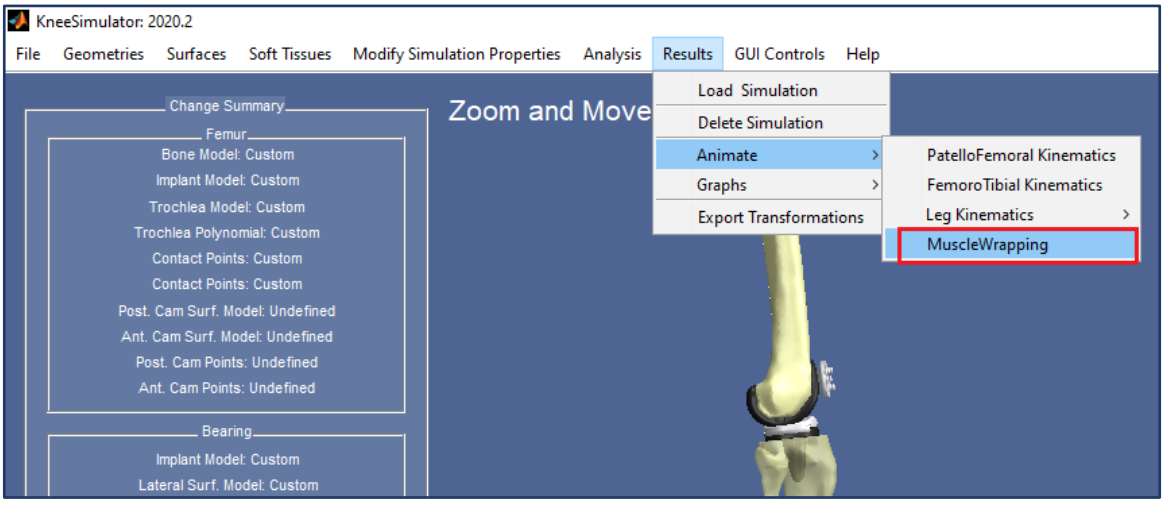


Figure 4-67: A GUI has been incorporated in the main GUI to visualize the muscle wrapping algorithm.

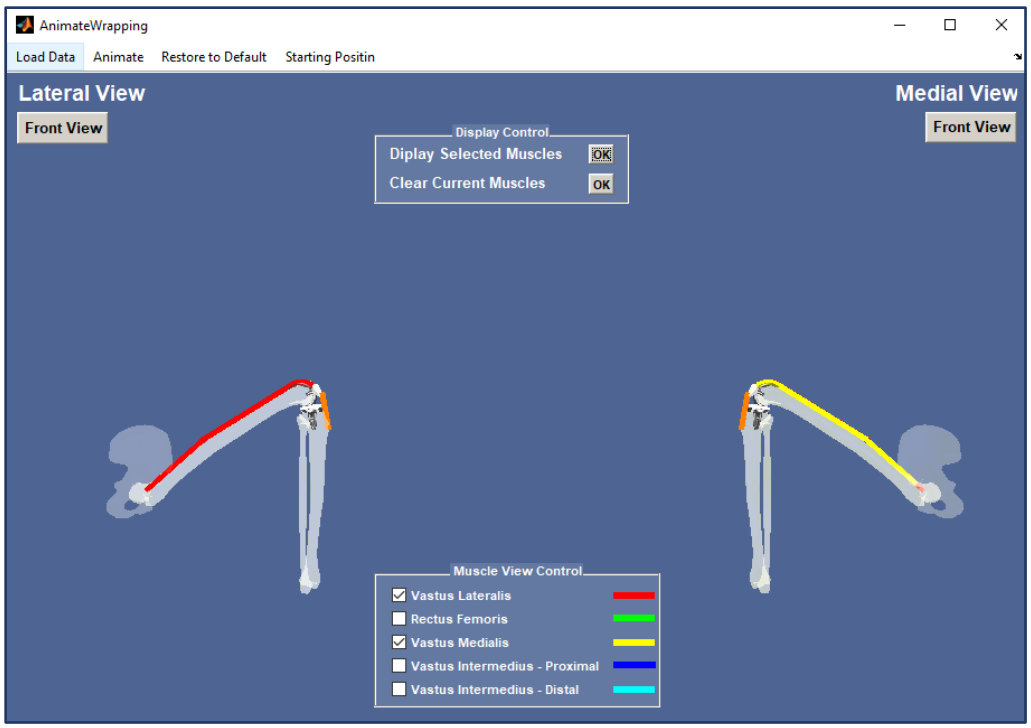


Figure 4-68: The user can select which muscle to visualize. The default camera views are lateral and medial, but the user can select to view the wrapping from the front view.

4.8.3 Physiological Knee Mathematical Model

4.8.3.1 Multiple subjects

As stated earlier, the GUI has been updated to include multiple subjects. Therefore, another feature has been added to the menu of the GUI that allows the user to efficient load these new subjects (Figure 4-69). For each subject, several default simulations were created which includes different TKA types, such as fixed-bearing PCR, fixed-bearing PS, mobile-bearing PCR, and mobile-bearing PS. When the user selects a new subject, the GUI loads the geometries of the bones and proper implant components. These subjects have different bone geometries and therefore different parameters such as muscle attachment, bodyweight, etc. Default values for these parameters are stored in external MATLAB files, and when a subject is selected, the specific values are loaded as well.

4.8.3.2 Default simulations

As mentioned in section 4.5.3 it is important to incorporate clinically relevant simulations. Several types of TKA simulations are created based on the fluoroscopic images to make the simulation more clinically relevant. A new feature was incorporated in the latest GUI that allows the user to select and load one of these predefined TKA simulations for various TKA designs (Figure 4-70). To create these default models, efforts have been made to replicate the actual surgical condition. Different tibial posterior slopes were considered for different TKA types: PS design without posterior slope, 6° posterior slope for CR, and 2° and 6° posterior slopes for ASTKA design. The placement of the component was done based on the average fluoroscopy data. To this end, average fluoroscopy data for the exact same model gathered from our fluoroscopy studies and similar initial conditions were considered for each TKA design (Figure 4-71).

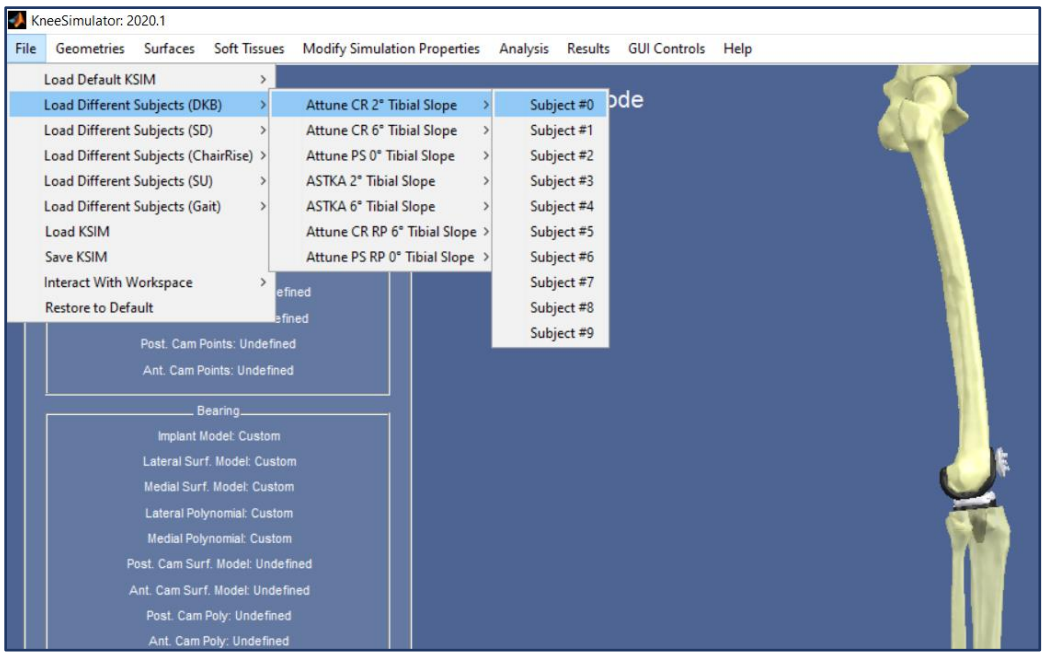


Figure 4-69: The user can easily select various subjects with different implant type to perform different activities simulations.

4.8.4 Tibia Bone modification

In the original version of the FSM, the user had the ability to change and modify the position and rotation of most of the implant and bone parameters to simulate different surgical condition and also misalignment. However, the tibial bone position and location could not be modified. For most primary TKAs this would not cause an issue since the changes can be applied on the tibial implant instead on the tibia bone. For instance, to simulate a varus/valgus situation, the user could simply rotate the tibial tray to replicate the actual situation. However, for revision TKAs, such as hinge designs, which are highly constrained, only modifying the tibial tray alignment cannot completely replicate the in vivo situation. Due to the highly constrained design of such TKAs, tibial tray alignment cannot be modified without changing the femoral component alignment.

To address this issue in the most recent FSM, in the "Modify Initial Position" Tab, a tab was created for the tibia bone (Figure 4-72). Similar to other bones and components, the user can manually change the rotation and position.

4.8.5 Initial Position

The placement of the components with respect to the bones is one of the essential factors of the efficiency of the knee mathematical model. In the FSM GUI, the user has the ability to modify the implant components positions, both translations and rotations, to any desired scenario to simulate different surgical conditions as well as investigate the effects of component misplacement on the TKA outcome. Although the previous GUI allowed the user to move the components (Figure 4-73) freely, the user had to place the component in such a way that there would be a clearance between the contacting surfaces, e.g., the femoral condyles and polyethylene insert plateaus

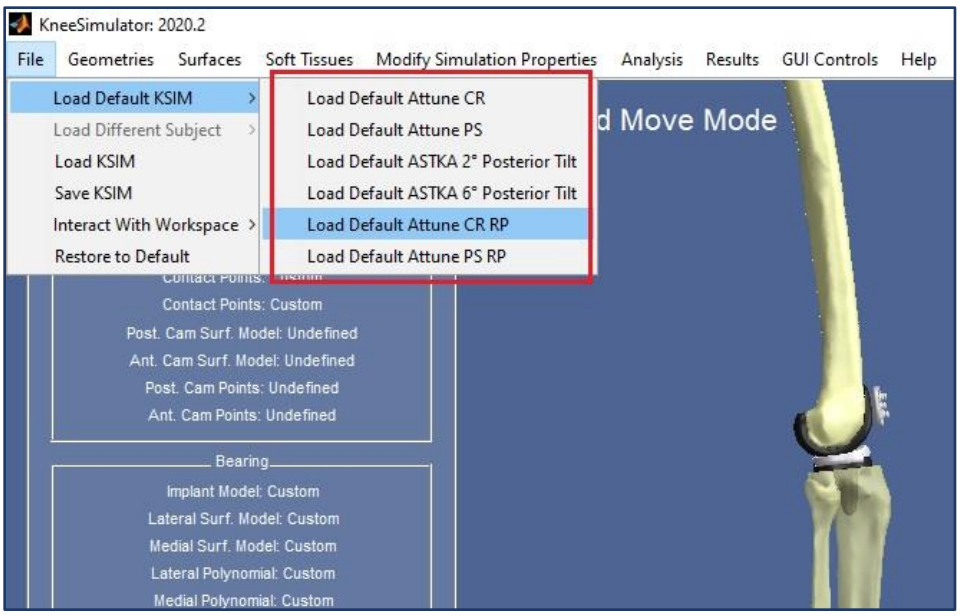


Figure 4-70: Different default simulations for different implants have been added to the latest GUI.

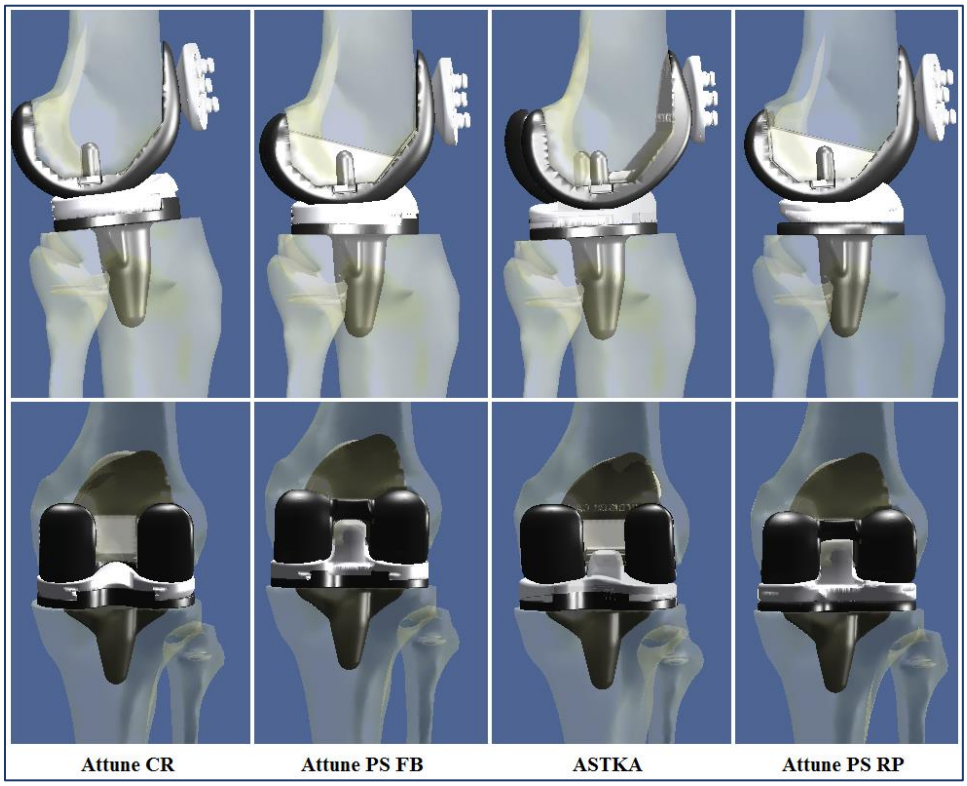


Figure 4-71: Default models were created and incorporated in the GUI for various TKA design.

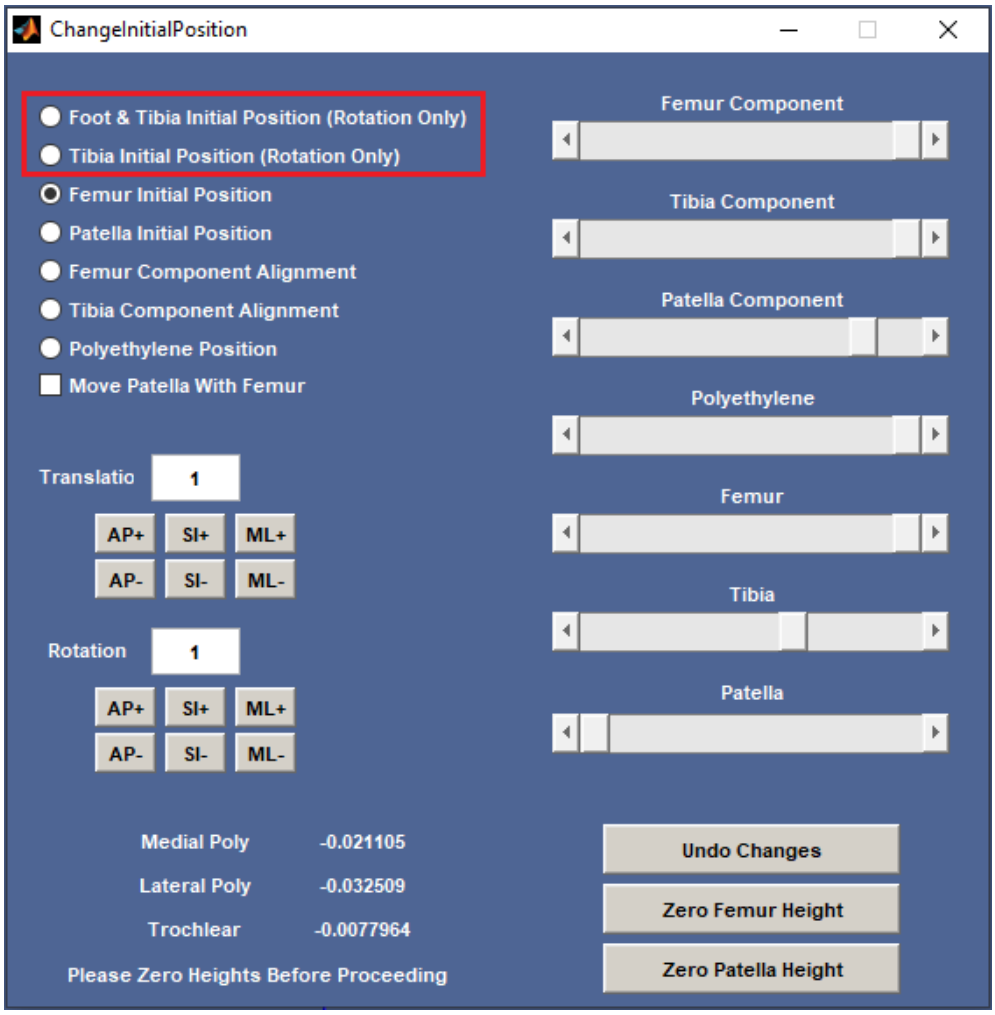


Figure 4-72: In the most recent version of the FSM user can modify the initial position of the tibia bone.

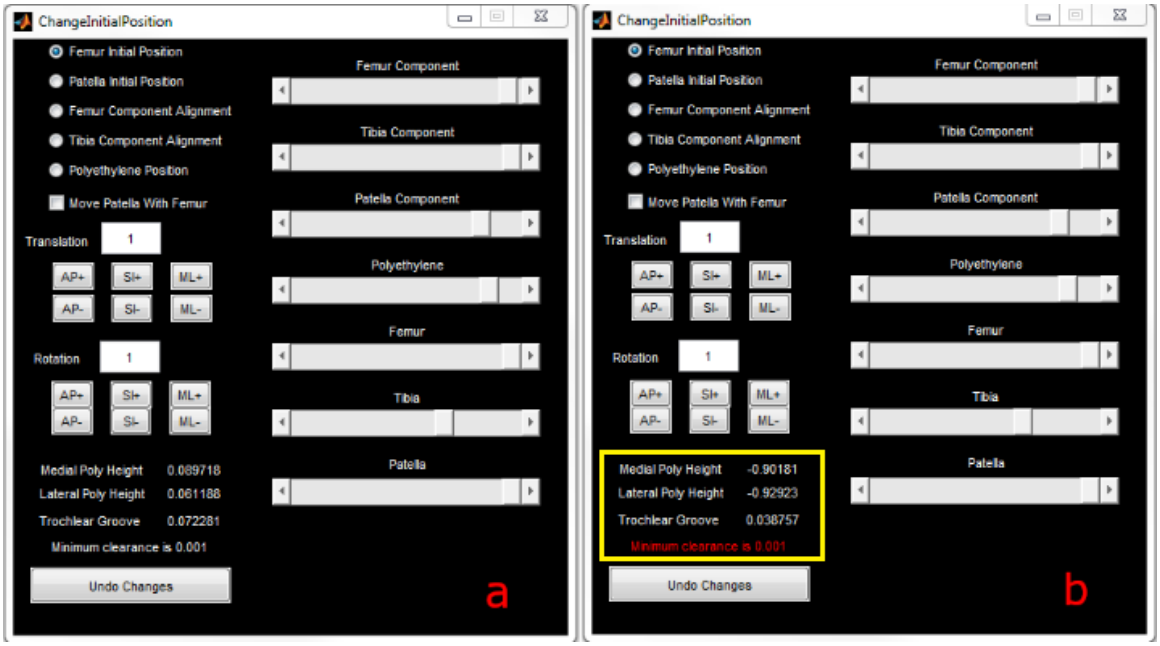


Figure 4-73: In the previous version of the GUI, the user selects the close initial condition (left), components cannot be placed in contacting condition (right).

or the trochlear groove and anterior patellar surface. The contact detection algorithm cannot be executed if the components are in contact.

Therefore, two main modifications have been implemented in the latest version of the FSM. First, the contact detection algorithm was slightly updated to support components being in contact at the beginning of the simulation. The previous contact detection crashed when there was a penetration at the first time step. Using a simple "if statement," the contact forces are no longer calculated at the first time step. The importance of this feature is twofold; first, it gave the user more freedom to place the implant the way it is implanted by surgeons. Secondly, and more importantly, when there is clearance at the initial time step, it causes a slight jump in contact forces right after the components were in contact. Therefore, having the ability to start in contact resolves the unrealistic increase in contact forces at the beginning of the simulation.

The second improvement in this regard is incorporating the ability to automatically change the contacting components. Two buttons have been added to the Change Initial Position window to alter the femur and patella position to get the exact starting position (Figure 4-74). The "Zero Patella Height" button changes the position of the patella in the AP direction to set the distance between the trochlear groove and the patellar surface to zero. The "Zero Femur Height" button has similar functionality, changing the femur distance in SI direction to have zero distance between the femoral condyle and insert plateaus. However, the mechanism is slightly more complicated. Since there are two contacting surfaces at the tibiofemoral joint, the algorithm first calculates the differences between the heights on the lateral and medial side, and therefore based on this difference, the femur is rotated to get the same height and then this distance is set to zero. This way, the height on the lateral side and the medial side would be the same.



Figure 4-74: The new version of the GUI features the ability to place the components at the close contact condition automatically.

4.8.6 Multiple Activities

To facilitate analyzing various activities, the GUI menu was updated to incorporate various activities (Figure 4-75). The menu is similar to the "multiple subjects" menu. However, when selecting various subjects, the GUI loads a file already created for each subject with proper bone geometries. This cannot reasonably be done for multiple activities for two reasons: first, this would mean creating several simulation files and storing them externally, which is time-consuming and takes unnecessary space. Second, if the user wants to create a simulation from scratch, there would be no default file to load to get the initial starting position.

To overcome this issue, a set of default simulation files is created for each activity only for one subject and one implant type. When selecting a new activity, the transformation matrix for each component relative to its proper bone is calculated and stored. Then, the transformations of each bone relative to the global reference frame are calculated for that activity. Finally, using the relative transformation matrices calculated in the first step, the components are placed with respect to the bones in the activity-specific location.

Additionally, as mentioned in section 4.8.3.1, the default simulations were created for each subject with different TKA types. The initial placement of the components has an effect on TKA outcomes. Therefore, it is crucial to place the simulation at accurate locations. For a given activity, each subject with a specific implant to the certain flexion angle of that activity. Then the position and orientation of components and bones at that flexion angle will be used as initial condition for that subjects and that specific activity. This way there is a default simulation for each subject with multiple implants for each activity. The GUI has been updated to take into account these default simulations. The user can easily select different activities for each subject by implant type (Figure 4-76).

It was mentioned in section 4.6.2 that some patients lift their heel off the ground when performing a lunge activity, and the updated GUI has incorporated this feature. Therefore, when the user selects to simulate the lunge activity, a pop-up menu appears asking the user whether lifting the heel off the ground is required. If the user selects "Yes," another window pops up, asking about the maximum foot rotation angle. Then, based on this user-specified value, the flexion rate of the foot is calculated. Also, the starting flexion angle or time can be updated by the user by updating the Simulation Control Variables menu.

Additionally, to better visualize and distinguish between the activities, different platforms are considered for different activities, i.e., chair, steps, etc. The bodies, bones and implants, are of type stl/wrl, which is essentially a combination of faces and vertices. Therefore, each platform has its own faces and vertices. These faces and vertices are created and stored. When selecting an activity, the GUI calls the proper faces and vertices from these stored matrices to load the proper platform for that specific activity.

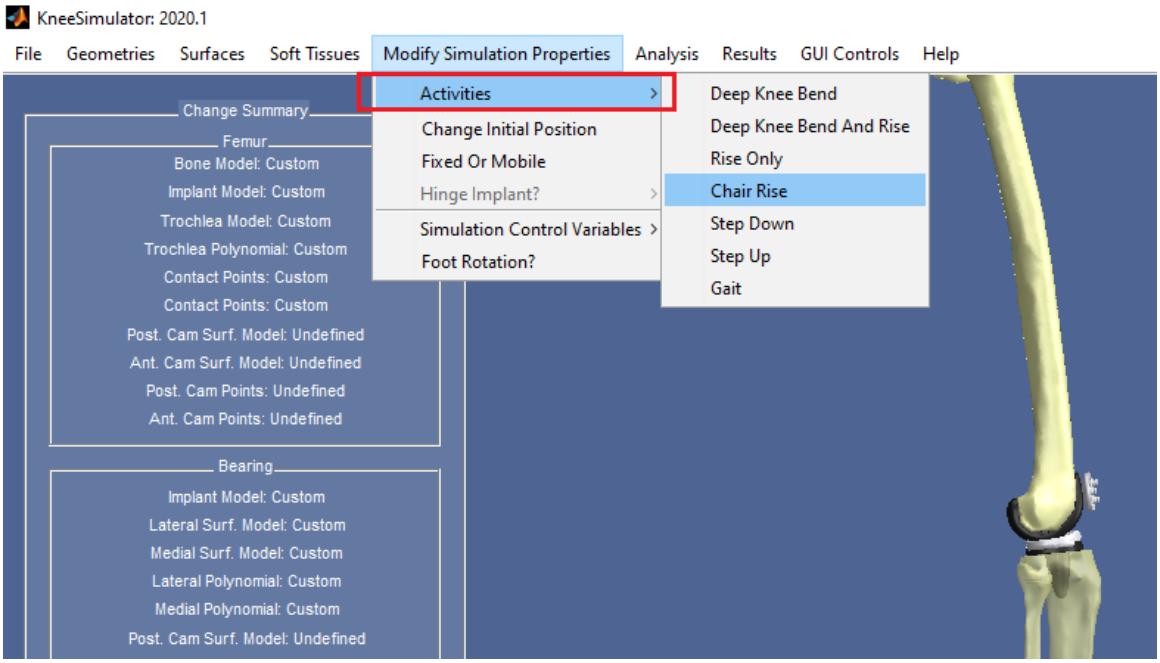


Figure 4-75: To perform different activities, the user needs to select the proper activity. The GUI creates the approximation of the starting position for that activity.

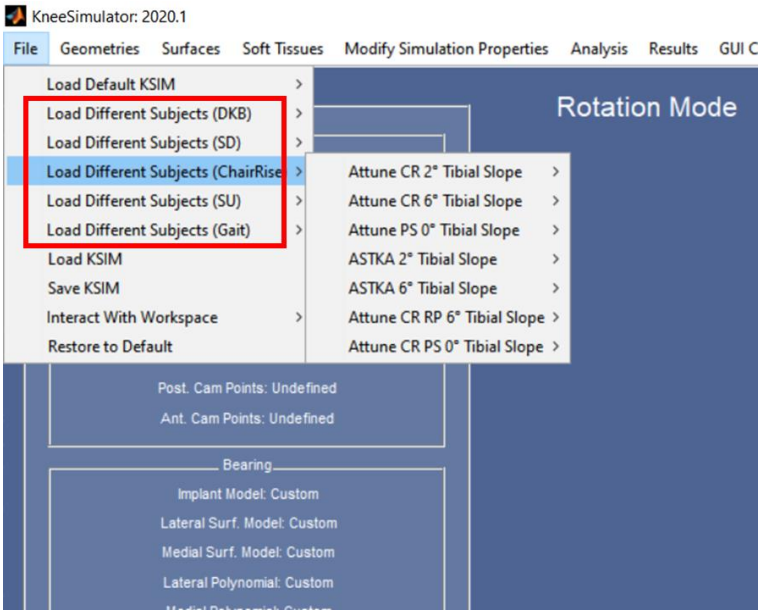


Figure 4-76: The current GUI allows the user to select various subjects with different implant type performing different activity.

Chapter 5: Results and Discussion

Initially, in this section, the effects of the new updates on TKA outcomes will be investigated. Then, the model will be used to assess the effects of various surgical conditions and implant designs on TKA outcomes.

5.1 Muscle Wrapping

The recently developed muscle wrapping algorithm was derived to accurately predict the wrapping of the muscle around the TKA implants and the bones. In Figure 5-1, the vastus lateralis wraps around the femoral component and the rectus femoris wraps around the femur bone and pelvis.

The developed muscle wrapping algorithm is capable of detecting the exact flexion angle where wrapping occurs for each quadriceps muscle fiber as opposed to the previous wrapping algorithm in which wrapping turns on and off based on predefined fixed parameters.

The wrapping algorithm was also able to differentiate between various types of TKA implant designs. In Table 5-1, the starting flexion angle where the wrapping turns on is shown.

This proves that the wrapping algorithm successfully detects unique wrapping angles for each muscle fibers and then differentiate between various types of TKA design.

For instance, for vastus lateralis, the wrapping occurs at 60.2°, 55.7°, and 59.3° of knee flexion for PCR, PS, and ACL substituting TKA designs, respectively.

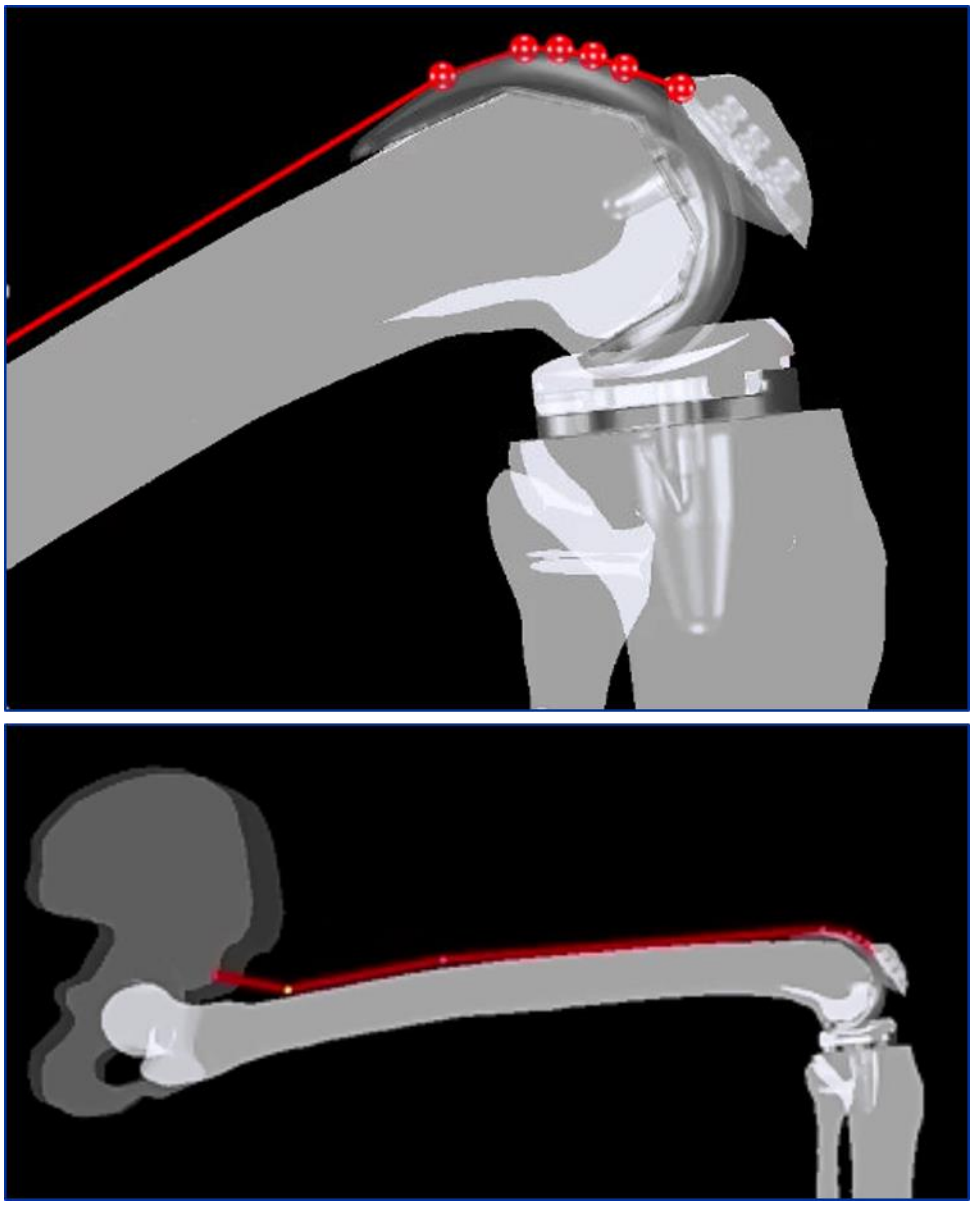


Figure 5-1: The developed muscle wrapping algorithm is capable of accurately muscle wrapping around the femoral component (top) and also around the bones (bottom).

Table 5-1: The flexion angles where the wrapping algorithm starts for different quadriceps muscle fibers and different implant types.

	VL	RF	VM	VID	VIM
PCR	60.2	65.6	65.2	68.3	68.3
PS	55.7	60.3	58.2	61.7	61.7
ACL Substituting	59.3	63.9	62.0	65.2	65.2

The extensor mechanism plays an essential role in the functionality of the human knee joint. The patella increases the moment arm of the quadriceps muscle and therefore decreases the required quadriceps muscle force to perform deep flexion activities. Hence, the accuracy of the muscle wrapping, which dictates the quadriceps muscle fibers' lines of action, affects the quadriceps muscle force.

In Figure 5-2, the quadricep muscle comparison between the old wrapping method and the new wrapping algorithm are shown. The quadriceps force is lower for the new wrapping algorithm. This difference is due to the fact that in the new wrapping algorithm, the line of action of the muscle is more accurately computed and therefore does not pass through the bone and femoral component. This finding results in an increased quadriceps moment arm and a subsequenty reduction in the quadriceps muscle forces.

Similar to the quadricep muscle force, the patellofemoral joint force is also reduced in the new wrapping algorithm (Figure 5-3). This occurs because the patellofemoral joint is a three-force system in its simplified form, including quadriceps muscle, the patellofemoral joint force, and the patellar ligament force. Therefore, when the direction and amount of one of these forces changes, the other two will change as well.

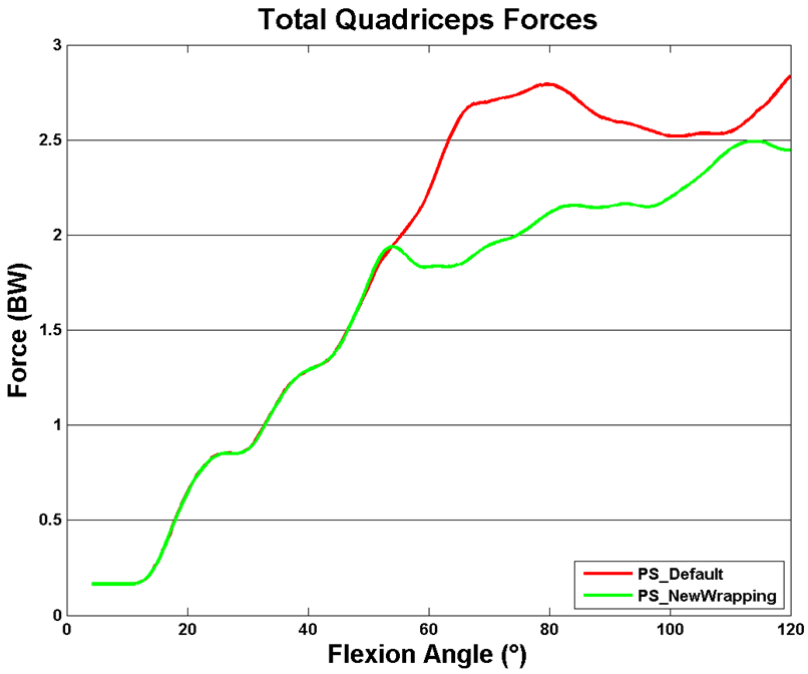


Figure 5-2: Comparison of quadriceps forces between the old wrapping method (red) and the new wrapping algorithm (green).

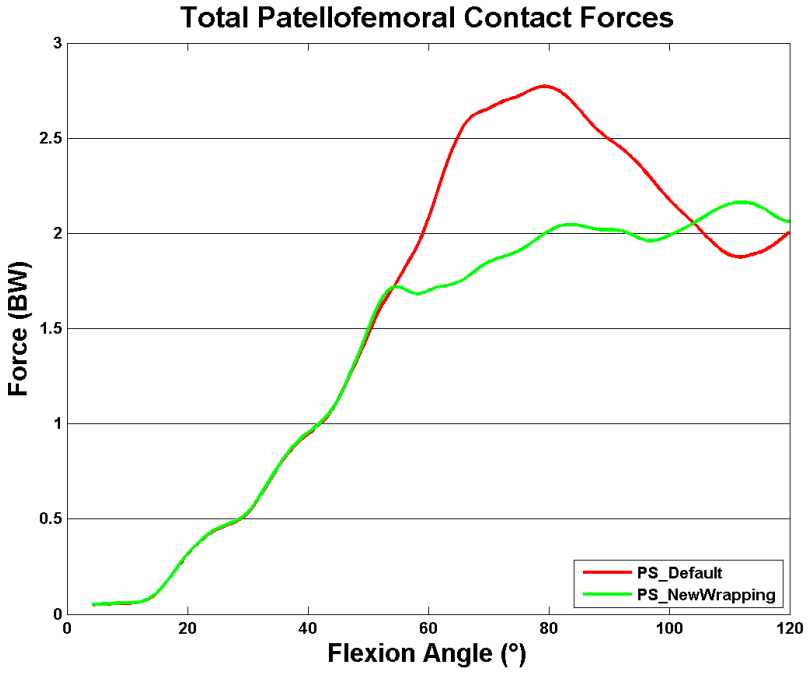


Figure 5-3: Comparison of patellofemoral joint forces between the old wrapping method (red) and the new wrapping algorithm (green).

The changes in quadriceps muscle force direction and magnitude affect not only the patellofemoral joint but also the tibiofemoral joint. One of the TKA procedure goals is to distribute tibiofemoral contact forces evenly between the lateral and the medial compartments.

The magnitude of the contact forces in lateral and medial tibiofemoral joints are shown in Figure 5-4 and Figure 5-5. The amount of the lateral tibiofemoral force was significantly higher compared to the medial side in the old wrapping algorithm, peaking at about 2 × BW. However, with the new wrapping algorithm, the tibiofemoral forces are more evenly distributed, around 1.2 × BW and 1.4 × BW for lateral and medial compartments, respectively.

Similarly, the tibiofemoral kinematics are affected by the new wrapping algorithm as well. The lateral femoral condyle translates about 1 mm less posteriorly compared to the old algorithm from full extension to maximum knee flexion (Figure 5-6).

Conversely, the medial condyle translates 1 mm more posteriorly throughout the range of motion with the new wrapping algorithm compared to the old wrapping algorithm (Figure 5-7). Also, the femur experiences a smaller magnitude of external rotation with the new wrapping algorithm (Figure 5-8).

5.1.1 Effects of a Larger Femoral Component Size

To investigate the viability of the new wrapping algorithm, a larger sized femoral component was imported in the FSM. As can be seen in Figure 5-9, a larger femoral component means that the wrapping points are further from the femoral component center of mass. Two identical simulations have been created in the FSM with one difference: one with Attune CR femoral component size 4 and another with femoral component size 5. The wrapping points are also updated for the larger femoral component accordingly.

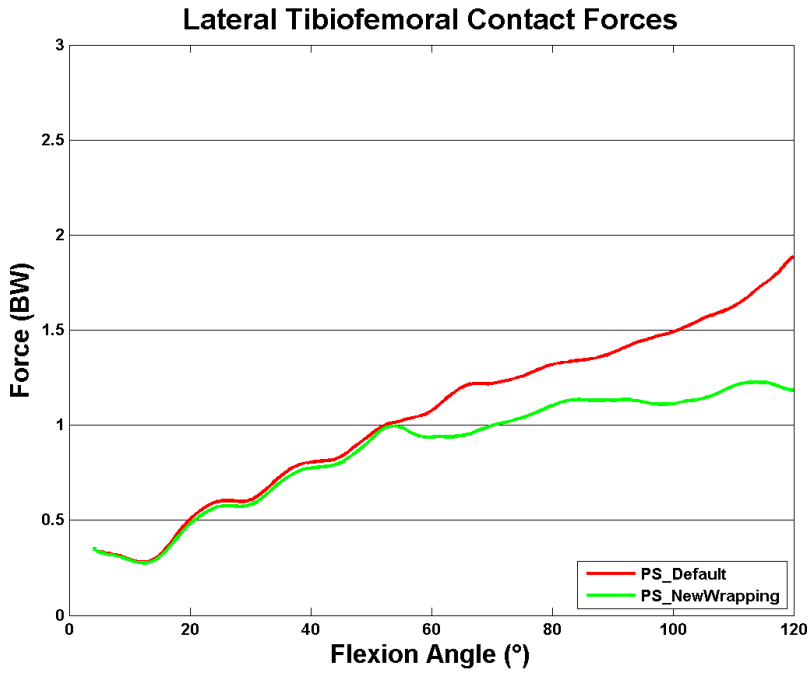


Figure 5-4: Comparison of lateral tibiofemoral joint forces between the old wrapping method (red) and the new wrapping algorithm (green).

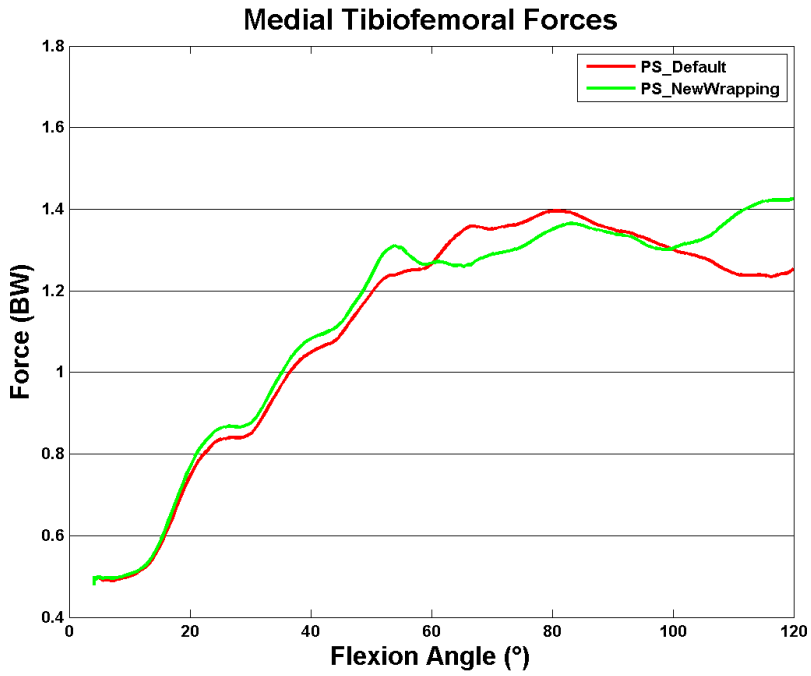


Figure 5-5: Comparison of medial tibiofemoral joint forces between the old wrapping method (red) and the new wrapping algorithm (green).

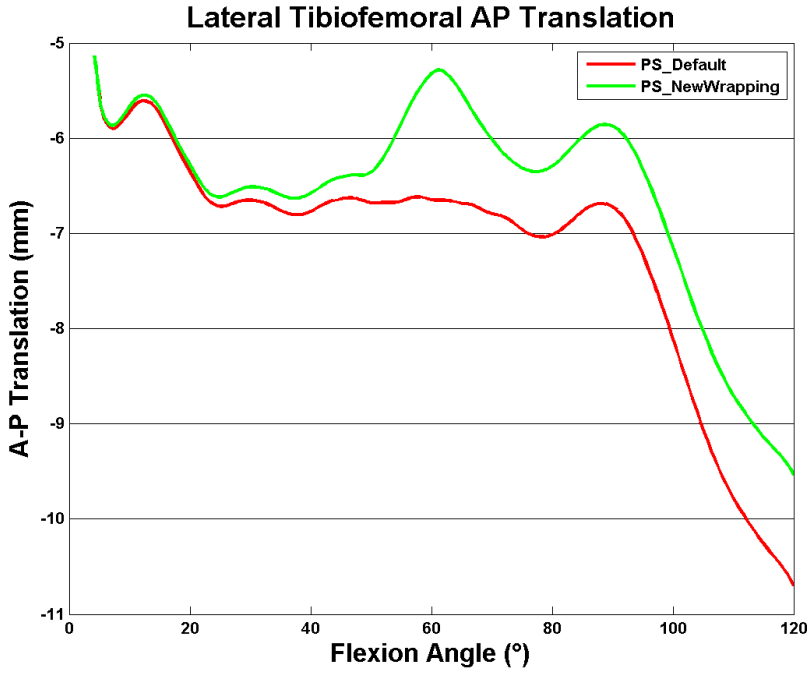


Figure 5-6: Comparison of lateral tibiofemoral AP translation between the old wrapping method (red) and the new wrapping algorithm (green).

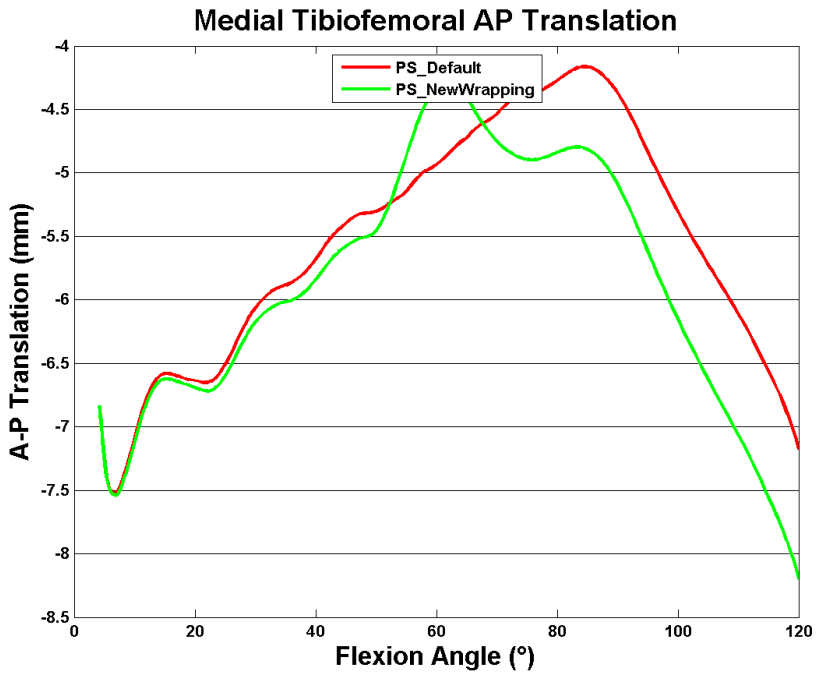


Figure 5-7: Comparison of medial tibiofemoral AP translation between the old wrapping method (red) and the new wrapping algorithm (green).

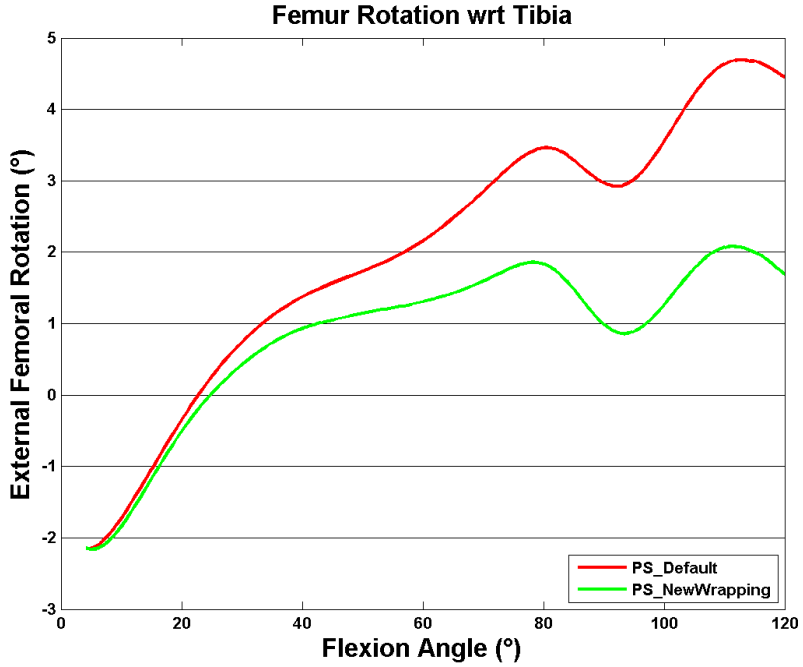


Figure 5-8: Comparison of tibiofemoral axial rotation between the old wrapping method (red) and the new wrapping algorithm (green).

The quadriceps muscle force is smaller when a larger femoral component is incorporated (Figure 5-10). As mentioned previously, one of the advantages of the new wrapping algorithm is to accurately represent the muscle wrapping and line of action of the muscles, and subsequently, the muscle moment arm.

Therefore, when a larger femoral component is used, the muscles wrap further away from the point of rotation, increasing the muscle moment. Consequently, once could assume that the simulation would lead to lower quadriceps forces. The FSM with the new wrapping algorithm was capable of capturing this difference and therefore predicting lower quadriceps muscle force and patellofemoral joint force (Figure 5-11) when a larger femoral component is implanted.

5.2 Inverse Model

The inverse solution model has been successfully integrated in the GUI that encompasses the forward solution model. Once a forward solution simulation has been completed, the user can simply run the inverse solution model based on the kinematics obtained from the forward results. The inverse solution model determines joint forces (tibiofemoral contact forces, patellofemoral contact forces, hip joint, etc.) and torques and soft-tissue forces such as quadriceps muscle forces.

A PCR TKA was initially used to investigate the use of inverse model. The quadriceps muscle force peaks at about 4.1 × BW at late flexion (Figure 5-12). The predicted quadriceps force is consistent with the quadriceps forces reported in the literature. Another study using the same inverse model by Sharma et al. [9] reported the quadricep forces for a PCR TKA about 3.5 × BW. Also, Innocenti et al. [164] reported a range of 3.2 – 4.4 × BW for quadriceps forces for various types of TKA designs.

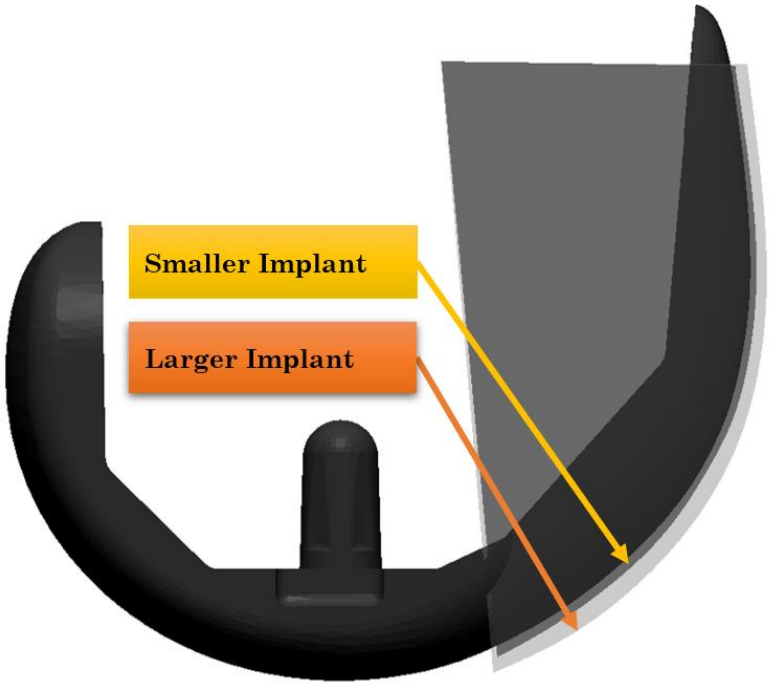


Figure 5-9: Quadriceps tendon wraps further from the center of mass of the femoral component when a larger implant size is used.

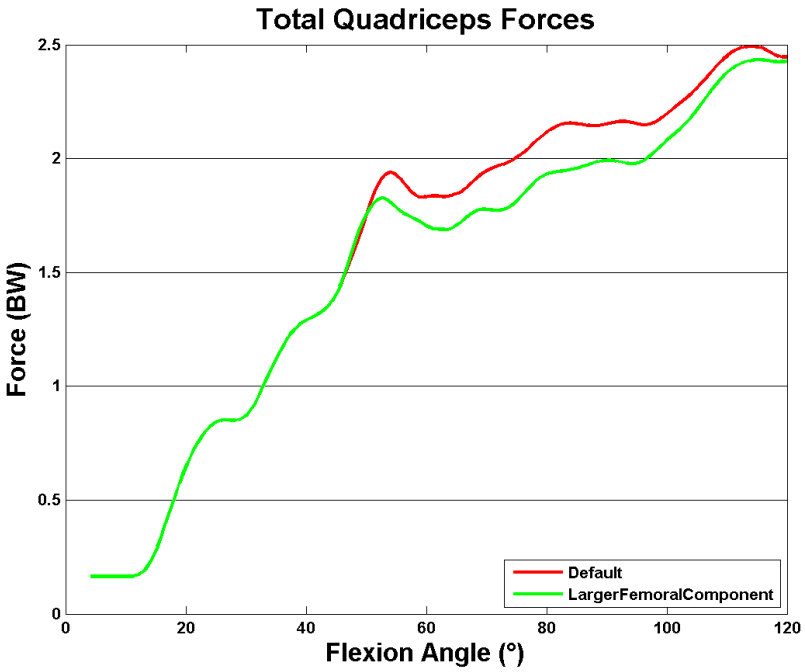


Figure 5-10: Quadriceps force is lower when the larger femoral component (green) is implanted.

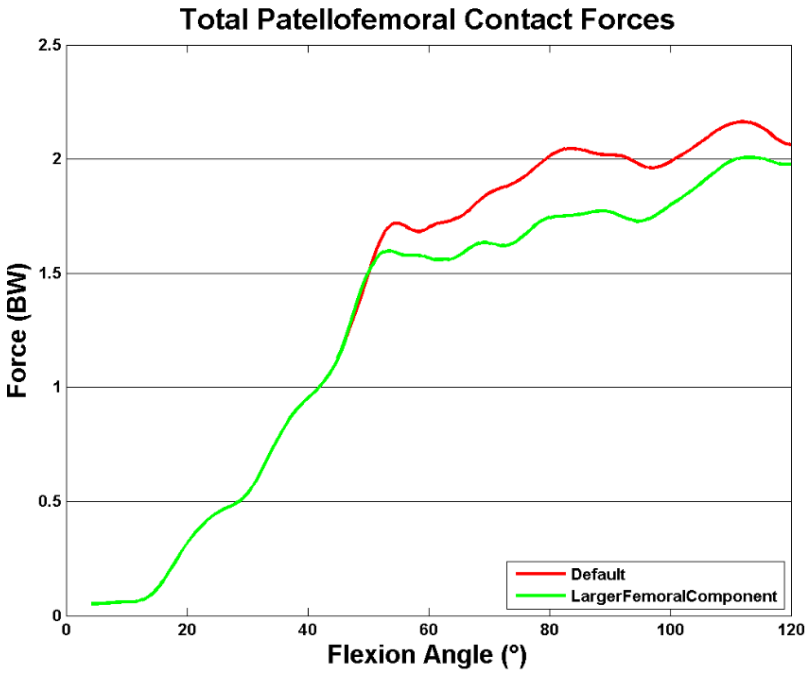


Figure 5-11: Patellofemoral joint forces comparison between the default femoral component size (red) and one size larger femoral component (green).

The peak patellofemoral force predicted using the inverse model for the same PCR TKA was about 4.1 × BW (Figure 5-13).

The predicted patellofemoral contact force is also in agreement with the literature. Early mathematical models have reported patellofemoral forces as high as 7.6 × BW [165], and recent mathematical models have reported significantly lower patellofemoral contact forces, in the range of 3 – 5 × BW [9,165,166].

The tibiofemoral contact force starts at about 1.1 × BW at early flexion and peaks at about 3.9 × BW at late flexion (Figure 5-14). This predicted force is also consistent with the contact force reported in the literature [167]. The maximum hip joint force for the PCR TKA was 4.4 × BW (Figure 5-15).

5.2.1 Effects of AP Translation

One of the applications of the integrated inverse model is to compare the soft tissue and contact forces between various TKA types that reveal different kinematics patterns. The forward model has proven to predict the soft tissue and contact forces very accurately.

However, the forces calculated in the forward model take into account the interaction of other forces happening at the knee joint. For example, in an ACL substituting TKA design, the contact force at the anterior cam and post mechanism can affect the predict knee forces.

The forward model provides the means to investigate the effects of bearing surface contact force as it related to the kinematics and kinetics of the TKA. The inverse model, on the other hand, solely takes the kinematics and does not incorporate the other forces. Therefore, we can uniquely investigate the effects of different kinematic patterns on the predicted forces.

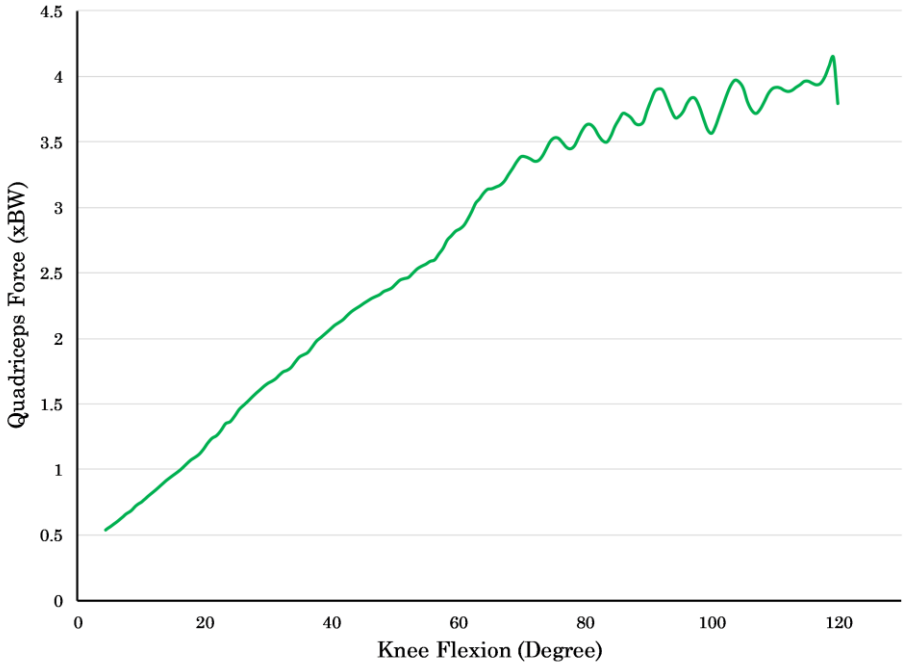


Figure 5-12: the quadriceps muscle force for a PCR TKA design using the inverse solution model.

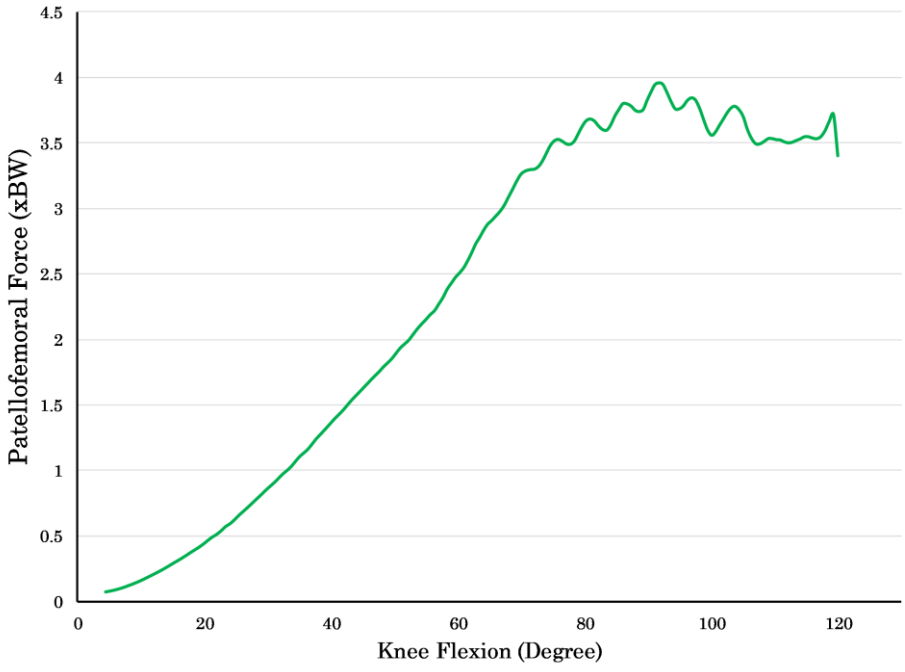


Figure 5-13: the patellofemoral contact force for a PCR TKA design using the inverse solution model.

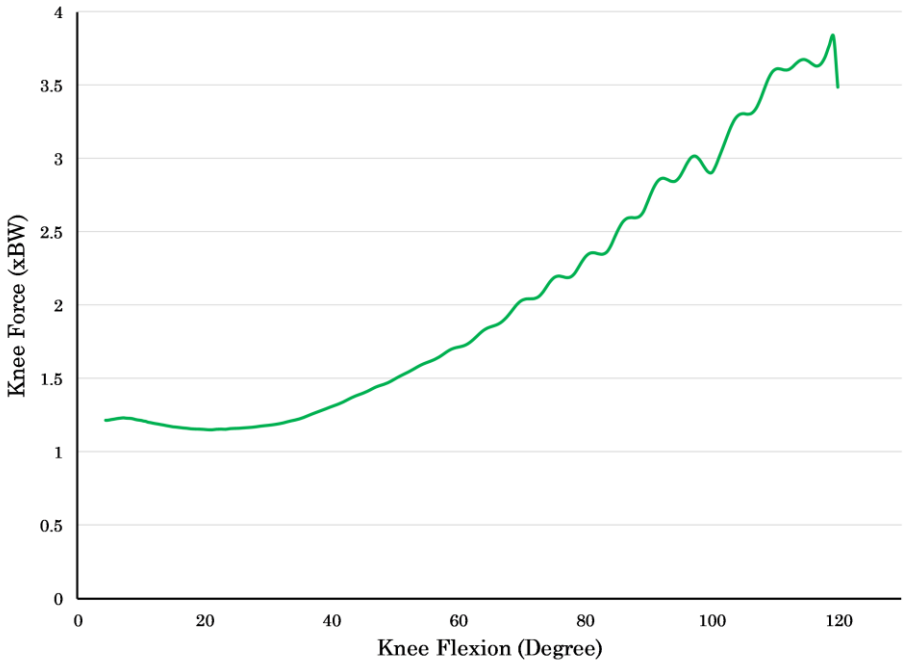


Figure 5-14: The total tibiofemoral contact force for a PCR TKA design using the inverse solution model.

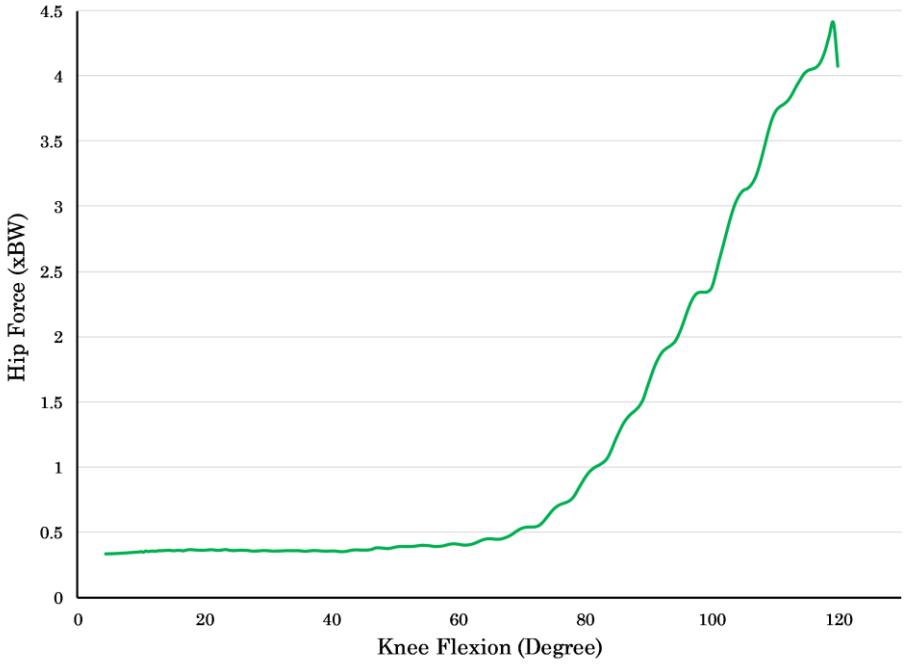


Figure 5-15: The hip joint force for a PCR TKA design using the inverse solution model.

Two TKA designs were simulated to determine the forces using the inverse model, an ACL substituting and a PCR TKA design. Initially, using the forward model, the kinematics for each design was determined. The ACL substituting design revealed an increase in lateral and medial rollback compared to the PCR design (Figure 5-16). From full extension to 120° of knee flexion, the lateral condyle AP translations were about -7.8 mm and 0.3 for the ACL substituting and the PCR TKA, respectively. The medial condyle translations were -1.5 mm and 2.6 mm for the ACL substituting and the PCR TKA, respectively.

It has been hypothesized that increase femoral rollback is beneficial to the TKA outcomes. The increased femoral rollback increases the extensor moment arm and therefore reduces the quadriceps muscle force and the patellofemoral contact force [74,168]. To investigate whether this can be shown using the mathematical model, two TKA designs mentioned above are incorporated into the inverse model. Therefore, it is expected that the ACL substituting design would show reduced extensor mechanism forces compared to the PCR design due to the increased femoral rollback.

The peak quadriceps forces were 3.61 × BW and 4.15 × BW for the ACL substituting and the PCR design, respectively (Figure 5-17). The peak patellofemoral forces are also decreased for the ACL substituting design compared to the PCR design, 3.6 × BW compared to 4.0 × BW respectively (Figure 5-18).

The peak tibiofemoral force is also smaller for the ACL substituting design, 3.3 × BW, compare to the PCR design, 3.8 × BW (Figure 5-19). These results revealed that increased femoral rollback can have a positive effect in reducing the extensor mechanism forces and reduced anterior knee pain often experienced by TKA patients [119,169]. these findings are also in agreement with the literature [170,171].

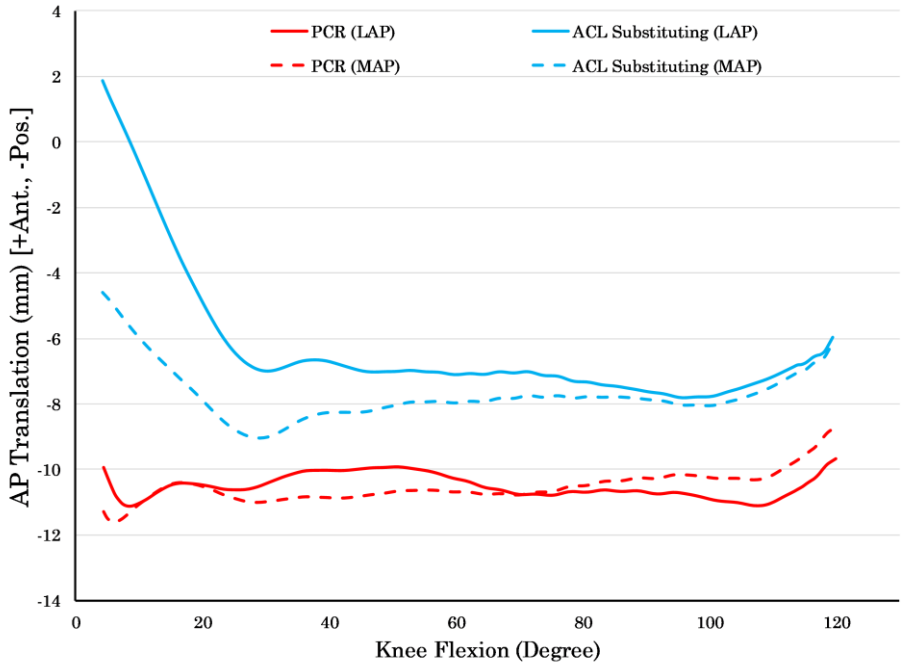


Figure 5-16: The comparison between the lateral A-P translation for a PCR TKA (solid red) and an ACL substituting TKA (Solid blue) and the medial A-P translation for a PCR TKA (dashed red) and an ACL substituting TKA (dashed blue).

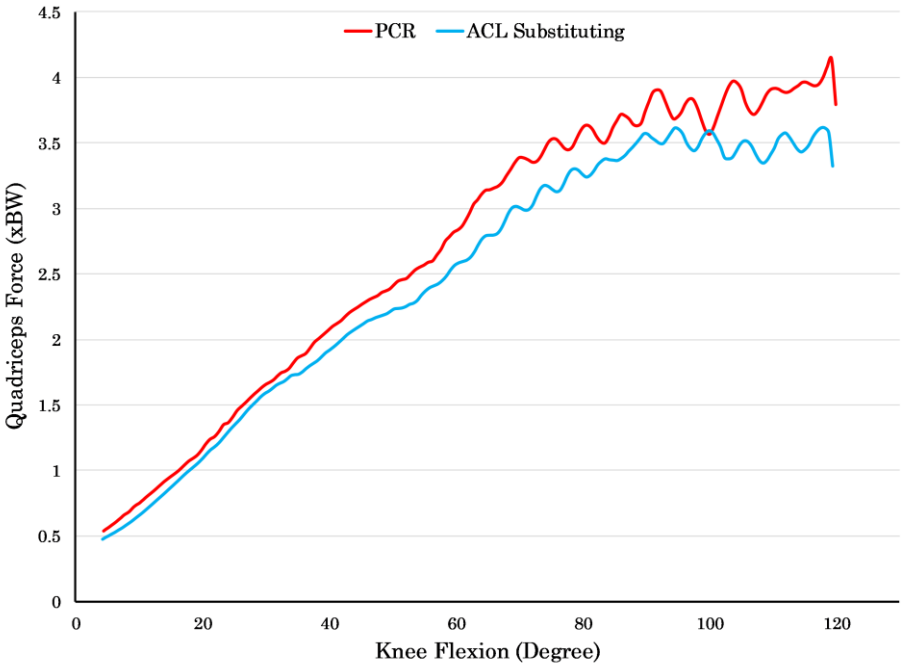


Figure 5-17: The comparison between the quadriceps muscle forces for a PCR TKA (solid red) and an ACL substituting TKA (Solid blue).

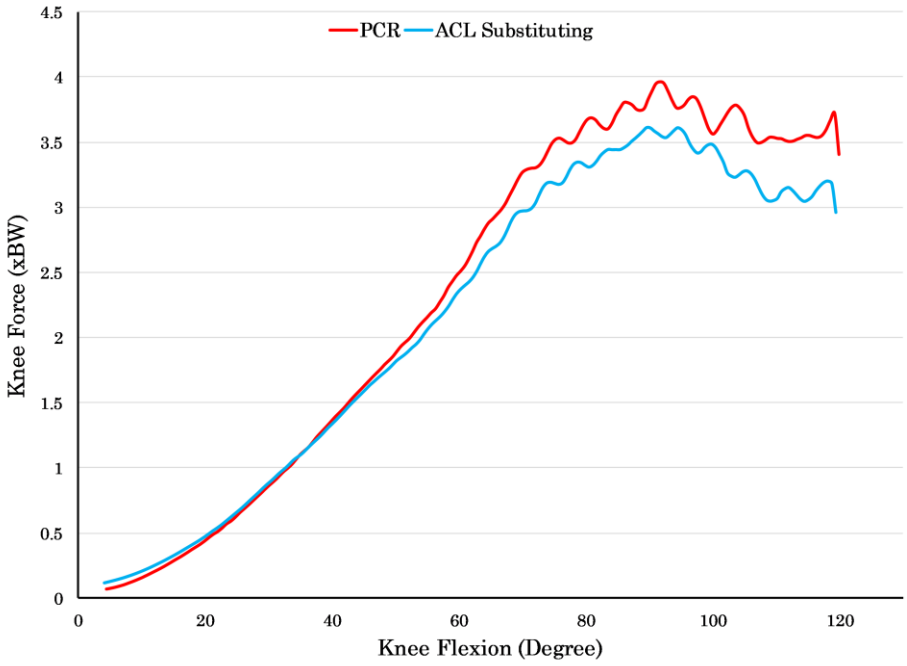


Figure 5-18: The comparison between the patellofemoral contact forces for a PCR TKA (solid red) and an ACL substituting TKA (Solid blue).

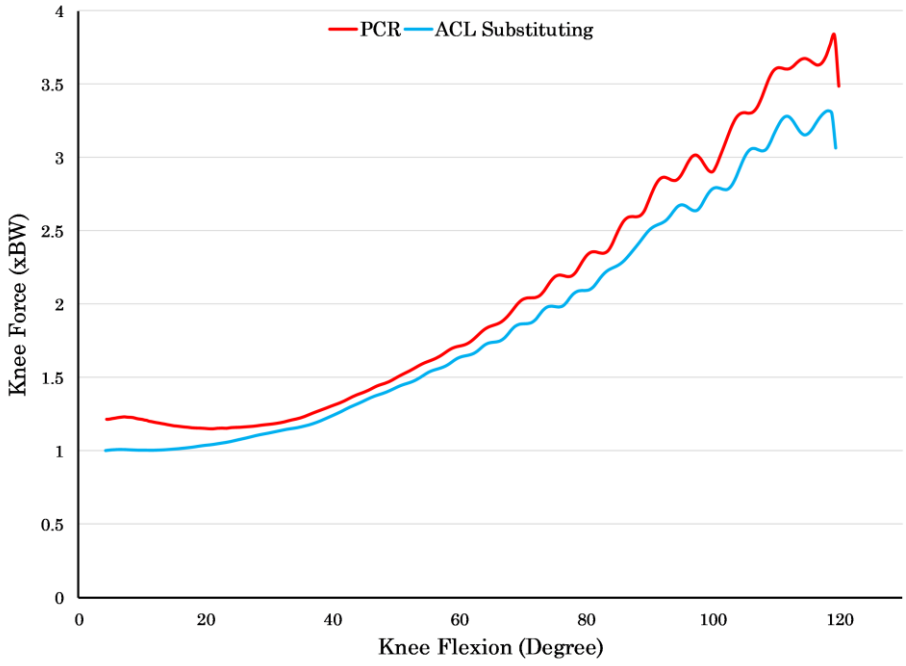


Figure 5-19: The comparison between the tibiofemoral contact forces for a PCR TKA (solid red) and an ACL substituting TKA (Solid blue).

5.3 Settling Algorithm

The settling algorithm effectively eliminates the early oscillations observed in the results from the earlier versions of the forward solution model. In the previous FSM, the lateral and medial AP translations exhibited oscillations in the results in early flexion. Using the settling algorithm, theses oscillation were eliminated (Figure 5-20 and Figure 5-21). These improvements were also evident in the kinetics prediction of the FSM. The improvement in tibiofemoral contact force, quadriceps muscle force, and knee joint torque in the ML direction are shown in Figure 5-22, Figure 5-23, and Figure 5-24, respectively. Additionally, with the settling algorithm, the anterior cam force in the ACL substituting design can be studied more accurately since, in the previous FSM, early oscillations prevented accurate analysis in early flexion where cam and post replace the functionality of the ACL (Figure 5-25).

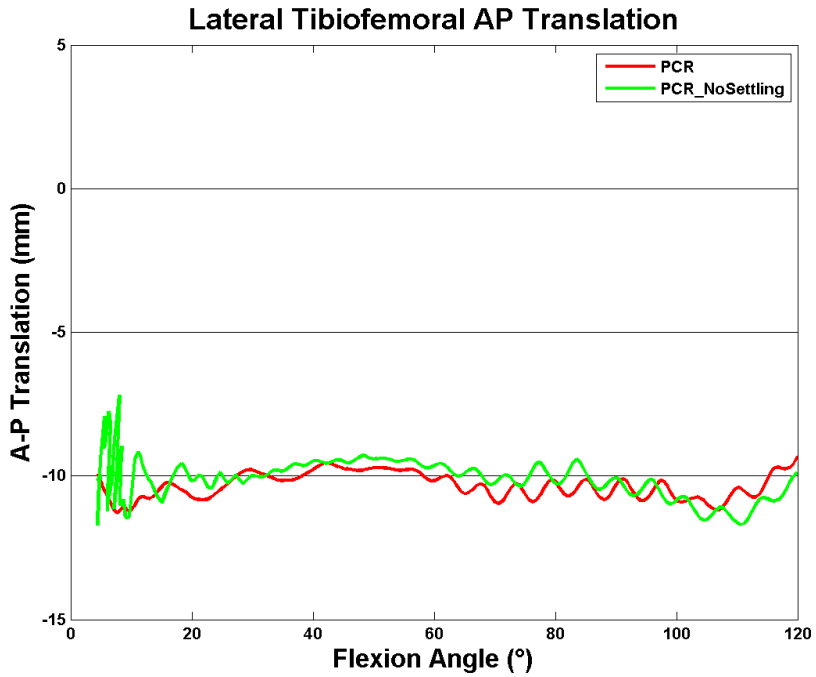


Figure 5-20: The developed settling algorithm (red) effectively eliminates the early oscillations observed in the lateral AP translation compared to the previous FSM (green).

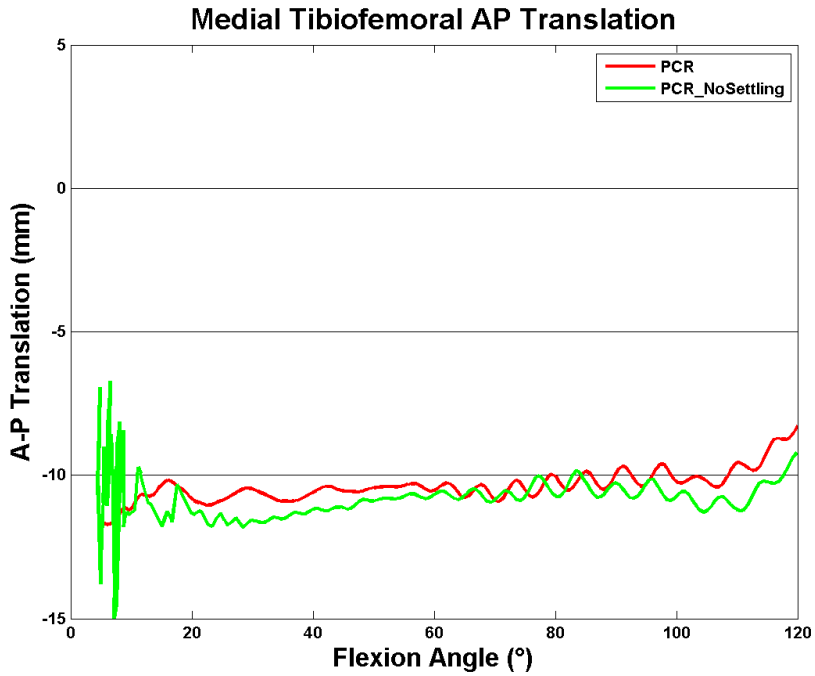


Figure 5-21: Comparison between the medial AP translation for a PCR TKA using the settling algorithm (red) and without the settling algorithm (green).

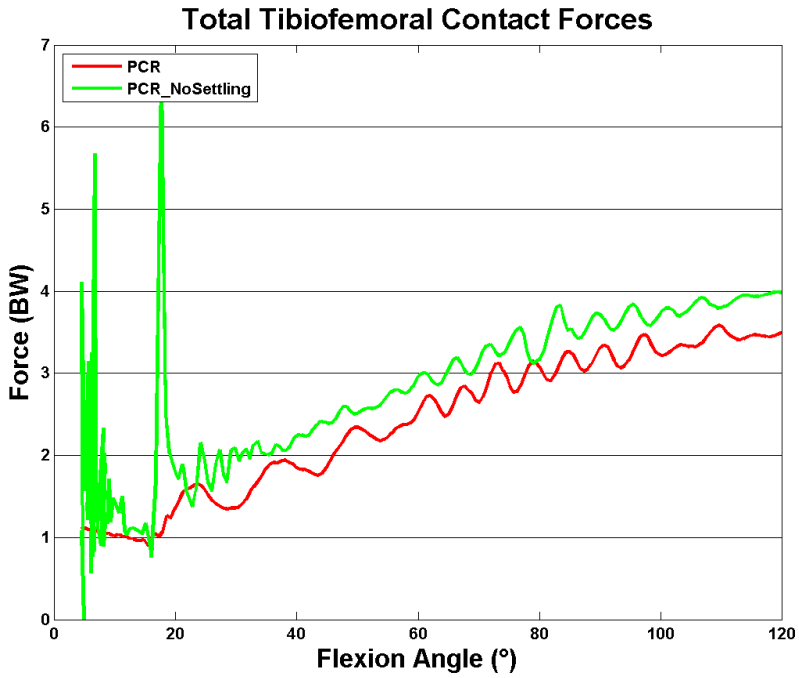


Figure 5-22: Comparison between the total tibiofemoral contact force for a PCR TKA using the settling algorithm (red) and without the settling algorithm (green).

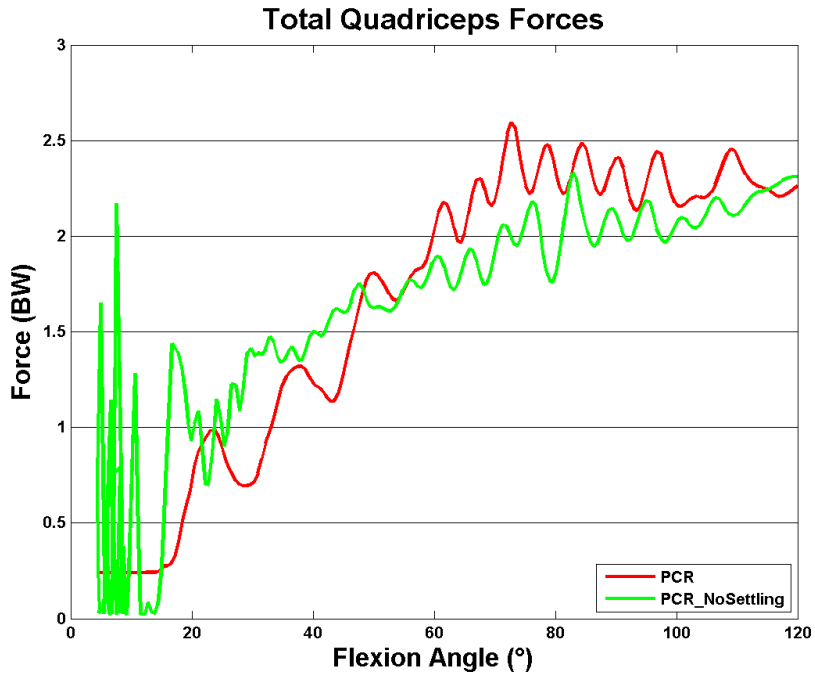


Figure 5-23: Comparison between the quadriceps force for a PCR TKA using the settling algorithm (red) and without the settling algorithm (green).

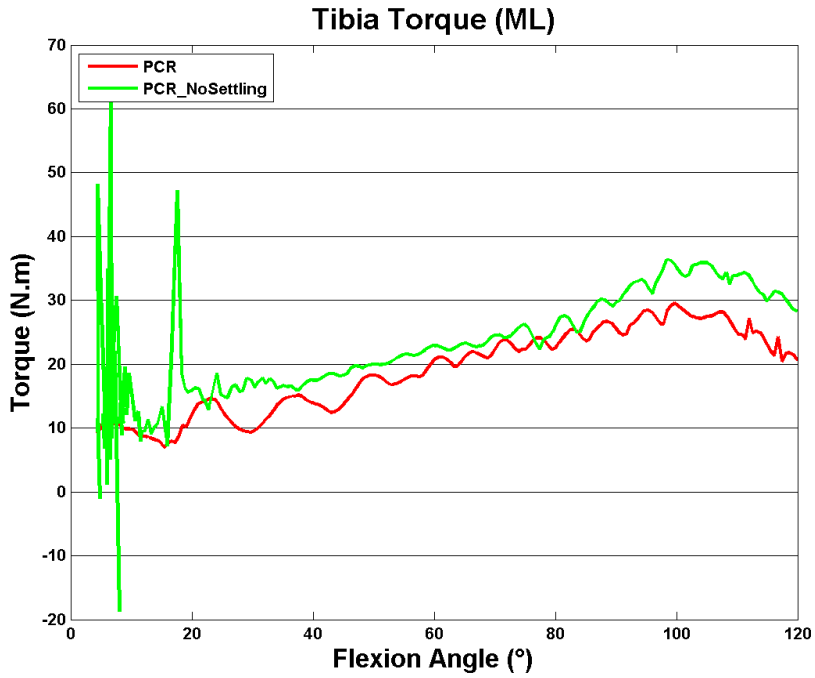


Figure 5-24: Comparison between the ML torque applied to the tibial tray for a PCR TKA using the settling algorithm (red) and without the settling algorithm (green).

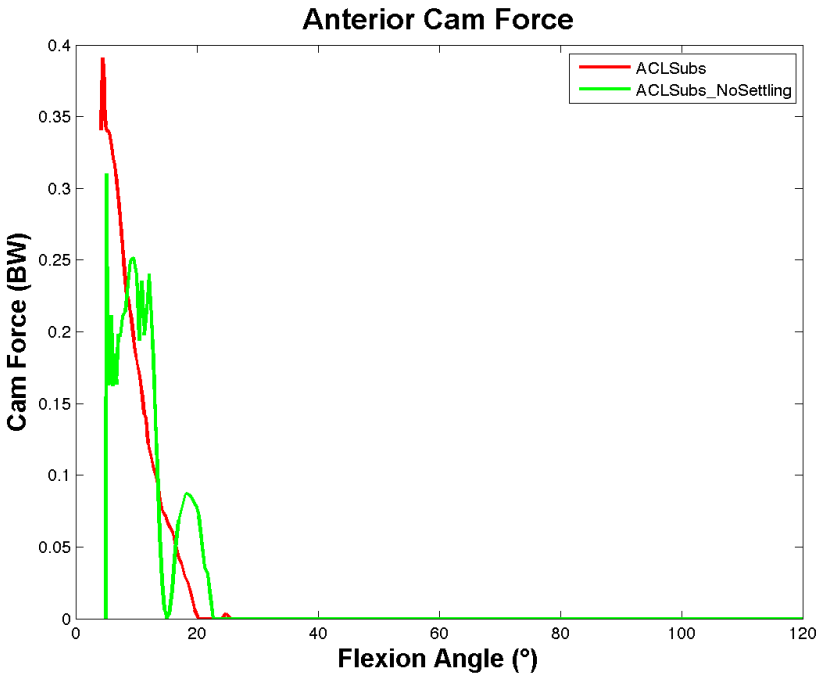


Figure 5-25: Using the settling algorithm, the effects of the anterior cam and the contact force can be analyzed more accurately in an ACL substituting design.

5.3.1 Settling Algorithm for Various TKA Type

The settling algorithm is also able to eliminate the oscillations for all types of TKA. In Figure 5-26, the tibiofemoral contact force for several TKA types are shown, and none of these TKA experienced early oscillation in tibiofemoral contact forces.

Also, the settling algorithm effectively eliminates the oscillation in extensor mechanism forces (Figure 5-27 and Figure 5-28). Not only does the addition of a settling algorithm result in better kinetic outcomes, but all kinematics predictions were improved for all types of TKA.

This is especially important because each TKA type has different geometry and soft tissue interaction, and the settling algorithm confirms this. For example, in a PS TKA, the PCL is resected while in a PCR design, the PCL is retained. The main function of the PCL is to keep the femur posterior relative to the tibia.

The PCL in the PCR design keeps the femur more posteriorly compared to the PS design in both lateral and medial condyles (Figure 5-29 and Figure 5-30). Additionally, the same difference between implant types can be seen in the patellofemoral joint, where the settling algorithm can detect differences between the starting patella flexion angles for different implant types (Figure 5-31).

5.4 Foot

Previous version of the FSM did not include a foot and therefore, the simulations were with respect to the ankle joint, but in actuality a person rotates from their heal to their toes. To investigate the viability of incorporating the foot into the FSM, a sensitivity analysis was performed on the effects of foot rotation on the knee joint mechanics.

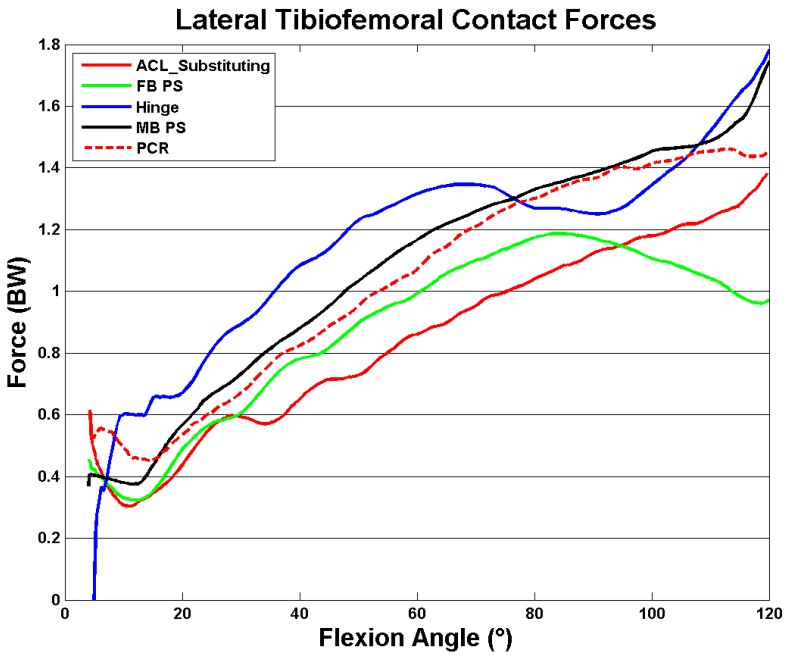


Figure 5-26: The settling algorithm successfully eliminates the early oscillation in the lateral tibiofemoral contact force for all types of TKA.

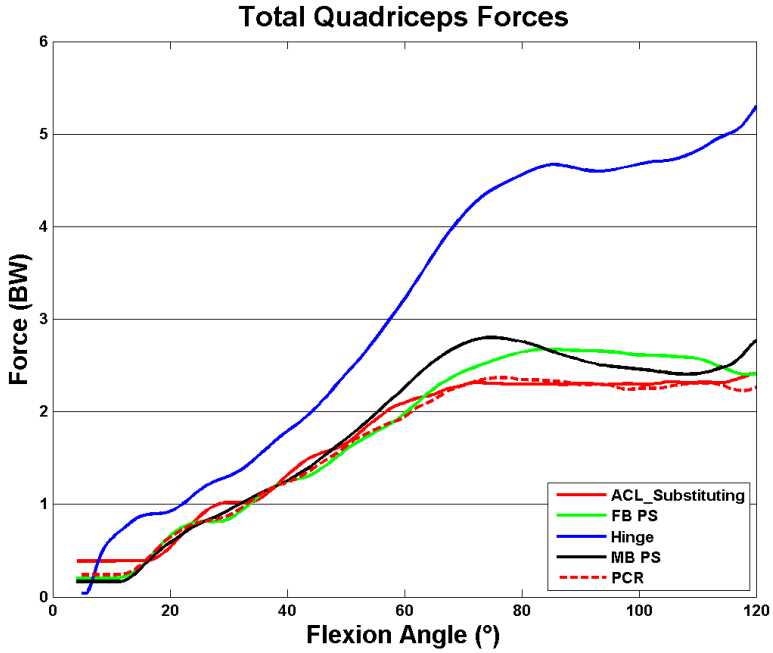


Figure 5-27: The settling algorithm successfully eliminates the early oscillation in the quadriceps muscle force for all types of TKA.

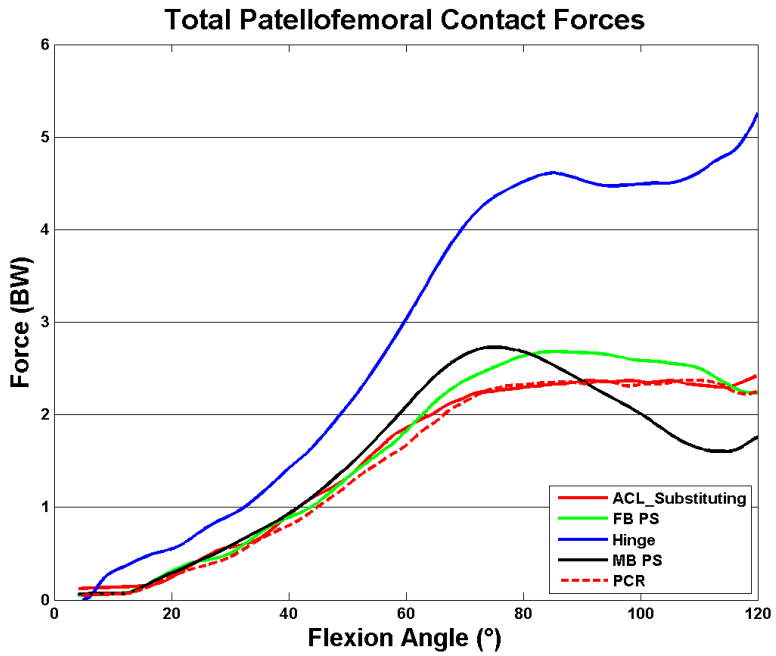


Figure 5-28: The settling algorithm successfully eliminates the early oscillation in the patellofemoral contact force for all types of TKA.

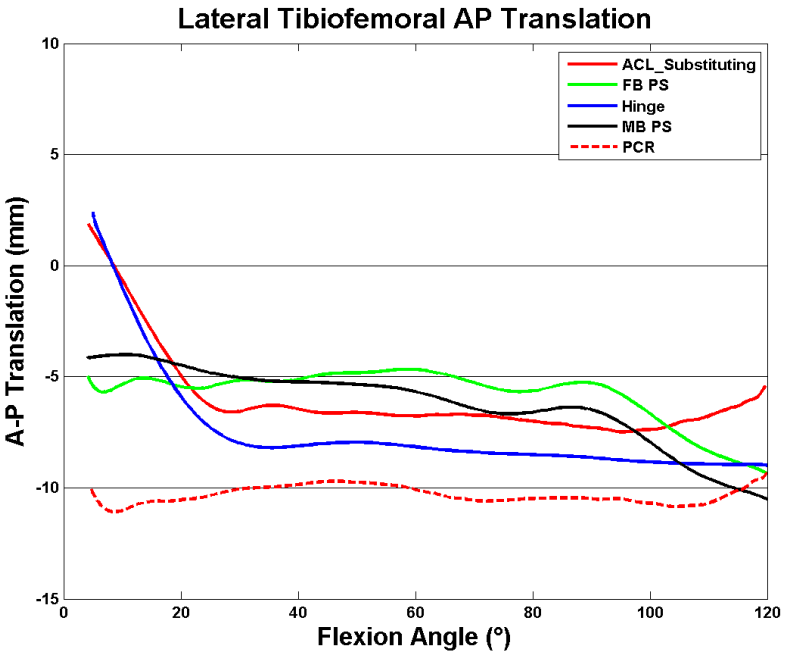


Figure 5-29: The settling algorithm successfully eliminates the early oscillation in the lateral AP translation for all types of TKA.

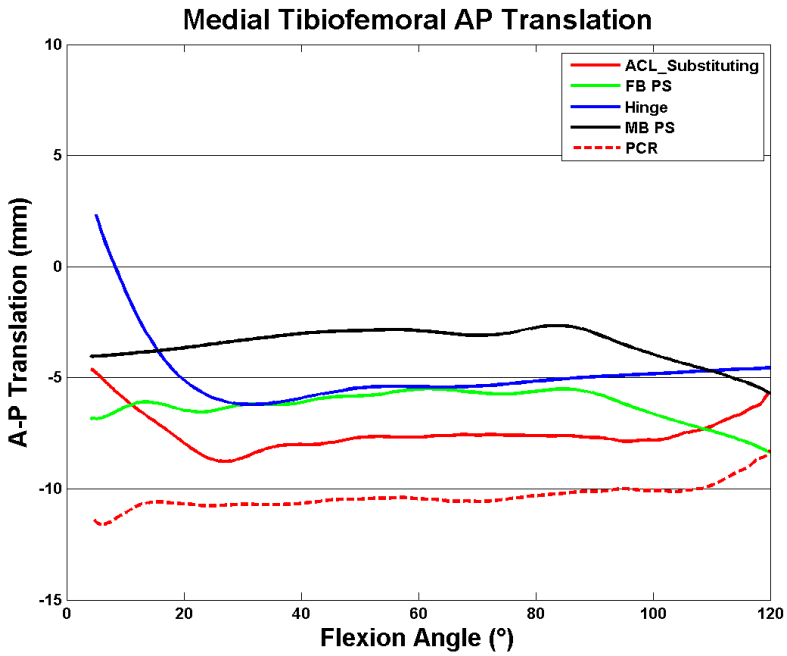


Figure 5-30: The settling algorithm successfully eliminates the early oscillation in the medial AP translation for all types of TKA.

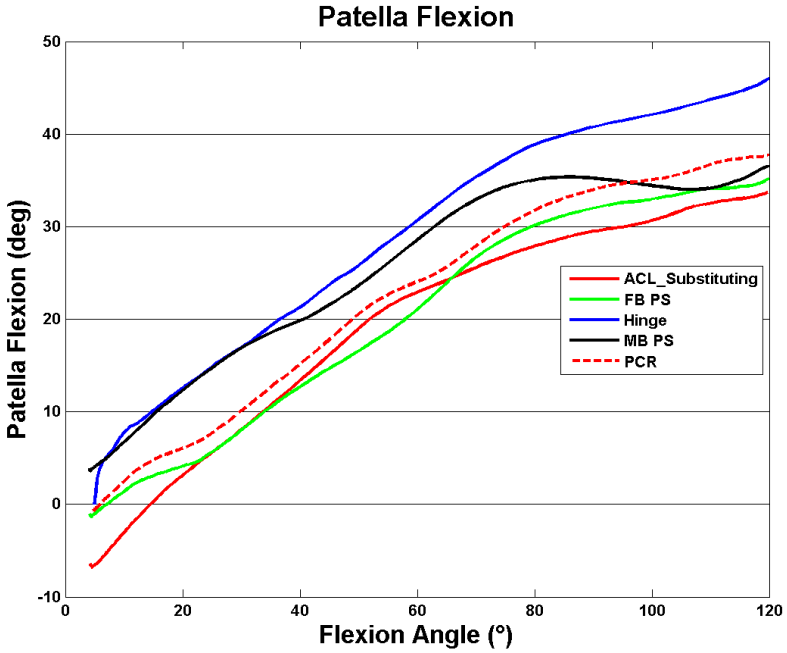


Figure 5-31: The settling algorithm successfully eliminates the early oscillation in the patella flexion angle for all types of TKA.

The rationale behind this comes from the idea that some patients following TKA procedure rotate their foot off the ground when performing a DKB activity or lunge activity. These patients, when they approach maximum weight-bearing flexion, start rotating their foot off the ground, most likely due to the soft tissue tightness at the knee and ankle joints.

To investigate whether the FSM can predict this phenomenon, a simulation for a theoretical patient was created where the foot starts rotating at about 80° of flexion (Figure 5-32).

The results of this theoretical patient were compared to the baseline simulation, where there is no foot rotation occurs, and the foot remained completely stationary through the whole range of motion.

The sensitivity analysis revealed that the quadriceps muscle force for the simulation with foot rotation starts decreasing once the foot starts leaving off the ground (Figure 5-33).

This possibly can be described by the increased moment arm of the patellofemoral ligament, which decreases the extensor mechanism forces (Figure 5-34). Similarly, due to decreased extensor mechanism forces, the tibiofemoral contact forces decreased as well (Figure 5-35).

5.5 Multiple Subjects

As described in section 4.8.3.1, for each subjects several default simulations were created for different implant types. In following sections, the results of these simulation for these 10 subjects with a PCR fixed-bearing a PS fixed-bearing TKAs are described.

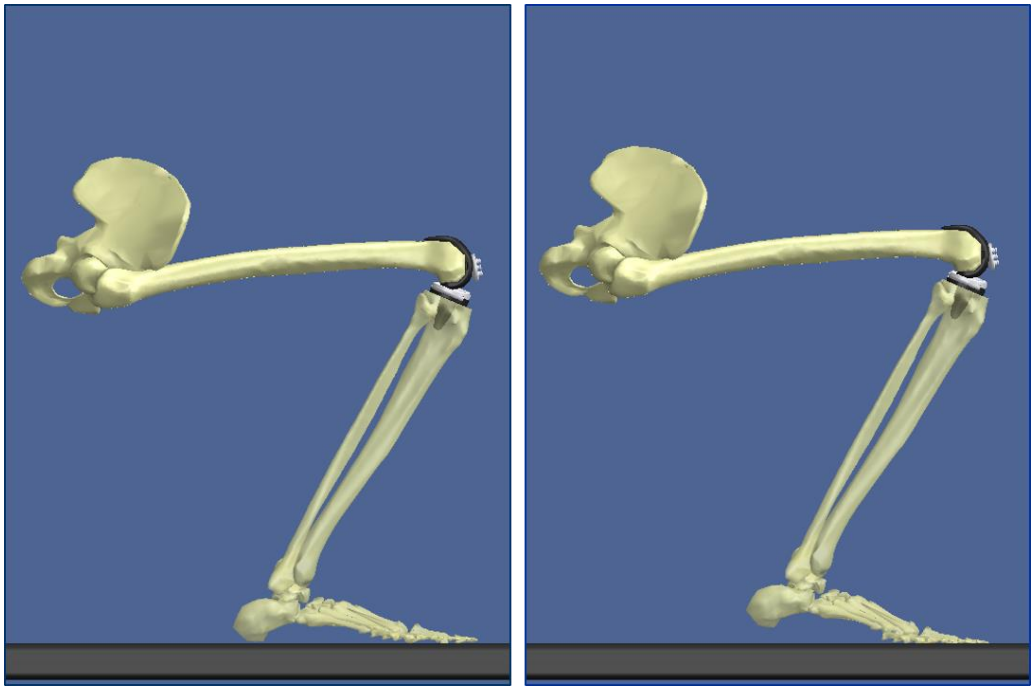


Figure 5-32: A theoretical patient was created in the FSM, where the patient starts rotating the foot close to the end of the DKB activity.

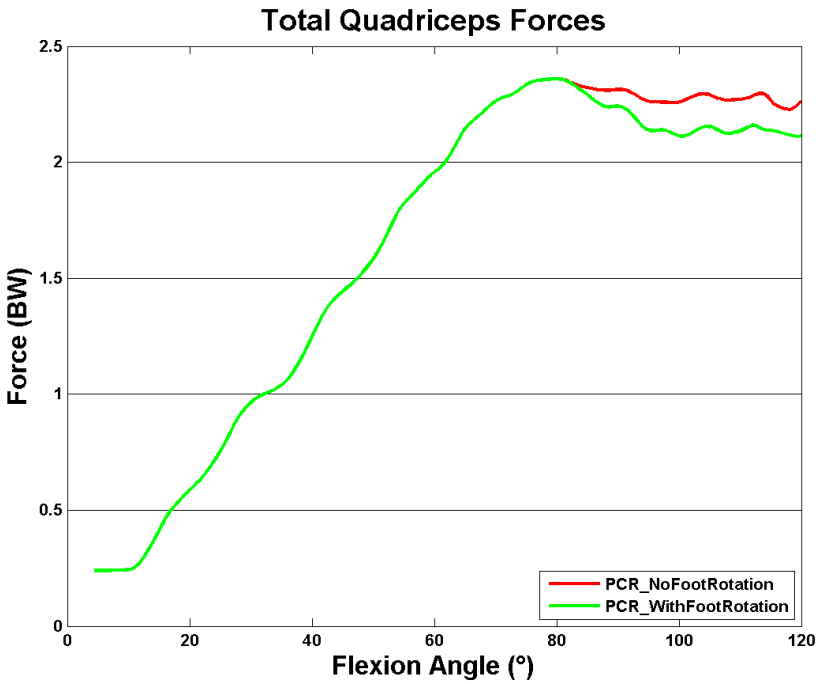


Figure 5-33: Comparison between the quadriceps muscle forces between a simulation with foot rotation (green) and a simulation with the stationary foot (red).

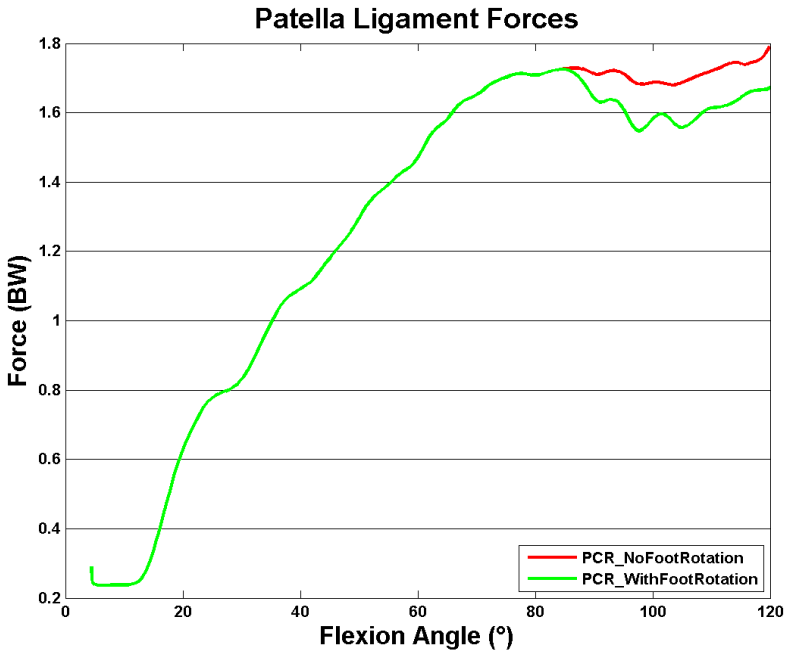


Figure 5-34: Comparison between the patellar ligament forces between a simulation with foot rotation (green) and a simulation with the stationary foot (red).

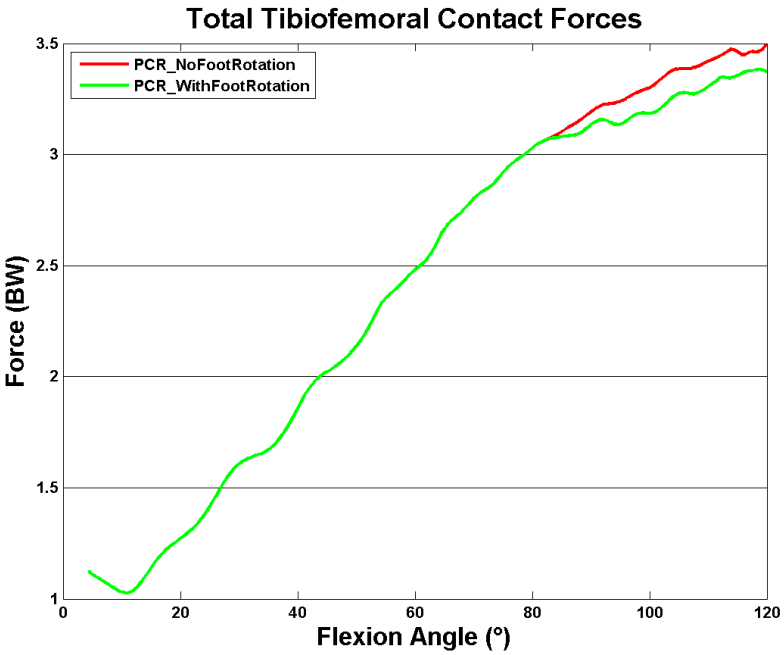


Figure 5-35: Comparison between the tibiofemoral contact forces between a simulation with foot rotation (green) and a simulation with the stationary foot (red).

5.5.1 PCR TKA

Similar to fluoroscopic studies where subject exhibit different kinematic pattern, the FSM also predicts various kinematics patterns for different subjects. The FSM was even able to predict paradoxical anterior sliding for multiple subjects. This abnormal kinematic pattern is quite common for PCR subjects. During a deep knee bend, on average, the lateral condyle translated about 3.0 mm posteriorly, and the FSM predicted an average of 0.4 mm of medial condyle rollback (Figure 5-36 and Figure 5-37). Additionally, the FSM predicted reverse axial rotation for two subjects (subject #2 and subject #8). The average predicted axial rotation was 2.9º (Figure 5-38). These results are in agreement with fluoroscopic study for a similar TKA design.

5.5.2 PS TKA

Similar to the PCR TKA subjects, there is variability observed in the kinematics predicted for PS TKA subjects. However, after cam/post engagement, all subjects showed rollback. Before cam/post engagement, the medial condyle showed higher incidences of anterior sliding compared to the PCR TKA subjects. This is due to the lack of PCL in the PS design. One of the main functions of the PCL is to resist anterior sliding of the femur relative to the tibia. The average lateral condylar translation for PS subjects was -8.0 mm (Figure 5-42).

The FSM predicted -2.3 mm of medial posterior rollback. Before cam/post engagement the medial condyle moved about 1.6 mm of anteriorly (Figure 5-43). The average femoral external rotation was about 6.3º (Figure 5-44). Additionally, the FSM predicted different flexion angle where cam/post starts engaging for different subjects. Again, this has been observed in fluoroscopic studies on PS TKA designs. On average, the cam/post starts engaging at about 62.2º of knee flexion (Figure 5-48).

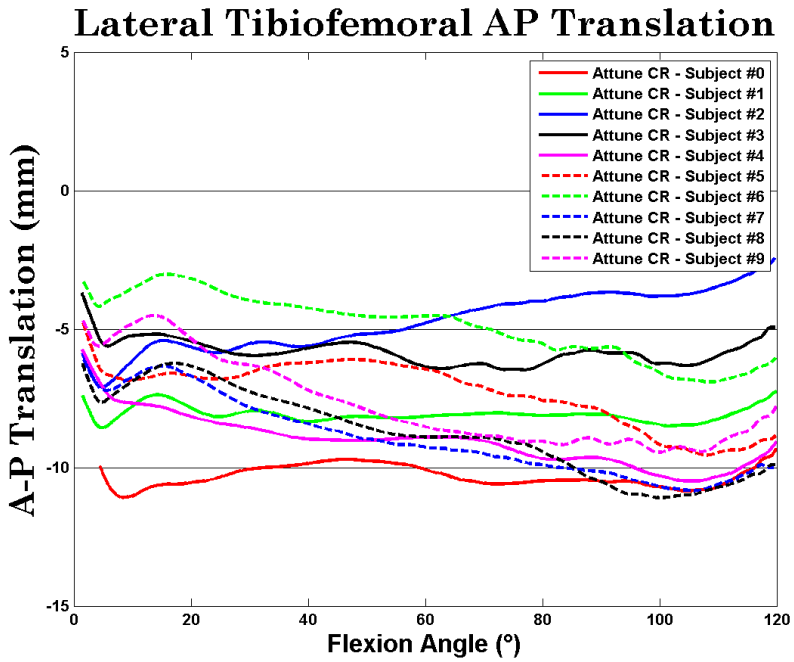


Figure 5-36: Comparison of lateral condylar AP translation between ten subjects implanted with Attune CR TKA.

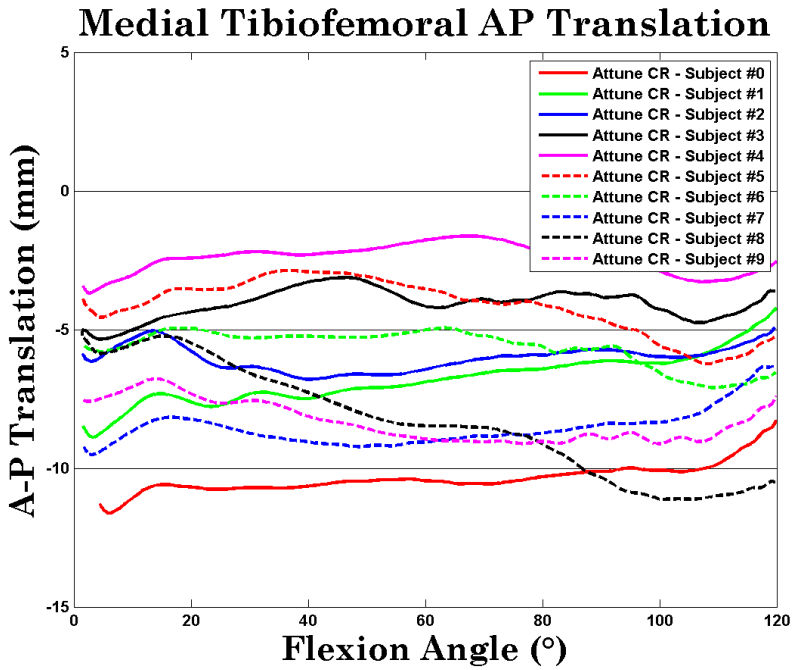


Figure 5-37: Comparison of medial condylar AP translation between ten subjects implanted with Attune CR TKA.

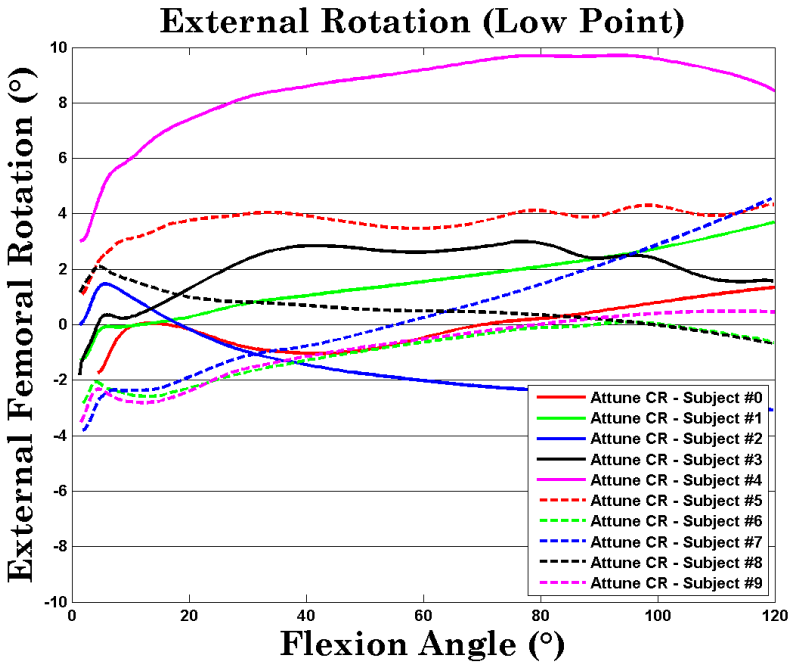


Figure 5-38: Comparison of femoral axial rotation between ten subjects implanted with Attune CR TKA.

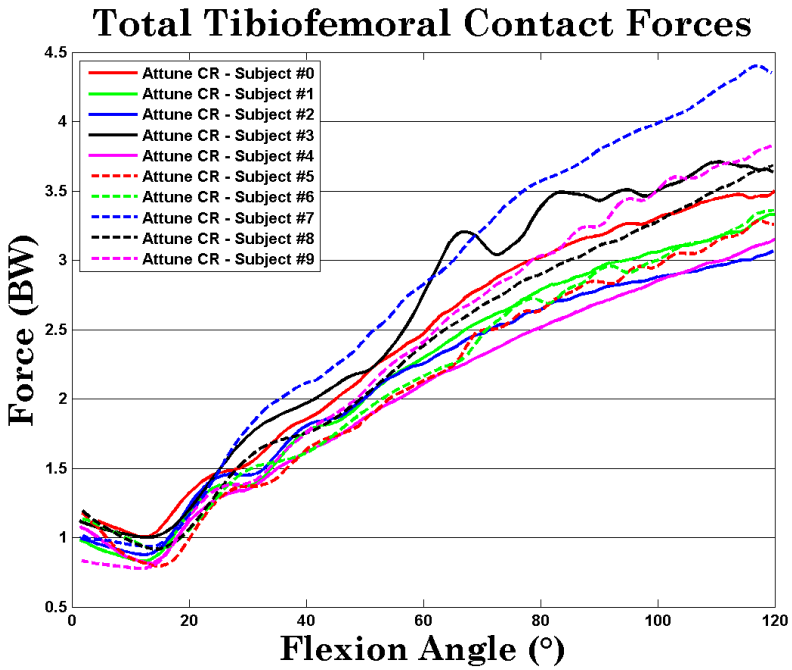


Figure 5-39: Comparison of tibiofemoral contact force between ten subjects implanted with Attune CR TKA.

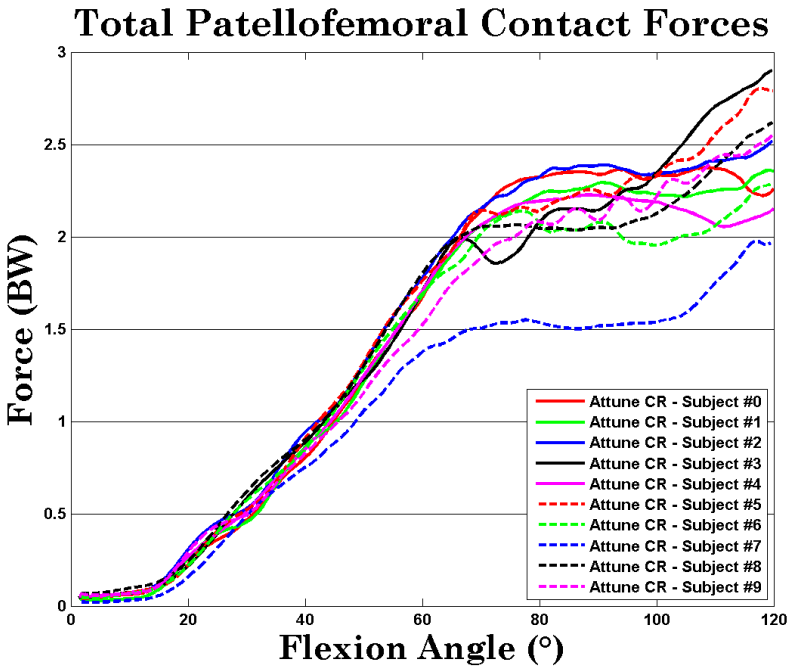


Figure 5-40: Comparison of patellofemoral contact force between ten subjects implanted with Attune CR TKA.

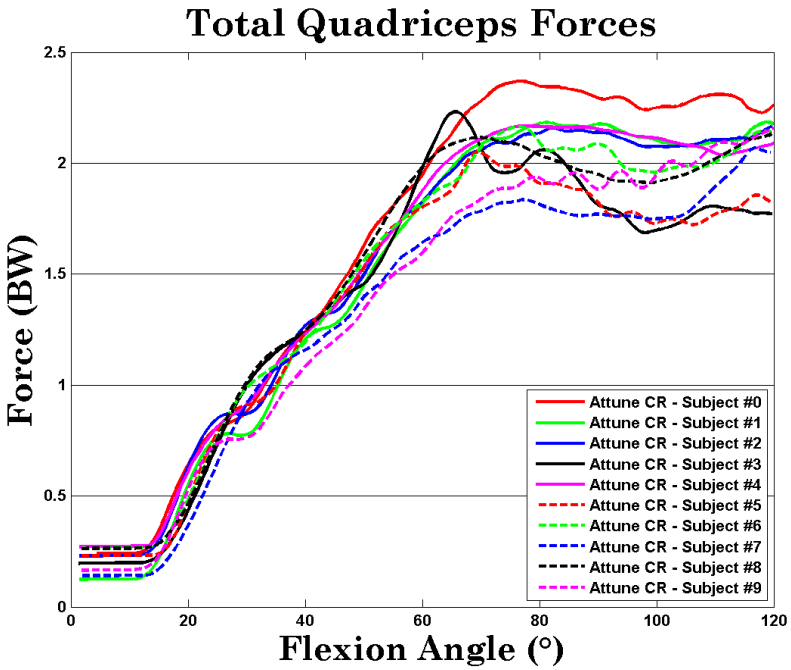


Figure 5-41: Comparison of quadriceps muscle force between ten subjects implanted with Attune CR TKA.

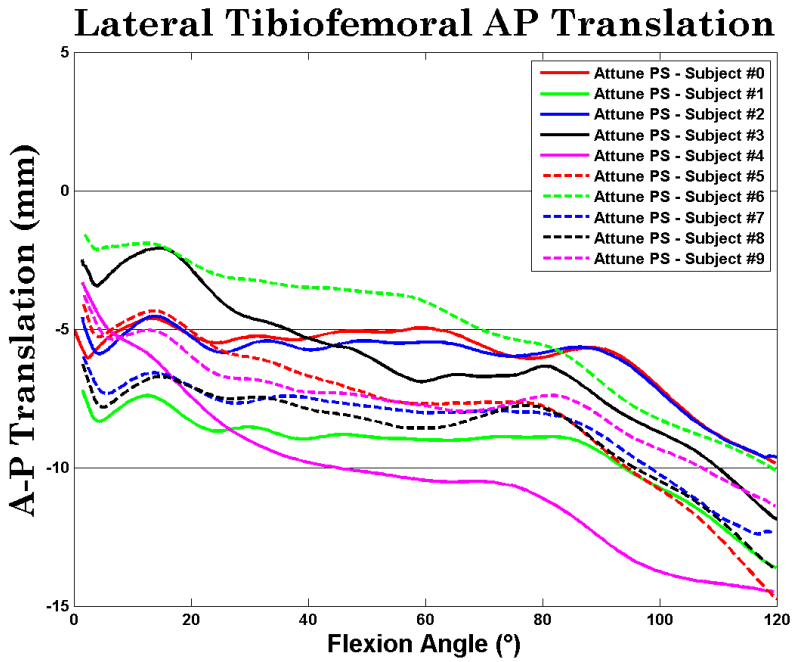


Figure 5-42: Comparison of lateral condylar AP translation between ten subjects implanted with Attune PS TKA.

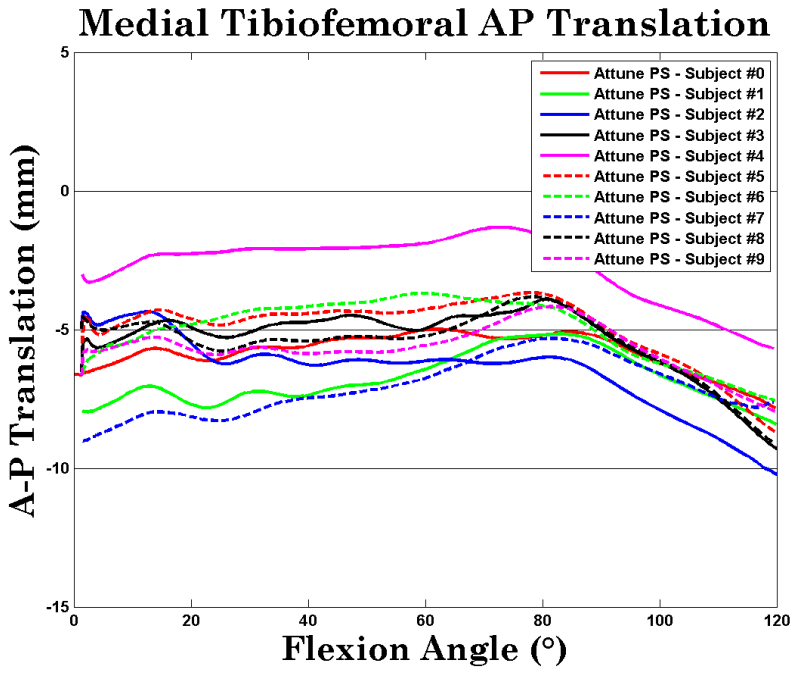


Figure 5-43: Comparison of medial condylar AP translation between ten subjects implanted with Attune PS TKA.

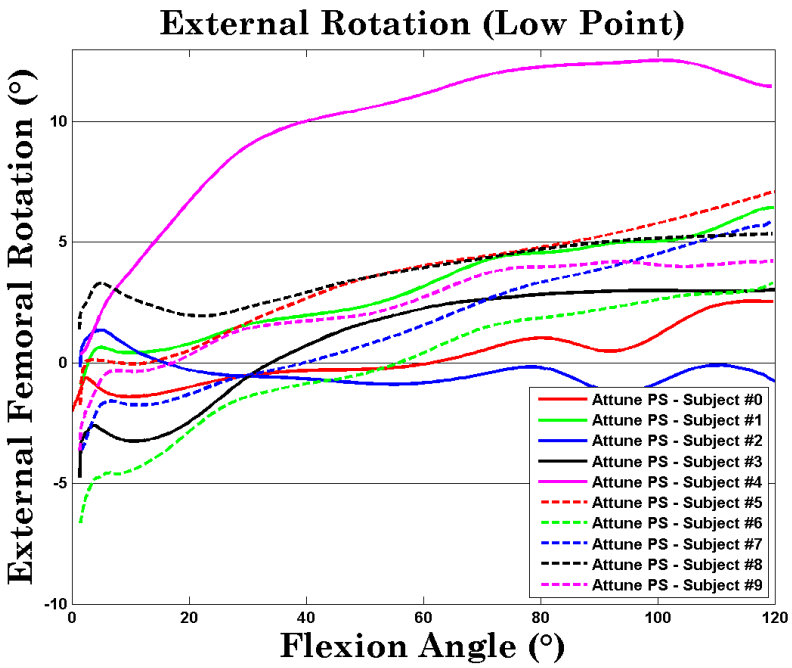


Figure 5-44: Comparison of femoral axial rotation between ten subjects implanted with Attune PS TKA.

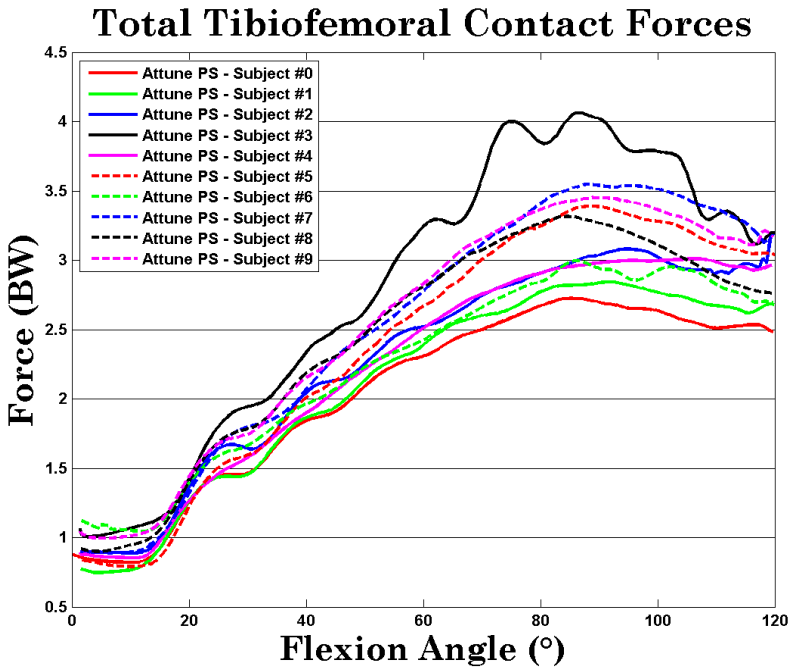


Figure 5-45: Comparison of tibiofemoral contact force between ten subjects implanted with Attune PS TKA.

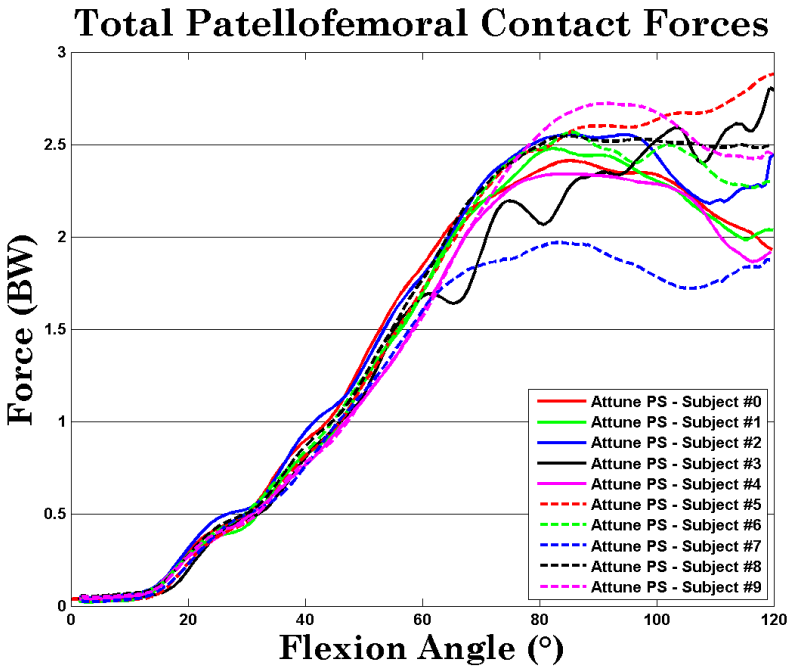


Figure 5-46: Comparison of patellofemoral contact force between ten subjects implanted with Attune PS TKA.

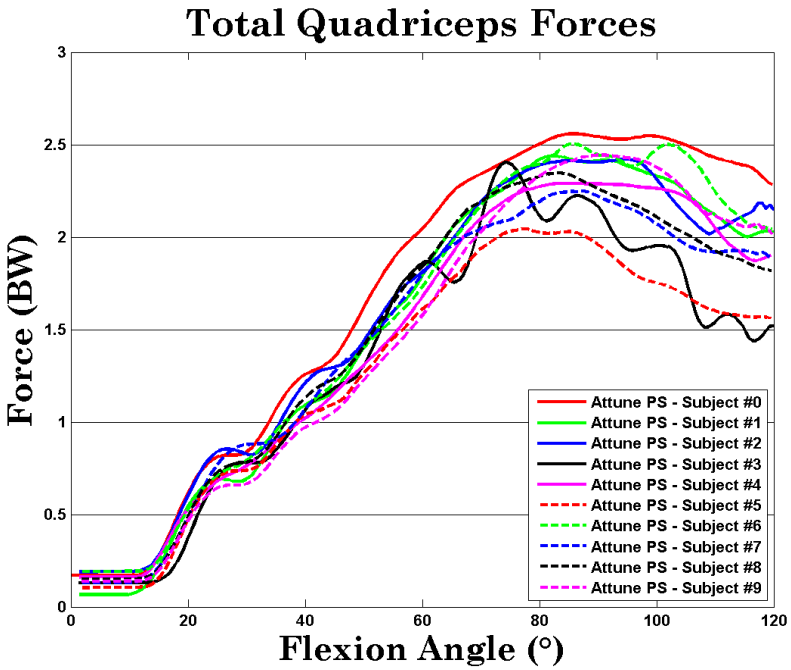


Figure 5-47: Comparison of quadriceps muscle force between ten subjects implanted with Attune PS TKA.

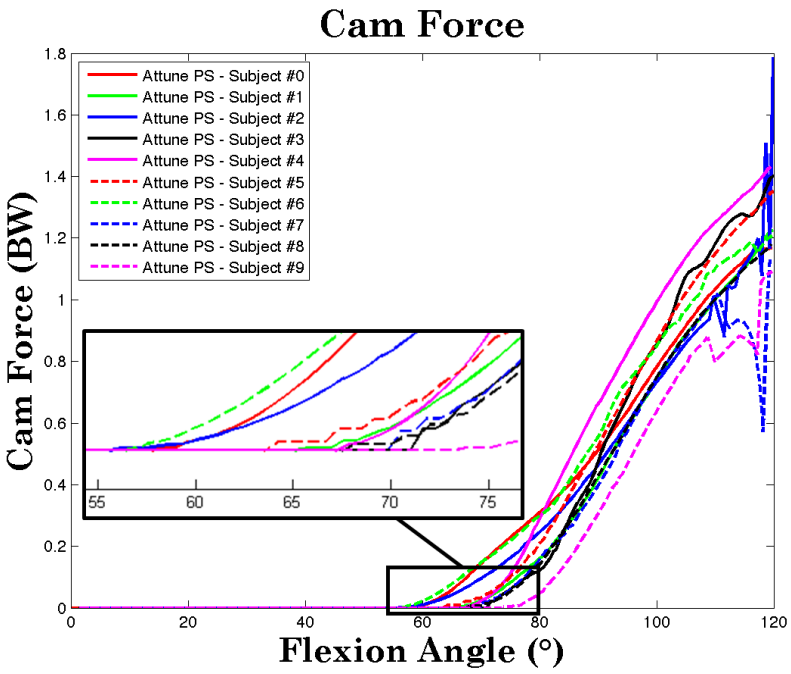


Figure 5-48: Comparison of cam/post contact force between ten subjects implanted with Attune PS TKA.

5.6 Other Activities

In this section, the TKA outcomes for other activities besides the DKB activity are described.

5.6.1 Squat to Rise

As stated before, the previous FSM incorporated a squat to rise activity. The main concern in the previous model was the run time of the simulation. In the current FSM, this activity is updated to decrease the run time. The current squat to rise activity takes about an hour to complete as opposed to 4.5 hours in the previous FSM. The kinematics do not change significantly except for a slight improvement in the amount of oscillations observed at the turning flexion (Figure 5-49 and Figure 5-50). Similarly, the quadriceps muscle forces exhibited similar magnitude and pattern to the previous FSM. Finally, more improvement was observed at the turning flexion angle with regards to the oscillations at the quadriceps force prediction (Figure 5-51).

5.6.2 Chair Rise

From seated position (90° of knee flexion) to the full extension, the chair rise simulation for the PCR design revealed 3.9 mm of anterior sliding of the lateral condyle (Figure 5-52) and about 5.2 mm of anterior sliding of the medial condyle (Figure 5-53). The femoral component experienced 1.7° of internal rotation (Figure 5-54).

The peak tibiofemoral contact force is 3.1 × BW at the seated position and starts decreasing as the flexion angle decrease to about 1.1 × BW (Figure 5-55). The peak quadriceps muscle force is 3.4 × BW (Figure 5-56), and the peak patellofemoral contact force is 3.1 × BW (Figure 5-57). These results are consistent with reported quadriceps force in literature, about 3 × BW at 90° of flexion and about 0.5 × BW at full extension [172,173].

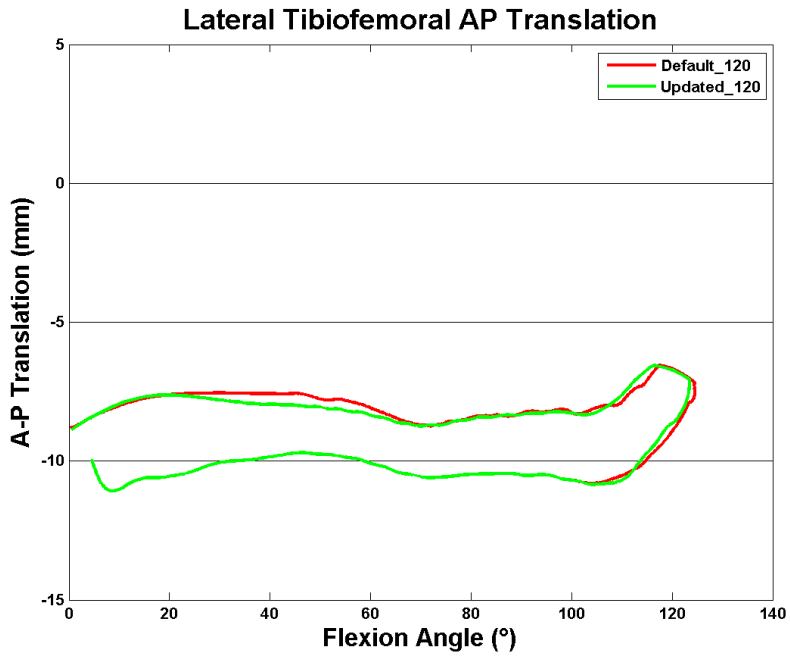


Figure 5-49: Comparison of the lateral AP translation between the current FSM (green) and the previous FSM (red) for a squat to rise activity.

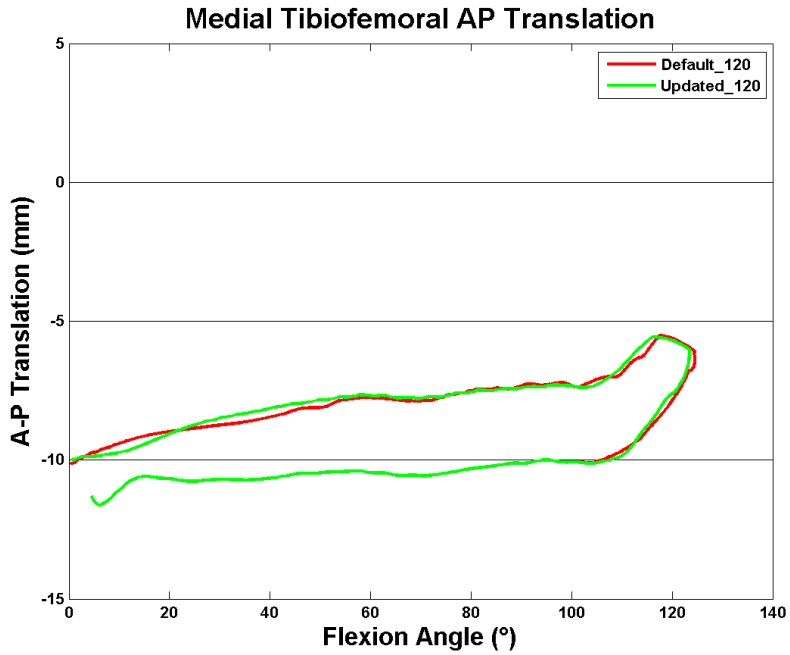


Figure 5-50: Comparison of the medial AP translation between the current FSM (green) and the previous FSM (red) for a squat to rise activity.

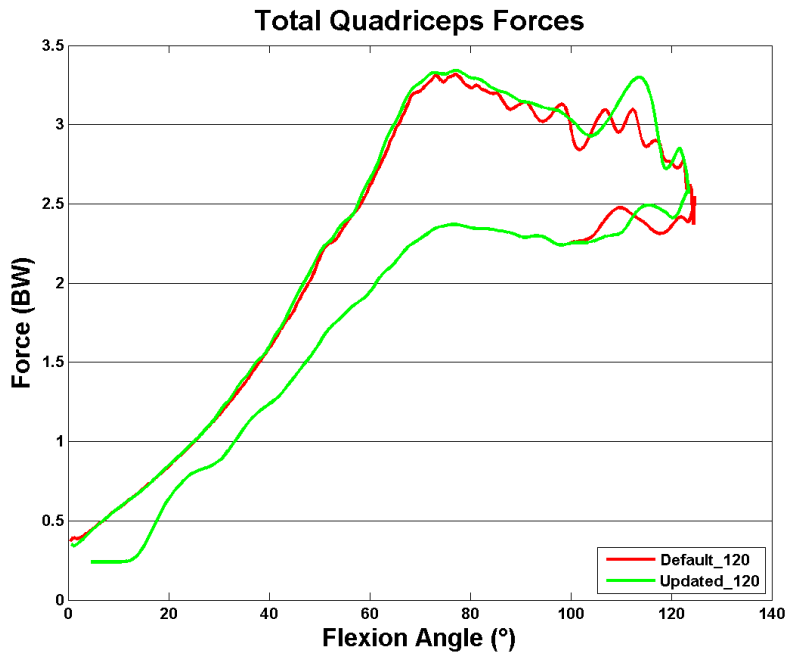


Figure 5-51: Comparison of the quadriceps muscle between the current FSM (green) and the previous FSM (red) for a squat to rise activity.

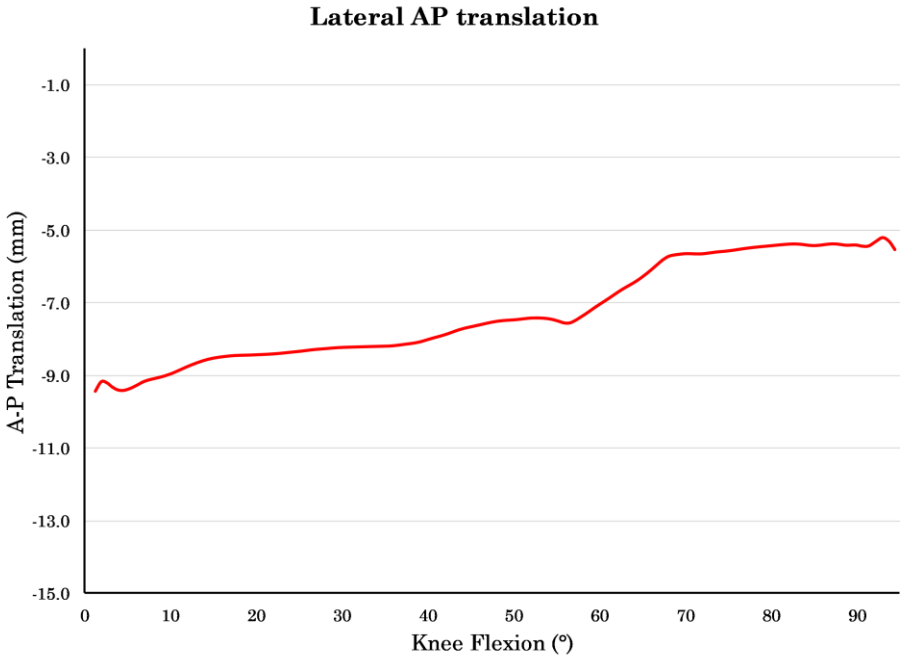


Figure 5-52: The lateral AP translation for a PCR TKA design during the chair rise activity.

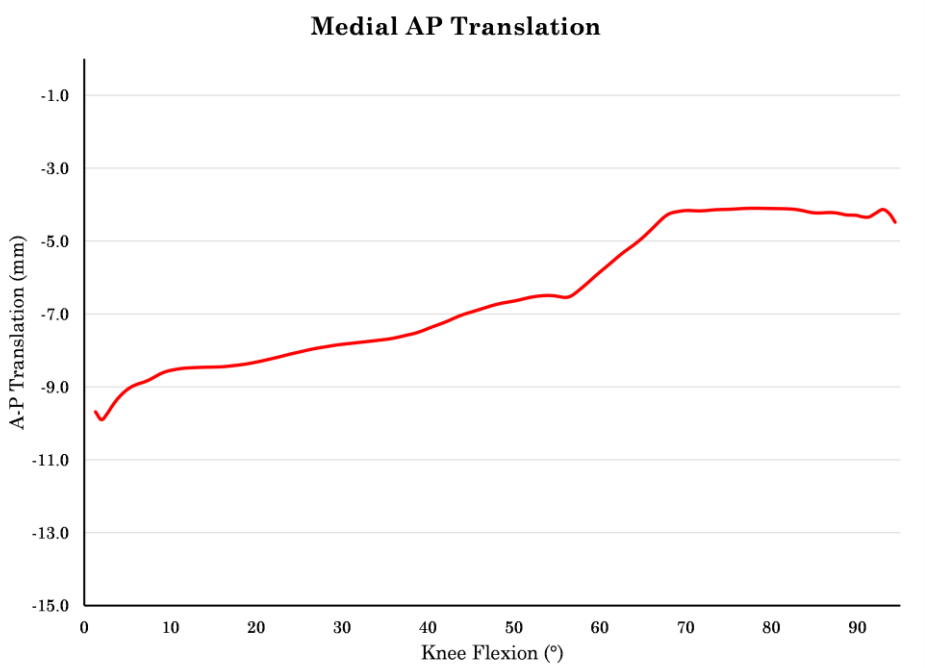


Figure 5-53: The medial AP translation for a PCR TKA design during the chair rise activity.

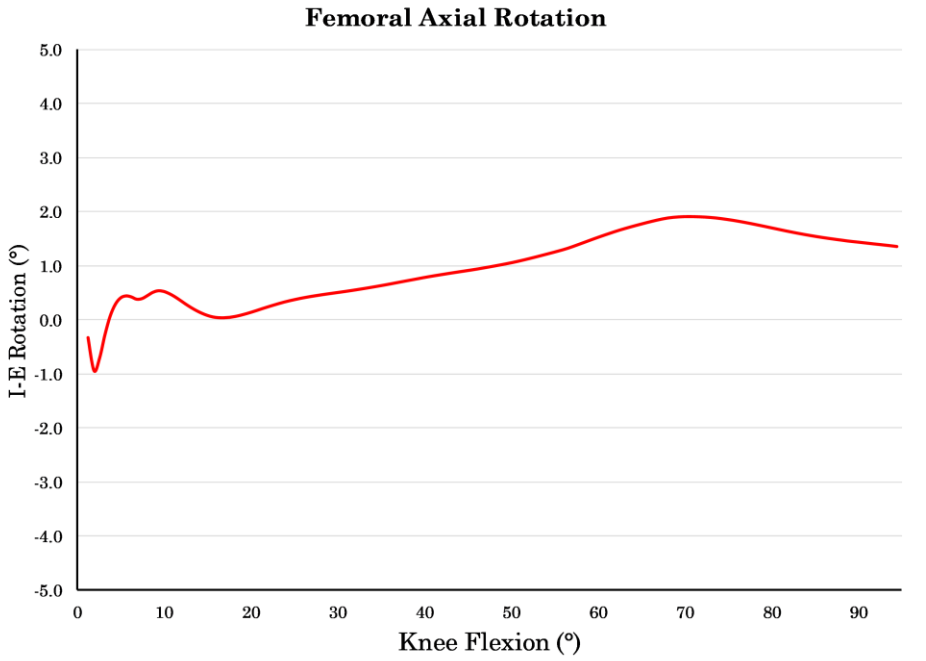


Figure 5-54: The femoral axial rotation for a PCR TKA design during the chair rise activity.

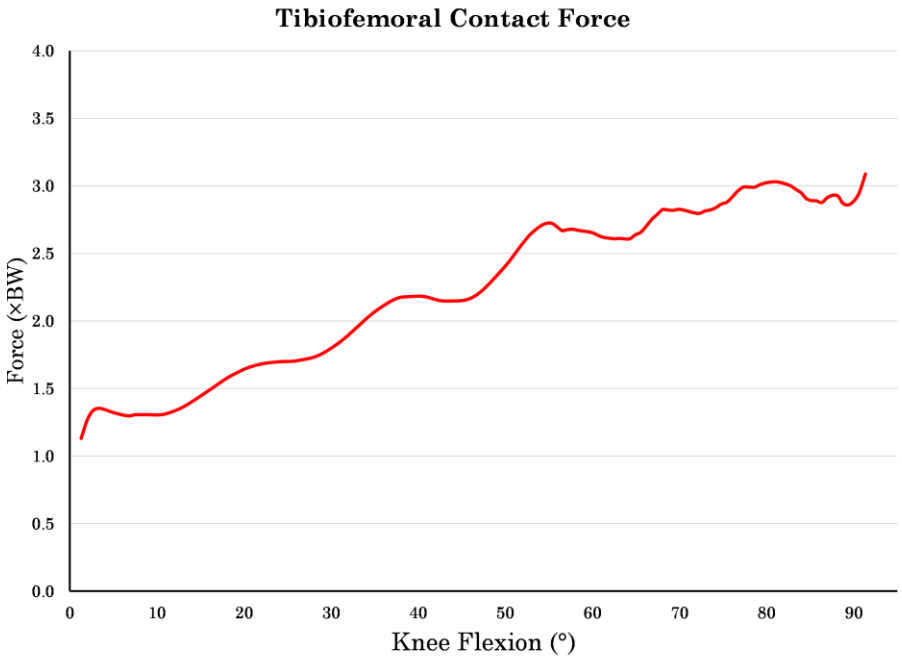


Figure 5-55: The tibiofemoral contact force for a PCR TKA design during the chair rise activity.

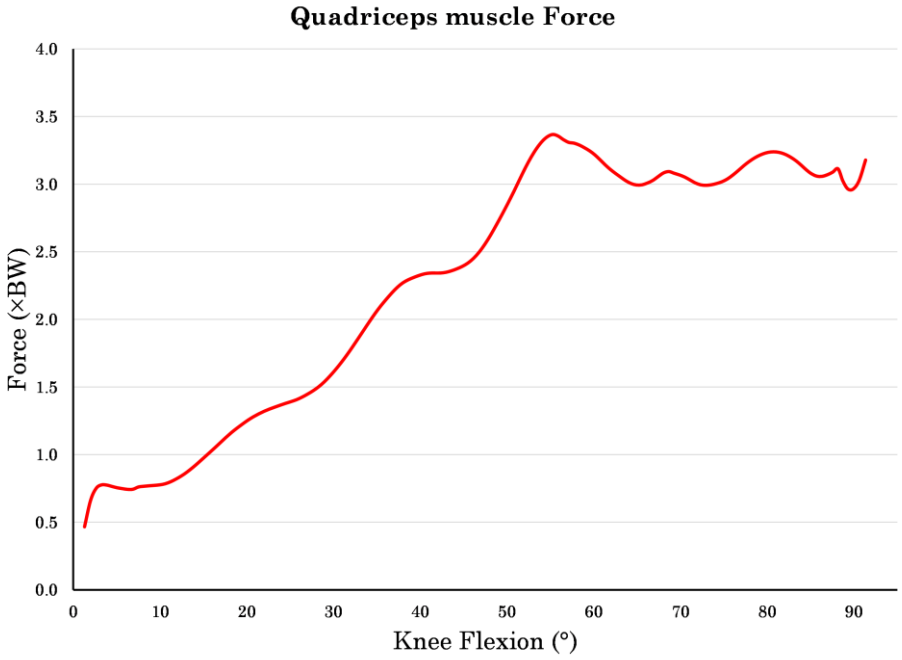


Figure 5-56: the quadriceps muscle force for a PCR TKA design during the chair rise activity.

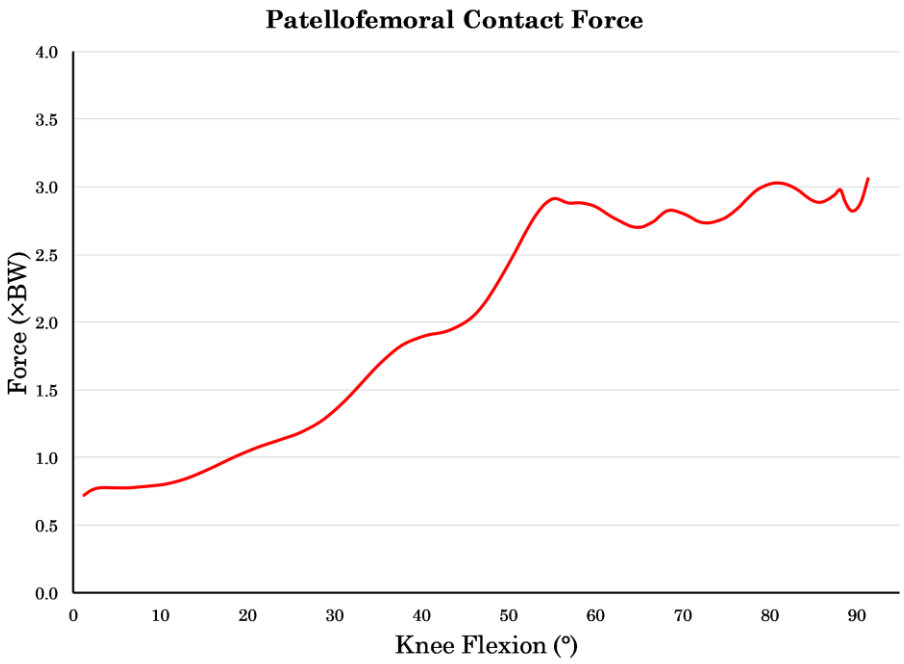


Figure 5-57: the patellofemoral contact force for a PCR TKA design during the chair rise activity.

5.6.3 Lunge

There are three main differences between the lunge activity and the deep knee bend activity. First, in the DKB activity, the tibia flexes to about 30° while in the lunge activity, the tibia stays almost upright with minimal flexion, about 5° from full extension to the end of the activity.

Secondly, the upper body flexes in the DKB activity while the range of motion of the upper body is limited in the lunge activity (Figure 5-58). Thirdly, the knee only flexes to about 95° in the lunge activity, while the maximum knee flexion in the DKB activity is 120°.

During the lunge activity, the lateral condyle experienced slightly less translation compared to the lunge activity (Figure 5-59). The trend of medial AP translation is similar for both activities, although, in the lunge activity, the medial condyle experienced smaller anterior sliding (Figure 5-60). This smaller anterior sliding, coupled with almost identical lateral translations, resulted in slightly reduced external rotation during the lunge activity compared to the DKB activity (Figure 5-61).

Although there is not a substantial difference in the kinematics between these two activities, the muscle forces and the contact forces are significantly higher for the lunge activity. The peak tibiofemoral contact force during the lunge activity was 4.1 × BW, while during a deep knee bend, occurring at 95° of knee flexion was 3.3 × BW (Figure 5-62).

The peak quadriceps force was 3.5 × BW during the lunge activity, while during a deep knee bend, occurring at 95° of knee flexion, the quadriceps force was 2.3 × BW (Figure 5-63). Similarly, the patellofemoral contact force showed a significant increase during the lunge activity, peaking at 3.6 × BW, compared to 2.3 × BW at 95° of knee flexion during the DKB (Figure 5-64).

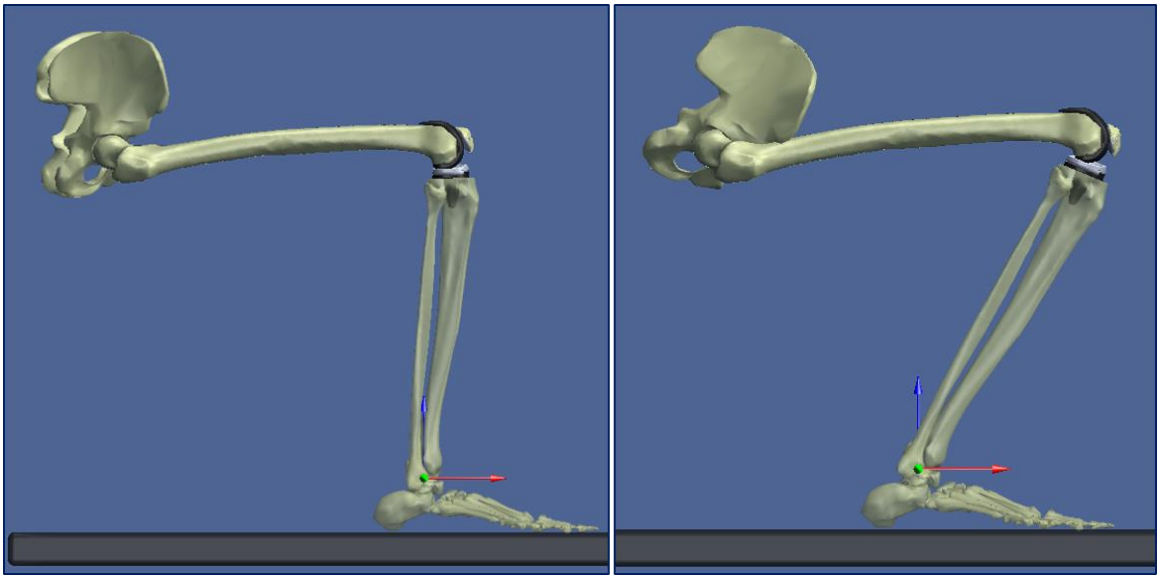


Figure 5-58: Comparison between the end position of the lunge activity (left) with the DKB activity (right). The range of motion of the tibia and the upper body is limited in the lunge activity.

There are several reasons why the muscle forces and contact forces are significantly higher during the lunge activity. First, due to the lack of upper body flexion, the upper body center of mass stays more posteriorly in the lunge activity compared to the DKB activity. This results in an increased moment at the knee joint and therefore increased joint forces.

Secondly, the patella plays an important role in increasing the extensor mechanism moment arm. During the lunge activity, due to the lack of tibia flexion, the patella cannot increase the muscle moment arm as effectively as the DKB activity; hence, the extensor mechanism forces increase during the lunge activity.

This lack of patella motion can be seen by comparing the patellar ligament length for these activities (Figure 5-65). The patellar ligament length and therefore patellar ligament forces are higher during the lunge activity (Figure 5-66).

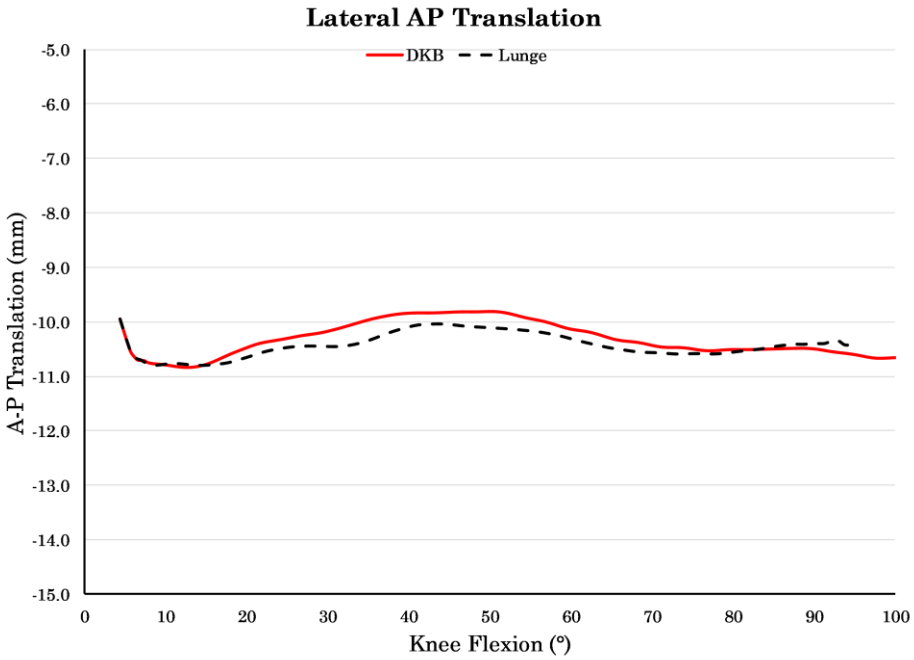


Figure 5-59: Comparison between the lateral AP translation between the DKB activity (solid red) and the lunge activity (dashed black).

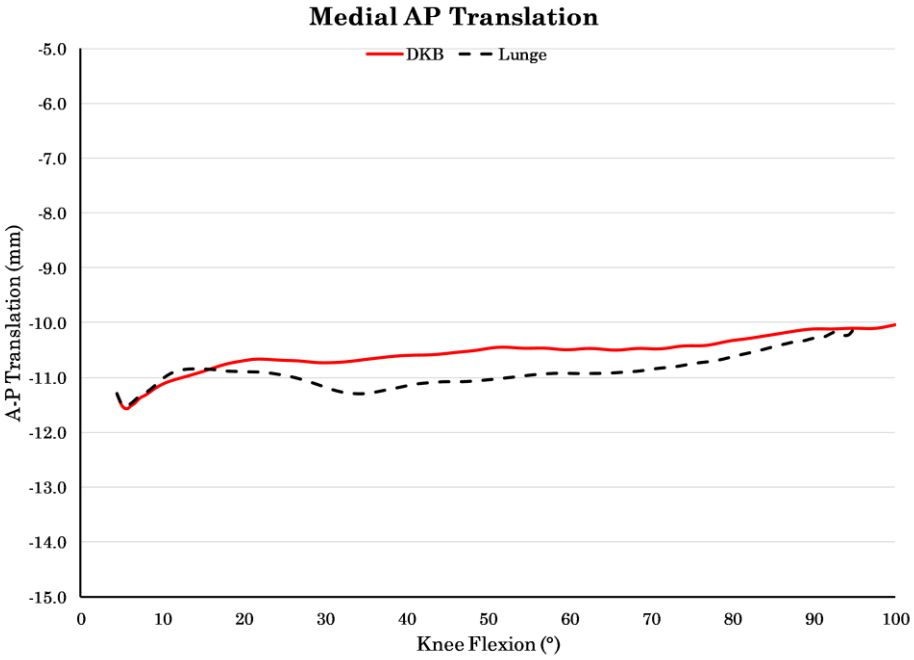


Figure 5-60: Comparison between the medial AP translation between the DKB activity (solid red) and the lunge activity (dashed black).

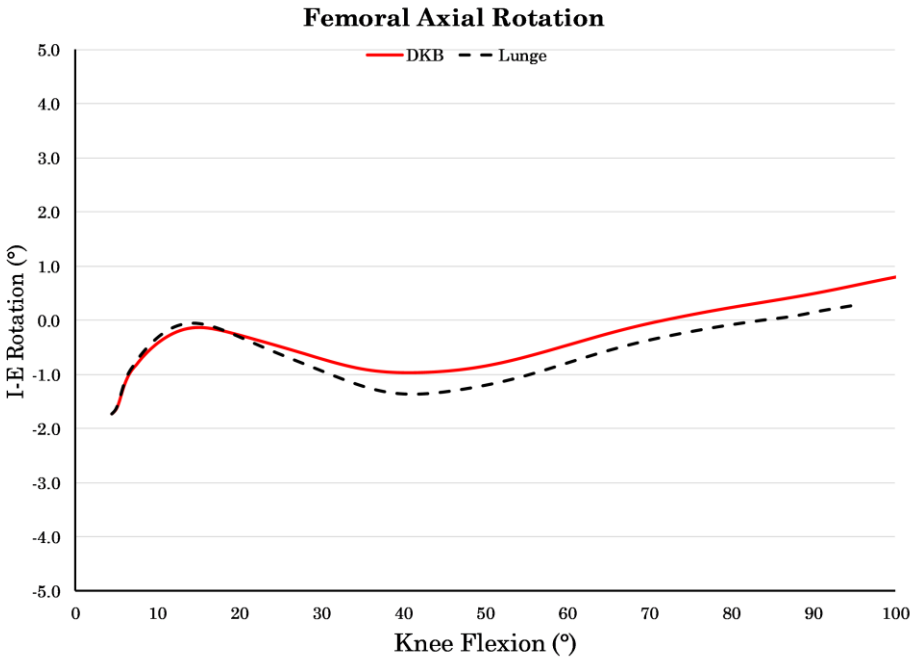


Figure 5-61: Comparison between the femoral axial rotation between the DKB activity (solid red) and the lunge activity (dashed black).

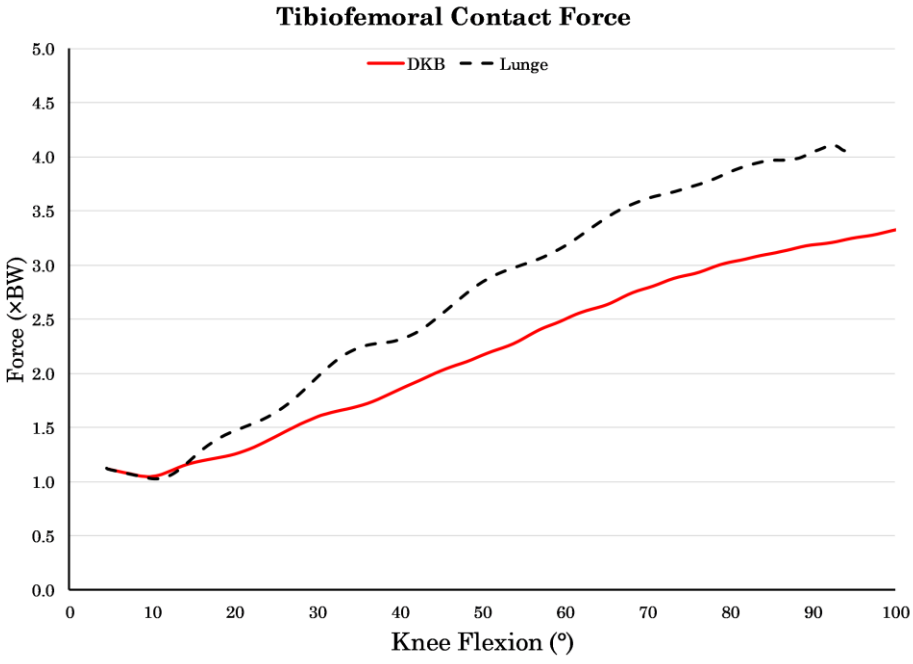


Figure 5-62: Comparison between the tibiofemoral contact force between the DKB activity (solid red) and the lunge activity (dashed black).

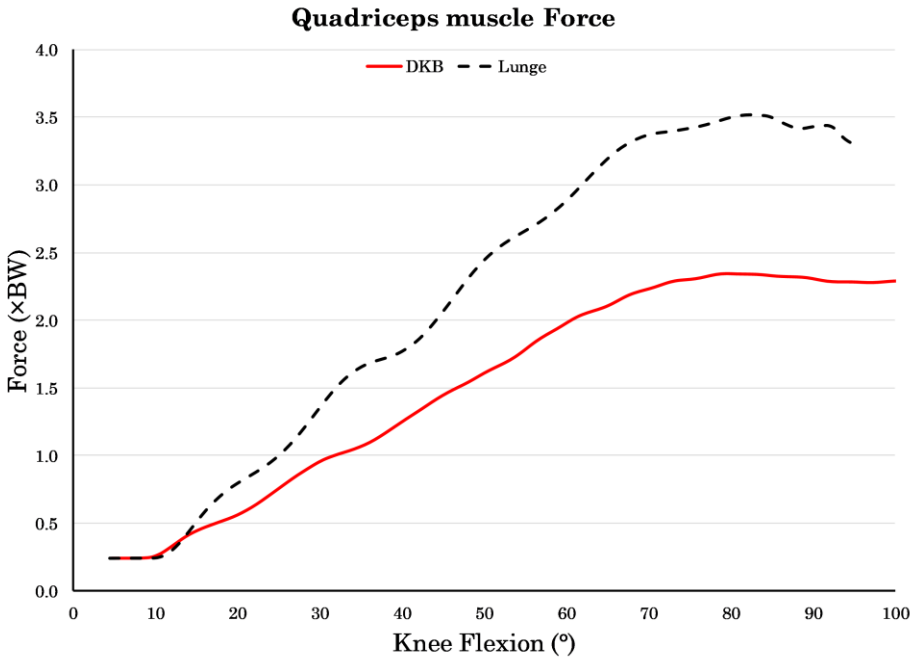


Figure 5-63: Comparison between the quadriceps muscle force between the DKB activity (solid red) and the lunge activity (dashed black).

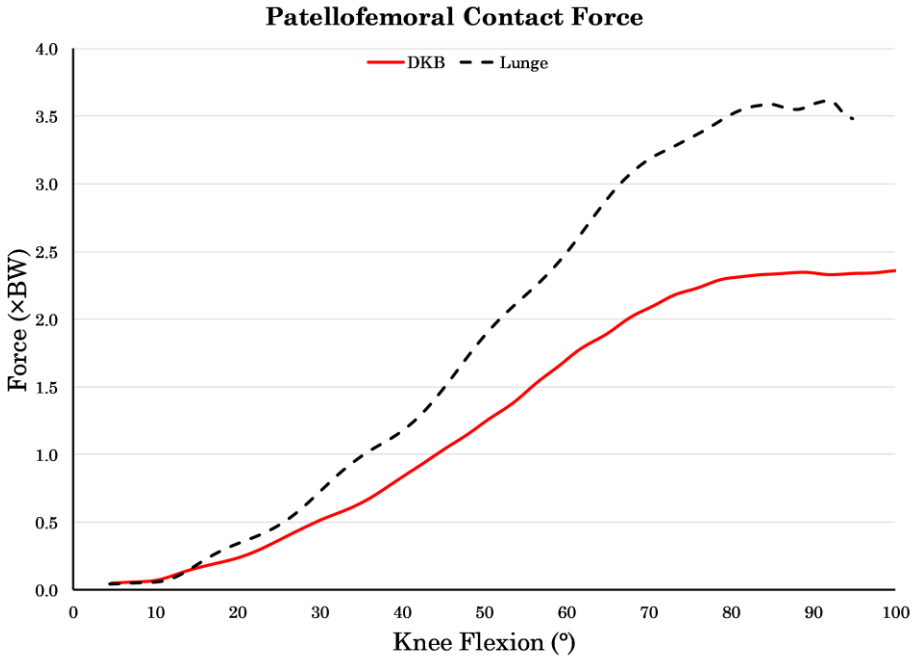


Figure 5-64: Comparison between the patellofemoral contact force between the DKB activity (solid red) and the lunge activity (dashed black).

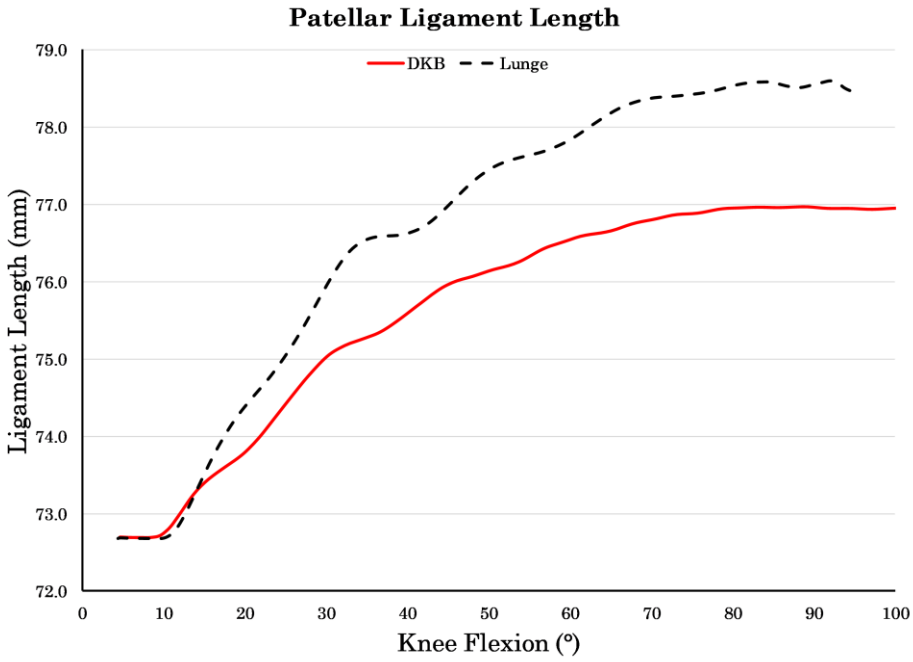


Figure 5-65: Comparison between the patellar ligament length between the DKB activity (solid red) and the lunge activity (dashed black).

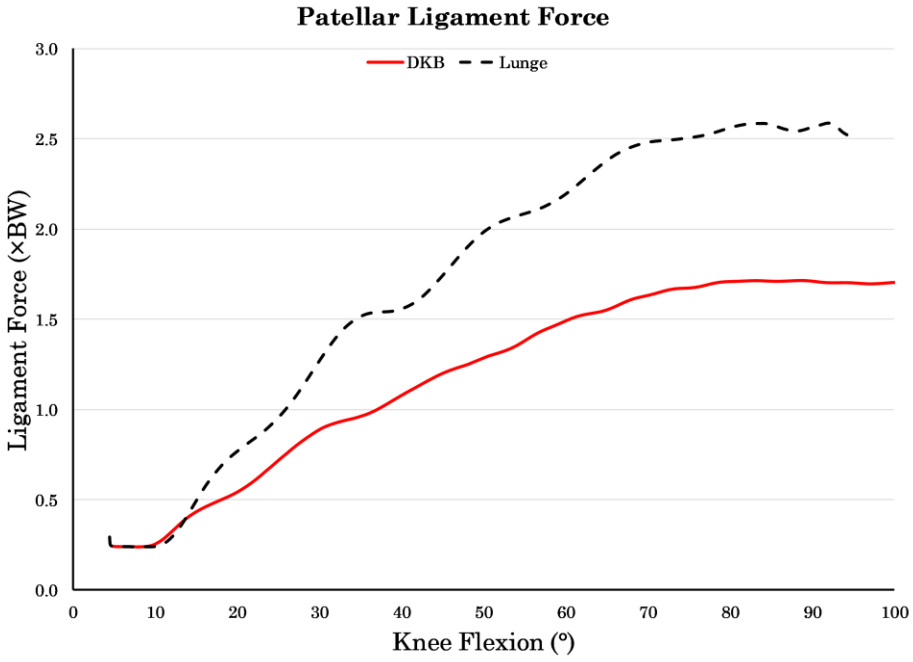


Figure 5-66: Comparison between the patellar ligament force between the DKB activity (solid red) and the lunge activity (dashed black).

5.6.4 Stair Descent

During the stair descent activity, the lateral condyle translates about -0.2 mm from heel strike to toe-off. However, during the initial part of the stance phase, weight acceptance, the lateral condyle moves posteriorly about -1.1 mm. After the initial phase to the end of the stance phase, the lateral condyle moves anteriorly about 1.5 mm (Figure 5-67).

Unlike the lateral condyle, the medial condyle translates anteriorly during the activity in the amount of 2.4 mm (Figure 5-68). The femur was internally rotated at heel strike, -2.9°, and externally rotated from heel strike to toe-off, about 2.5° (Figure 5-69).

The knee force during stair descent activity follows an M curve shape, showing two peak forces during the stance phase. The first peak tibiofemoral contact force was 3.9 × BW, and the second peak contact force was about 3.89 × BW (Figure 5-70). Both the M curve trends and the magnitudes are in agreement with the literature, which reported mostly reported a range of 3 - 4 × BW peak contact forces [159,174–176].

The quadriceps muscle shows a similar M curve force profile, with the peak force of about 2.2 × BW (Figure 5-71). The patellofemoral contact force, although showed an M curve force profile with two peaks, the second peak was higher, about 1.8 × BW compared to 1.2 × BW (Figure 5-72). Brechter et al. reported a similar trend for the patellofemoral contact force [177].

5.6.5 Stair Ascent

From heel strike to toe-off, the lateral condyle translates anteriorly about 0.2 mm. In the initial part of the stance phase, the lateral condyle moves anteriorly about 1.8 mm, and from there, it moves posteriorly about 0.5 mm (Figure 5-73).

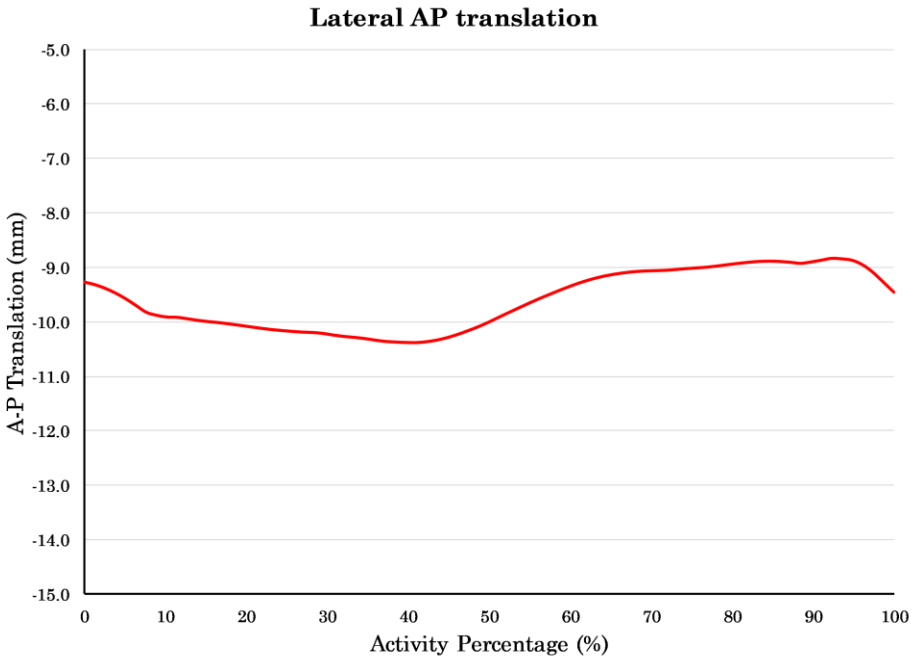


Figure 5-67: The lateral AP translation for a PCR TKA during the stair descent activity.

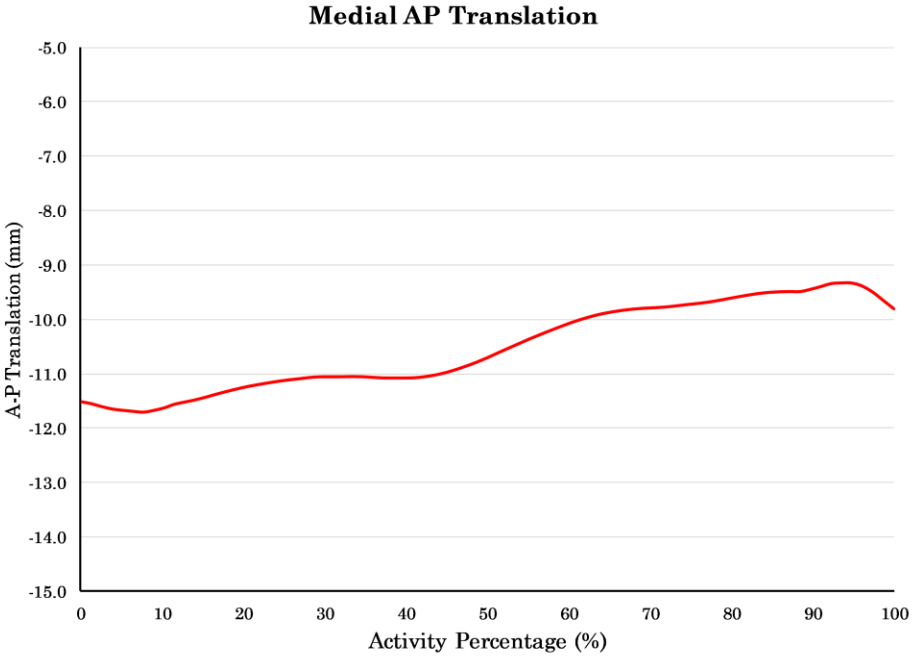


Figure 5-68: The medial AP translation for a PCR TKA during the stair descent activity.

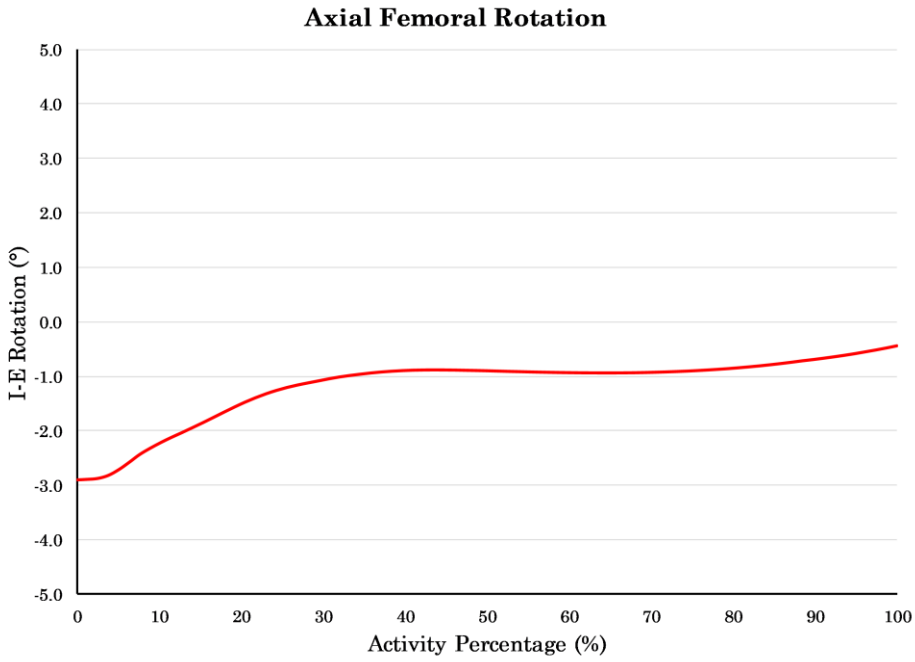


Figure 5-69: The femoral axial rotation for a PCR TKA during the stair descent activity.

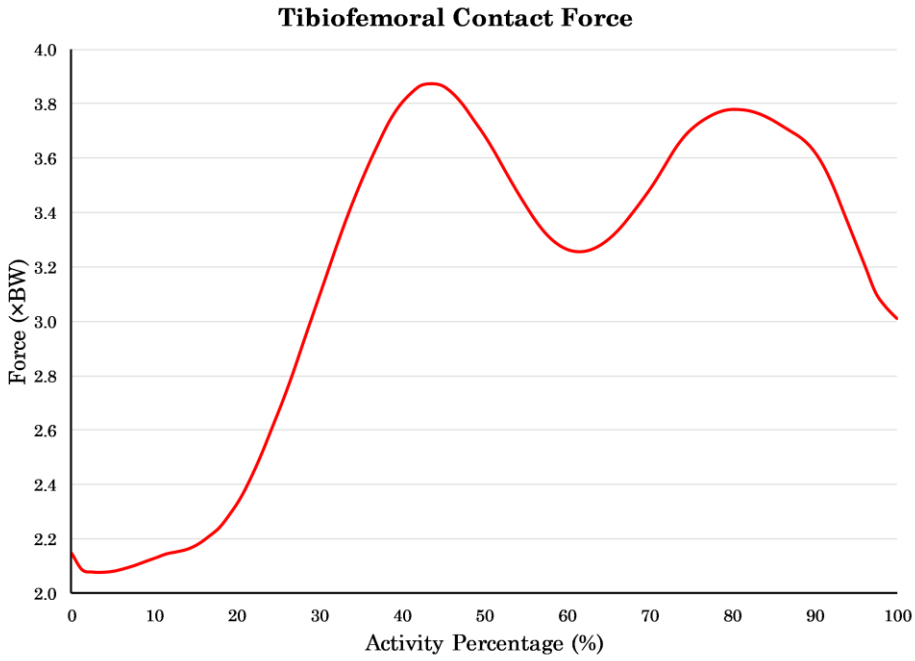


Figure 5-70: The tibiofemoral contact force for a PCR TKA during the stair descent activity.



Figure 5-71: The quadriceps muscle force for a PCR TKA during the stair descent activity.

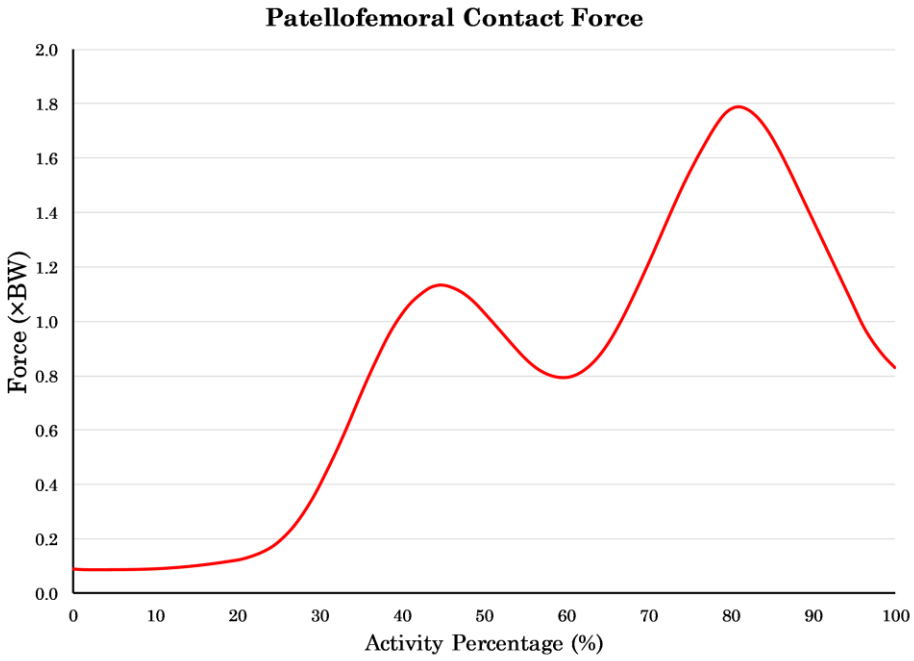


Figure 5-72: The patellofemoral contact force for a PCR TKA during the stair descent activity.

A similar pattern was observed for the medial condyle translation. During the initial part of the activity, the medial condyle moves anteriorly about 1.5 mm, and after that until the end of the activity is moves posteriorly about -1.4 mm (Figure 5-74). The femur showed minimal axial rotation during the initial phase and internally rotates about 1.3° until the end (Figure 5-75).

Similar to the stair decent activity, the stair ascent activity exhibited an M curve contact force profile for the tibiofemoral joint. The first and the second peak contact forces are almost identical at about 3.8 × BW (Figure 5-76). The quadriceps muscle force follows a similar pattern. The peak quadriceps force is about 3.87 × BW (Figure 5-77).

The peak patellofemoral force is 3.5 × BW (Figure 5-78). The tibiofemoral contact forces are slightly smaller for the stair ascent activity compared to the stair descent activity. The literature reports lower contact forces and ground reaction forces for stair ascent activity compared to the stair descent activity, as well [155,174,178].

5.6.6 Gait

From heel strike to toe-off, the lateral condyle moved anteriorly about 0.9 mm. During the first half of the stance phase the lateral condyle stays relatively constant. Then moves anteriorly about 2 mm and toward the end of the stance phase moves posteriorly about 1.4 mm (Figure 5-79).

The medial condyle contacts the bearing insert more posteriorly compared to the lateral condyle. Similar to the lateral condyle, minimal movement is observed during the first half of stance phase. After that about 2.1 mm of anteriorly sliding is observed, followed by about 1.5 mm of rollback (Figure 5-80). From heel strike to toe-off the femur exhibits about 0.1 of internal rotation (Figure 5-81).

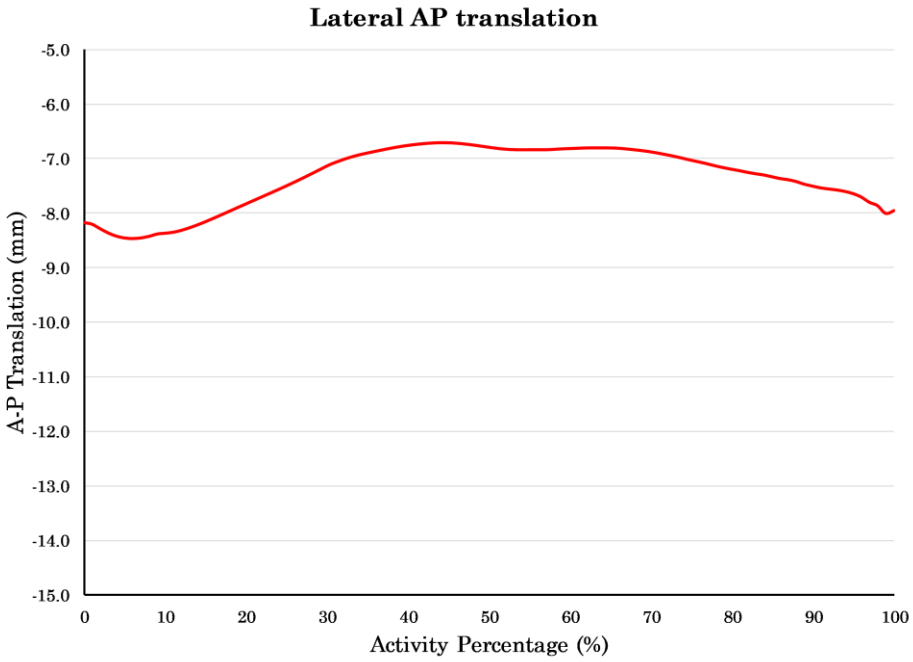


Figure 5-73: The lateral AP translation for a PCR TKA during stair ascent activity.

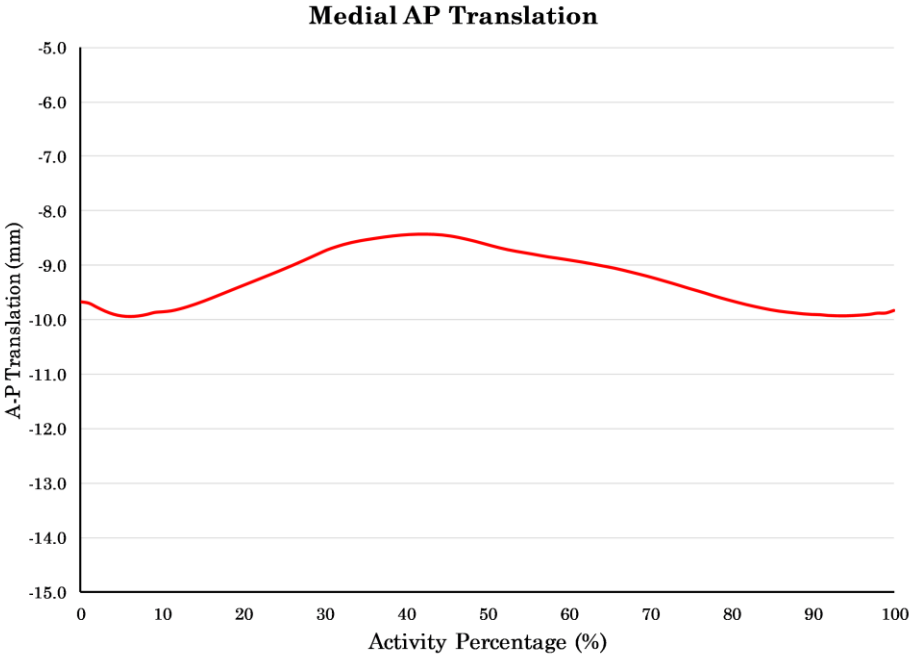


Figure 5-74: The medial AP translation for a PCR TKA during stair ascent activity.

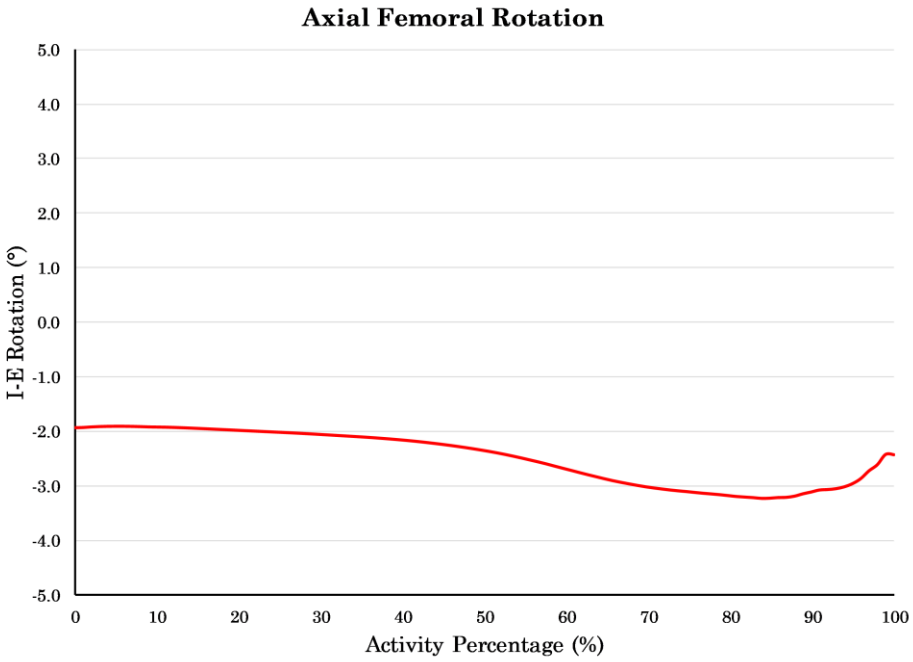


Figure 5-75: The femoral axial rotation for a PCR TKA during stair ascent activity.

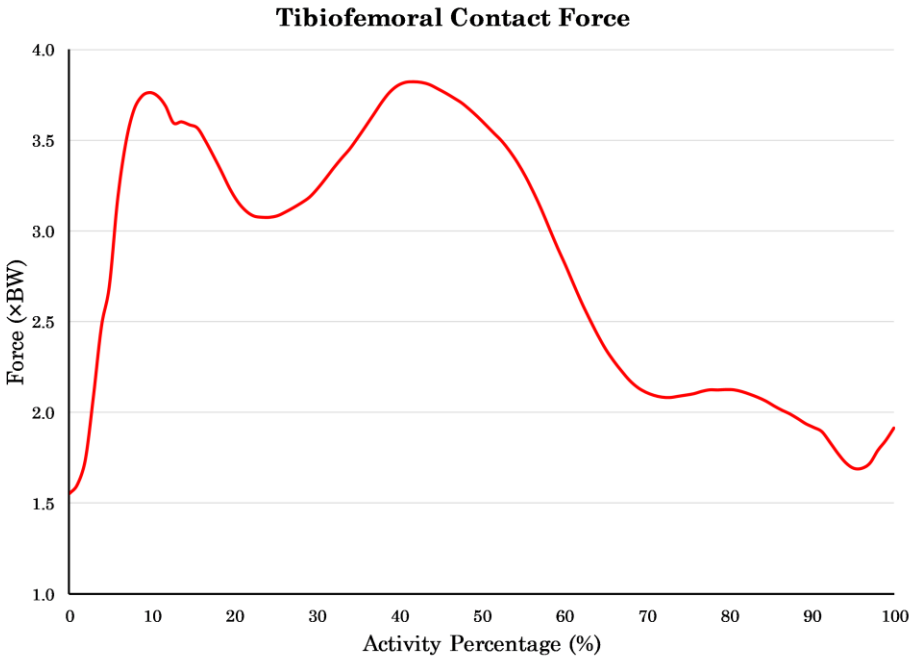


Figure 5-76: The tibiofemoral contact force for a PCR TKA during stair ascent activity.

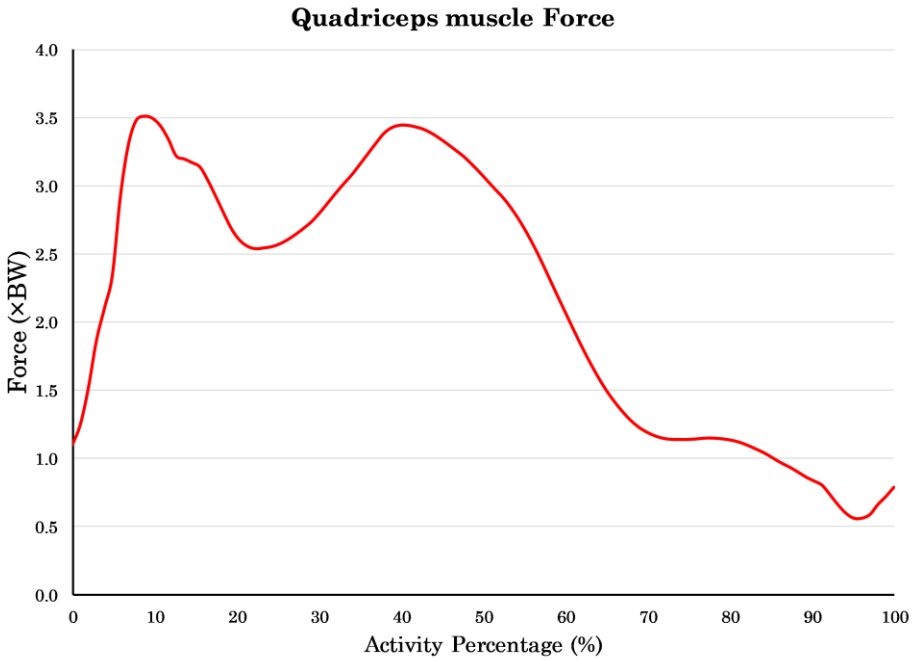


Figure 5-77: The quadriceps muscle force for a PCR TKA during stair ascent activity.

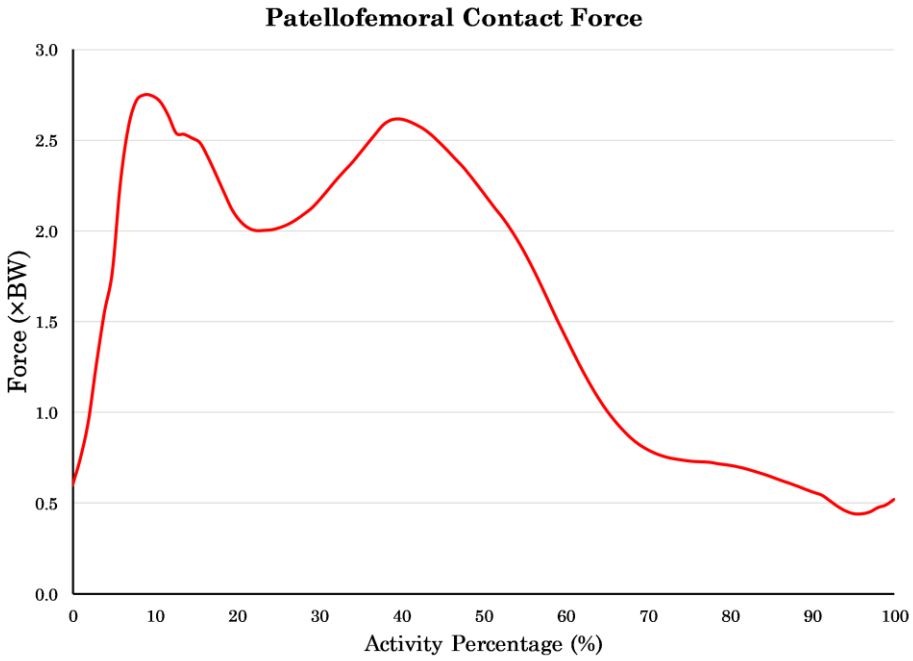


Figure 5-78: The patellofemoral contact force for a PCR TKA during stair ascent activity.

Similar to other gait-based activities, an M curve contact force is predicted for gait activity. The first peak contact force is about 2.5 × BW and the second peak contact force is about 3.3 × BW (Figure 5-82). The quadriceps muscle forces follow similar patterns, and the first and the second peak quadriceps forces are 1.6 × BW and 2.6 × BW, respectively (Figure 5-83). The first and second peak patellofemoral forces are similar to the quadriceps muscle force (Figure 5-84). The pattern and magnitude of the tibiofemoral contact force is also similar to the average telemetric forces reported in Orthoload dataset [179].

5.7 Revision TKA

In this section, the kinematics and kinetics of revision TKA designs are described.

5.7.1 Rotating-bearing Hinge

From full extension to 120° of knee flexion, the lateral condyle in the rotating-bearing hinge design exhibited about -11.4 mm of posterior rollback. Most of this posterior rollback (about -10.2 mm) happens in the first 30° of flexion (Figure 5-85). The medial condyle exhibited -6.9 mm of posterior rollback. In the first 30° of flexion, the medial AP movement was -8.6 mm. After this point, the medial condyle starts moving anteriorly by about 1.7 mm (Figure 5-86). The femur experienced a consistent external rotation from full extension to maximum knee flexion of approximately 6.1° (Figure 5-87). Similarly, the bearing insert externally rotates relative to the tibial tray about 6.2° (Figure 5-88). There is minimal difference in axial rotation of the femur and the bearing insert. This finding could be attributed to the interaction between the cam and post and also the highly conforming surface of the bearing insert plateaus, which means that the femoral component stays relatively constant relative to the bearing insert.

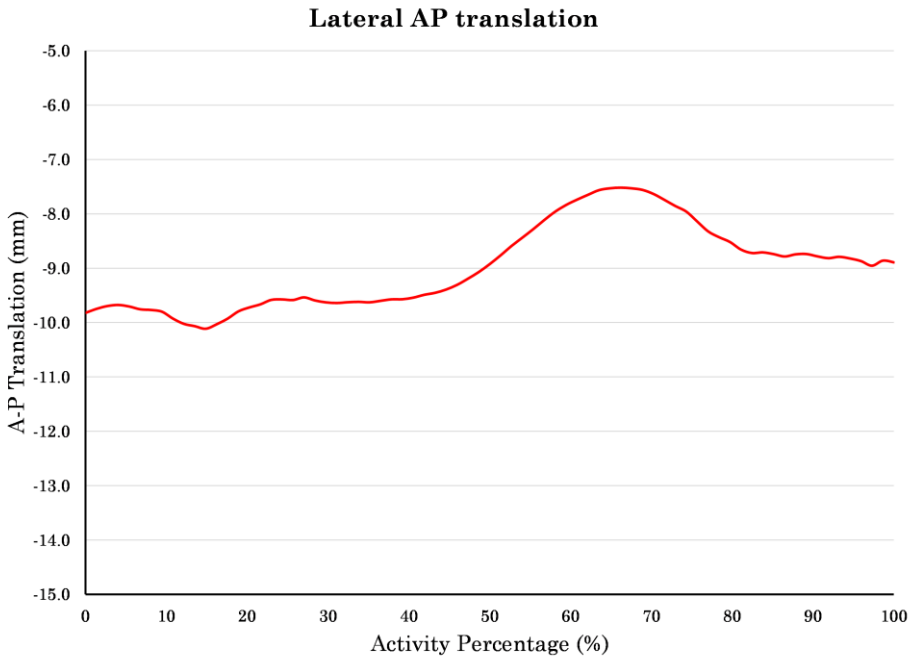


Figure 5-79: The lateral AP translation for a PCR TKA during gait activity.

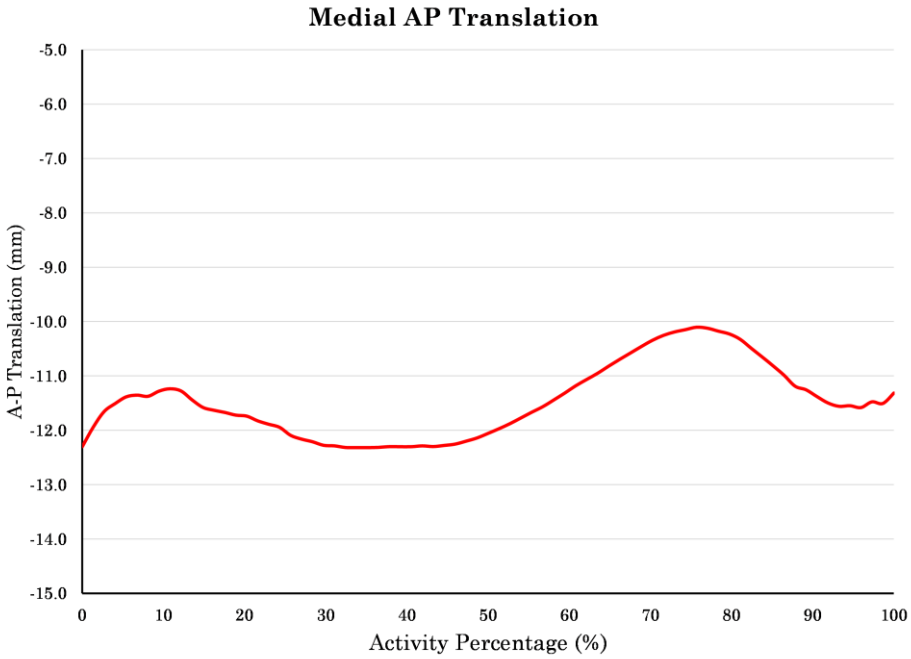


Figure 5-80: The medial AP translation for a PCR TKA during gait activity.

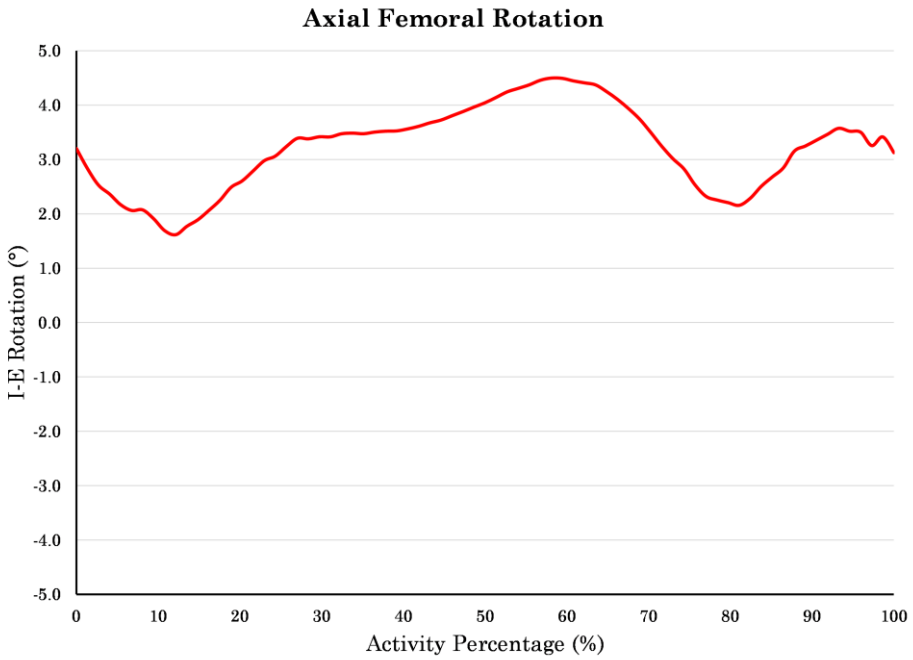


Figure 5-81: The femoral axial rotation for a PCR TKA during gait activity.

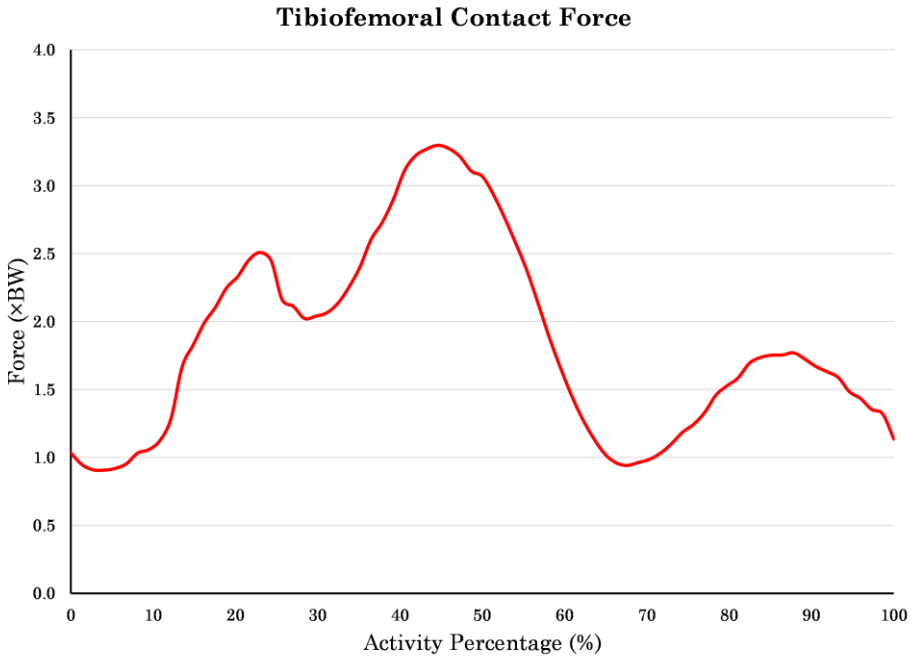


Figure 5-82: The tibiofemoral contact force for a PCR TKA during gait activity.

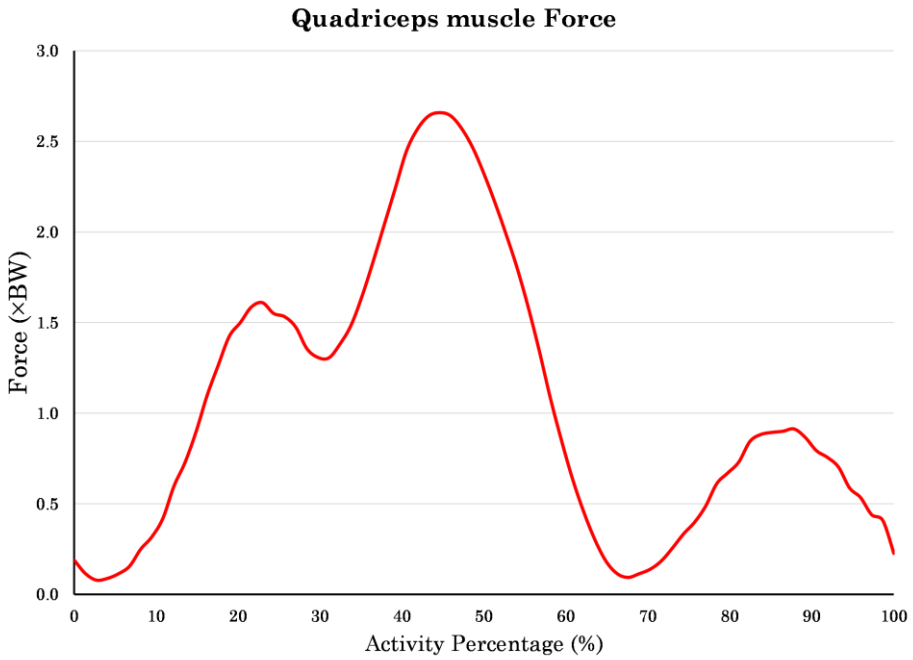


Figure 5-83: The quadriceps muscle force for a PCR TKA during gait activity.

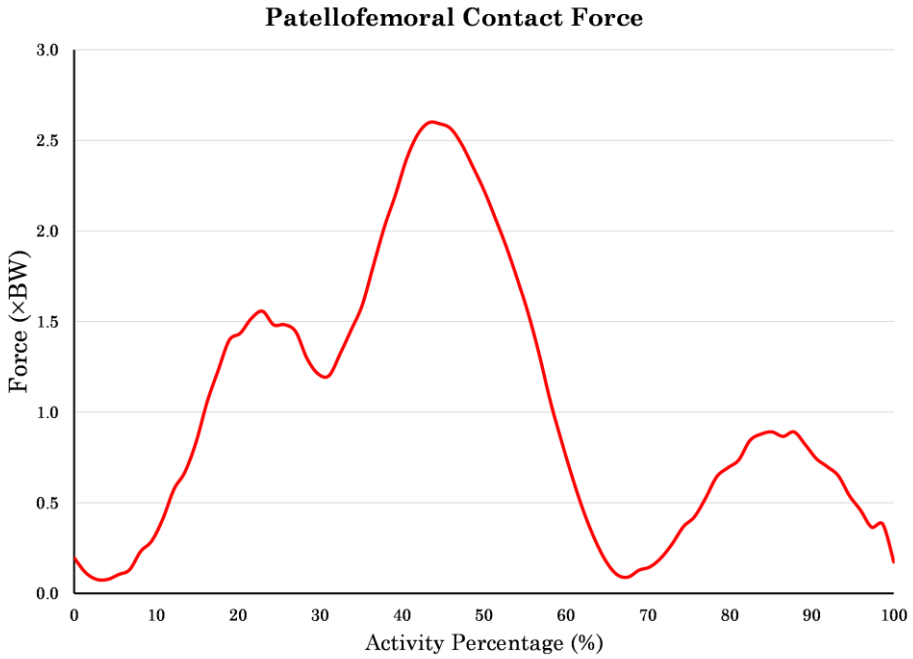


Figure 5-84: The patellofemoral contact force for a PCR TKA during gait activity.

The peak tibiofemoral contact force is about 3.7 × BW (Figure 5-89), the peak quadriceps muscle force is 5.3 × BW (Figure 5-90), and the peak patellofemoral force is 5.2 × BW (Figure 5-91). Compared to primary TKAs, the rotating-bearing hinge revealed significantly higher extensor mechanism forces due to high constraints in a revision TKA. The literature showed higher forces for the hinge design as well [164].

Normally in hinge designs, all the cruciate and collateral ligaments are resected, and hence the simulations performed for the hinge design were without any ligament forces applied at the knee joint. The function of these ligaments is to prevent the knee from excessive motion.

These ligaments apply interactive forces between the tibial and the femur. Hence, the lack of these ligaments can reduce the tibiofemoral contact force. The difference between the tibiofemoral contact force and the extensor mechanism force can be described with a lack of ligament forces for hinge design.

5.7.2 Fixed-bearing Hinge

To have a better understanding of the differences between the two revision TKA types, the results of the fixed-bearing hinge were compared to the rotating-bearing hinge design. The lateral condyle moved -2.8 mm posteriorly from full extension to the 80° of knee flexion, and from there to maximum knee flexion it moved anteriorly by 3.0 mm (Figure 5-92).

The medial condyle moved anteriorly from full extension to the maximum knee flexion about 4.6 mm (Figure 5-93). The femur externally rotates approximately 5.4° throughout the range of motion (Figure 5-94), and the pin rotates approximately 2.8° externally (Figure 5-95).

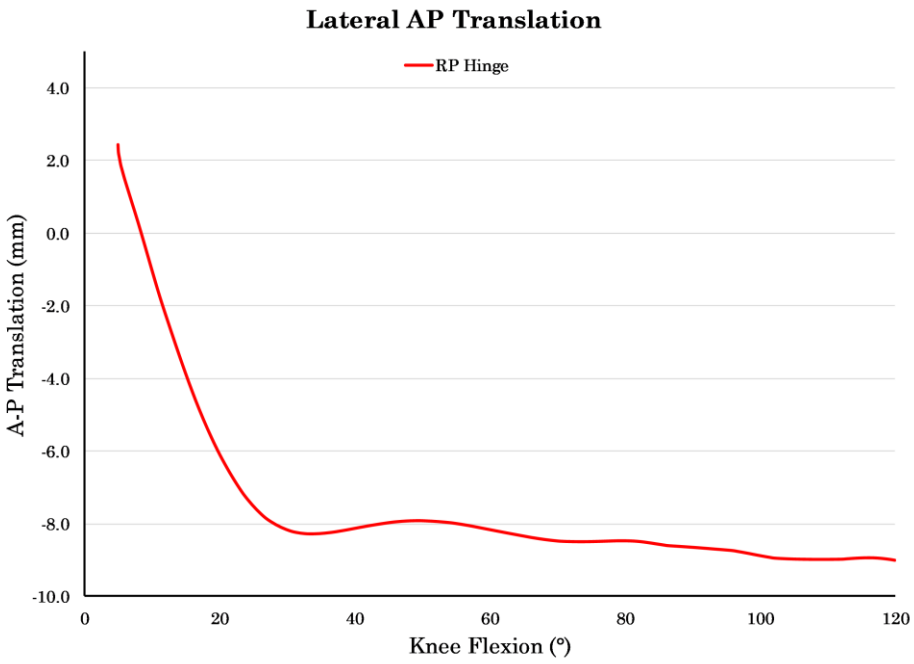


Figure 5-85: The lateral AP translation for the rotating bearing hinge design during the DKB activity.

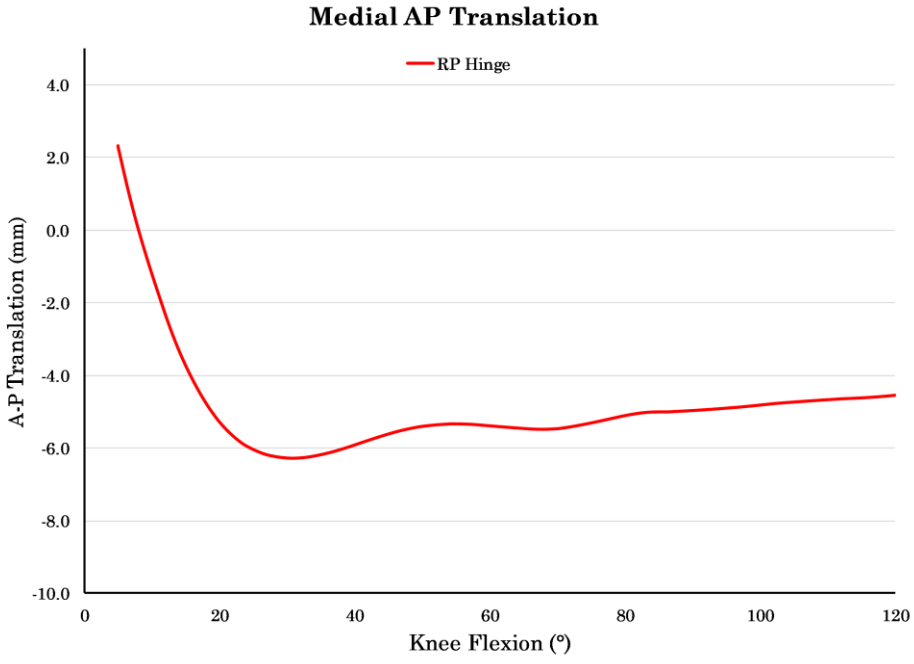


Figure 5-86: The medial AP translation for the rotating bearing hinge design during the DKB activity.

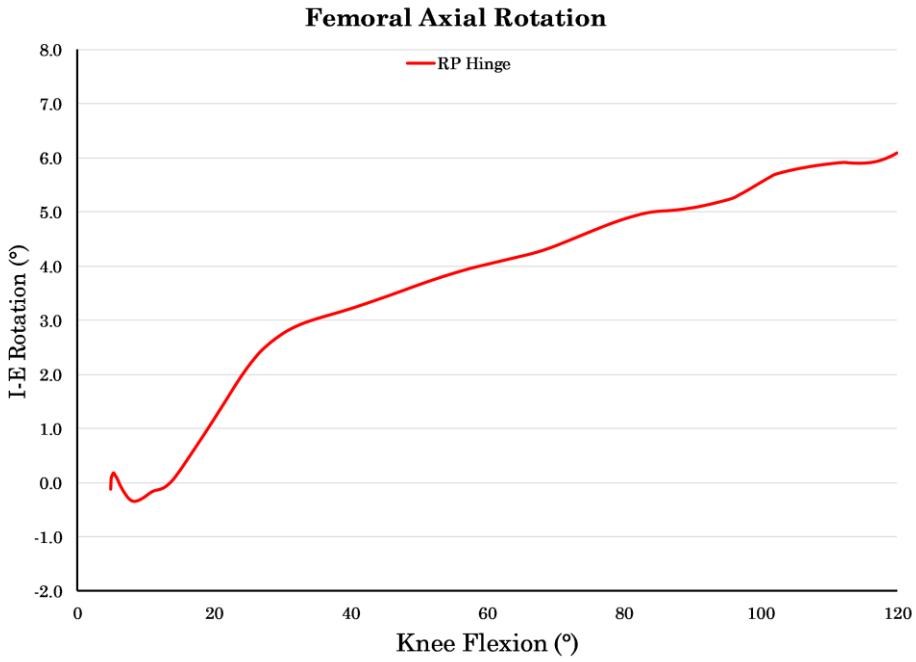


Figure 5-87: The femoral axial rotation for the rotating bearing hinge design during the DKB activity.

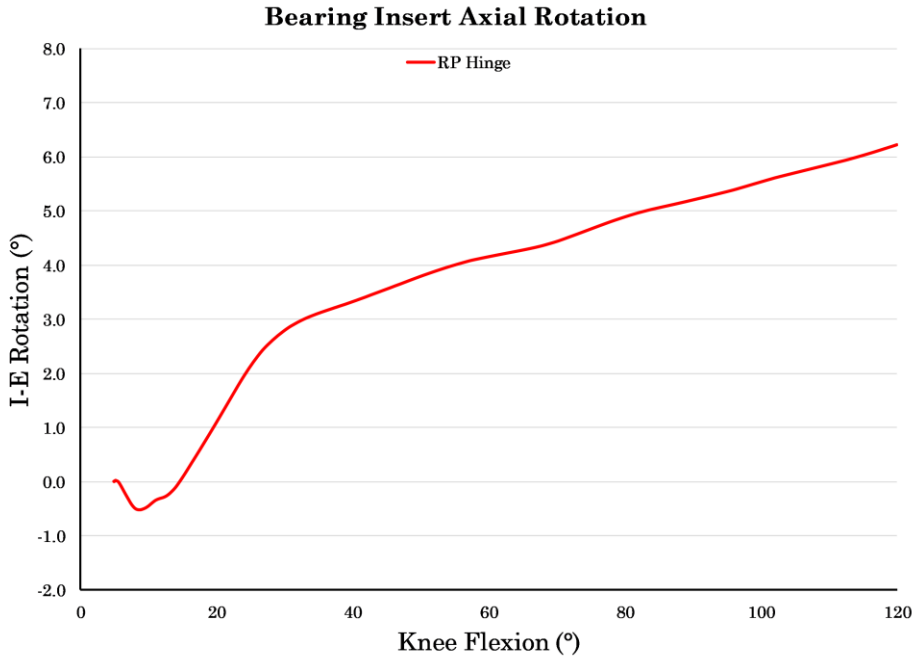


Figure 5-88: The bearing axial rotation relative to the tibial tray for the rotating bearing hinge design during the DKB activity.

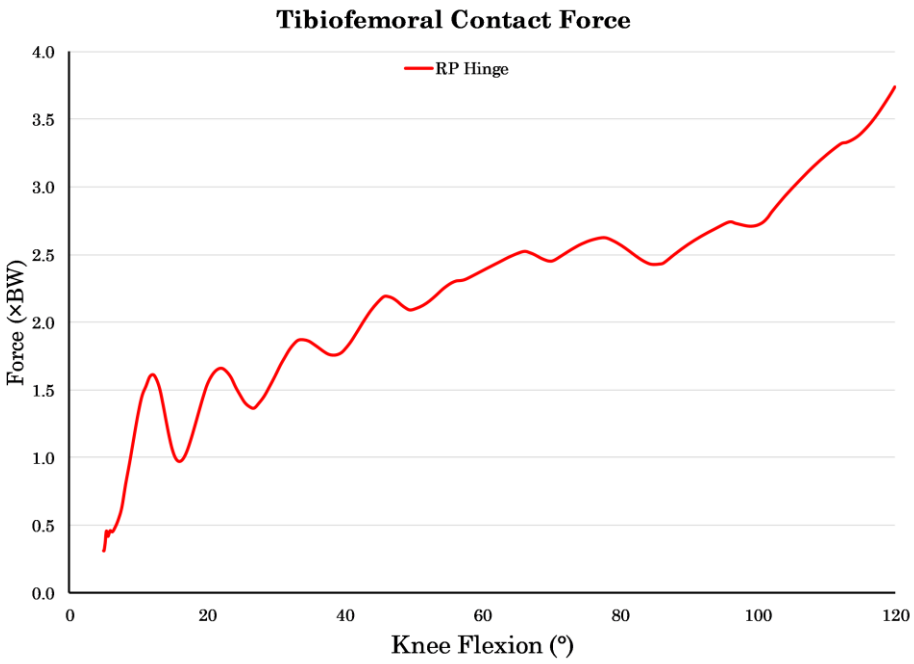


Figure 5-89: The tibiofemoral contact force for the rotating bearing hinge design during the DKB activity.

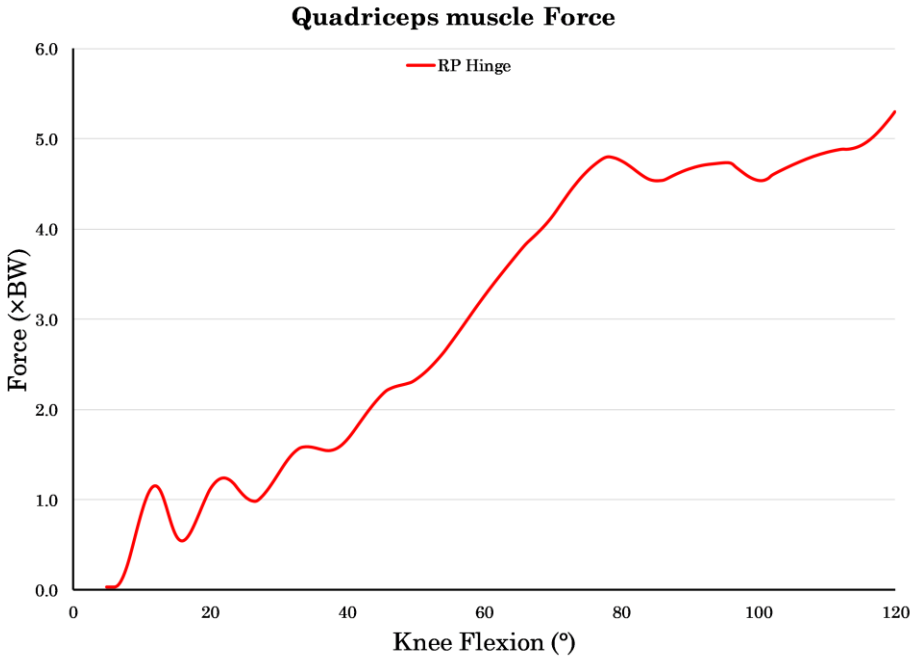


Figure 5-90: The quadriceps muscle force for the rotating bearing hinge design during the DKB activity.

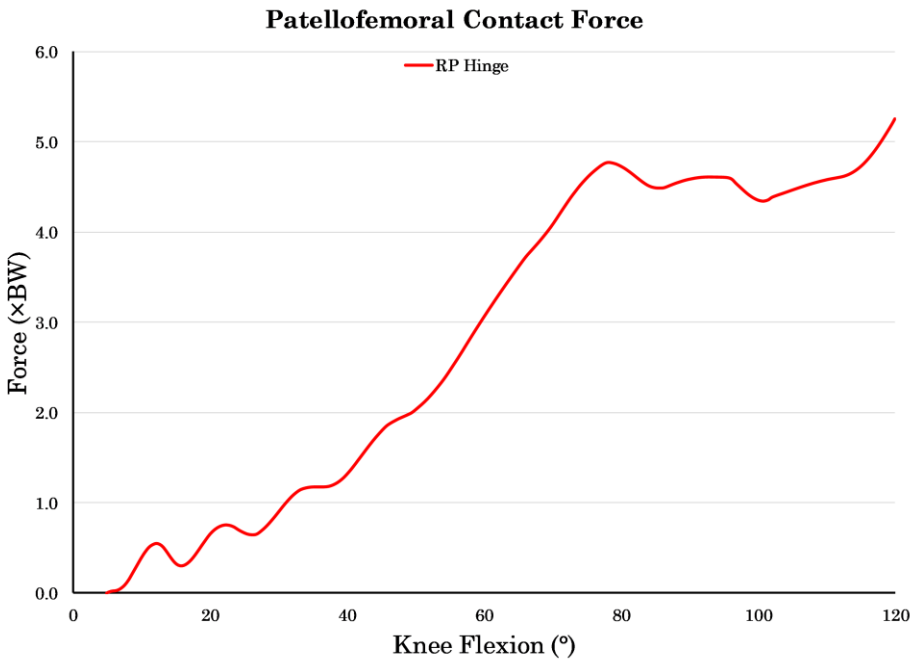


Figure 5-91: The patellofemoral contact force for the rotating bearing hinge design during the DKB activity.

Overall, the motion of the fixed-bearing design is limited compared to the rotating-bearing design. Both condyles translated posteriorly in the rotating-bearing design, while the lateral condyle exhibited anterior sliding in late flexion and the medial condyle exhibited paradoxical AP motion from extension to the maximum knee flexion for the fixed bearing design.

The femoral component external rotation was similar to the bearing rotation for the rotating-bearing design while the amount of external rotation for the femoral component was higher compared to the pin rotation for the fixed-bearing design.

The tibiofemoral contact force is slightly lower for the fixed-bearing design compared to the rotating-bearing design. The tibiofemoral contact force peak was 3.1 × BW (Figure 5-96).

The quadriceps muscle force was significantly lower for the fixed-bearing design, peaking at 3.2 × BW (Figure 5-97). Similarly, the patellofemoral force was also lower for the fixed-bearing design, peaking at about 4.0 × BW (Figure 5-98).

One reason for the observed differences in the extensor mechanism forces could be attributed to the more constraining nature of the rotating-bearing design. As described in the Methods section, the femoral component in the fixed-bearing hinge design has a J-curve radius and the interaction between the femoral component and the pin is designed to allow the femoral component to move in the SI direction inside the surfaces of the pin.

This freedom of the movement in the SI direction is possibly the main reason that the extensor mechanism forces are lower.

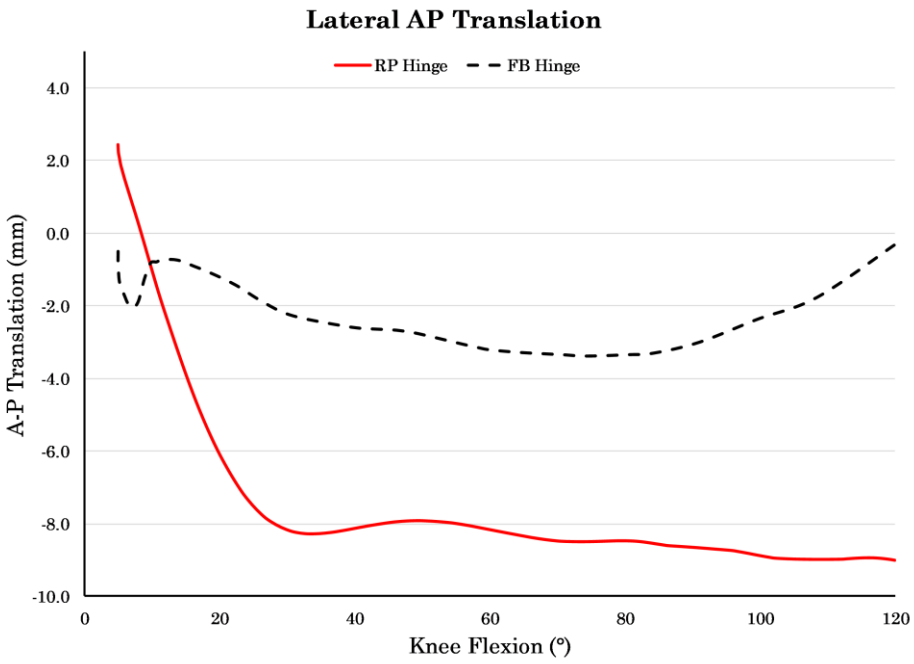


Figure 5-92: Comparison of the lateral AP translation between the rotating-bearing hinge (solid red) and the fixed-bearing hinge (dashed black).

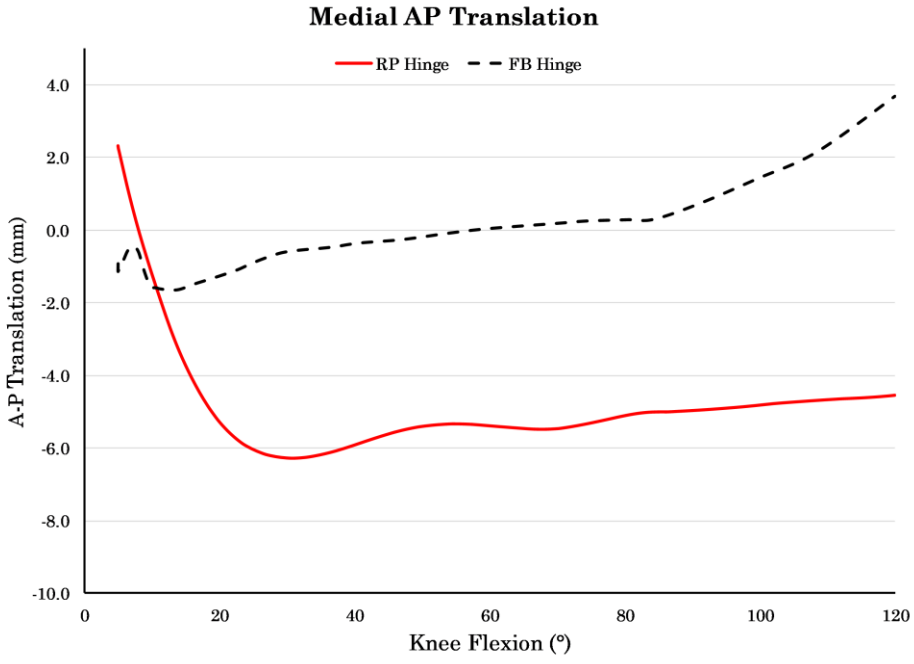


Figure 5-93: Comparison of the medial AP translation between the rotating-bearing hinge (solid red) and the fixed-bearing hinge (dashed black).

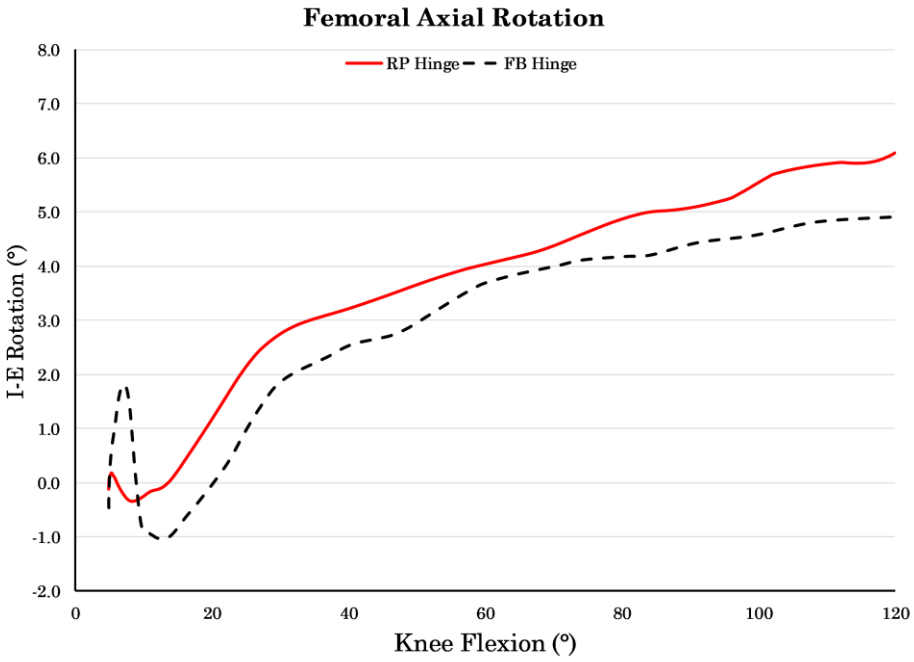


Figure 5-94: Comparison of the femoral axial rotation between the rotating-bearing hinge (solid red) and the fixed-bearing hinge (dashed black).

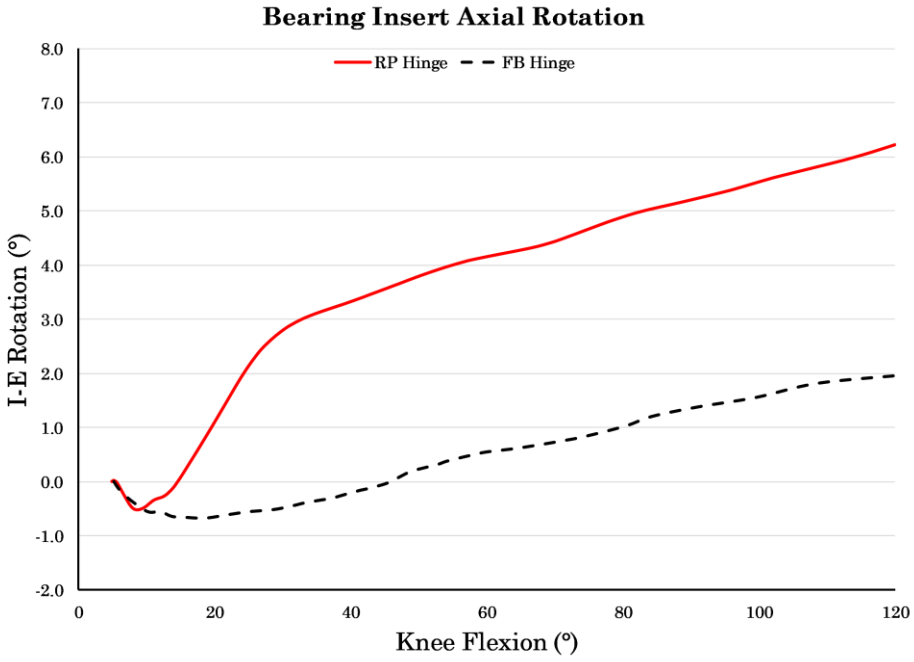


Figure 5-95: Comparison of the bearing axial rotation between the rotating-bearing hinge (solid red) and the fixed-bearing hinge (dashed black).

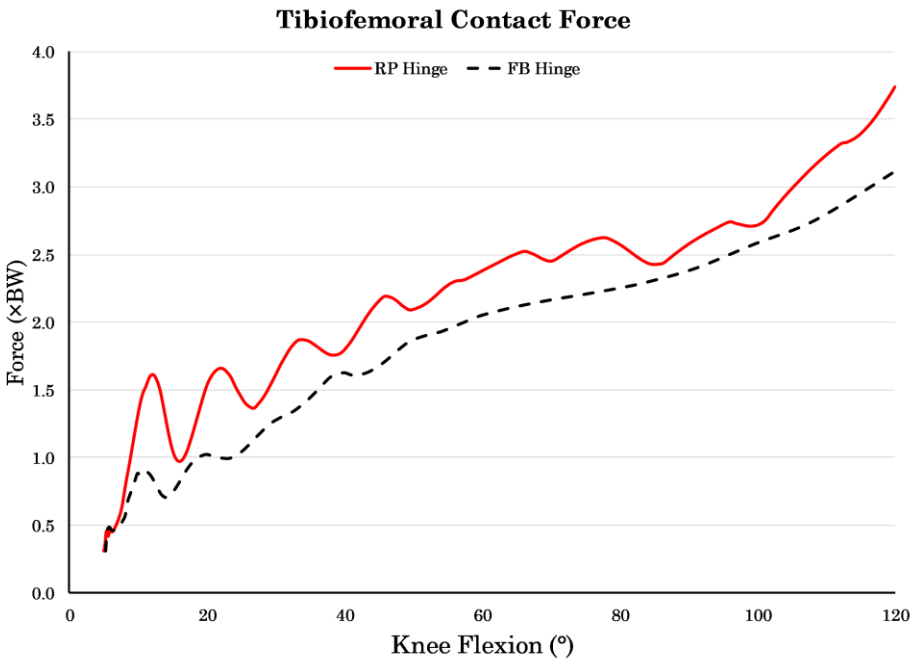


Figure 5-96: Comparison of the tibiofemoral contact force between the rotating-bearing hinge (solid red) and the fixed-bearing hinge (dashed black).

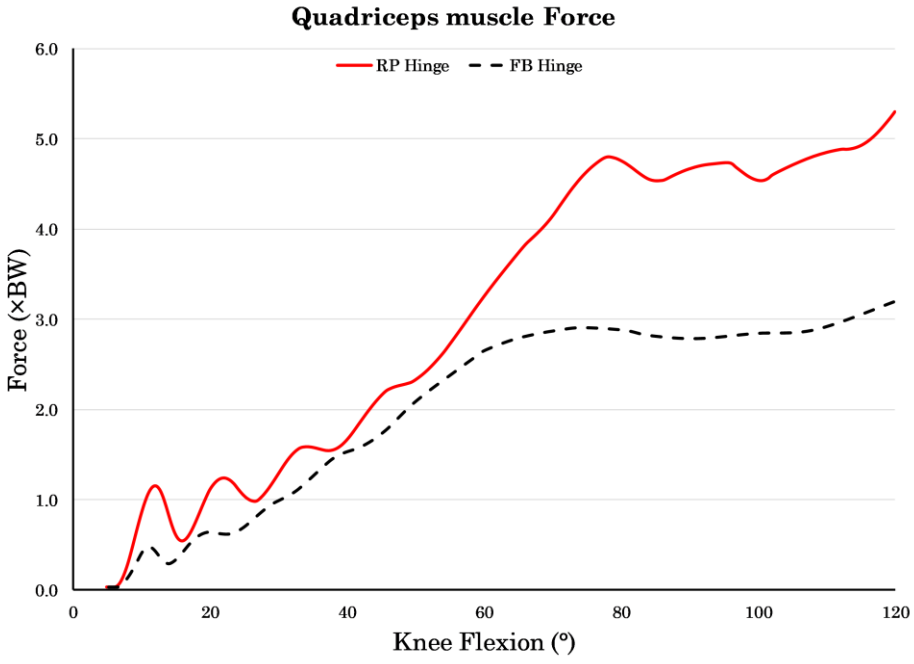


Figure 5-97: Comparison of the quadriceps muscle force between the rotating-bearing hinge (solid red) and the fixed-bearing hinge (dashed black).

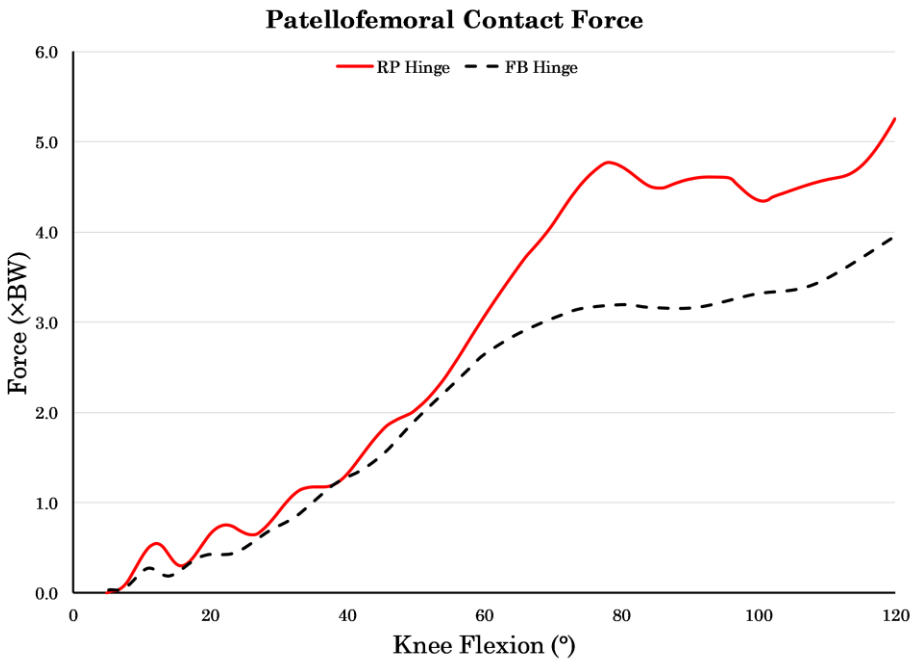


Figure 5-98: Comparison of the patellofemoral contact force between the rotating-bearing hinge (solid red) and the fixed-bearing hinge (dashed black).

5.8 Sensitivity Analysis

The forward solution model has been utilized to investigate the effects of various parameters, such as varying component alignment, surgical technique, and implant design feature by performing sensitivity analyses. The purpose of these analyses is twofold; first, to evaluate the FSM to determine if it is robust enough to perform activities under the various condition and if it is sensitive enough to determine the effects of these changes. Secondly, to have a baseline understating of how various surgical conditions or different implant features affect the outcomes of TKA. Whenever applicable, the results were compared to the literature.

5.8.1 Posterior Tibial Slope

The posterior tibial slope is defined as the angle between the tangent line on the tibial plateaus and a line perpendicular to the tibia mechanical axis. In the normal knee, the average anatomical posterior tibial slope is about 6° – 9° [180,181]. During the TKA procedure, surgeons try to incorporate a different posterior tibial slope by proximal tibial resection, and it has shown that a decrease in posterior tibial slope could decrease the maximum knee flexion [125].

For PCR TKA designs, surgeons try to mimic the natural posterior tibial slope and aim for 5° - 9° posterior slope. For the PS designs they usually use no slope (0°). Although the increase in posterior tibial slope is correlated with an increase in knee flexion, the significant increase in posterior tibial slope could result in abnormal kinematics and excessive wear on the polyethylene [182]. To investigate the effects of the posterior tibial slope, several posterior slopes, 0°, 2°, 4°, and 6°, were incorporated for a PCR TKA and an ACL substituting TKA.

5.8.1.1 PCR TKA

The lateral condyle position at full extension was -5.6 mm, -7.1 mm, -8.6 mm, and -9.9 mm for the 0°, 2°, 4°, and 6° slopes, respectively. The maximum amount of lateral condyle rollback was -2.2 mm, -1.7 mm, -1.3 mm, and -1.1 mm for the 0°, 2°, 4°, and 6° slopes, respectively (Figure 5-99). Similar to the lateral condyle, by increasing the posterior slope the medial condyle is positioned more posteriorly, -7.3 mm, -8.7 mm, -10.0 mm, and -11.3 mm from 0° to 6° posterior slopes, respectively (Figure 5-100). The medial condyle sides anteriorly about 2.0 mm, 2.2 mm, 2.6 mm, and 3.0 mm for 0°, 2°, 4°, and 6° slopes, respectively. Overall, increasing the posterior slope does not seem to have meaningful effects on the femoral axial rotation (Figure 5-101).

The tibiofemoral contact forces are slightly decreased by increasing the posterior tibial slope (Figure 5-102), although the difference is insignificant. The quadriceps muscle force, on the other hand, increases by increasing the posterior tibial slope. Again, the differences are insignificant (Figure 5-103).

Overall, increasing the posterior slope decreased the posterior femoral rollback, although the difference is about 1 mm. However, by increasing the posterior tibial slope, the femoral condyles remain more posteriorly on the bearing plateaus. The more posterior position of the femur throughout the flexion range means that there is less likelihood for bearing insert impingement with the femur, which radiographic analyses have shown [183]. Positioned more posteriorly means that the PCL ligament has less tension and therefore lower forces (Figure 5-104). The reduction in the femoral rollback can be explained by the fact that the PCL forces are lower and therefore there is lower forces to pull back the femur on top of the tibia. A similar pattern has been reported in the literature for the effects of the posterior tibial slope for AP translations, contact forces, and PCL forces [184,185].

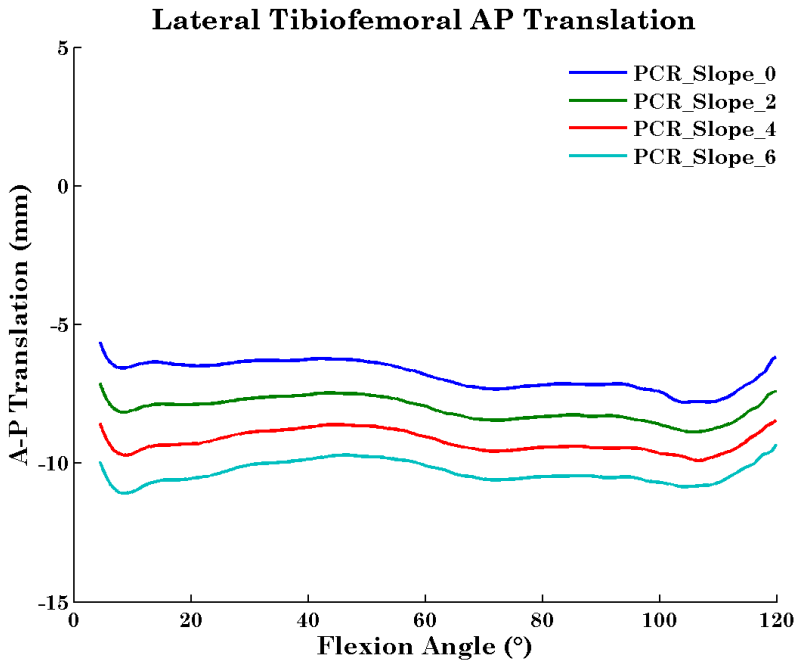


Figure 5-99: Comparison of the lateral AP translation between different posterior tibial slopes for a PCR TKA.

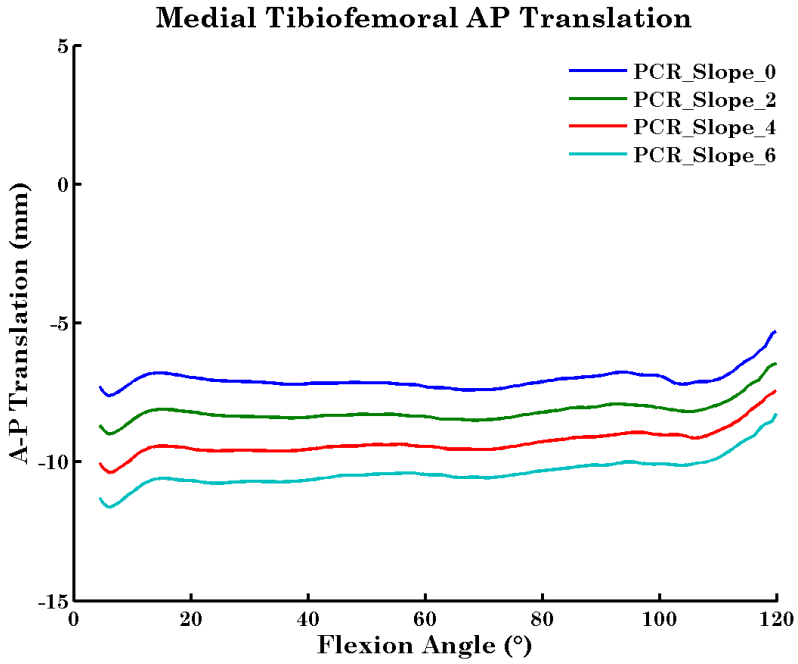


Figure 5-100: Comparison of the medial AP translation between different posterior tibial slopes for a PCR TKA.

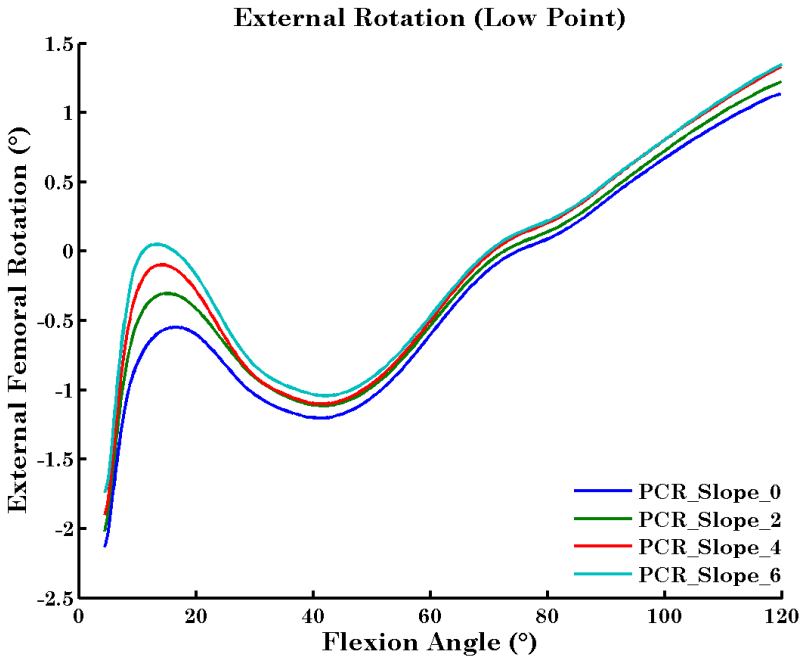


Figure 5-101: Comparison of the femoral axial rotation between different posterior tibial slopes for a PCR TKA.

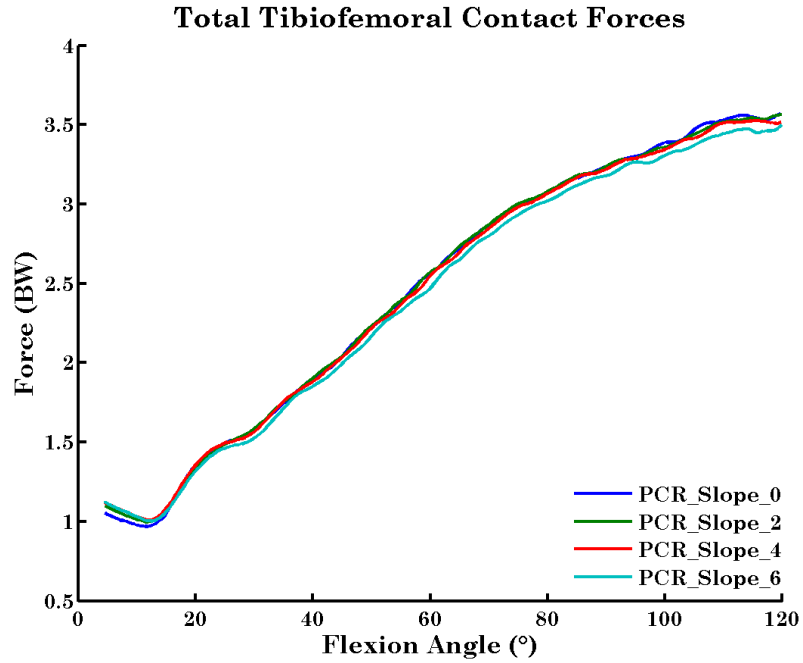


Figure 5-102: Comparison of the tibiofemoral contact force between different posterior tibial slopes for a PCR TKA.

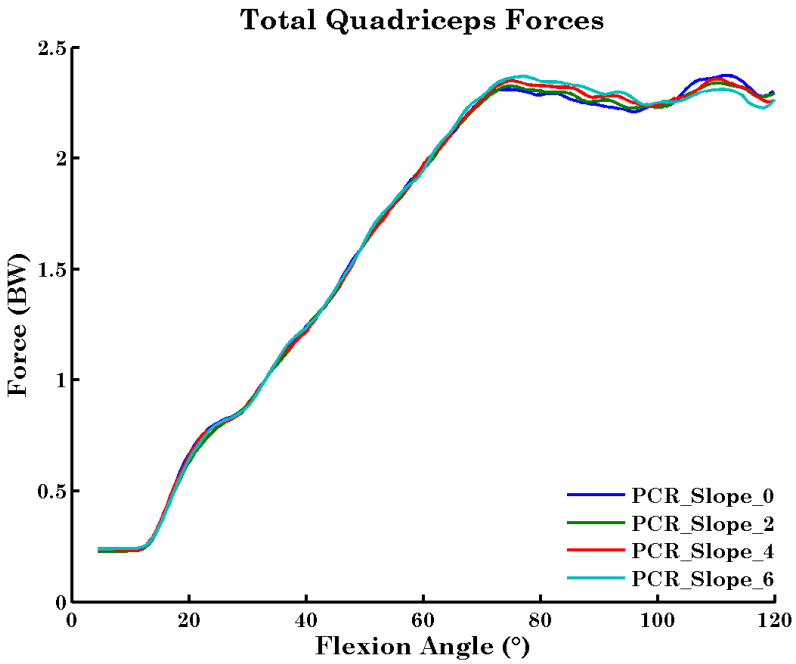


Figure 5-103: Comparison of the quadriceps muscle force between different posterior tibial slopes for a PCR TKA.

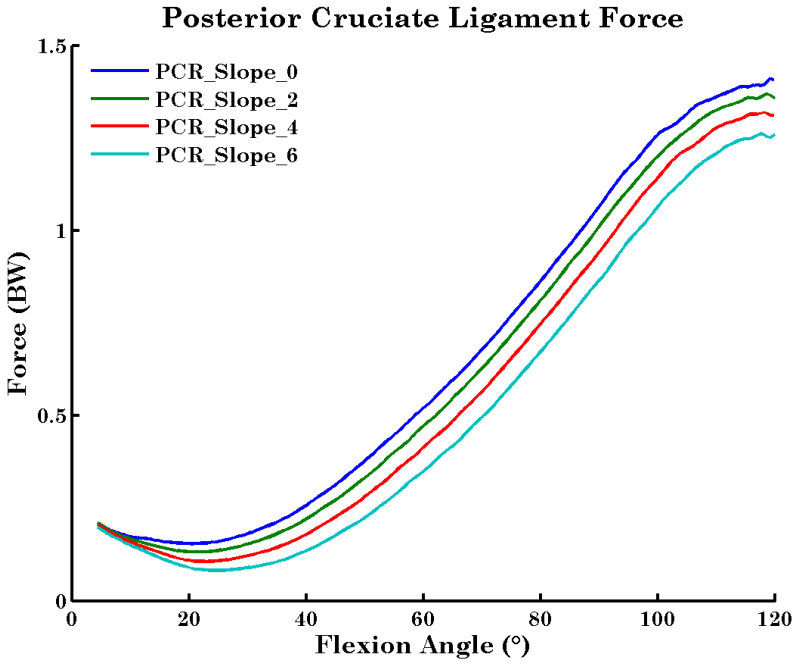


Figure 5-104: Comparison of the PCL ligament force between different posterior tibial slopes for a PCR TKA.

5.8.1.2 ACL Substituting

In PCR TKA design evaluations, increasing the posterior slope moved the femoral condyles more posterior. In the ACL substituting design the femoral condyles position does not change significantly by increasing the posterior slope. This is the effect of the anterior cam/post design of these types of TKA, which prevents the femur from seating excessively posterior at full extension. This can be observed by investigating the cam/post mechanism contact force. Higher posterior slopes did increase the cam/post contact forces (Figure 5-105), albeit much less than PS TKA having a posterior cam/post mechanism. The anterior cam/post is a design developed to replicate the functionality of the ACL and provide a screw-home mechanism similar to the normal knee, in which the femur internally rotates relative to the tibia at full extension. The lateral femoral condyle exhibits more rollback with increasing slope. The lateral rollback was -6.5 mm, -7.3 mm, -8.1 mm, and -8.5 mm for the 0°, 2°, 4°, and 6° slopes, respectively (Figure 5-106). The medial condyle experienced a similar pattern. The medial condyle translated about 0.5 mm anteriorly for 0° slope and -1.1 mm, -1.8 mm, and -2.1 mm posteriorly for 2°, 4°, and 6° slopes, respectively (Figure 5-107). Since both condyles moved posteriorly by increasing the slope, there was not a substantial difference in the femoral axial rotation. The femoral axial rotation increased from 7.5° to 8.1° from 0° tibial slope to 6° tibial slope (Figure 5-108).

The tibiofemoral contact forces were lower for higher posterior slopes. The peak tibiofemoral contact forces were 3.52 × BW, 3.44 × BW, 3.34 × BW, and 3.25 × BW from lower to higher posterior slopes, respectively (Figure 5-109). The quadriceps muscle forces were slightly higher for higher posterior slopes (Figure 5-110). And similar to the PCR TKA design, the PCL forces were decreased by increasing the posterior tibial slope (Figure 5-111).

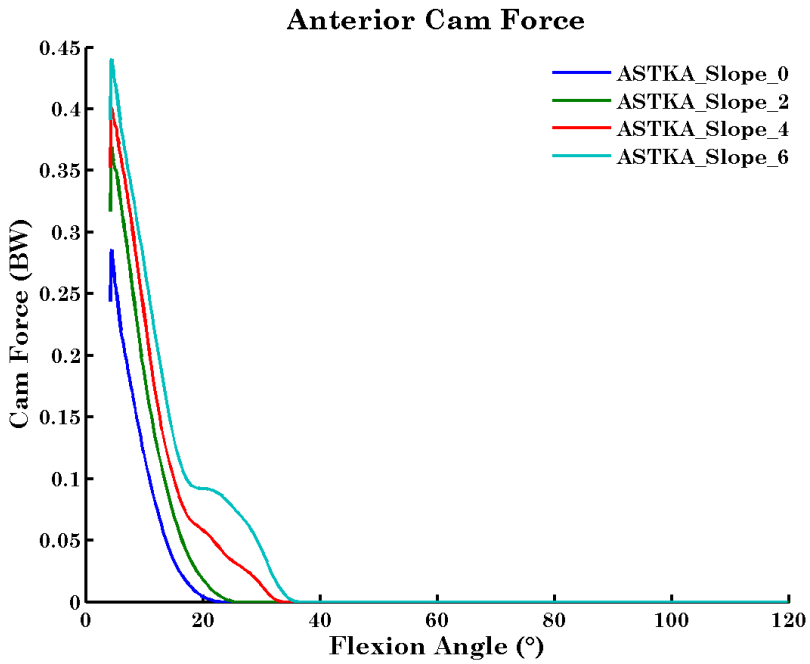


Figure 5-105: Comparison of the anterior cam/post contact force between different posterior tibial slopes for an ACL substituting TKA.

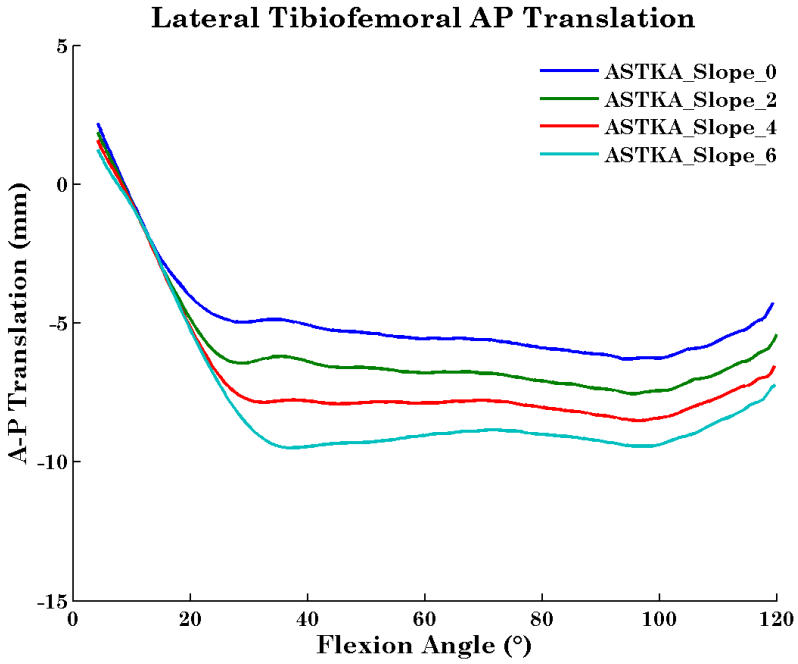


Figure 5-106: Comparison of the lateral AP translation between different posterior tibial slopes for an ACL substituting TKA.

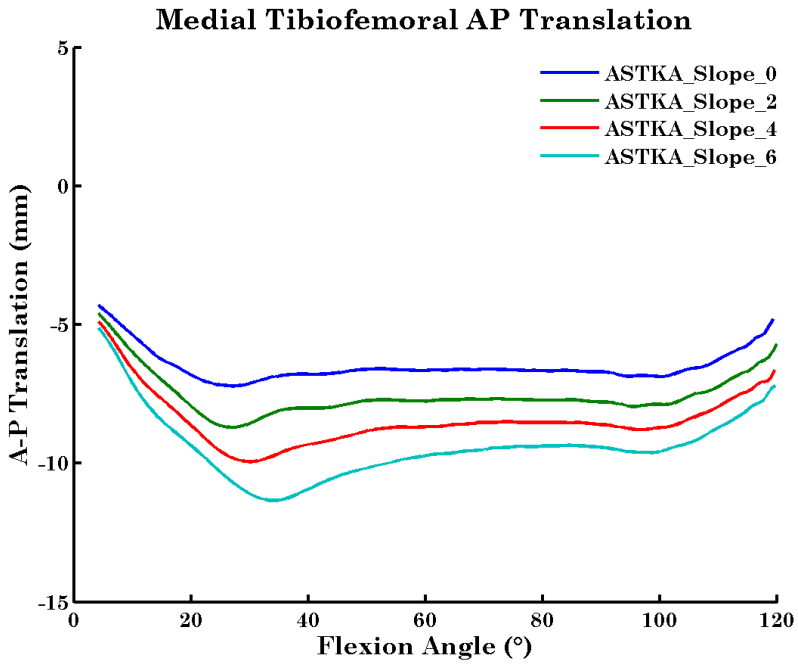


Figure 5-107: Comparison of the medial AP translation between different posterior tibial slopes for an ACL substituting TKA.

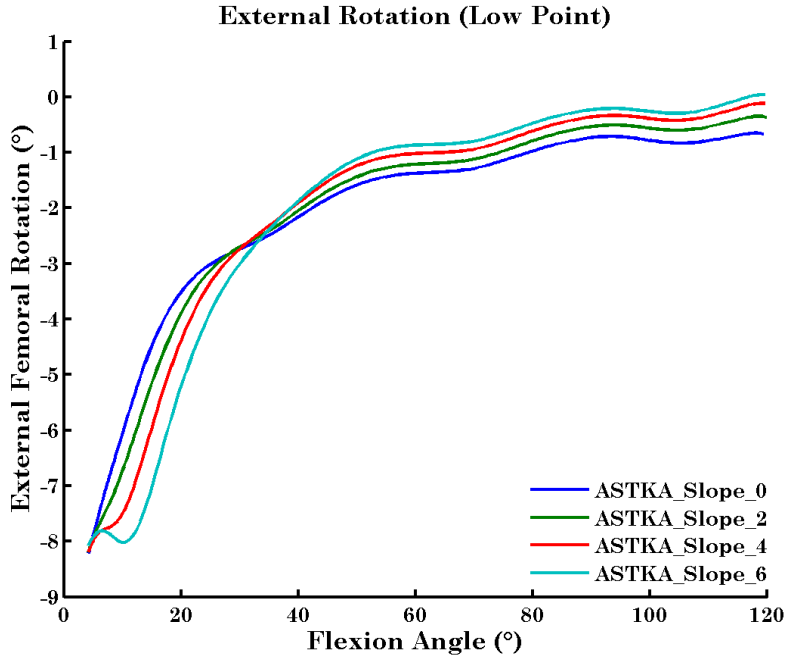


Figure 5-108: Comparison of the femoral axial rotation between different posterior tibial slopes for an ACL substituting TKA.

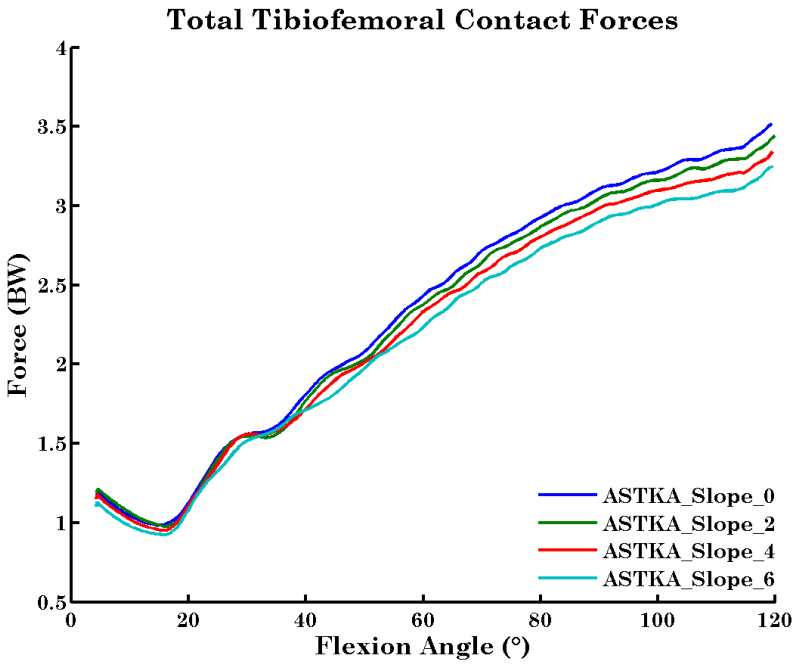


Figure 5-109: Comparison of the tibiofemoral contact force between different posterior tibial slopes for an ACL substituting TKA.

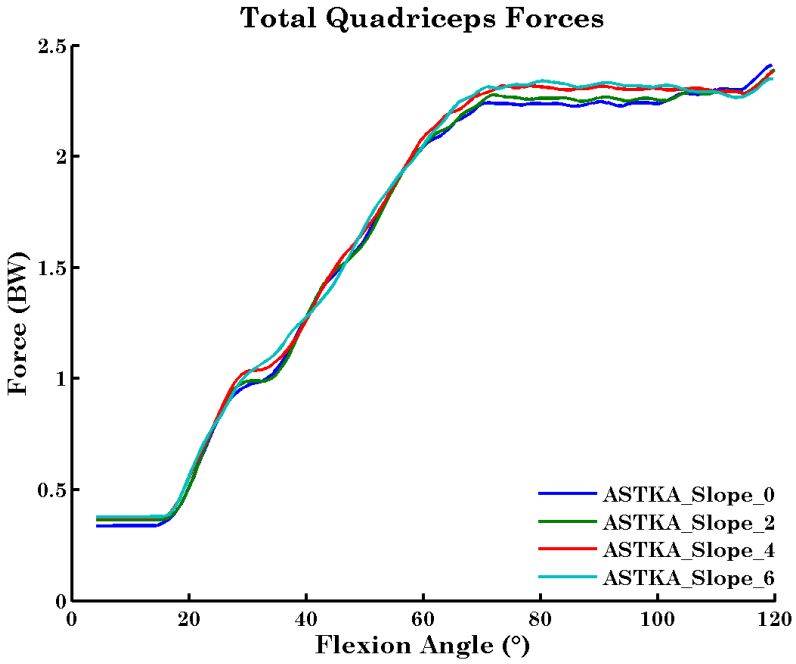


Figure 5-110: Comparison of the quadriceps muscle force between different posterior tibial slopes for an ACL substituting TKA.

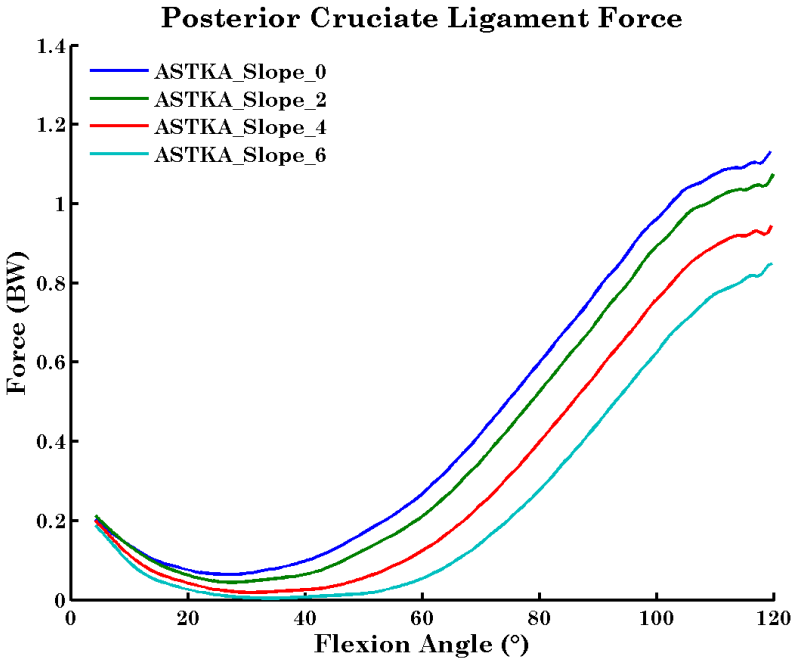


Figure 5-111: Comparison of the PCL ligament force between different posterior tibial slopes for an ACL substituting TKA.

5.8.2 Initial Placement

Using the forward solution model, the effect of the implant placement on TKA outcome were investigated. The use of mathematical models have document that component placement can play a role in kinematics and kinetics of TKA [164,186]. The effects of femoral component axial rotation at the full extension on the TKA outcome were therefore investigated. Three theoretical patients with a PCR TKA were created in the FSM with different femoral axial rotation values the full extension (Figure 5-112).

A default rotation for a PCR where the femoral component was internally rotated (the lateral condyle is more anterior than the medial condyle), and then externally rotated (the lateral condyle is more posterior than the medial condyle) were evaluated. The patella position is kept consistent with the femoral component.

The PCR TKA with the internal femoral component achieves greater overall external rotation, 4.6° compared to 3.1°, and 0.9° external rotation for the default and externally rotated PCR TKAs (Figure 5-113). This finding is consistent with the fluoroscopic results from our previous studies. 1100 TKA subjects were categorized into two groups with internal or external initial axial femoral component rotation. The internally rotated group achieved significantly higher overall axial rotation, 6.9° compared to 4.4° for the externally rotated group. Also, the internally rotated group experienced significantly higher maximum weight-bearing flexion, 108.1° compared to 105.5° for externally rotated group (Table 5-2).

These findings in these results can be explained by the effects of the soft tissues. In an externally rotated TKA, the MCL is tighter, and higher MCL forces prevent the medial condyle from sliding anteriorly and therefore reduces the overall external rotation (Figure 5-114). Additionally, due to the different

orientation of the femur relative to the tibial, the tension in the PCL is also different (Figure 5-115).

The PCL forces are higher for the internally rotated PCR, which can induce more rollback. Another interesting finding is the higher patellofemoral contact force for the externally rotated PCR, 2.5 × BW, compared to 2.4 × BW for the internally rotated PCR (Figure 5-116).

This finding may explain why subjects with externally rotated femurs achieve lower weight-bearing flexion. Increased patellofemoral contact forces can result in anterior knee pain and prevent a patient from flexing their knee further.

5.8.3 Patella Baja

A sensitivity analysis was performed for PCR and PS implants based on the patella position. For each TKA design, three simulations were created based on the Blackburne-Peel index [187]: a control, a patella baja, and a patella alta (Figure 5-117). The knee joint outcomes were compared for these groups.

The presented mathematical model is sensitive to both initial conditions and TKA designs. The results of the sensitivity analysis revealed that extensor mechanism forces increase for patella alta compared to normal position and patella baja for both a PCR and PS design. These results are in agreement with previously reported kinetics [164] and can be attributed to increased patellar ligament tension (Figure 5-118).

In patella alta, the increased height of the patella increases the tension in the patellar ligament and thus increases patellofemoral contact forces. This is even more evident in higher flexion angles where the patellar ligament is no longer in an almost vertical orientation. In these higher flexion angles, an increase in patellar ligament force results in an increase in patellofemoral contact force.

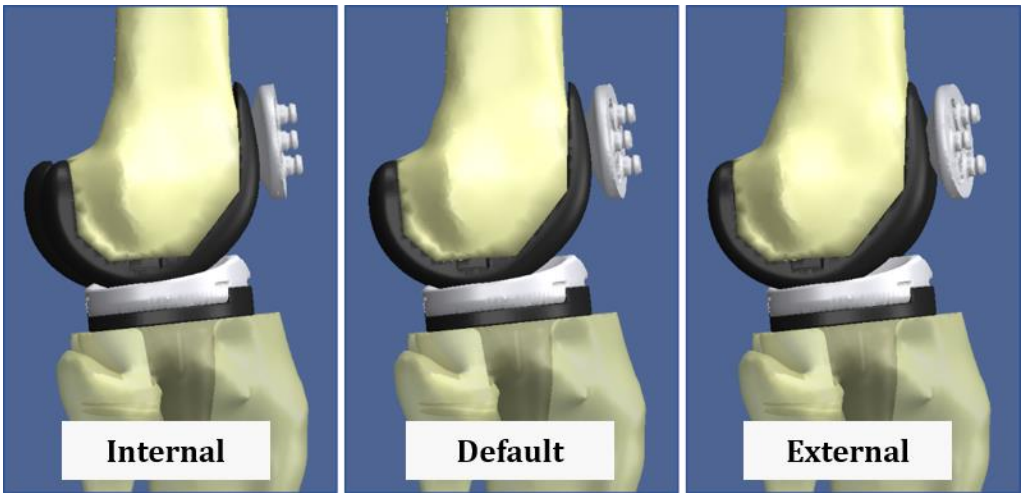


Figure 5-112: Three theoretical PCR TKA patients were created with different femoral component orientations at the full extension.

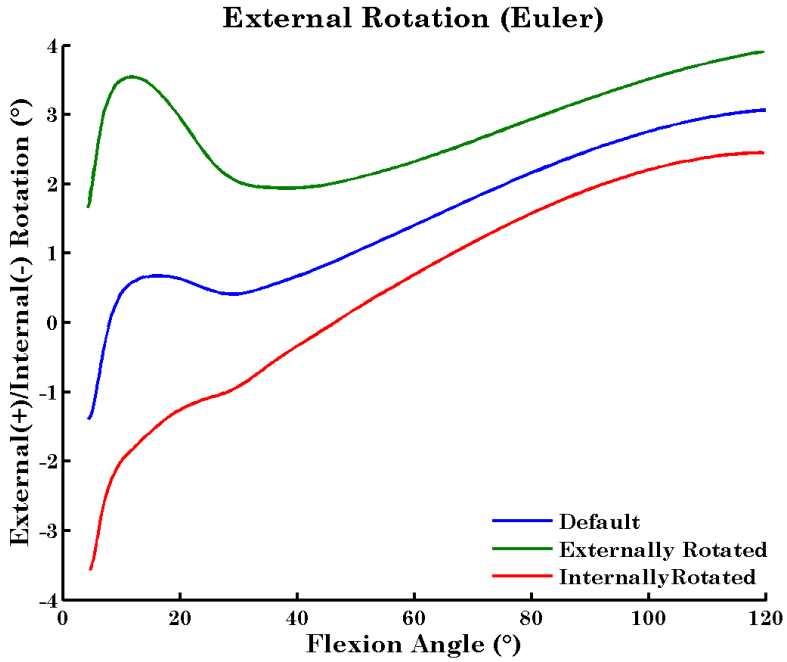


Figure 5-113: Comparison between the femoral axial rotation between the reference PCR (blue), the externally rotated PCR (green), and the internally rotated PCR (red).

Table 5-2: The average femora axial rotation and maximum weight-bearing flexion for subjects with initial internal or external femoral component rotation.

	Number	External Rotation	Max. Flexion
Int. Rotated	438	6.9 ± 5.9	108.1 ± 15.8
Ext. Rotated	673	4.4 ± 5.5	105.5 ± 16.7
P-value		<0.0001*	0.005*

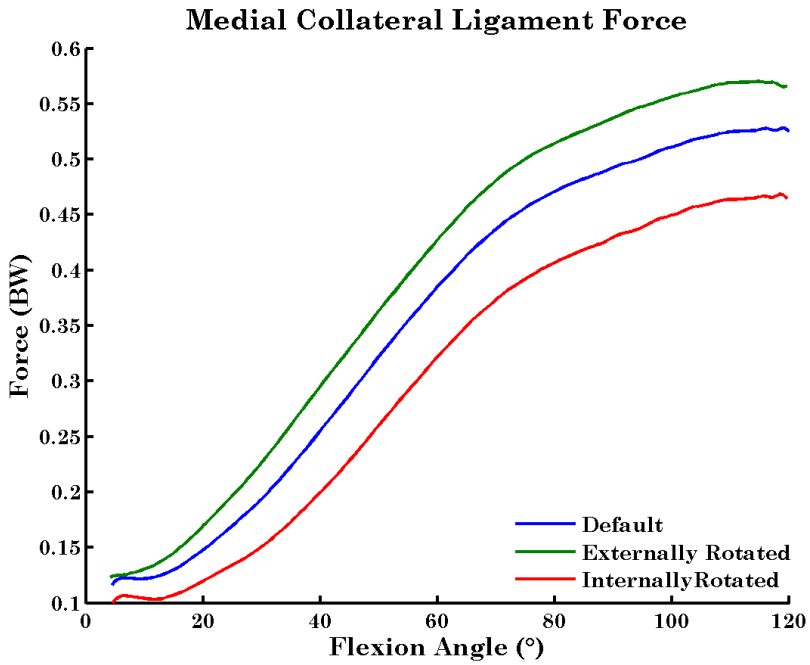


Figure 5-114: Comparison between the MCL ligament force between the reference PCR (blue), the externally rotated PCR (green), and the internally rotated PCR (red).

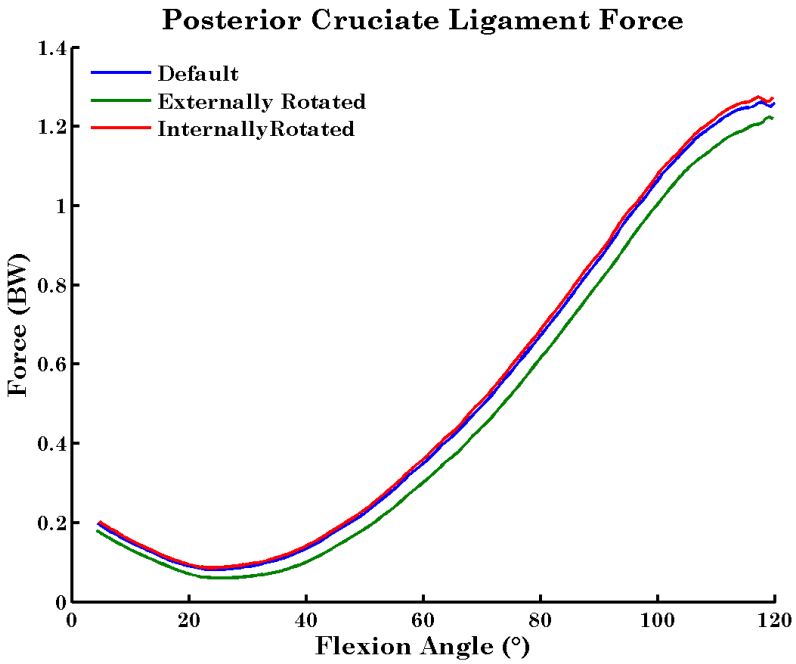


Figure 5-115: Comparison between the PCL ligament force between the reference PCR (blue), the externally rotated PCR (green), and the internally rotated PCR (red).

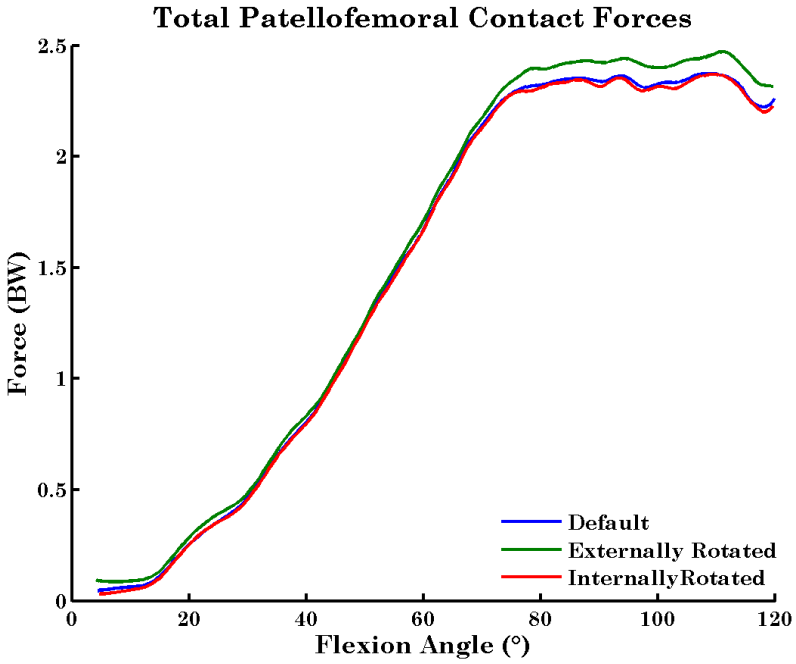


Figure 5-116: Comparison between the patellofemoral contact force between the reference PCR (blue), the externally rotated PCR (green), and the internally rotated PCR (red).

Moreover, the current mathematical model revealed that the peak patellofemoral force and trend for a PS and a PCR TKA are different (Figure 5-119). Several studies have investigated the patellofemoral contact force for different implants and showed that the patellofemoral force is indeed different for various implant types [9,10,164].

The interesting finding is that the extensor mechanism forces in the PCR TKA were lower compared to the PS TKA, while the tibiofemoral contact forces were higher in the PCR TKA. This can be described by the different features of each design. The most distinct difference in force profiles between these two designs is when the cam and post engage in the PS design or the PCL starts firing in the PCR design (Figure 5-120).

The PCL force of approximately 640 N at 90° of flexion and peak force of 1.25 × BW (940 N) at maximum knee flexion is consistent with the literature [185,188]. Since the interactive contact force between cam and post is in A-P direction, the extensor mechanism forces are higher for the PS design. While in the PCR design, the PCL is nearly vertical after mid-flexion, and therefore the increase in PCL tension increases the tibiofemoral contact forces (Figure 5-121).

The tibiofemoral contact forces in the PCR design increase with flexion while forces in the PS design increase with flexion up to about 80° of flexion and then decrease afterwards, when the femoral component starts rolling back on the bearing insert after cam and post engagement. Several studies have shown that increased rollback decreases the contact forces [170,171]. This finding is likely due to the fact that increased rollback increases the extensor mechanism moment arm and therefore lowers the forces.

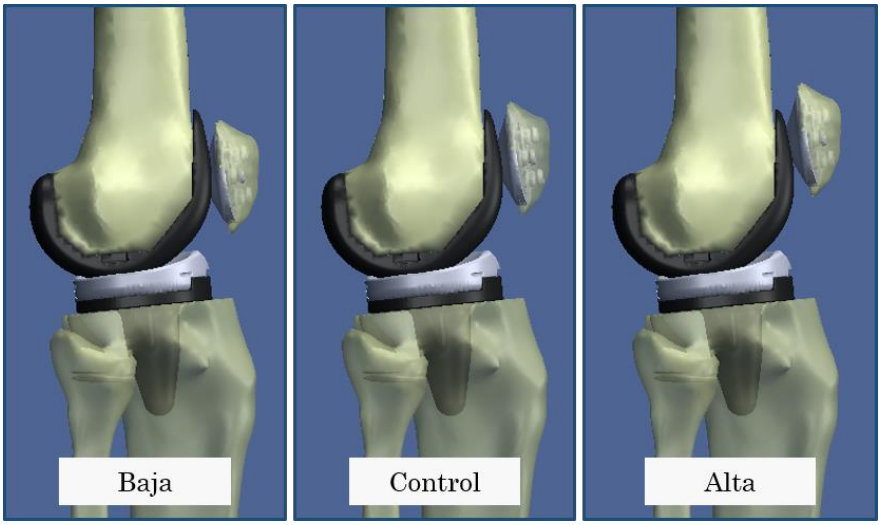


Figure 5-117: Three simulations were created using the FSM to investigate the effects of patella positioning on TKA outcomes.

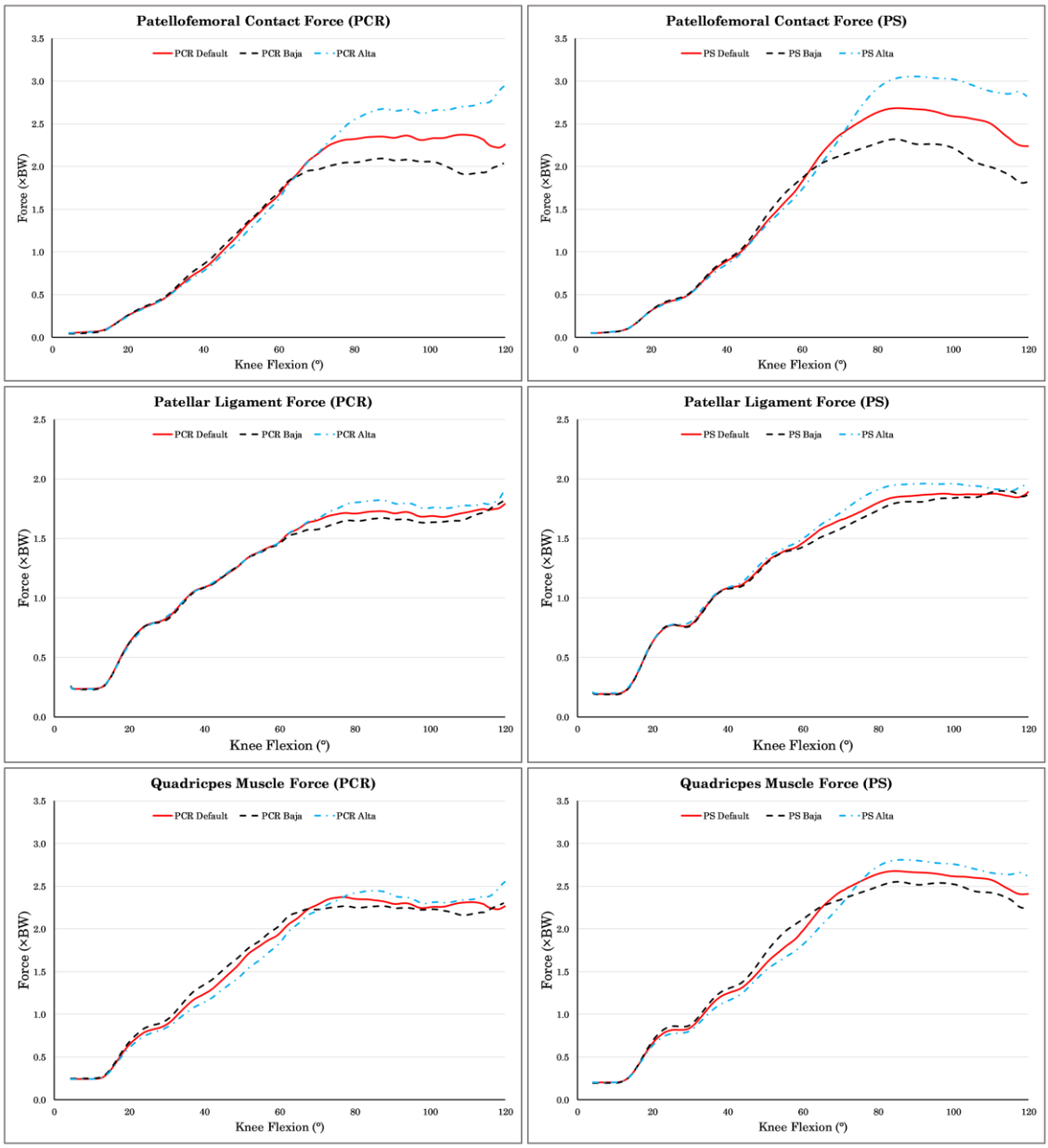


Figure 5-118: The sensitivity analysis of the patella baja (dashed black), the patella alta (dash-dotted blue), and the reference (solid red). The left graphs show the extensor mechanism forces for the PCR design, and the right graphs are for the PS design.

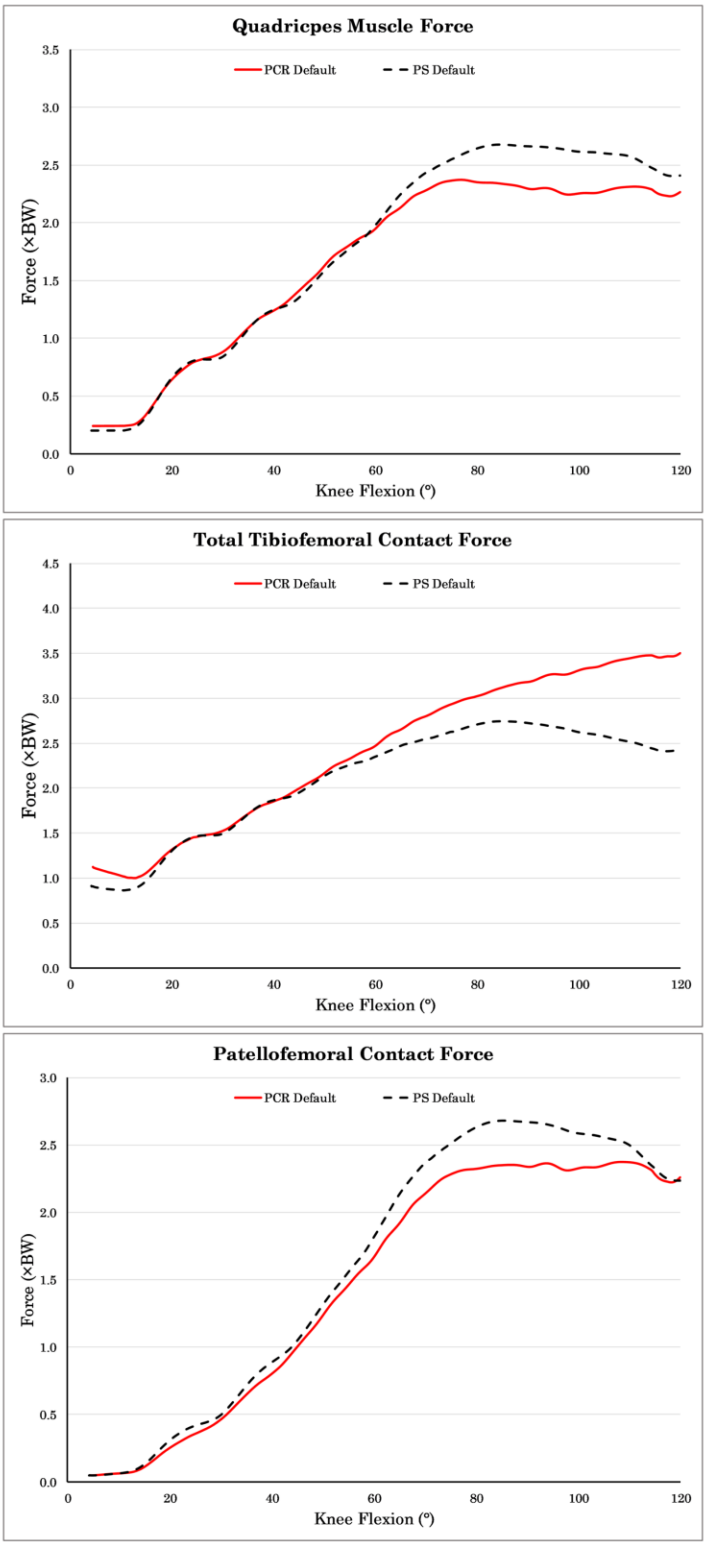


Figure 5-119: Comparison between the quadriceps force (top), tibiofemoral contact force (middle), and the patellofemoral force (bottom) for the PCR (solid red) and the PS (dashed black) designs.

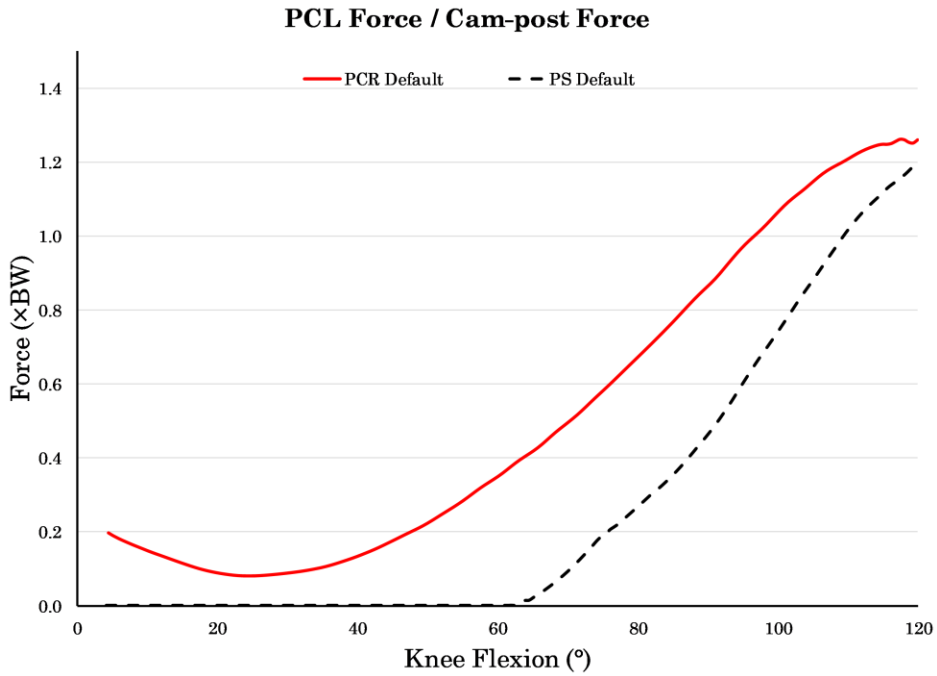


Figure 5-120: Comparison in the PCL force in the PCR design (solid red) with the cam-post force in the PS design (dashed black).

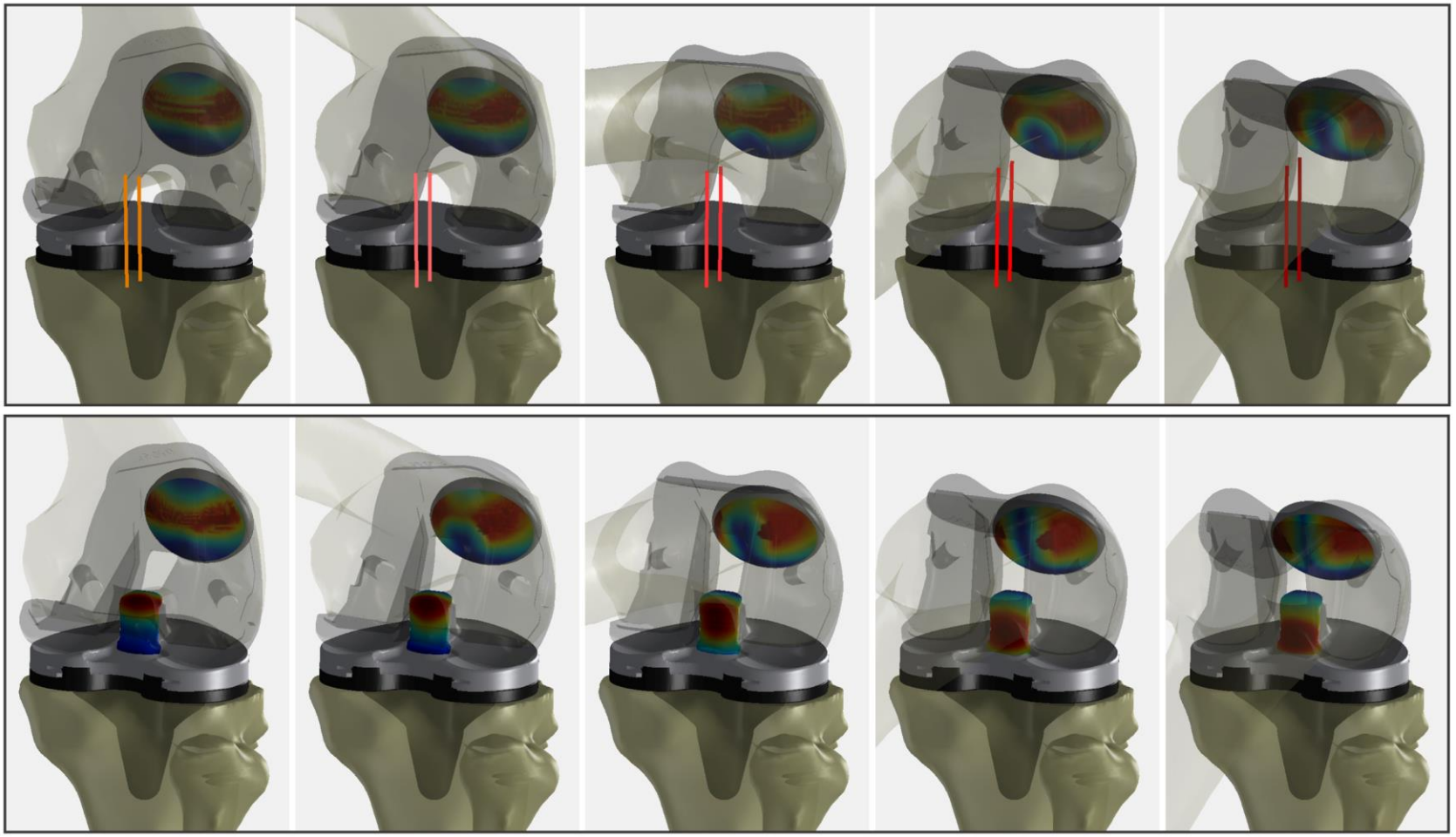


Figure 5-121: The PCL is almost in the vertical direction in mid to late flexion and therefore the PCL forces is more in the SI direction (top) and cam/post mechanism forces is applied in the AP direction (bottom).

5.8.4 Bearing Insert Conformity

To assess the viability of the model to investigate various TKA design parameters, the effects of the sagittal conformity of the lateral and medial plateaus of bearing insert were investigated. Using the GUI, sagittal conformity of the medial plateau of a PS TKA was altered (Figure 5-122) by adjusting the appropriate coefficients of the surface polynomial representing the polyethylene. The TKA outcomes were compared for increased, decreased, and baseline conformity.

Overall, adjusting the surface polynomial to increase medial plateau conformity reduces the mid-flexion medial condylar translation before cam-post engagement. From full extension to approximately 70° of knee flexion, the medial condyle stayed relatively constant for the increased conformity medial plateau design, while it translated anteriorly about 1.8 mm and 3.9 mm for the control and decreased conformity medial plateau designs, respectively (Figure 5-123). After cam-post engagement to maximum knee flexion, the MAP was -4.6 mm, -5.7 mm, and -3.8 mm for control, increased conformity, and decreased conformity designs, respectively (Figure 5-123). The lateral condyle rollback was -9.6 mm, -10.5 mm, -8.0 mm for control, increased conformity, and decreased conformity designs, respectively (Figure 5-123). The cam-post started engaging earlier for the increased medial conformity design at 64° compared to 67° and 70° of flexion for control and decreased medial conformity designs, respectively. The maximum cam-post mechanism force was 1.37×BW, 1.68×BW, and 1.18×BW for control, increased conformity, and decreased conformity designs, respectively (Figure 5-123). Although the tibiofemoral forces were similar for all three designs, the increased conformity design experienced a slightly higher tibiofemoral contact force, peaking at 3.13 ×BW compared to 3.0×BW contact force other two designs, but revealed higher cam-post forces with increased medial conformity (Figure 5-123).

In normal knee, both condyles move posteriorly with increasing flexion, but the medial condyle exhibits minimal rollback compared to the lateral condyle. Some TKA's are designed to minimize medial condyle motion. Furthermore paradoxical anterior sliding is believed to have negative effects of TKA outcomes such as increasing patellofemoral pressure and anterior knee pain [68,77]. The cam-post mechanism in PS TKAs is designed to prevent paradoxical anterior translation; however, the cam-post does not engage until after mid-flexion. With no cam-post force and a resected PCL, the PS designs have shown anterior sliding before cam-post engagement [63,73]. The model shows that increased medial conformity of the bearing insert does reduced mid-flexion medial AP translations. Although the results of the sensitivity analysis revealed less paradoxical anterior motion, it came at the expense of increased tibiofemoral and cam-post contact force. Studies show that TKA designs with more bearing conformity have demonstrated higher wear [189,190], and increasing insert conformity can eliminate excessive anterior sliding and reduce uniform wear pattern while induces higher contact stress and increases fatigue wear [190].

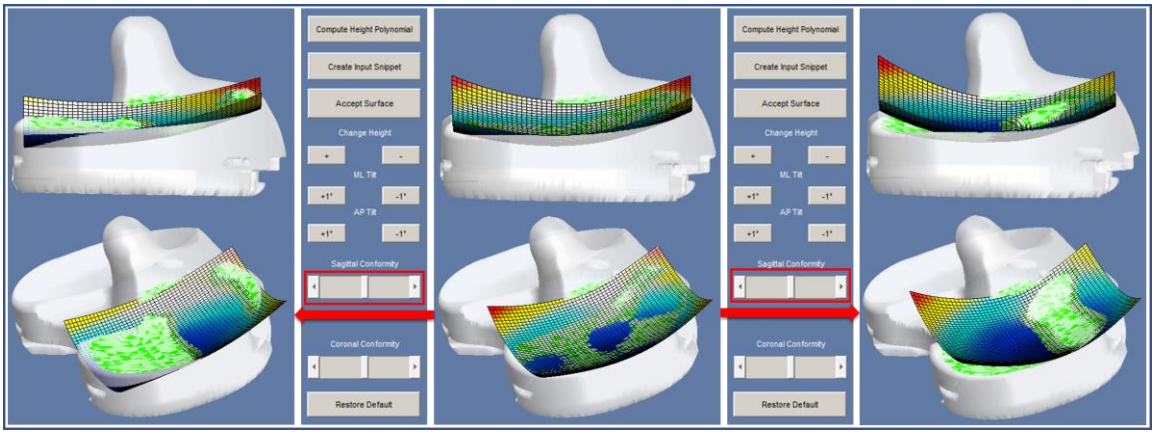


Figure 5-122: The user can alter the geometries of TKA components and component alignment using the GUI and perform sensitivity analyses to study the effects of TKA design aspects and surgical conditions as related to knee mechanics. The sagittal conformity of medial plateau was increased (right) to make the medial plateau more conforming and decreased to make the medial plateau flatter (left).

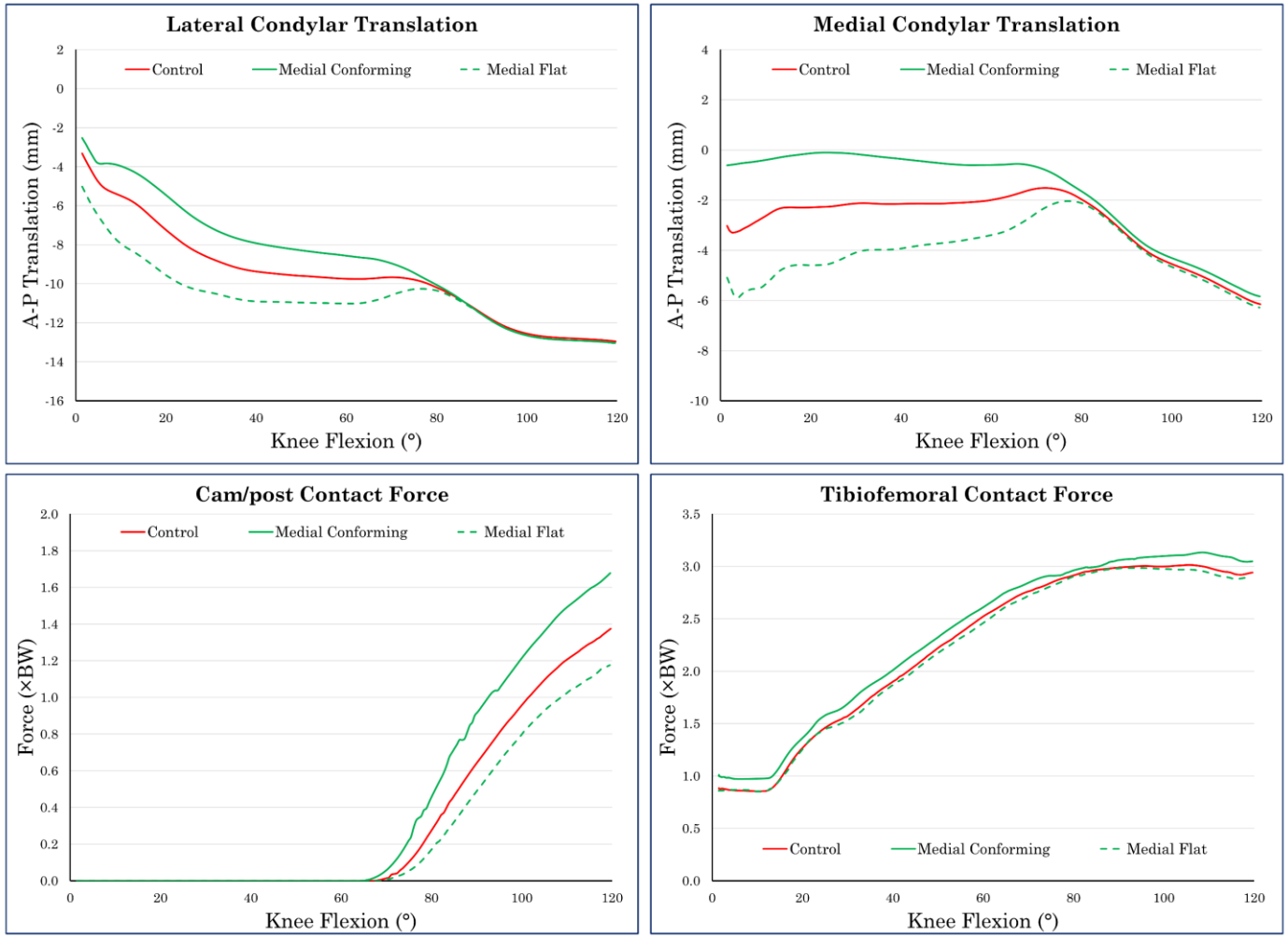


Figure 5-123: The sensitivity analysis of the reference (solid red), increased medial conformity (solid green), and decreased medial conformity (dashed green) designs are included for a PS TKA. LAP (top left), MAP (top right), cam-post contact force (bottom left), and tibiofemoral contact force (bottom right) are represented.

5.8.5 PS TKA Post location

A sensitivity analysis of the post on the bearing insert in PS TKA designs was performed using the FSM. As mentioned before, the FSM has a GUI which allows the user to modify parameters of any TKA and perform analyses. The posterior surface of the post on the bearing was moved in anterior and posterior directions for a PS TKA design (Figure 5-124). For convenience, these designs are being referred to as the reference (no change in post location), design #1 (post is moved anteriorly), and design #2 (post is moved posteriorly).

The lateral condyle translated posteriorly from full extension to the maximum knee flexion, about -3.3 mm, -4.4 mm, and -5.4 mm for the design #1, the reference design, and the design #2, respectively (Figure 5-125). Similarly, the medial condyle moved posteriorly about -0.6 mm, -1.5 mm, and -2.4 mm, respectively (Figure 5-126). The femoral axial rotations were slightly different, 4.3°, 4.5°, and 4.7° for the design #1, the reference design, and the design #2, respectively (Figure 5-127). The similarity of the external rotation profile is because of the cam/post engagement moved both lateral and medial condyles.

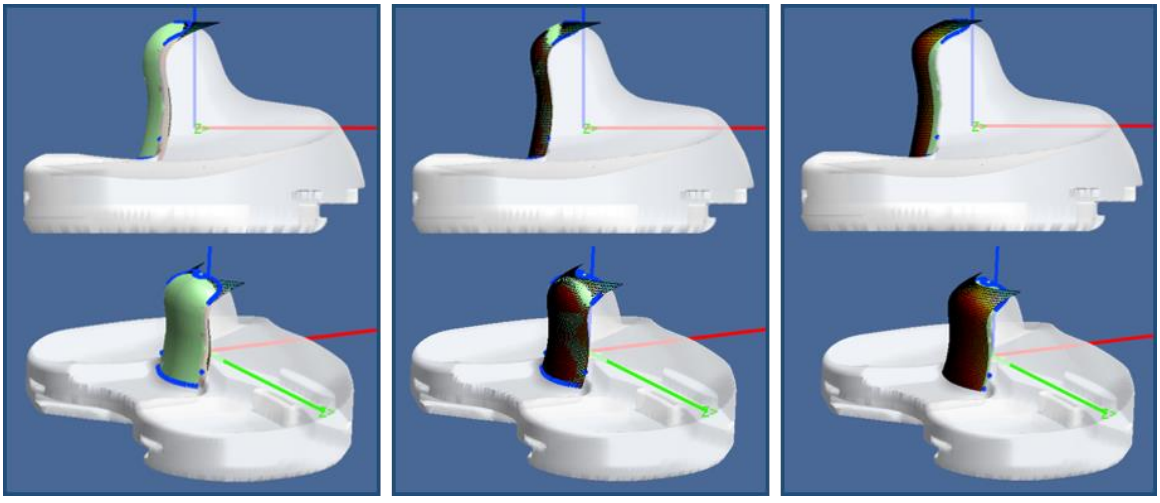


Figure 5-124: Three different simulations were created for a PS TKA design. One with a normal post position, the reference design (middle), one with the post moved anteriorly, design #1 (left), and one with post moved posteriorly, design #2 (right).

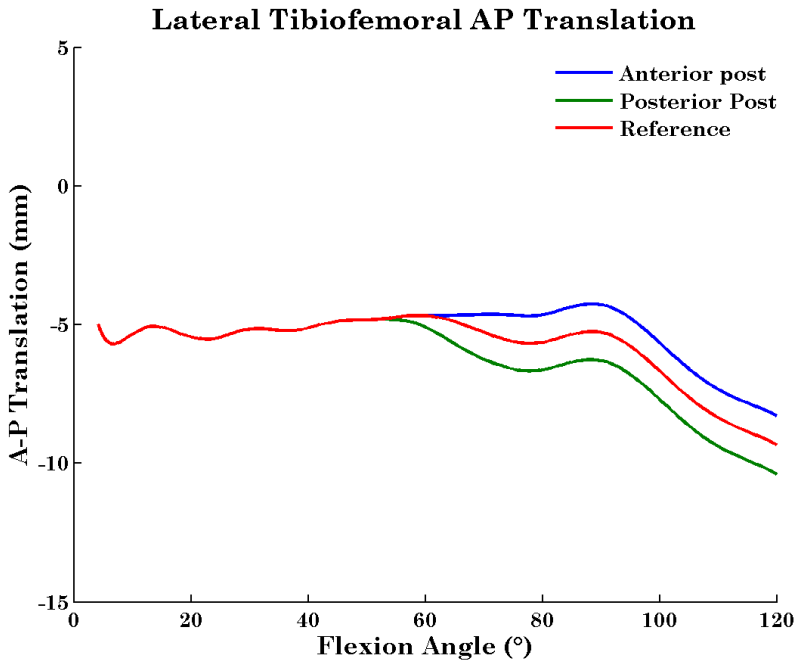


Figure 5-125: Comparison of the lateral AP translation between the reference PS (red), the anteriorized post PS (blue), and the posteriorized post PS (green).

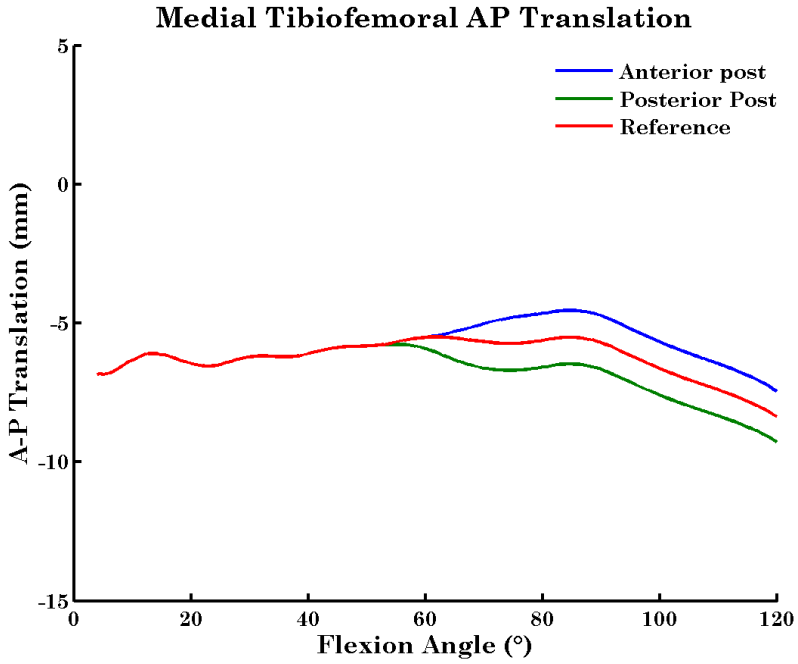


Figure 5-126: Comparison of the medial AP translation between the reference PS (red), the anteriorized post PS (blue), and the posteriorized post PS (green).

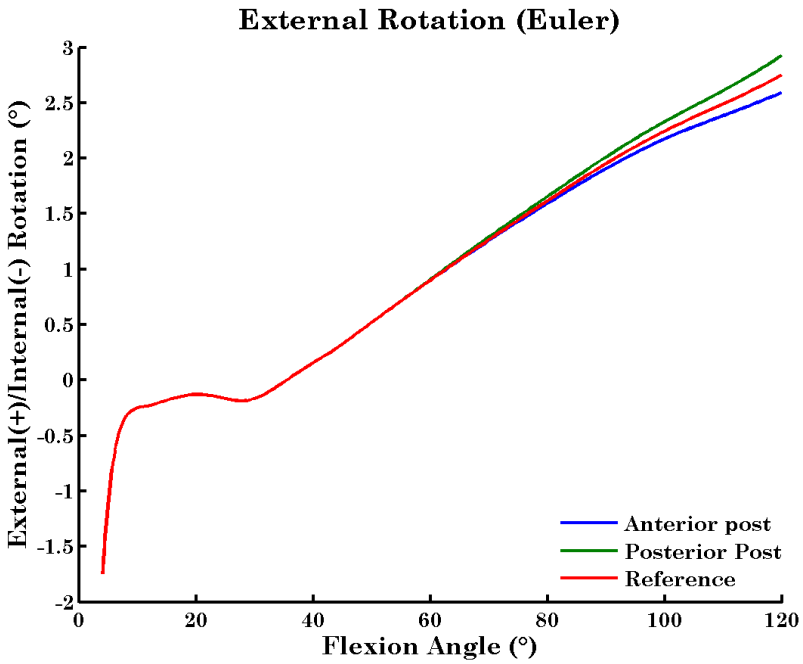


Figure 5-127: Comparison of the femoral axial rotation between the reference PS (red), the anteriorized post PS (blue), and the posteriorized post PS (green).

The changes in the kinematics are due to different flexion angles where the cam/post starts engaging. For the design #2, the cam/post start engaging sooner and therefore forces the condyles to move more posteriorly, as opposed to the design #1 where late cam/post engagement allows the condyles to slide further anterior (Figure 5-128). The design #2 exhibited lower patellofemoral condyle contact force due to more femoral condyle rollback (Figure 5-129). However, the cam/post contact forces increase for the design #2. Although moving the post in the posterior direction showed better kinematics profile and slight reduction in the patellofemoral force, the cam/post forces increased. Subsequently, the stress on the post increases and can cause excessive wear and eventually failure of the post. Similar results were reported in the literature. Churchill et al. investigated the effects of moving the post in the AP direction and found that posteriorizing the post increased the femoral rollback and reduced the patellofemoral contact force [171].

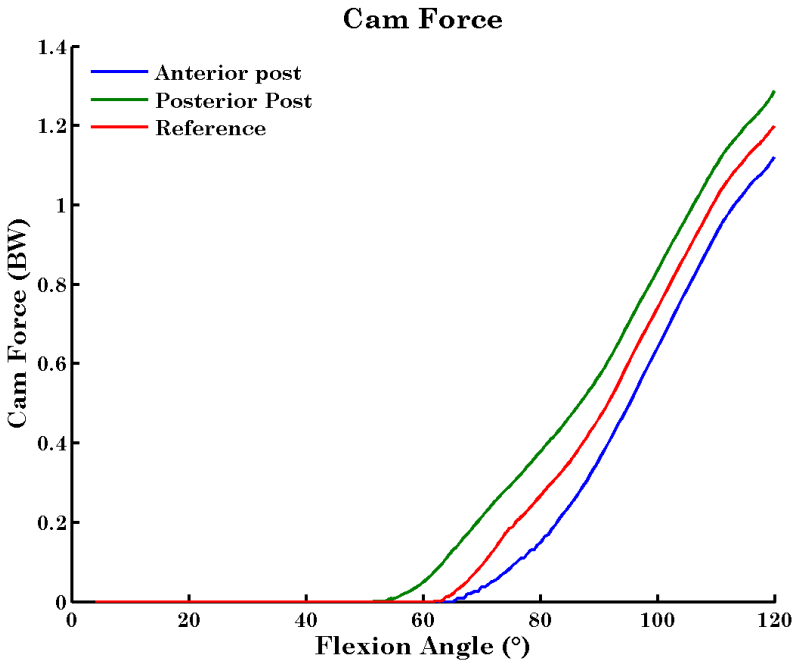


Figure 5-128: Comparison of the cam/post contact force between the reference PS (red), the anteriorized post PS (blue), and the posteriorized post PS (green).

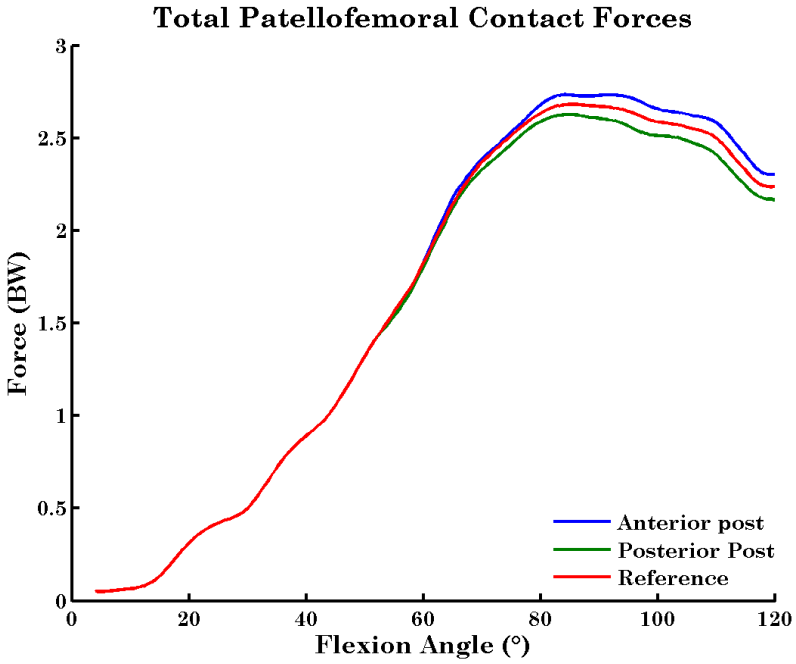


Figure 5-129: Comparison of the patellofemoral contact between the reference PS (red), the anteriorized post PS (blue), and the posteriorized post PS (green).

5.8.6 Pin Design in Fixed-bearing Hinge

The fixed-bearing hinge design has two contacting surfaces, anterior cam/post, and posterior cam post. The distance between these two surfaces of the diameter of the pin contacting between these two surfaces can be altered to achieve different outcomes. A simulation was created by moving these two surfaces further from each other, meaning the post surface moved more posteriorly and the anterior surface moved more anteriorly (Figure 5-130). The results were compared to the default fixed-bearing design to investigate the effects of increasing the clearance between these two surfaces.

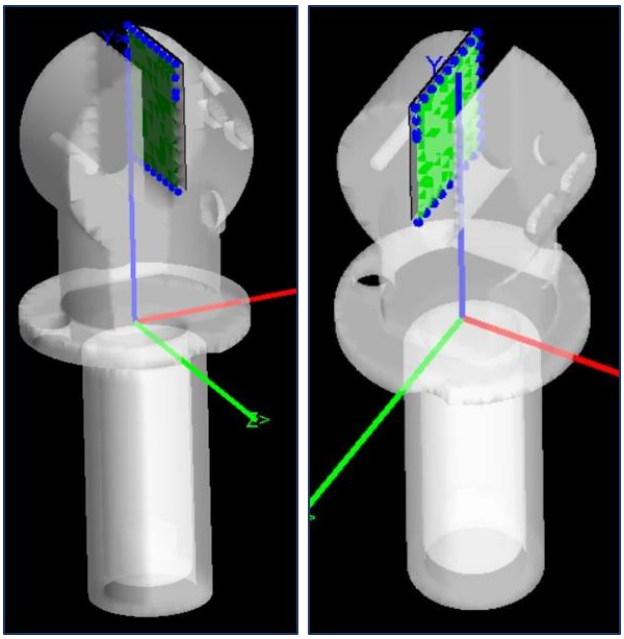


Figure 5-130: Increasing the clearing of the cam/post mechanism by moving the anterior surface further anterior (left) and the posterior surface more posterior (right).

From full extension to maximum knee flexion, the lateral condyle translated posteriorly about -0.8 mm for the increased clearance design and 0.2 mm anteriorly for the default design (Figure 5-131). The medial condyle revealed improvement as well. In the default design, the medial condyle moved

anteriorly about 4.6 mm, while the anterior sliding was 3.7 mm for the increased clearance design (Figure 5-132). The axial rotation did not reveal a substantial difference since the medial condyle of the default design moved more anteriorly (Figure 5-133).

The patellofemoral contact force was slightly lower for the increased clearance design (Figure 5-134). In the increased clearance design, the pin did not come in contact with the posterior surface throughout the range of motion (Figure 5-135), and the forces on the anterior surface decreased significantly (Figure 5-136). Reduced contact forces and improved kinematics suggest that slightly increasing the clearance for the fixed-bearing hinge design might be beneficial to the TKA outcomes.

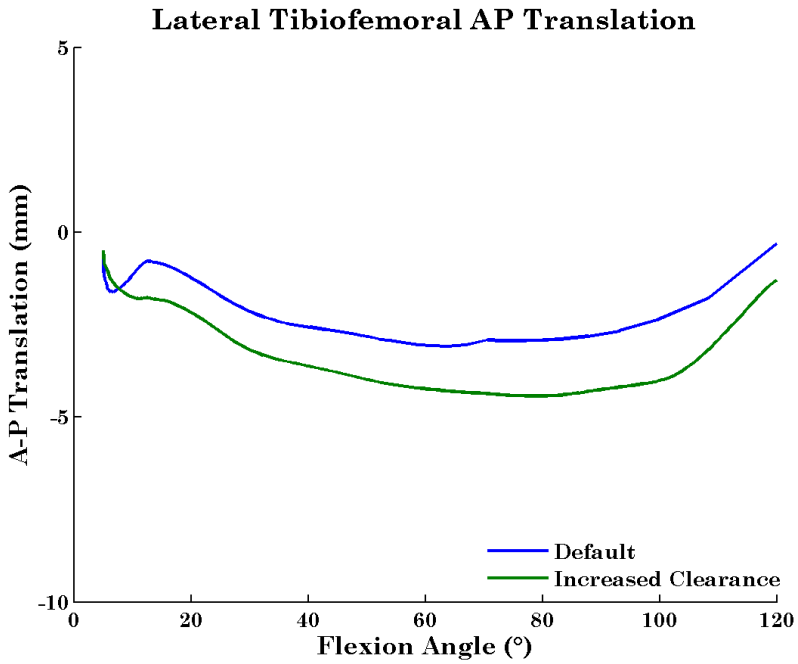


Figure 5-131: Comparison of the lateral AP translation between the default (blue) and the increased clearance design (green).

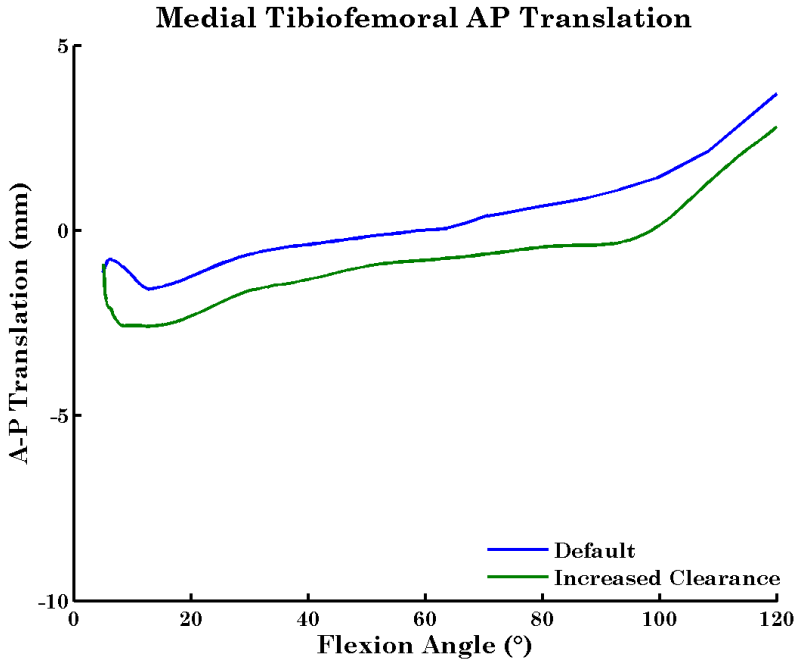


Figure 5-132: Comparison of the medial AP translation between the default (blue) and the increased clearance design (green).

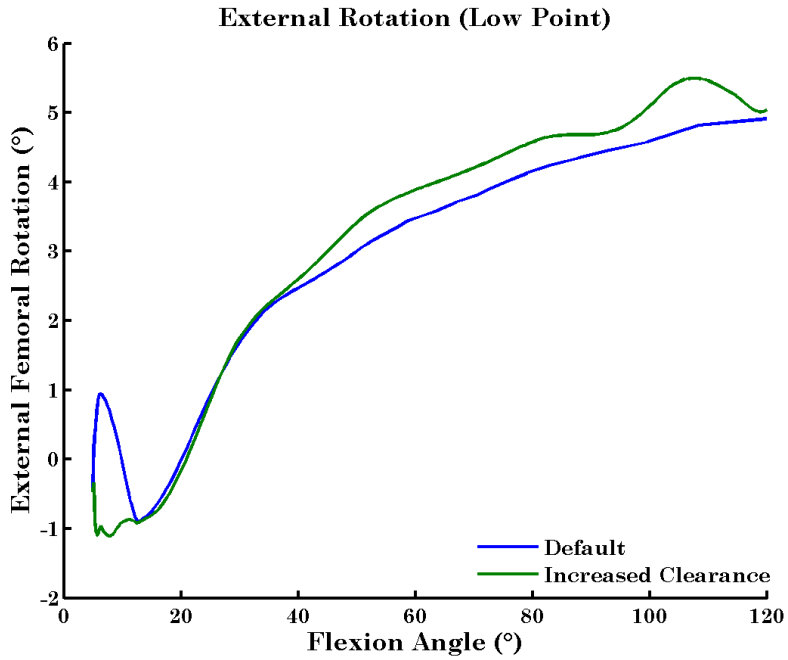


Figure 5-133: Comparison of the femoral axial rotation between the default (blue) and the increased clearance design (green).

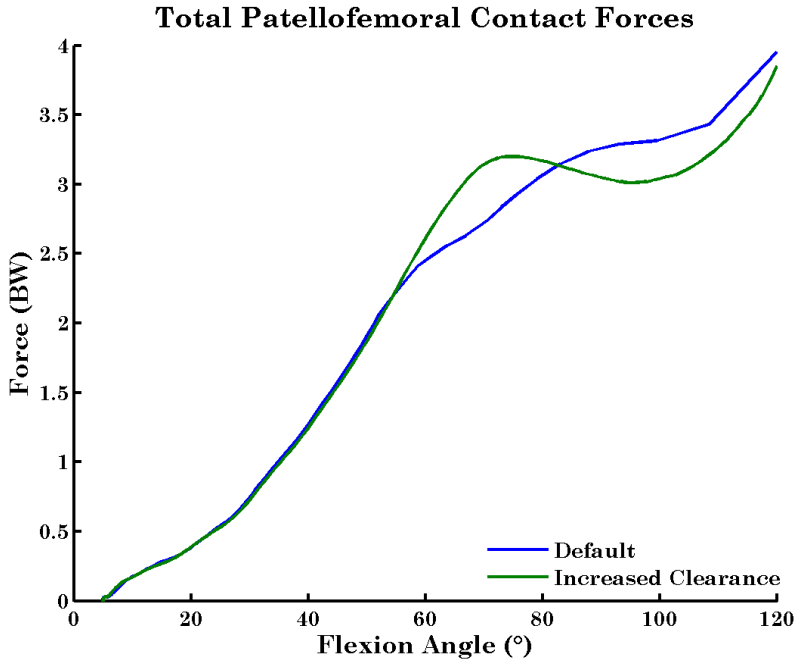


Figure 5-134: Comparison of the patellofemoral contact force between the default (blue) and the increased clearance design (green).

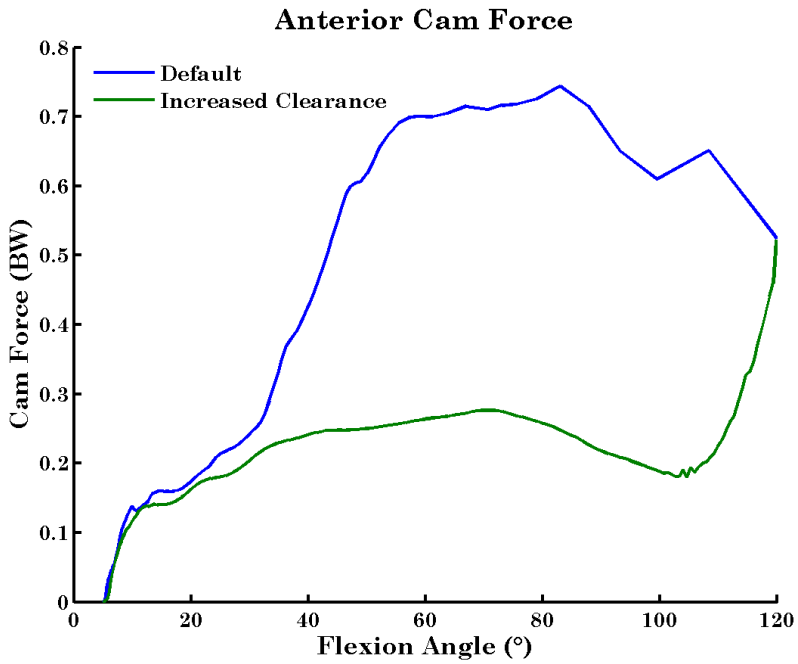


Figure 5-135: Comparison of the anterior cam/post contact force between the default (blue) and the increased clearance design (green).

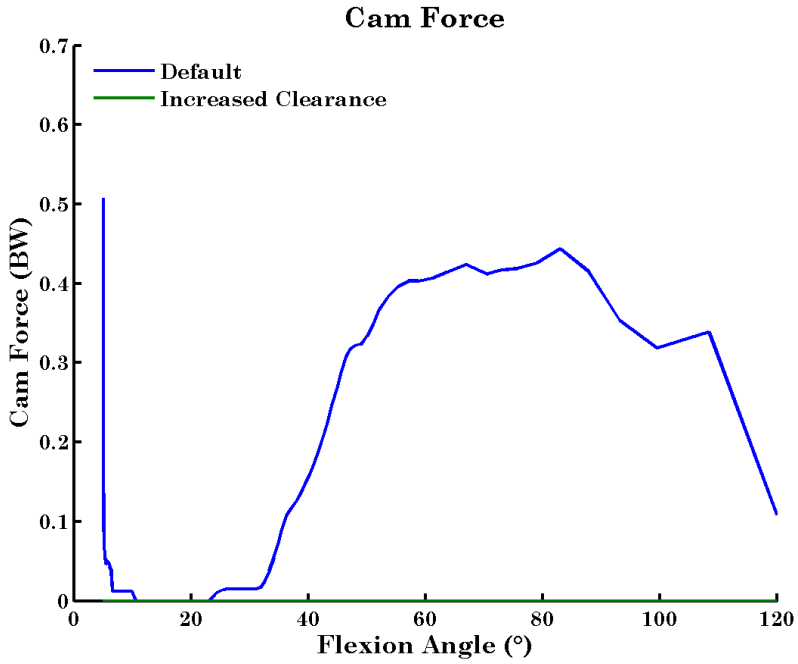


Figure 5-136: Comparison of the posterior cam/post contact force between the default (blue) and the increased clearance design (green).

Chapter 6: Validation

The kinetics of the FSM was validated against the telemetric implants and the kinematics were validated against fluoroscopic data.

6.1 Kinetics validation

The telemetric tibiofemoral contact forces were captured and downloaded for two subjects implanted with a fixed-bearing (FB) PCR telemetric TKA [191,192]. Both subjects were evaluated during a DKB, while the first subject was also evaluated during chair rise and stair ascent activities. The bone models were created from computed tomography (CT) scan data using a segmentation technique. These bone geometries and implant CAD models were imported into the mathematical model. The placement of the components in the mathematical model was created based on the actual implant placement, collected from CT data. Predicted kinetics from the mathematical model were compared with this data.

6.1.1 Deep Knee Bend

For the first subject, the mathematical model predicted the total tibiofemoral contact force with a root-mean-square (RMS) accuracy of 0.17 times body weight (×BW) compared to the contact force obtained from the telemetric implant (Figure 6-3). The RMS accuracies for lateral and medial condyle forces were 0.18 × BW and 0.15 × BW, respectively. Expressed as a percentage of the maximum force, the mathematical model revealed an error of 4.7%, 9.7%, and 8.6% for total, lateral, and medial tibiofemoral forces, respectively (Figure 6-1, Figure 6-2, and Figure 6-3). The peak tibiofemoral contact forces for the mathematical model and telemetric device were 3.72 × BW and 3.71 × BW for subject 1, respectively.

Additionally, there is excellent agreement between the mathematical model and the telemetric forces for the second subject. For the second subject, the mathematical model prediction compared to the telemetric forces revealed RMS accuracies of 0.10 × BW, 0.12 × BW, and 0.18 × BW for the lateral, medial, and total knee forces, respectively (Figure 6-4, Figure 6-5, and Figure 6-6). These correspond to 5.3%, 6.9%, and 4.6% of error when expressed as a percentage of the output range. For subject 2, the mathematical model and telemetric device peak forces were 3.82 × BW and 3.84 × BW for subject #2, respectively.

6.1.2 Chair Rise

During the chair rise activity, which was only conducted on the first subject, the mathematical model predicted 3.09 × BW for maximum tibiofemoral contact force while the peak telemetric force was 3.08 × BW (Figure 6-7). Additionally, the minimum contact force predicted by the model was 1.13 × BW and telemetry revealed a minimum contact force of 1.1 × BW. The model predicted tibiofemoral contact forces during chair rise activity with an accuracy of 0.43 × BW. Although the RMS is higher compared to the DKB activity, the maximum and minimum force predictions are very accurate, with error less than 0.05 × BW. The trend of the contact forces also matches between the model prediction and teletibia subject.

6.1.3 Stair Ascent

During the weight-bearing portion of the stair ascent activity, which was only conducted on the first subject, the first peak tibiofemoral forces were 3.56 × BW and 3.52 × BW for the mathematical model and telemetry, respectively. The second peak contact forces were 3.62 × BW and 3.02 × BW for the mathematical model and telemetry, respectively (Figure 6-8). The model predicted the contact force with an accuracy of 0.38 × BW.

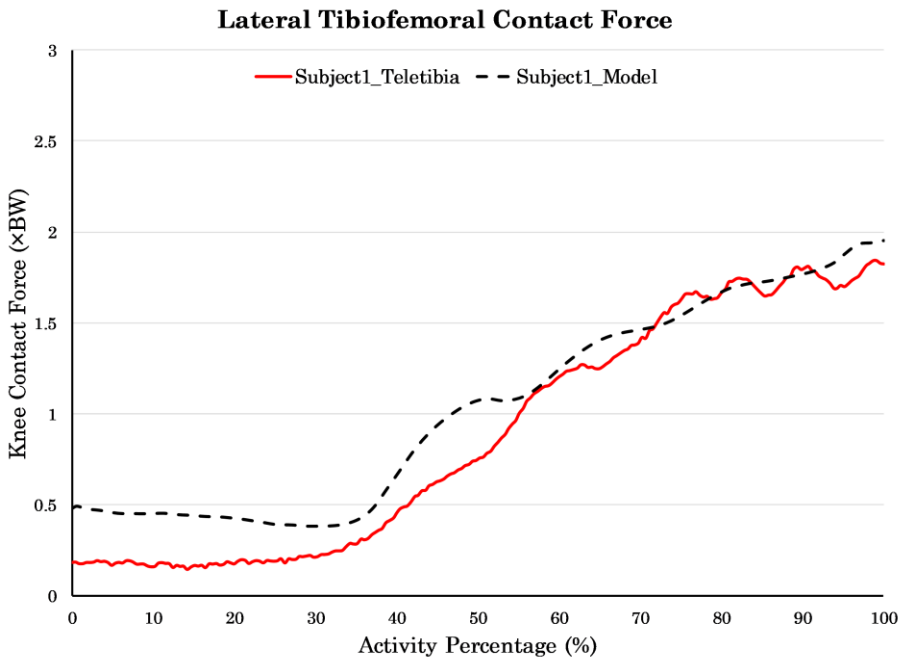


Figure 6-1: The lateral contact force comparison between model prediction (dashed black line) and the telemetric device (solid red line) for subject 1.

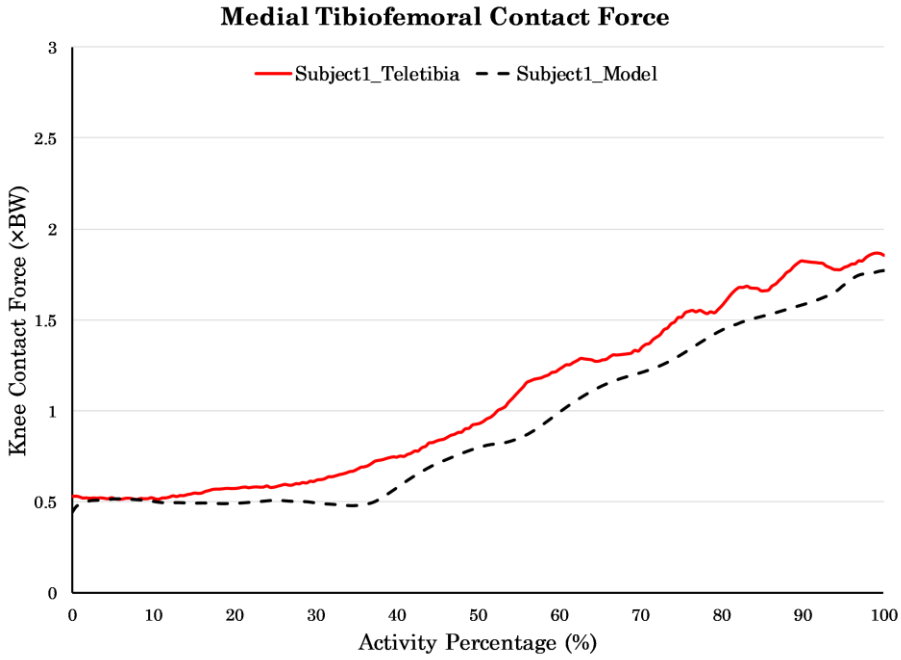


Figure 6-2: The medial contact force comparison between model prediction (dashed black line) and the telemetric device (solid red line) for subject 1.

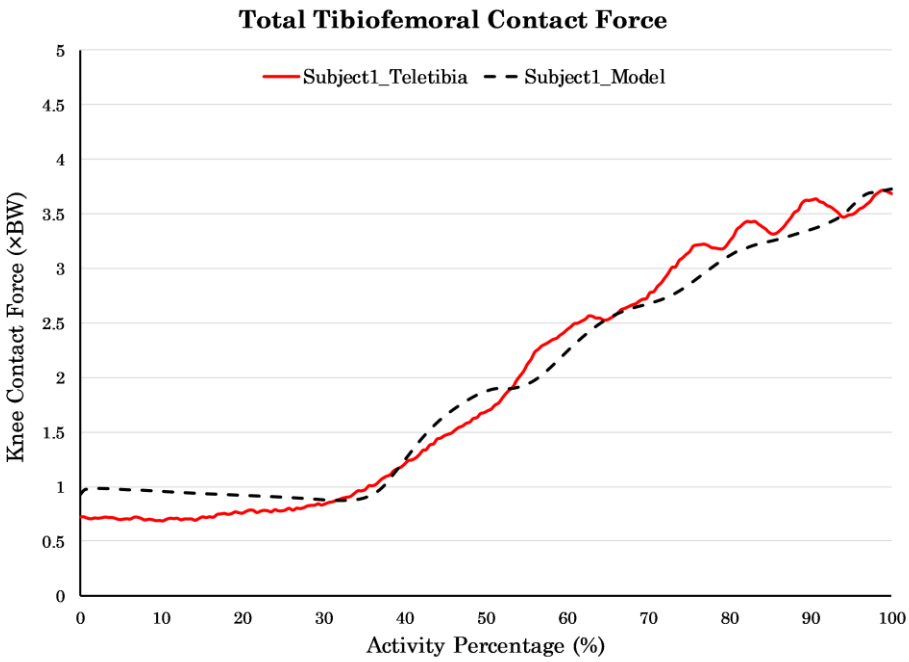


Figure 6-3: The total contact force comparison between model prediction (dashed black line) and the telemetric device (solid red line) for subject 1.

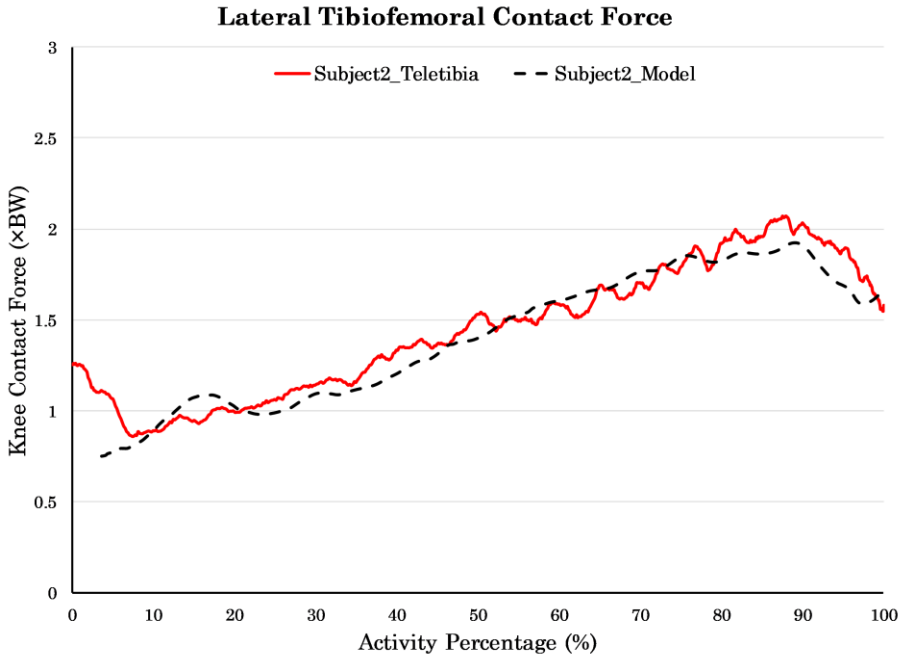


Figure 6-4: The lateral contact force comparison between model prediction (dashed black line) and the telemetric device (solid red line) for subject 2.

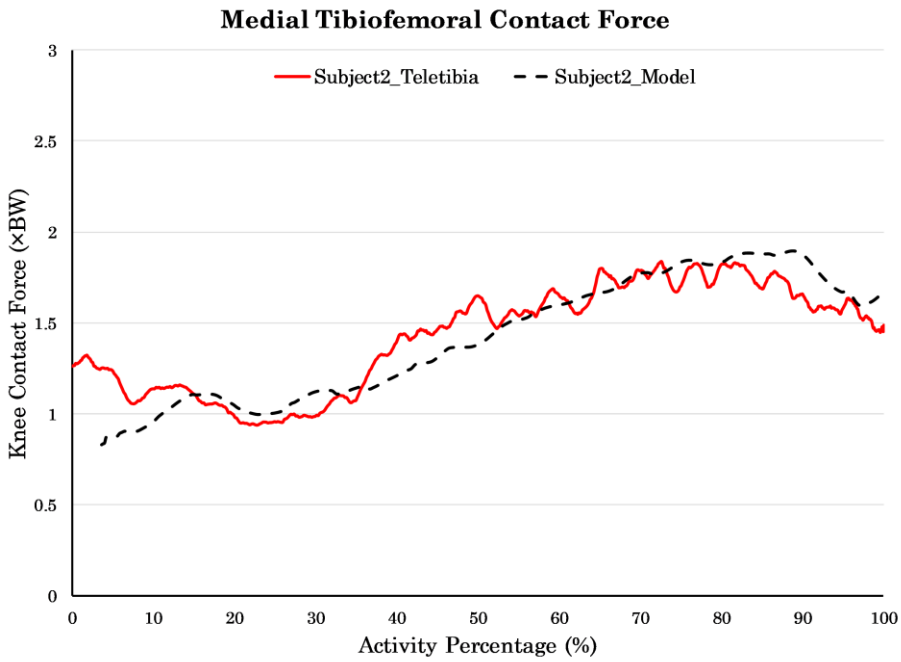


Figure 6-5: The medial contact force comparison between model prediction (dashed black line) and the telemetric device (solid red line) for subject 2.

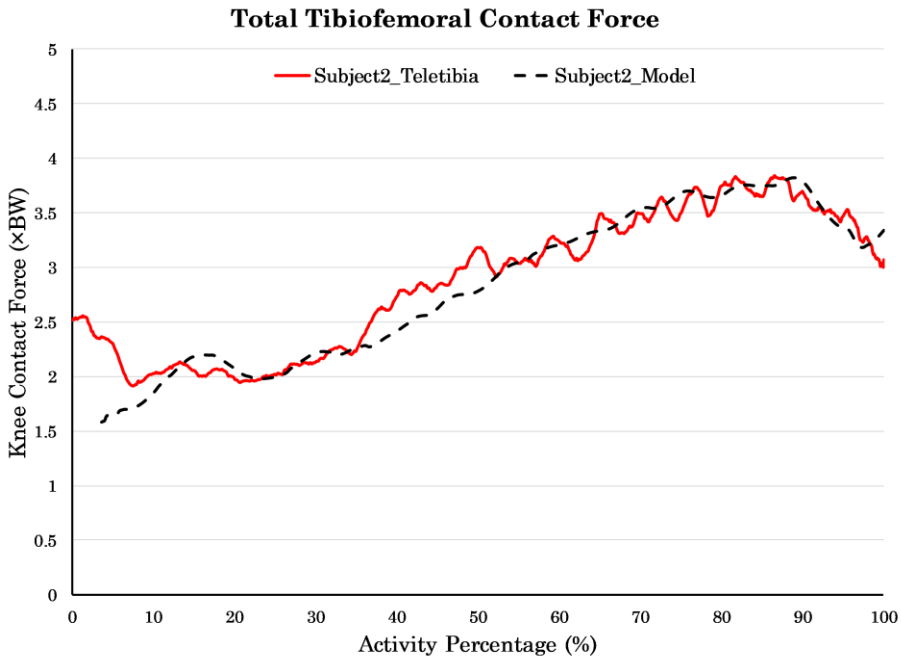


Figure 6-6: The total contact force comparison between model prediction (dashed black line) and the telemetric device (solid red line) for subject 2.

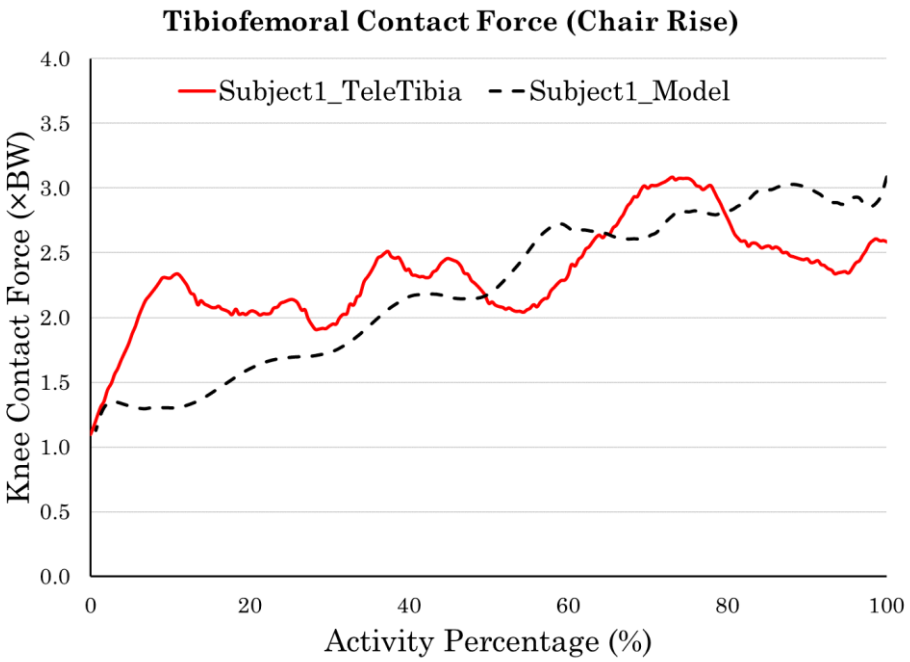


Figure 6-7: The contact force comparison between model prediction (dashed black line) and the telemetric device (solid red line) during a chair rise activity.

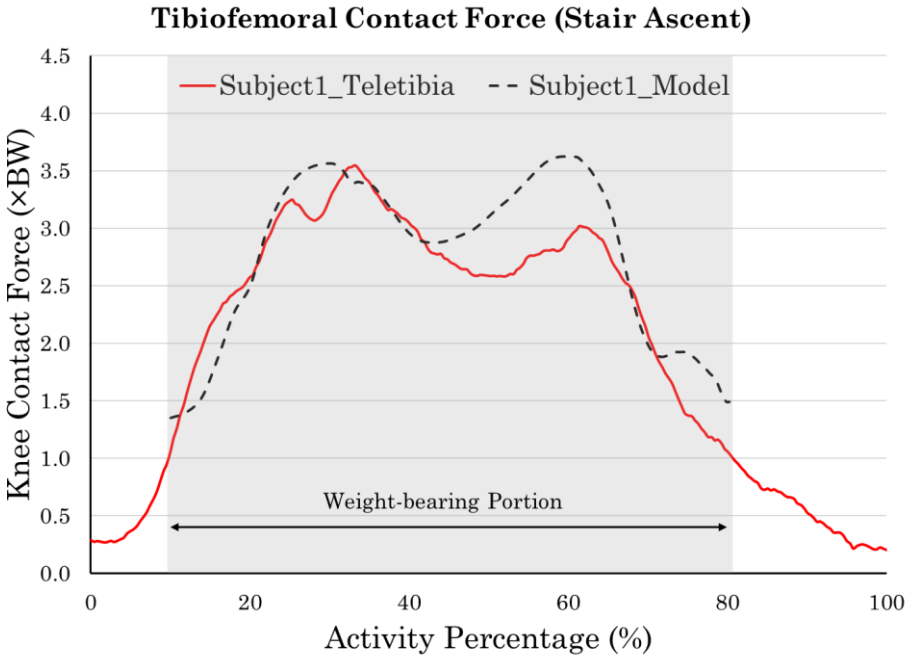


Figure 6-8: The contact force comparison between model prediction (dashed black line) and the telemetric device (solid red line) during a stair ascent activity.

6.2 Kinematics Validation

Additionally, the kinematics were validated by comparing the results for average theoretical subjects with various TKA types in the model to the average fluoroscopy data of 60 total TKA subjects implanted with various implant types. Of these subjects, 20 were implanted with a fixed-bearing PS TKA, 20 with a mobile-bearing PS TKA, and 20 subjects were implanted with medial pivot TKA. All subjects performed a deep knee bend activity under fluoroscopic surveillance. The kinematics of these subjects were obtained using a validated 3D-to-2D registration technique [77]. The TKA implant geometries were incorporated into the model, and the model predictions were compared to the average fluoroscopy data.

6.2.1 Fixed-bearing PS TKA

From full extension to 120° of flexion, the model predicted -5.87 mm, -1.39 mm, and 5.99° of lateral rollback, medial rollback, and femoral axial rotation for the FB PS design, respectively. On average, FB PS patients experienced -6.83 mm, -2.95 mm, and 5.07° of lateral rollback, medial rollback, and femoral axial rotation, respectively (Figure 6-9, Figure 6-10, and Figure 6-11).

Overall, the model predicted the LAP translation with RMS accuracies of 0.35 mm for FB PS TKA. The RMS error for MAP translations was 1.02 mm for FB PS TKA. And the model predicted the axial rotation with RMS accuracies of 0.64° for FB PS TKA (Table 6-1).

6.2.2 Mobile-bearing PS TKA

The model predictions of the lateral rollback, medial rollback, and femoral axial rotation for the MB PS design were -6.29 mm, -2.35 mm, and 4.22°, respectively. The derived fluoroscopic data was -6.45 mm, -2.51 mm, and 4.53° of lateral rollback, medial rollback, and femoral axial rotation for subjects

implanted with MB PS, respectively (Figure 6-12, Figure 6-13, and Figure 6-14).

Overall, the model predicted the LAP translation with RMS accuracies of 0.57 mm for MB design. The RMS error for MAP translations was 0.54 mm for MB PS design. And the model predicted the axial rotation with RMS accuracies of 1.13° for MB PS design (Table 6-2).

6.2.3 Posterior Cruciate Retaining Medial Pivot TKA

The model prediction of the lateral rollback, medial rollback, and femoral axial rotation for the medial pivot design were -3.0 mm, -0.1 mm, and 4.3°, respectively. The fluoroscopy data revealed -4.1 mm, -0.6 mm, and 4.9° of lateral rollback, medial rollback, and femoral axial rotation for subjects implanted with medial pivot design, respectively (Figure 6-15, Figure 6-16, and Figure 6-17).

Overall, the model predicted the LAP translation with RMS accuracies of 0.41 mm for medial pivot design. The RMS error for MAP translations was 0.30 mm for the medial pivot design. And the model predicted the axial rotation with RMS accuracies of 0.54° for the medial pivot design (Table 6-3).

Minimal medial translations predicted by the FSM for medial pivot design is also in agreement with other published kinematics studies on this type of TKA, where medial tibiofemoral joint is designed like a ball and socket joint to minimize medial condyle movement [193,194].

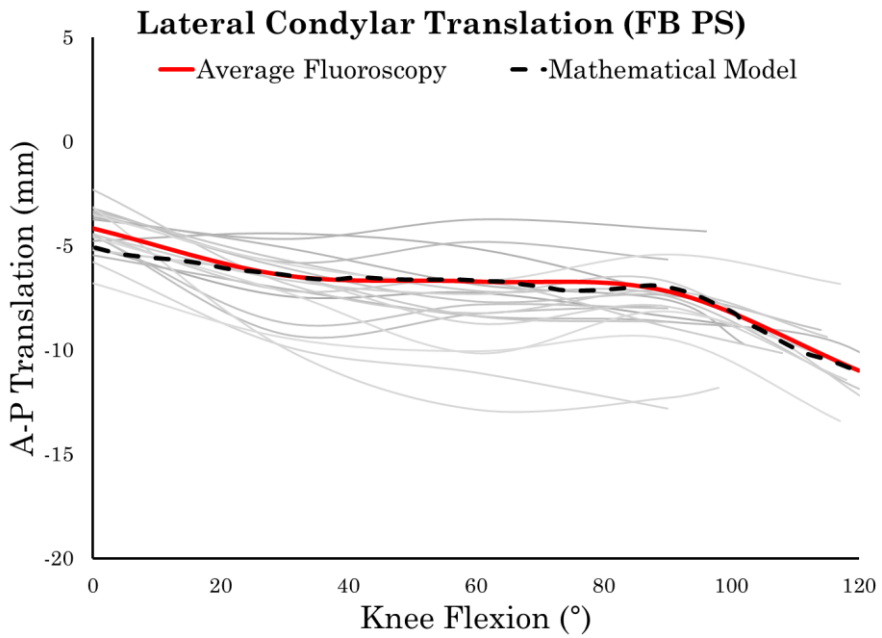


Figure 6-9: The predicted lateral rollback is validated against average fluoroscopic data for FB PS. The solid red line shows the average fluoroscopy of subjects (shown with thin grey lines), and the mathematical model predictions are shown with dashed black lines.

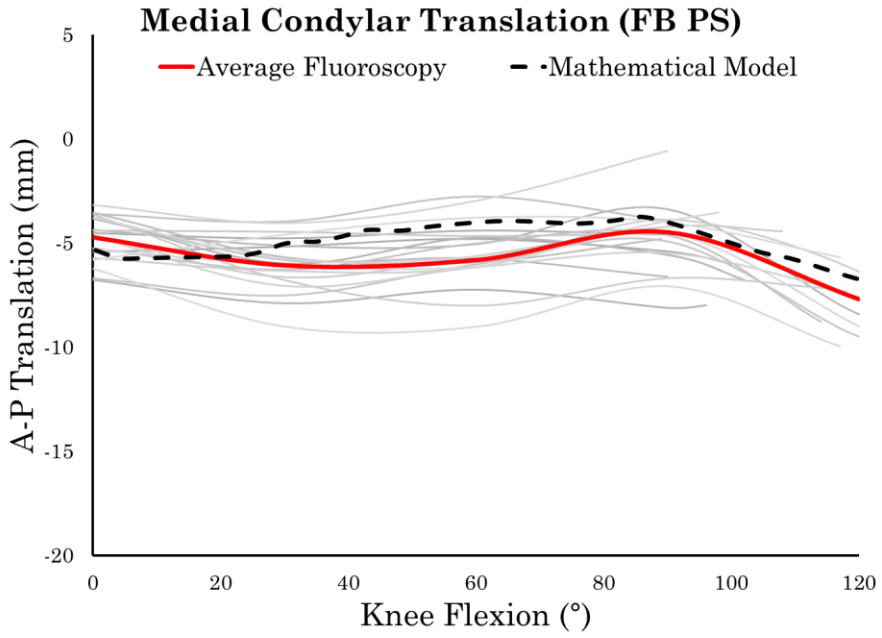


Figure 6-10: The predicted medial rollback is validated against average fluoroscopic data for FB PS. The solid red line shows the average fluoroscopy of subjects (shown with thin grey lines), and the mathematical model predictions are shown with dashed black lines.

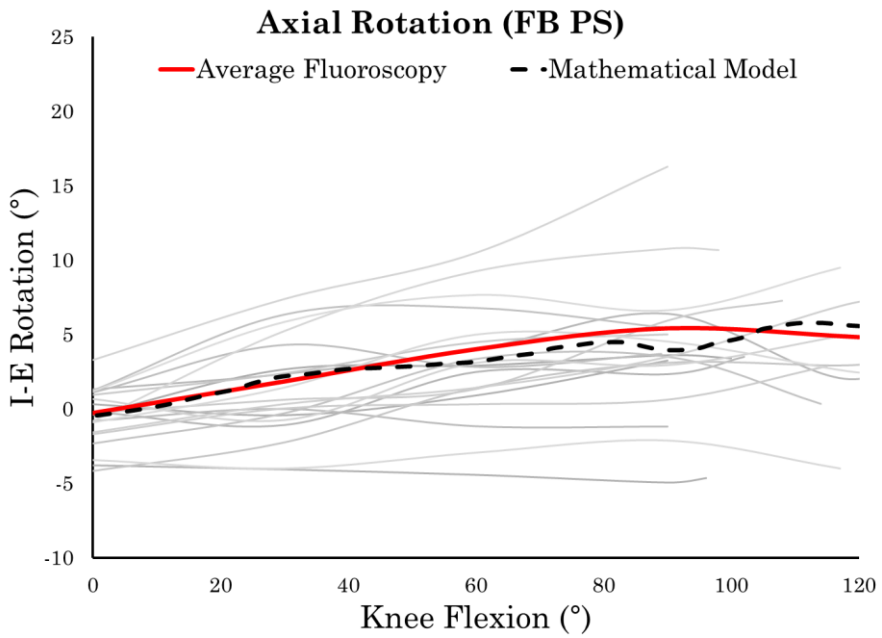


Figure 6-11: The predicted axial rotation is validated against average fluoroscopic data for FB PS. The solid red line shows the average fluoroscopy of subjects (shown with thin grey lines), and the mathematical model predictions are shown with dashed black lines.

Table 6-1: The lateral and medial AP translation and axial rotation for the average fluoroscopy and the mathematical model as well as root-mean-square errors between model prediction and average fluoroscopy for FB PS group.

	From Full extension to 120°		RMS
	Model	**Fluoro**	**FB**
LAP	-5.87	-6.83	0.35
MAP	-1.39	-2.95	1.02
Axial Rotation	5.99	5.07	0.64

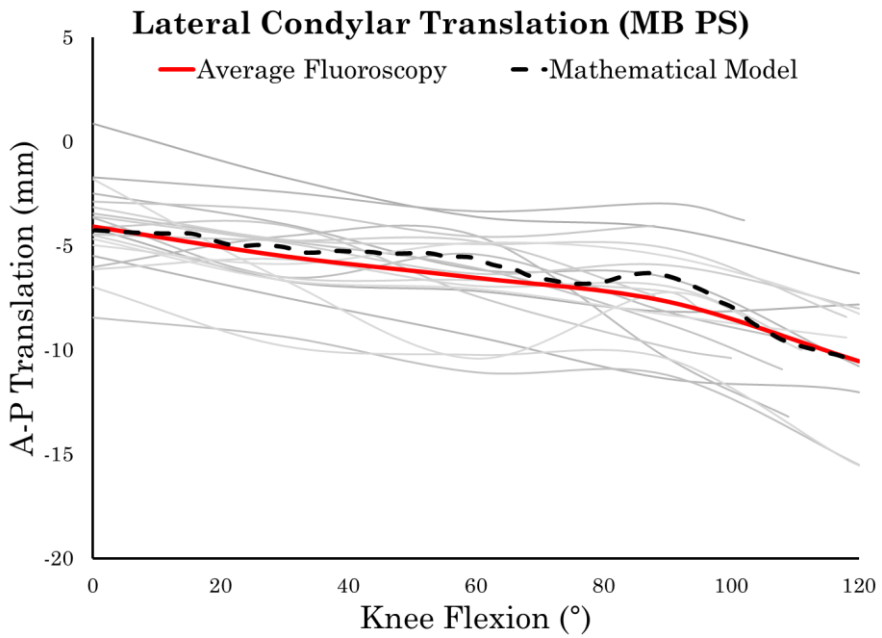


Figure 6-12: The predicted lateral rollback is validated against average fluoroscopic data for MB PS. The solid red line shows the average fluoroscopy of subjects (shown with thin grey lines), and the mathematical model predictions are shown with dashed black lines.

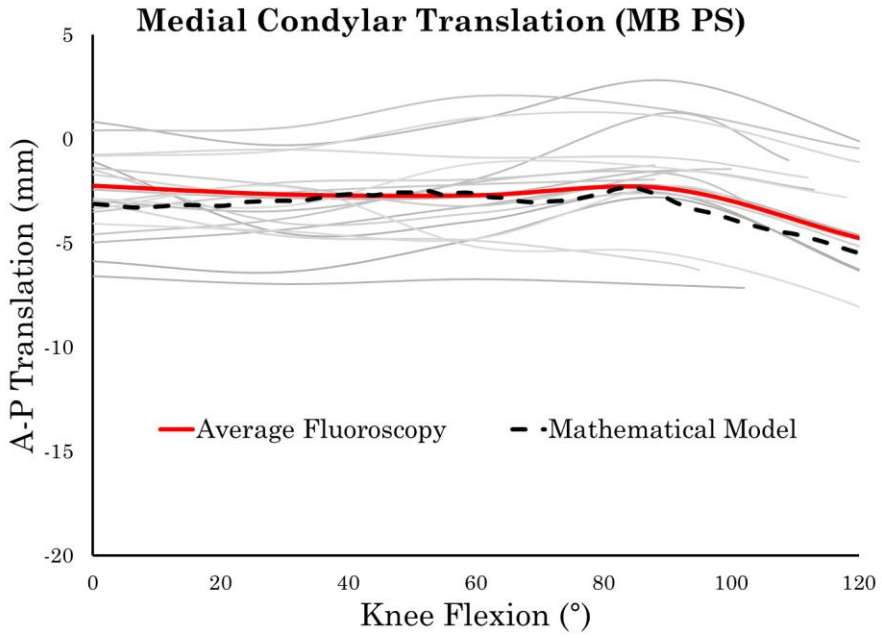


Figure 6-13: The predicted medial rollback is validated against average fluoroscopic data for MB PS. The solid red line shows the average fluoroscopy of subjects (shown with thin grey lines), and the mathematical model predictions are shown with dashed black lines.

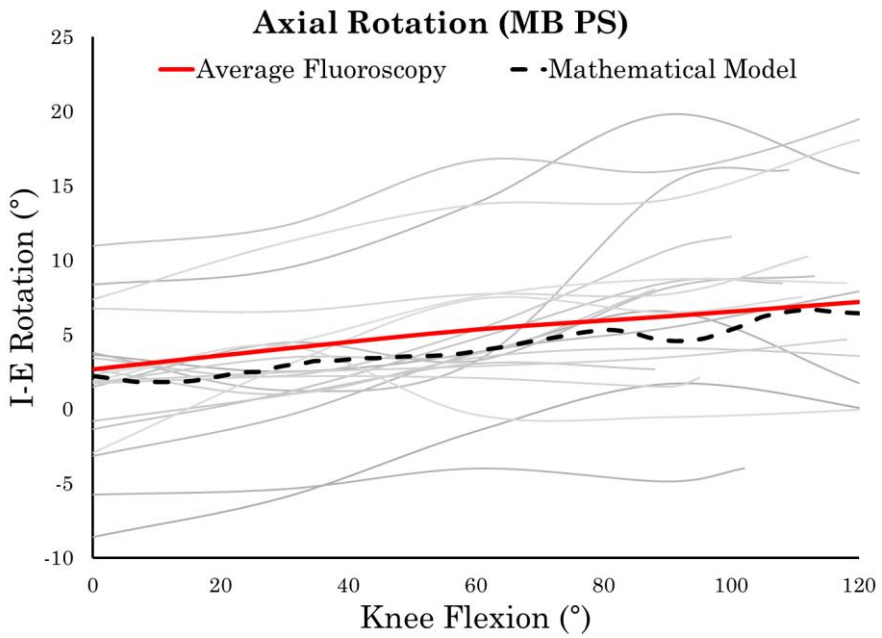


Figure 6-14: The predicted axial rotation is validated against average fluoroscopic data for MB PS. The solid red line shows the average fluoroscopy of subjects (shown with thin grey lines), and the mathematical model predictions are shown with dashed black lines.

Table 6-2: The lateral and medial AP translation and axial rotation for the average fluoroscopy and the mathematical model as well as root-mean-square errors between model prediction and average fluoroscopy for MB PS group.

	From Full extension to 120°		RMS
	Model	**Fluoro**	**FB**
LAP	-6.29	-6.45	0.57
MAP	-2.35	-2.51	0.54
Axial Rotation	4.22	4.53	1.13

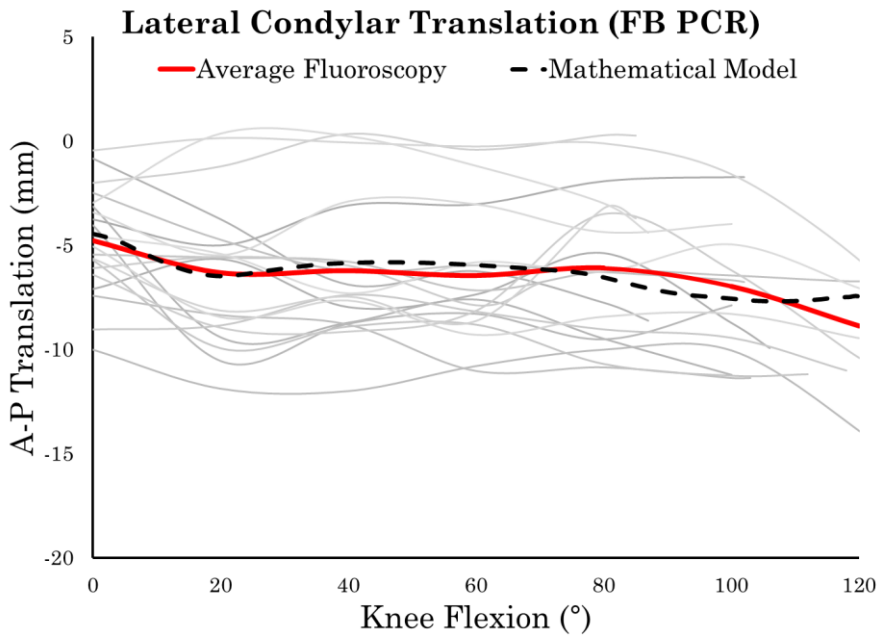


Figure 6-15: The predicted lateral rollback is validated against average fluoroscopic data for medial pivot design. The solid red line shows the average fluoroscopy of subjects (shown with thin grey lines), and the mathematical model predictions are shown with dashed black lines.

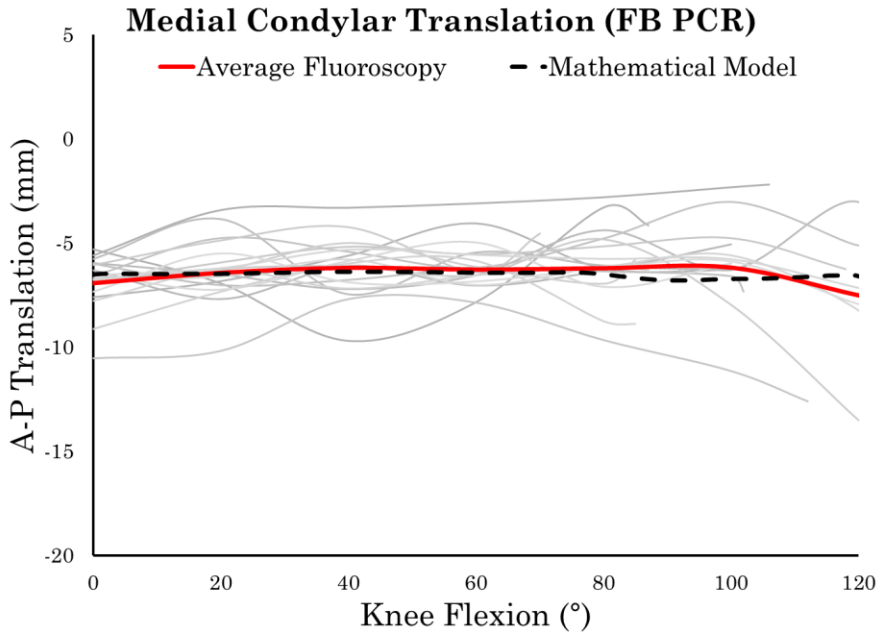


Figure 6-16: The predicted medial rollback is validated against average fluoroscopic data for medial pivot design. The solid red line shows the average fluoroscopy of subjects (shown with thin grey lines), and the mathematical model predictions are shown with dashed black lines.

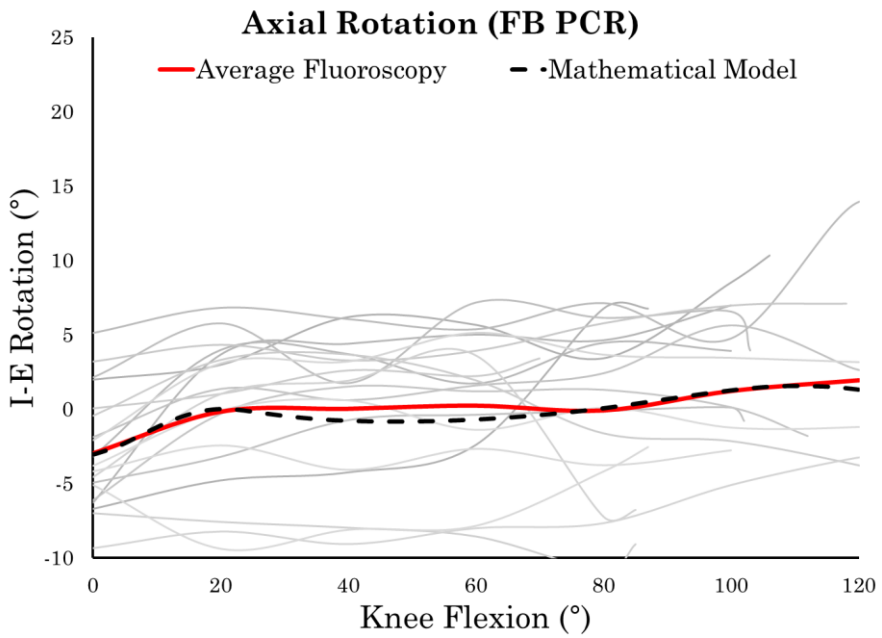


Figure 6-17: The predicted axial rotation is validated against average fluoroscopic data for the medial pivot design. The solid red line shows the average fluoroscopy of subjects (shown with thin grey lines), and the mathematical model predictions are shown with dashed black lines.

Table 6-3: The lateral and medial AP translation and axial rotation for the average fluoroscopy and the mathematical model as well as root-mean-square errors between model prediction and average fluoroscopy for medial pivot TKA.

	From Full extension to 120°		RMS
	Model	**Fluoro**	**FB**
LAP	-3.0	-4.1	0.41
MAP	-0.1	-0.6	0.30
Axial Rotation	4.3	4.9	0.54

Chapter 7: Summary

Through the course of this dissertation, several novel contributions have been made to an existing forward solution mathematical model to increase the functionality and accuracy of the software package. These contributions can advance our understanding of the mechanics of the human knee joint through creating a more realistic and physiological mathematical model of the knee.

The muscle force prediction capabilities have been improved through the development of an advanced muscle wrapping algorithm. This muscle wrapping algorithm can accurately detect the geometries of the components and bones and can wrap around them. Hence, the changes in the muscle moment arms and lines of action can be modeled which provides a more accurate muscle force prediction.

An inverse solution model was integrated into the FSM. The inverse model takes the predicted outcomes of the FSM and predict the joint forces based on these kinematic outcomes. The inverse model can be particularly important when the effects of the kinematics on the forces are of interest without the effects of other forces, for example when we want to compare the knee forces between a PCR TKA a PS TKA without having to include the cam/post force or PCL force on predicted kinetics.

A settling algorithm was developed to eliminate the early flexion oscillations seen in the previous FSM. Not only did this settling algorithm successfully eliminate the oscillations, it also enabled simulations of other activities, where larger forces and torques applied at the joint can cause severe instability.

The mathematical model was extensively expanded through incorporating the foot as a body and by adding more muscles, including several patients with different geometries and properties, and making the simulations more

clinically relevant. Previous studies have documented that the kinematics and kinetics of TKA are different for different subjects. The model was also capable of conducting analyses pertaining to different joint mechanics for various subjects.

The model was advanced by incorporating several other daily activities, such as chair rise, lunge, stair descent, stair ascent, and gait. The previous model only included a DKB and squat to rise activity. The DKB activity has been of interest to investigate the kinematics pattern of TKA design throughout the whole range of motion of the knee. However, other activities are more prevalent in patients following a TKA procedure. Also, the joint moments and forces during these activities are of interest to orthopaedic companies for the design and evaluation of existing and new TKA.

The mathematical model was expanded to include the analysis of revision TKA as well as primary TKA. Two types of revision TKA designs were incorporated into the FSM, a rotating bearing hinge design a fixed bearing hinge design. These types of TKAs are used for patients with severe damage to their knee, and therefore they are highly constrained designs.

All these changes not only made the mathematical model a more versatile tool to assess the knee joint mechanics, but also improved the accuracy of the model significantly. Figure 7-1 document the previous validation that was performed on the FSM before all the current modification. This is the same validation technique that was performed on the kinetics validation pertaining to subject 2, implanted with telemetric device. Figure 7-1 is comparable with Figure 6-6, which shows the same tibiofemoral contact force prediction for the same subjects. Significant improvement has been observed and document for all of the new modifications incorporated in the model. Further assessment revealed that in early flexion and late flexion, advancements have been made which can primarily be attributed to the settling and wrapping algorithms, respectively.

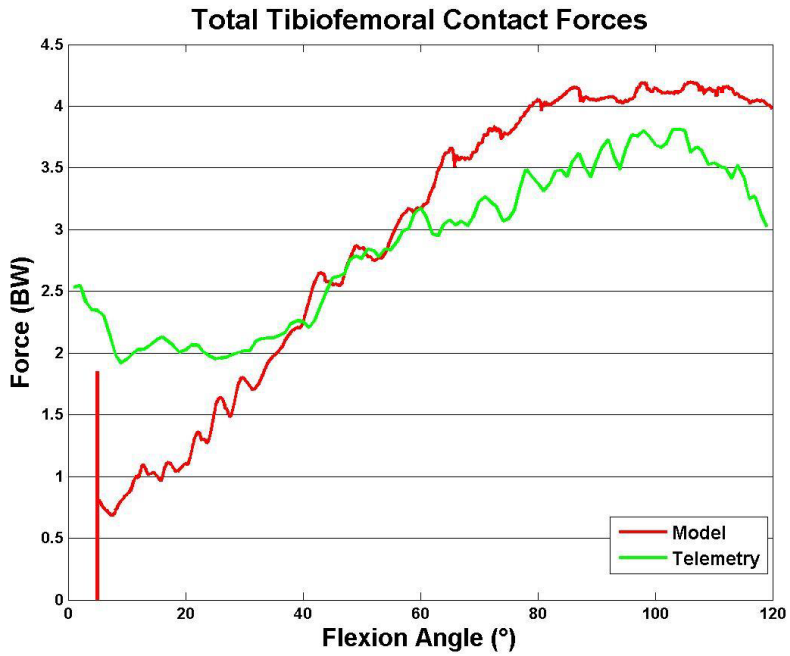


Figure 7-1: The same validation technique with the same patient was used in the previous FSM. The model tibiofemoral joint force prediction (red) was compared to the telemetric forces (green) [98].

Hundreds of simulations have been performed using the forward solution model throughout this dissertation. The effects of different implant features, surgical conditions, soft tissue properties, and component alignment were investigated through sensitivity analyses. These sensitivity analyses first revealed that the model is capable of detecting the changes and also is robust enough to perform under various loading conditions. Theses sensitivity analyses have led to a more in-depth evaluation pertaining to our understanding of human knee joint mechanics and can be of interest to orthopaedic community, both for implant developers and orthopaedic surgeons.

The document results in our evaluations have revealed that ACL substituting designs can replace the functionality of the ACL to some extent and can generate mechanics that mimic the screw-home mechanism. Additionally, the mathematical model results revealed why normal-like kinematics, consistent

femoral rollback, and consistent external rotation are important factors. By increasing femoral rollback, the muscle moment arms increase and hence the muscle forces decrease. Also, in several simulations, anterior rollback was associated with increased patellofemoral contact force, which may suggest why so many patients following TKA procedure experience anterior knee pain.

Furthermore, several sensitivity analyses have been conducted on implant positioning on the TKA outcomes. Patella alta revealed increase with regard to the quadriceps and patellofemoral contact forces regardless of the TKA type. It has been determined that, when the femoral component is placed in an internally rotated orientation relative to the bearing insert, it can induce more femoral external rotation, which was in agreement with fluoroscopic data.

In summary, the novel advancements of the documented in this dissertation have made the FSM a more versatile and powerful tool for analyzing different subjects, implanted with different types of TKA, performing various activities. This model can be utilized to assess various surgical techniques and loading conditions.

7.1 Assumptions and Limitations

For the presented mathematical model, there were several assumptions and limitations. The mass of each body segment, i.e., foot, foreleg, thigh, etc., was calculated as a percentage of total body mass. These data were obtained from the literature for an average person [139] and hence the model does not, by default, differentiate between two subjects with different mass distributions in their body parts. The same applies to the moment of inertia of each body segment. The data were obtained from the literature.

Muscles were modeled as a bundle of fibers. The total muscle force was distributed between fibers using constant values throughout the activities.

This is particularly of importance for the quadriceps muscle since the quadriceps is the main driver of knee flexion-extension. There are several studies assessing force distribution on quadriceps muscle fibers based on EMG data or physiological cross-sectional areas [195–198]. The force distribution between quadriceps fibers in this study is based on physiological cross-sectional area studies [197,198].

The mathematical model is based on a reduction technique that only incorporated three major muscle groups at the knee joint: quadriceps, hamstring, and gastrocnemius muscle groups. It is common for knee mathematical models only to include the quadriceps and hamstring muscle groups [164,199]. The quadriceps muscle forces were controlled using a muscle controller, and the other two were specified forces.

The bone geometries in this model are created using CT scan data and segmentation techniques. Therefore, soft tissue attachments on the bones were created based on average anatomy data available in the literature. In general, all mathematical models must make assumptions about ligament properties, such as ligament stiffness or slack lengths, as they cannot be directly measured for individual subjects.

The developed settling algorithm is sensitive to the initial conditions. The settling algorithm was developed as a local optimizer to find small forces and torques as well as accurate component locations and orientations at the start of the activity. If the components are placed far from the optimized position, the settling algorithm cannot find the optimized solution. The soft tissue properties should be balanced for this situation, which requires a bit of training and familiarity with how the soft tissue work in the mathematical model.

The integrated inverse solution is particularly sensitive to the tibial flexion profile. Excessive tibial flexion or a small amount of flexion yield unrealistic

joint forces. Hence, to use the inverse model in conjunction with the forward model, the tibial flexion must be selected carefully.

7.2 Future Works

The mathematics model described herein has become a very powerful tool to assess the mechanics of various TKA designs and different subjects performing various activities. The continuation of this model has the potential to yield a more realistic and user-friendly model to assess TKA functionality.

First, the model can be improved by developing a muscle controller algorithm for other muscle groups, such as the hamstrings and gastrocnemius. These muscles are particularly important for investigating activities such as gait and stair climbing. In the current study, these muscle forces are specified based on force profiles reported in the literature. Using muscle controller for these muscles can provide insight into the forces for different subjects and different implant designs.

Second, the structure of the ligaments can be improved as well. Similar to the muscle wrapping algorithm described herein for muscles, a wrapping algorithm for ligaments can improve the predicted ligament forces and therefore improve the mechanics of the knee joint. Additionally, the current model does not incorporate all the soft tissues around the knee joint. Adding more soft tissues, such as the posterior capsule, can improve the FSM prediction abilities.

Third, the process of adding a new patient with new bone geometries is a tedious process in the current mathematical model. The attachment sites for each soft tissue, ligaments, and muscle must be selected manually by the user. An automated anatomical landmarking algorithm can make the model more

user-friendly. Using an anatomical landmarking method, the soft tissue origins and insertion can be extracted for new bone geometries in a couple of minutes.

Lastly, in the current model, the user can change the alignment of the components to simulate different surgical techniques, and multiple sensitivity analyses have been performed using this model. However, developing a virtual surgery algorithm that can be used to perform different surgical procedures can improve the functionality of the knee model by making the model more user-friendly and standardizing the component placement for different subjects.

REFERENCES

[1] Neuprez A, Delcour J-P, Fatemi F, Gillet P, Crielaard J-M, Bruyère O, et al. Patients' Expectations Impact Their Satisfaction following Total Hip or Knee Arthroplasty. PLoS One 2016;11:e0167911–e0167911. https://doi.org/10.1371/journal.pone.0167911.

[2] Jacobs CA, Christensen CP. Factors Influencing Patient Satisfaction Two to Five Years After Primary Total Knee Arthroplasty. J Arthroplasty 2014;29:1189–91. https://doi.org/10.1016/J.ARTH.2014.01.008.

[3] Khasian M, Meccia BA, LaCour MT, Komistek RD. A Validated Forward Solution Dynamics Mathematical Model of the Knee Joint: Can It Be an Effective Alternative for Implant Evaluation? J Arthroplasty 2020. https://doi.org/https://doi.org/10.1016/j.arth.2020.06.017.

[4] Kulowski J. Flexion contracture of the knee: the mechanics of the muscular contracture and the turnbuckle cast method of treatment; with a review of fifty-five cases. 1932. Clin Orthop Relat Res 2007;464:4–10. https://doi.org/10.1097/BLO.0b013e31815760ca.

[5] Aglietti P, Menchetti PPM. Biomechanics of the Patellofemoral Joint BT - The Patella. In: Scuderi GR, editor., New York, NY: Springer New York; 1995, p. 25–48. https://doi.org/10.1007/978-1-4612-4188-1_3.

[6] HUNGERFORD DS, BARRY M. Biomechanics of the Patellofemoral Joint. Clin Orthop Relat Res 1979:9–15.

[7] HEHNE H-J. Biomechanics of the Patellofemoral Joint and Its Clinical Relevance. Clin Orthop Relat Res 1990;258.

[8] Grelsamer RP, Weinstein CH. Applied Biomechanics of the Patella. Clin Orthop Relat Res 2001;389.

[9] Sharma A, Leszko F, Komistek RD, Scuderi GR, Cates HE, Liu F. In vivo patellofemoral forces in high flexion total knee arthroplasty. J Biomech 2008;41:642–8. https://doi.org/10.1016/J.JBIOMECH.2007.09.027.

[10] Sharma A, Komistek RD, Ranawat CS, Dennis DA, Mahfouz MR. In Vivo Contact Pressures in Total Knee Arthroplasty. J Arthroplasty 2007;22:404–16. https://doi.org/10.1016/J.ARTH.2006.07.008.

[11] Sharma A, Komistek RD, Scuderi GR, Cates HEJ. High-flexion TKA Designs: What Are Their In Vivo Contact Mechanics? Clin Orthop Relat Res 2007;464.

[12] SAXBY DJ, BRYANT AL, MODENESE L, GERUS P, KILLEN BA, KONRATH J, et al. Tibiofemoral Contact Forces in the Anterior Cruciate Ligament–Reconstructed Knee. Med Sci Sport Exerc 2016;48. https://doi.org/10.1177/03635465990270042301.

[13] Cleather DJ, Czasche MB. Knee Forces During Landing in Men and Women. J Hum Kinet 2019;68:177–92. https://doi.org/10.2478/hukin-2019-0065.

[14] Blackburn TA, Craig E. Knee Anatomy: A Brief Review. Phys Ther 1980;60:1556–60. https://doi.org/10.1093/ptj/60.12.1556.

[15] Fu FH, Harner CD, Johnson DL, Miller MD, Woo SL-Y. Biomechanics of knee ligaments: basic concepts and clinical application. JBJS 1993;75:1716–27.

[16] Woo SL-Y, Abramowitch SD, Kilger R, Liang R. Biomechanics of knee ligaments: injury, healing, and repair. J Biomech 2006;39:1–20. https://doi.org/https://doi.org/10.1016/j.jbiomech.2004.10.025.

[17] Woo SL-Y, Debski RE, Withrow JD, Janaushek MA. Biomechanics of Knee Ligaments. Am J Sports Med 1999;27:533–43. https://doi.org/10.1177/03635465990270042301.

[18] Dathe H, Gezzi R, Fiedler C, Kubein-Meesenburg D, Nägerl H. The description of the human knee as four-bar linkage. Acta Bioeng Biomech 2016;18:107–15. https://doi.org/10.5277/ABB-00464-2015-03.

[19] Olinski M, Gronowicz A, Handke A, Ceccarelli M. Design and Characterization of a Novel Knee Articulation Mechanism. Int J Appl Mech Eng 2016;21:611–22. https://doi.org/10.1515/ijame-2016-0037 Open access.

[20] Shenoy R, Pastides PS, Nathwani D. (iii) Biomechanics of the knee and TKR. Orthop Trauma 2013;27:364–71. https://doi.org/10.1016/J.MPORTH.2013.10.003.

[21] Stiehl JB, Dennis DA, Komistek RD, Crane HS. In vivo determination of condylar lift-off and screw-home in a mobile-bearing total knee arthroplasty. J Arthroplasty 1999;14:293–9. https://doi.org/10.1016/S0883-5403(99)90054-2.

[22] Inoue M, McGurk-Burleson E, Hollis JM, Woo SL-Y. Treatment of the medial collateral ligament injury: I: The importance of anterior cruciate ligament on the varus-valgus knee laxity. Am J Sports Med 1987;15:15–21. https://doi.org/10.1177/036354658701500103.

[23] Basso O, Johnson DP, Amis AA, Biomechanics O. The anatomy of the patellar tendon 2001. https://doi.org/10.1007/s001670000133.

[24] DeFrate LE, Nha KW, Papannagari R, Moses JM, Gill TJ, Li G. The biomechanical function of the patellar tendon during in-vivo weight-bearing flexion. J Biomech 2007;40:1716–22.

[25] Andriacchi TP, Stanwyck TS, Galante JO. Knee biomechanics and total knee replacement. J Arthroplasty 1986;1:211–9. https://doi.org/https://doi.org/10.1016/S0883-5403(86)80033-X.

[26] Iwaki H, Pinskerova V, Freeman MAR. Tibiofemoral movement 1: the shapes and relative movements of the femur and tibia in the unloaded cadaver knee. J Bone Joint Surg Br 2000;82-B:1189–95. https://doi.org/10.1302/0301-620X.82B8.0821189.

[27] Komistek RD, Dennis DA, Mahfouz M. In Vivo Fluoroscopic Analysis of the Normal Human Knee. Clin Orthop Relat Res 2003;410:69–81. https://doi.org/10.1097/01.blo.0000062384.79828.3b.

[28] Antonsson EK, Mann RW. Automatic 6-D.O.F. Kinematic Trajectory Acquisition and Analysis. J Dyn Syst Meas Control 1989;111:31. https://doi.org/10.1115/1.3153016.

[29] Leszko F, Hovinga KR, Lerner AL, Komistek RD, Mahfouz MR. In Vivo Normal Knee Kinematics: Is Ethnicity or Gender an Influencing Factor? Clin Orthop Relat Res 2011;469:95–106. https://doi.org/10.1007/s11999-010-1517-z.

[30] Dennis DA, Mahfouz MR, Komistek RD, Hoff W. In vivo determination of normal and anterior cruciate ligament-deficient knee kinematics. J Biomech 2005;38:241–53. https://doi.org/10.1016/J.JBIOMECH.2004.02.042.

[31] Johal P, Williams A, Wragg P, Hunt D, Gedroyc W. Tibio-femoral movement in the living knee. A study of weight bearing and non-weight bearing knee kinematics using 'interventional' MRI. J Biomech 2005;38:269–76. https://doi.org/10.1016/J.JBIOMECH.2004.02.008.

[32] Komdeur P, Pollo FE, Jackson RW. Dynamic knee motion in anterior cruciate impairment: a report and case study. Proc (Bayl Univ Med Cent) 2002;15:257–9. https://doi.org/10.1080/08998280.2002.11927850.

[33] Felson DT. Epidemiology of hip and knee osteoarthritis. Epidemiol Rev 1988;10:1–28.

[34] Berger RA, Rosenberg AG, Barden RM, Sheinkop MB, Jacobs JJ, Galante JO. Long-term followup of the Miller-Galante total knee replacement. Clin Orthop Relat Res 2001;388:58–67.

[35] Font-Rodriguez DE, Scuderi GR, Insall JN. Survivorship of cemented total knee arthroplasty. Clin Orthop Relat Res 1997;345:79–86.

[36] Melton JTK, Mayahi R, Baxter SE, Facek M, Glezos C. Long-term outcome in an uncemented, hydroxyapatite-coated total knee replacement. J Bone Joint Surg Br 2012;94-B:1067–70. https://doi.org/10.1302/0301-620X.94B8.28350.

[37] Abram SGF, Nicol F, Hullin MG, Spencer SJ. The long-term outcome of uncemented Low Contact Stress total knee replacement in patients with rheumatoid arthritis. Bone Joint J 2013;95-B:1497–9. https://doi.org/10.1302/0301-620X.95B11.32257.

[38] Pavone V, Boettner F, Fickert S, Sculco TP. The long-term outcome of uncemented Low Contact Stress total knee replacement in patients with rheumatoid arthritis. Clin Orthop Relat Res 2001;388:18–25.

[39] Felson DT. Clinical practice. Osteoarthritis of the knee. N Engl J Med 2006;354:841–8. https://doi.org/10.1056/NEJMcp051726.

[40] Cram P, Lu X, Kates SL, Singh JA, Li Y, Wolf BR. Total knee arthroplasty volume, utilization, and outcomes among Medicare beneficiaries, 1991-2010. JAMA 2012;308:1227–36. https://doi.org/10.1001/2012.jama.11153.

[41] Maradit Kremers H, Larson DR, Crowson CS, Kremers WK, Washington RE, Steiner CA, et al. Prevalence of Total Hip and Knee Replacement in the United States. JBJS 2015;97. https://doi.org/10.2106/JBJS.N.01141.

[42] Kurtz SM, Ong KL, Lau E, Bozic KJ. Impact of the Economic Downturn on Total Joint Replacement Demand in the United States: Updated Projections to 2021. JBJS 2014;96. https://doi.org/10.2106/JBJS.M.00285.

[43] Kurtz S, Ong K, Lau E, Mowat F, Halpern M. Projections of Primary and Revision Hip and Knee Arthroplasty in the United States from 2005 to 2030. J Bone Jt Surg 2007;89:780. https://doi.org/10.2106/JBJS.F.00222.

[44] Stoddard JE, Deehan DJ, Bull AMJ, McCaskie AW, Amis AA. The kinematics and stability of single-radius versus multi-radius femoral components related to Mid-range instability after TKA. J Orthop Res 2013;31:53–8. https://doi.org/10.1002/jor.22170.

[45] Clary CW, Fitzpatrick CK, Maletsky LP, Rullkoetter PJ. The influence of total knee arthroplasty geometry on mid-flexion stability: An experimental and finite element study. J Biomech 2013;46:1351–7. https://doi.org/10.1016/j.jbiomech.2013.01.025.

[46] Nowakowski AM, Vavken P, Pagenstert G, Valderrabano V. 8 Design, Shape, and Materials of Total Knee Replacement BT - The Unhappy Total Knee Replacement: A Comprehensive Review and Management Guide. In: Hirschmann MT, Becker R, editors., Cham: Springer International Publishing; 2015, p. 85–97. https://doi.org/10.1007/978-3-319-08099-4_8.

[47] Brinkman J-M, Bubra PS, Walker P, Walsh WR, Bruce WJM. Midterm results using a medial pivot total knee replacement compared with the Australian National Joint Replacement Registry data. ANZ J Surg 2014;84:172–6. https://doi.org/10.1111/ans.12428.

[48] Anderson JG, Wixson RL, Tsai D, Stulberg SD, Chang RW. Functional outcome and patient satisfaction in total knee patients over the age of 75. J Arthroplasty 1996;11:831–40. https://doi.org/10.1016/S0883-5403(96)80183-5.

[49] Du H, Tang H, Gu J-M, Zhou Y-X. Patient satisfaction after posterior-stabilized total knee arthroplasty: A functional specific analysis. Knee 2014;21:866–70. https://doi.org/10.1016/J.KNEE.2014.03.007.

[50] Baker PN, van der Meulen JH, Lewsey J, Gregg PJ. The role of pain and function in determining patient satisfaction after total knee replacement. J Bone Joint Surg Br 2007;89-B:893–900. https://doi.org/10.1302/0301-620X.89B7.19091.

[51] Bourne RB, Chesworth BM, Davis AM, Mahomed NN, Charron KDJ. Patient Satisfaction after Total Knee Arthroplasty: Who is Satisfied and Who is Not? Clin Orthop Relat Res 2010;468:57–63. https://doi.org/10.1007/s11999-009-1119-9.

[52] Masouros SD, Bull AMJ, Amis AA. (i) Biomechanics of the knee joint. Orthop Trauma 2010;24:84–91. https://doi.org/10.1016/j.mporth.2010.03.005.

[53] Gunaratne R, Pratt DN, Banda J, Fick DP, Khan RJK, Robertson BW. Patient Dissatisfaction Following Total Knee Arthroplasty: A Systematic Review of the Literature. J Arthroplasty 2017;32:3854–60. https://doi.org/10.1016/j.arth.2017.07.021.

[54] Argenson J-N, Parratte S, Ashour A, Komistek RD, Scuderi GR. Patient-reported Outcome Correlates With Knee Function After a Single-design Mobile-bearing TKA. Clin Orthop Relat Res 2008;466:2669–76. https://doi.org/10.1007/s11999-008-0418-x.

[55] Noble PC, Conditt MA, Cook KF, Mathis KB. The John Insall Award: Patient expectations affect satisfaction with total knee arthroplasty. Clin Orthop Relat Res 2006;452:35–43. https://doi.org/10.1097/01.blo.0000238825.63648.1e.

[56] Devers BN, Conditt MA, Jamieson ML, Driscoll MD, Noble PC, Parsley BS. Does Greater Knee Flexion Increase Patient Function and Satisfaction After Total Knee Arthroplasty? J Arthroplasty 2011;26:178–86. https://doi.org/10.1016/j.arth.2010.02.008.

[57] Kurtz SM, Lau E, Ong K, Zhao K, Kelly M, Bozic KJ. Future young patient demand for primary and revision joint replacement: national projections from 2010 to 2030. Clin Orthop Relat Res 2009;467:2606–12. https://doi.org/10.1007/s11999-009-0834-6.

[58] Victor J, Banks S, Bellemans J. Kinematics of posterior cruciate ligament-retaining and -substituting total knee arthroplasty. J Bone Joint Surg Br 2005;87-B:646–55. https://doi.org/10.1302/0301-620X.87B5.15602.

[59] Stiehl J, Komistek R, Dennis D, Paxson R, Hoff W. Fluoroscopic analysis of kinematics after posterior-cruciate-retaining knee arthroplasty. J Bone Joint Surg Br 1995;77-B:884–9. https://doi.org/10.1302/0301-620X.77B6.7593100.

[60] Sharma A, Dennis DA, Zingde SM, Mahfouz MR, Komistek RD. Femoral Condylar Contact Points Start and Remain Posterior in High Flexing Patients. J Arthroplasty 2014;29:945–9. https://doi.org/10.1016/J.ARTH.2013.09.037.

[61] Parsley BS, Bertolusso R, Harrington M, Brekke A, Noble PC. Influence of Gender on Age of Treatment with TKA and Functional Outcome. Clin Orthop Relat Res 2010;468:1759–64. https://doi.org/10.1007/s11999-010-1348-y.

[62] Guy SP, Farndon MA, Sidhom S, Al-Lami M, Bennett C, London NJ. Gender differences in distal femoral morphology and the role of gender specific implants in total knee replacement: A prospective clinical study. Knee 2012;19:28–31. https://doi.org/10.1016/J.KNEE.2010.12.005.

[63] Cates HE, Komistek RD, Mahfouz MR, Schmidt MA, Anderle M. In Vivo Comparison of Knee Kinematics for Subjects Having Either a Posterior Stabilized or Cruciate Retaining High-Flexion Total Knee Arthroplasty. J Arthroplasty 2008;23:1057–67. https://doi.org/10.1016/J.ARTH.2007.09.019.

[64] Bellemans J, Banks S, Victor J, Vandenneucker H, Moemans A. Fluoroscopic analysis of the kinematics of deep flexion in total knee arthroplasty. J Bone Joint Surg Br 2002;84-B:50–3. https://doi.org/10.1302/0301-620X.84B1.0840050.

[65] Argenson J-NA, Scuderi GR, Komistek RD, Scott WN, Kelly MA, Aubaniac J-M. In vivo kinematic evaluation and design considerations related to high flexion in total knee arthroplasty. J Biomech 2005;38:277–84. https://doi.org/10.1016/J.JBIOMECH.2004.02.027.

[66] Yue B, Varadarajan KM, Moynihan AL, Liu F, Rubash HE, Li G. Kinematics of medial osteoarthritic knees before and after posterior cruciate ligament retaining total knee arthroplasty. J Orthop Res 2011;29:40–6. https://doi.org/10.1002/jor.21203.

[67] Dennis DA, Komistek RD, Mahfouz MR, Haas BD, Stiehl JB. Conventry Award Paper: Multicenter Determination of In Vivo Kinematics After Total Knee Arthroplasty. Clin Orthop Relat Res 2003;416:37–57. https://doi.org/10.1097/01.blo.0000092986.12414.b5.

[68] Heyse TJ, Becher C, Kron N, Ostermeier S, Hurschler C, Schofer MD, et al. Patellofemoral pressure after TKA in vitro: highly conforming vs. posterior stabilized inlays. Arch Orthop Trauma Surg 2010;130:191–6. https://doi.org/10.1007/s00402-009-0920-y.

[69] Grieco TF, Sharma A, Komistek RD, Cates HE. Single Versus Multiple-Radii Cruciate-Retaining Total Knee Arthroplasty: An In Vivo Mobile Fluoroscopy Study. J Arthroplasty 2016;31:694–701. https://doi.org/10.1016/J.ARTH.2015.10.029.

[70] Donadio J, Pelissier A, Boyer P, Massin P. Control of paradoxical kinematics in posterior cruciate-retaining total knee arthroplasty by increasing posterior femoral offset. Knee Surgery, Sport Traumatol Arthrosc 2015;23:1631–7. https://doi.org/10.1007/s00167-015-3561-4.

[71] Becher C, Heyse TJ, Kron N, Ostermeier S, Hurschler C, Schofer MD, et al. Posterior stabilized TKA reduce patellofemoral contact pressure compared with cruciate retaining TKA in vitro. Knee Surgery, Sport Traumatol Arthrosc 2009;17:1159–65. https://doi.org/10.1007/s00167-009-0768-2.

[72] Pfitzner T, Moewis P, Stein P, Boeth H, Trepczynski A, von Roth P, et al. Modifications of femoral component design in multi-radius total knee arthroplasty lead to higher lateral posterior femoro-tibial translation. Knee Surgery, Sport Traumatol Arthrosc 2018;26:1645–55. https://doi.org/10.1007/s00167-017-4622-7.

[73] Yoshiya S, Matsui N, Komistek RD, Dennis DA, Mahfouz M, Kurosaka M. In Vivo Kinematic Comparison of Posterior Cruciate-Retaining and Posterior Stabilized Total Knee Arthroplasties Under Passive and Weight-Bearing Conditions. J Arthroplasty 2005;20:777–83. https://doi.org/10.1016/J.ARTH.2004.11.012.

[74] Fantozzi S, Catani F, Ensini A, Leardini A, Giannini S. Femoral rollback of cruciate-retaining and posterior-stabilized total knee replacements: In vivo fluoroscopic analysis during activities of daily living. J Orthop Res 2006;24:2222–9. https://doi.org/10.1002/jor.20306.

[75] Bontempi M, Roberti Di Sarsina T, Giulio ·, Muccioli MM, Pizza N, Cardinale · Umberto, et al. J-curve design total knee arthroplasty: the posterior stabilized shows wider medial pivot compared to the cruciate retaining during chair raising. Sport Traumatol Arthrosc n.d. https://doi.org/10.1007/s00167-019-05645-6.

[76] Kärrholm J, Jonsson H, Nilsson KG, Söderqvist I. Kinematics of successful knee prostheses during weight-bearing: Three-dimensional movements and positions of screw axes in the Tricon-M and Miller-Galante designs. Knee Surgery, Sport Traumatol Arthrosc 1994;2:50–9. https://doi.org/10.1007/BF01552655.

[77] Khasian M, Sharma A, Fehring TK, Griffin WL, Mason JB, Komistek RD. Kinematic Performance of Gradually Variable Radius Posterior-Stabilized Primary TKA During Various Activities: An In Vivo Study Using Fluoroscopy. J Arthroplasty 2020;35:1101–8. https://doi.org/https://doi.org/10.1016/j.arth.2019.10.053.

[78] Schmidt R, Komistek RD, Blaha JD, Penenberg BL, Maloney WJ. Fluoroscopic Analyses of Cruciate-Retaining and Medial Pivot Knee Implants. Clin Orthop Relat Res 2003;410.

[79] Catani F, Ensini A, Belvedere C, Feliciangeli A, Benedetti MG, Leardini A, et al. In vivo kinematics and kinetics of a bi-cruciate substituting total knee arthroplasty: A combined fluoroscopic and gait analysis study. J Orthop Res 2009;27:1569–75. https://doi.org/10.1002/jor.20941.

[80] Khasian M, LaCour MT, Coomer SC, Bolognesi MP, Komistek RD. In Vivo Knee Kinematics for a Cruciate Sacrificing Total Knee Arthroplasty Having Both a Symmetrical Femoral and Tibial Component. J Arthroplasty 2020;35:1712–9. https://doi.org/https://doi.org/10.1016/j.arth.2020.02.004.

[81] DeCook C, LaCour MMT, Nachtrab JKJ, Khasian M, Dessinger GMG, Komistek RDRD, et al. In Vivo Determination and Comparison of Total Hip Arthroplasty Kinematics for Normal, Preoperative Degenerative, and Postoperative Implanted Hips. J Arthroplasty 2020;35:588–96. https://doi.org/10.1016/j.arth.2019.08.057.

[82] Nachtrab J, Dessinger G, Khasian M, LaCour M, Sharma A, Komistek R. IN VIVO COMPARISION OF NORMAL HIP KINEMATICS WITH DEGENERATIVE HIPS BEFORE AND AFTER TOTAL HIP ARTHROPLASTY. Orthop. Proc., vol. 101, The British Editorial Society of Bone & Joint Surgery; 2019, p. 80.

[83] Khasian M, LaCour M, Coomer S, Komistek R. IN VIVO KINEMATICS FOR SUBJECTS HAVING A SYMMETRICAL FEMORAL AND TIBIAL COMPONENT. Orthop Proc 2020;102-B:100. https://doi.org/10.1302/1358-992X.2020.1.100.

[84] Crowninshield RD, Brand RA. A physiologically based criterion of muscle force prediction in locomotion. J Biomech 1981;14:793–801. https://doi.org/https://doi.org/10.1016/0021-9290(81)90035-X.

[85] Glitsch U, Baumann W. The three-dimensional determination of internal loads in the lower extremity. J Biomech 1997;30:1123–31. https://doi.org/https://doi.org/10.1016/S0021-9290(97)00089-4.

[86] Hardt DE. Determining Muscle Forces in the Leg During Normal Human Walking—An Application and Evaluation of Optimization Methods. J Biomech Eng 1978;100:72–8. https://doi.org/10.1115/1.3426195.

[87] Patriarco AG, Mann RW, Simon SR, Mansour JM. An evaluation of the approaches of optimization models in the prediction of muscle forces during human gait. J Biomech 1981;14:513–25. https://doi.org/https://doi.org/10.1016/0021-9290(81)90001-4.

[88] Pandy MG, Zajac FE, Sim E, Levine WS. An optimal control model for maximum-height human jumping. J Biomech 1990;23:1185–98. https://doi.org/https://doi.org/10.1016/0021-9290(90)90376-E.

[89] Shelburne KB, Pandy MG. A musculoskeletal model of the knee for evaluating ligament forces during isometric contractions. J Biomech 1997;30:163–76. https://doi.org/https://doi.org/10.1016/S0021-9290(96)00119-4.

[90] Anderson FC, Pandy MG. Dynamic Optimization of Human Walking. J Biomech Eng 2001;123:381–90. https://doi.org/10.1115/1.1392310.

[91] Davy DT, Audu ML. A dynamic optimization technique for predicting muscle forces in the swing phase of gait. J Biomech 1987;20:187–201. https://doi.org/https://doi.org/10.1016/0021-9290(87)90310-1.

[92] Piazza SJ. Muscle-driven forward dynamic simulations for the study of normal and pathological gait. J Neuroeng Rehabil 2006;3:5. https://doi.org/10.1186/1743-0003-3-5.

[93] Komistek RD, Stiehl JB, Dennis DA, Paxson RD, Soutas-Little RW. Mathematical model of the lower extremity joint reaction forces using Kane's method of dynamics. J Biomech 1997;31:185–9. https://doi.org/10.1016/S0021-9290(97)00128-0.

[94] LaCour MT. Development and Implementation of a Forward Solution Hip Mathematical Model to Determine In Vivo Mechanics and Predict Hip Separation. University of Tennessee, 2017.

[95] Halloran JP, Easley SK, Petrella AJ, Rullkoetter PJ. Comparison of Deformable and Elastic Foundation Finite Element Simulations for Predicting Knee Replacement Mechanics. J Biomech Eng 2005;127:813–8. https://doi.org/10.1115/1.1992522.

[96] Halloran JP, Petrella AJ, Rullkoetter PJ. Explicit finite element modeling of total knee replacement mechanics. J Biomech 2005;38:323–31. https://doi.org/https://doi.org/10.1016/j.jbiomech.2004.02.046.

[97] KWAK SD, BLANKEVOORT L, ATESHIAN GA. A Mathematical Formulation for 3D Quasi-Static Multibody Models of Diarthrodial Joints. Comput Methods Biomech Biomed Engin 2000;3:41–64. https://doi.org/10.1080/10255840008915253.

[98] Meccia B. Next Generation In-Vivo Forward Solution Physiological Model of the Human Lower Limb to Predict Implanted Knee Mechanics. University of Tennessee, 2016.

[99] Smith CR, Vignos MF, Lenhart RL, Kaiser J, Thelen DG. The Influence of Component Alignment and Ligament Properties on Tibiofemoral Contact Forces in Total Knee Replacement. J Biomech Eng 2016;138. https://doi.org/10.1115/1.4032464.

[100] Huang T, Long Y, George D, Wang W. Meta-analysis of gap balancing versus measured resection techniques in total knee arthroplasty. Bone Joint J 2017;99-B:151–8. https://doi.org/10.1302/0301-620X.99B2.BJJ-2016-0042.R2.

[101] Mason JB, Fehring TK, Estok R, Banel D, Fahrbach K. Meta-Analysis of Alignment Outcomes in Computer-Assisted Total Knee Arthroplasty Surgery. J Arthroplasty 2007;22:1097–106. https://doi.org/https://doi.org/10.1016/j.arth.2007.08.001.

[102] Scuderi GR, Komistek RD, Dennis DA, Insall JN. The Impact of Femoral Component Rotational Alignment on Condylar Lift-Off. Clin Orthop Relat Res 2003;410:148–54. https://doi.org/10.1097/01.blo.0000063603.67412.ca.

[103] Varadarajan KM, Harry RE, Johnson T, Li G. Can in vitro systems capture the characteristic differences between the flexion–extension kinematics of the healthy and TKA knee? Med Eng Phys 2009;31:899–906. https://doi.org/https://doi.org/10.1016/j.medengphy.2009.06.005.

[104] Mahfouz MR, Hoff WA, Komistek RD, Dennis DA. A robust method for registration of three-dimensional knee implant models to two-dimensional fluoroscopy images. IEEE Trans Med Imaging 2003;22:1561–74. https://doi.org/10.1109/TMI.2003.820027.

[105] Mueller JKP. Development of a Rigid Body Forward Solution Physiological Model of the Lower Leg to Predict Non Implanted and Implanted Knee Kinematics and Kinetics. University of Tennessee, 2011.

[106] Sharma A. Development of a Computational Model to Predict the In Vivo Contact Mechanics of Modern Total Knee Arthroplasty. University of Tennessee, 2008.

[107] Zeller IM. Parameterization of a Next Generation In-Vivo Forward Solution Physiological Model of the Human Lower Limb to Simulate and Predict Demographic and Pathology Specific Knee Mechanics. University of Tennessee, 2018.

[108] Kane TR, Levinson DA. Dynamics, theory and applications. McGraw Hill; 1985.

[109] Levinson DA, Kane TR. AUTOLEV—a new approach to multibody dynamics. Multibody Syst. Handb., Springer; 1990, p. 81–102. https://doi.org/10.1007/978-3-642-50995-7_7.

[110] Kane TR, Levinson DA. Dynamics online: theory and implementation with AUTOLEV. OnLine Dynamics; 2000.

[111] Schaechter DB, Levinson DA, Kane TR. Autolev user's manual. Online Dynamics; 1988.

[112] Shin CS, Chaudhari AM, Andriacchi TP. The influence of deceleration forces on ACL strain during single-leg landing: A simulation study. J Biomech 2007;40:1145–52. https://doi.org/https://doi.org/10.1016/j.jbiomech.2006.05.004.

[113] Abdel-Rahman EM, Hefzy MS. Three-dimensional dynamic behaviour of the human knee joint under impact loading. Med Eng Phys 1998;20:276–90. https://doi.org/https://doi.org/10.1016/S1350-4533(98)00010-1.

[114] Woo SL-Y, Hollis JM, Adams DJ, Lyon RM, Takai S. Tensile properties of the human femur-anterior cruciate ligament-tibia complex: The effects of specimen age and orientation. Am J Sports Med 1991;19:217–25. https://doi.org/10.1177/036354659101900303.

[115] Cooper DE, Deng XH, Burstein AL, Warren RF. The strength of the central third patellar. tendon graft: A biomechanical study. Am J Sports Med 1993;21:818–24. https://doi.org/10.1177/036354659302100610.

[116] Blankevoort L, Kuiper JH, Huiskes R, Grootenboer HJ. Articular contact in a three-dimensional model of the knee. J Biomech 1991;24:1019–31. https://doi.org/https://doi.org/10.1016/0021-9290(91)90019-J.

[117] Wretenberg P, Németh G, Lamontagne M, Lundin B. Passive knee muscle moment arms measured in vivo with MRI. Clin Biomech 1996;11:439–46. https://doi.org/https://doi.org/10.1016/S0268-0033(96)00030-7.

[118] Spoor CW, van Leeuwen JL. Knee muscle moment arms from MRI and from tendon travel. J Biomech 1992;25:201–6. https://doi.org/https://doi.org/10.1016/0021-9290(92)90276-7.

[119] D'Lima DD, Poole C, Chadha H, Hermida JC, Mahar A, Colwell Jr CW. Quadriceps moment arm and quadriceps forces after total knee arthroplasty. Clin Orthop Relat Res 2001;392:213–20. https://doi.org/10.1097/00003086-200111000-00026.

[120] Nussbaum MA, Chaffin DB, Rechtien CJ. Muscle lines-of-action affect predicted forces in optimization-based spine muscle modeling. J Biomech 1995;28:401–9. https://doi.org/https://doi.org/10.1016/0021-9290(94)00078-I.

[121] Merritt JS, Davies HMS, Burvill C, Pandy MG. Influence of muscle-tendon wrapping on calculations of joint reaction forces in the equine distal forelimb. J Biomed Biotechnol 2008;2008:165730. https://doi.org/10.1155/2008/165730.

[122] Kruidhof J, Pandy MG. Effect of muscle wrapping on model estimates of neck muscle strength. Comput Methods Biomech Biomed Engin 2006;9:343–52. https://doi.org/10.1080/10255840600924781.

[123] Arjmand N, Shirazi-Adl A, Bazrgari B. Wrapping of trunk thoracic extensor muscles influences muscle forces and spinal loads in lifting tasks. Clin Biomech 2006;21:668–75. https://doi.org/https://doi.org/10.1016/j.clinbiomech.2006.03.006.

[124] Arabori M, Matsui N, Kuroda R, Mizuno K, Doita M, Kurosaka M, et al. Posterior condylar offset and flexion in posterior cruciate-retaining and posterior stabilized TKA. J Orthop Sci 2008;13:46. https://doi.org/10.1007/s00776-007-1191-5.

[125] Massin P, Gournay A. Optimization of the Posterior Condylar Offset, Tibial Slope, and Condylar Roll-back in Total Knee Arthroplasty. J Arthroplasty 2006;21:889–96. https://doi.org/https://doi.org/10.1016/j.arth.2005.10.019.

[126] Tew M, Waugh W. Tibiofemoral alignment and the results of knee replacement. J Bone Joint Surg Br 1985;67-B:551–6. https://doi.org/10.1302/0301-620X.67B4.4030849.

[127] Huang NFR, Dowsey MM, Ee E, Stoney JD, Babazadeh S, Choong PF. Coronal Alignment Correlates With Outcome After Total Knee Arthroplasty: Five-Year Follow-Up of a Randomized Controlled Trial. J Arthroplasty 2012;27:1737–41. https://doi.org/https://doi.org/10.1016/j.arth.2012.03.058.

[128] Howell SM, Hull ML. Kinematic Alignment in Total Knee Arthroplasty. Insa. &amp Scott Surg. Knee, Elsevier; 2012, p. 1255–68. https://doi.org/10.1016/b978-1-4377-1503-3.00120-7.

[129] Johal P, Hassaballa MA, Eldridge JD, Porteous AJ. The Posterior Condylar Offset Ratio. Knee 2012;19:843–5. https://doi.org/10.1016/J.KNEE.2012.03.017.

[130] Bragonzoni L, Marcheggiani Muccioli GM, Bontempi M, Roberti di Sarsina T, Cardinale U, Alesi D, et al. New design total knee arthroplasty shows medial pivoting movement under weight-bearing conditions. Knee Surgery, Sport Traumatol Arthrosc 2018:1–8. https://doi.org/10.1007/s00167-018-5243-5.

[131] Sikorski JM. Alignment in total knee replacement. J Bone Joint Surg Br 2008;90:1121–7. https://doi.org/10.1302/0301-620X.90B9.20793.

[132] Schiraldi M, Bonzanini G, Chirillo D, de Tullio V. Mechanical and kinematic alignment in total knee arthroplasty n.d. https://doi.org/10.21037/atm.2016.03.31.

[133] Karuppal R. Kinematic alignment in total knee arthroplasty: Does it really matter? J Orthop 2016;13:A1–3. https://doi.org/10.1016/j.jor.2016.10.001.

[134] Cherian JJ, Kapadia BH, Banerjee S, Jauregui JJ, Issa K, Mont MA. Mechanical, Anatomical, and Kinematic Axis in TKA: Concepts and Practical Applications n.d. https://doi.org/10.1007/s12178-014-9218-y.

[135] Okamoto S, Mizu-uchi H, Okazaki K, Hamai S, Nakahara H, Iwamoto Y. Effect of Tibial Posterior Slope on Knee Kinematics, Quadriceps Force, and Patellofemoral Contact Force After Posterior-Stabilized Total Knee Arthroplasty. J Arthroplasty 2015;30:1439–43. https://doi.org/https://doi.org/10.1016/j.arth.2015.02.042.

[136] Khasian M, LaCour M, Dessinger G, Meccia B, Komistek R. IMPLEMENTATION OF A FORWARD SOLUTION MATHEMATICAL MODEL TO PREDICT FIXED-BEARING VERSUS MOBILE-BEARING TOTAL KNEE ARTHROPLASTY KINEMATICS. Orthop Proc 2020;102-B:70. https://doi.org/10.1302/1358-992X.2020.1.070.

[137] Grieco TF, Sharma A, Dessinger GM, Cates HE, Komistek RD. In Vivo Kinematic Comparison of a Bicruciate Stabilized Total Knee Arthroplasty and the Normal Knee Using Fluoroscopy. J Arthroplasty 2018;33:565–71. https://doi.org/10.1016/J.ARTH.2017.09.035.

[138] Erdmann WS. Geometry and inertia of the human body-review of research. Acta Bioeng Biomech 1999;1:23–35.

[139] Phillips CA. Human Factors Engineering. John Wiley & Sons; 2000.

[140] Pietak A, Ma S, Beck CW, Stringer MD. Fundamental ratios and logarithmic periodicity in human limb bones. J Anat 2013;222:526–37.

[141] Capkin S, Zeybek G, Ergur I, Kosay C, Kiray A. An anatomic study of the lateral patellofemoral ligament. Acta Orthop Traumatol Turc 2017;51:73–6. https://doi.org/https://doi.org/10.1016/j.aott.2016.07.009.

[142] Shah KN, DeFroda SF, Ware JK, Koruprolu SC, Owens BD. Lateral Patellofemoral Ligament: An Anatomic Study. Orthop J Sport Med 2017;5:2325967117741439–2325967117741439. https://doi.org/10.1177/2325967117741439.

[143] LaPrade RF, Engebretsen AH, Ly T V, Johansen S, Wentorf FA, Engebretsen L. The Anatomy of the Medial Part of the Knee. JBJS 2007;89.

[144] Last RJ. SOME ANATOMICAL DETAILS OF THE KNEE JOINT. J Bone Joint Surg Br 1948;30-B:683–8. https://doi.org/10.1302/0301-620X.30B4.683.

[145] Van Dommelen BA, Fowler PJ. Anatomy of the posterior cruciate ligament: A review. Am J Sports Med 1989;17:24–9. https://doi.org/10.1177/036354658901700104.

[146] Girgis FG, Marshall JL, MONA JEM ARSA. The Cruciate Ligaments of the Knee Joint: Anatomical. Functional and Experimental Analysis. Clin Orthop Relat Res 1975;106.

[147] Daggett M, Ockuly AC, Cullen M, Busch K, Lutz C, Imbert P, et al. Femoral Origin of the Anterolateral Ligament: An Anatomic Analysis. Arthrosc J Arthrosc Relat Surg 2016;32:835–41. https://doi.org/10.1016/J.ARTHRO.2015.10.006.

[148] Amis AA, Gupte CM, Bull AMJ, Edwards A. Anatomy of the posterior cruciate ligament and the meniscofemoral ligaments. Knee Surgery, Sport Traumatol Arthrosc 2006;14:257–63. https://doi.org/10.1007/s00167-005-0686-x.

[149] Meister BR, Michael SP, Moyer RA, Kelly JD, Schneck CD. Anatomy and Kinematics of the Lateral Collateral Ligament of the Knee. Am J Sports Med 2000;28:869–78. https://doi.org/10.1177/03635465000280061601.

[150] Andriacchi TP, Galante JO, Fermier RW. The influence of total knee-replacement design on walking and stair-climbing. JBJS 1982;64:1328–35.

[151] Larsen B, Jacofsky MC, Jacofsky DJ. Quantitative, Comparative Assessment of Gait Between Single-Radius and Multi-Radius Total Knee Arthroplasty Designs. J Arthroplasty 2015;30:1062–7. https://doi.org/10.1016/j.arth.2015.01.014.

[152] Fitzpatrick CK, Rullkoetter PJ. Estimating total knee replacement joint load ratios from kinematics. J Biomech 2014;47:3003–11. https://doi.org/10.1016/J.JBIOMECH.2014.07.002.

[153] Hatfield GL, Hubley-Kozey CL, Astephen Wilson JL, Dunbar MJ. The Effect of Total Knee Arthroplasty on Knee Joint Kinematics and Kinetics During Gait. J Arthroplasty 2011;26:309–18. https://doi.org/10.1016/j.arth.2010.03.021.

[154] Tamaki M, Tomita T, Yamazaki T, Yoshikawa H, Sugamoto K. Factors in High-Flex Posterior Stabilized Fixed-Bearing Total Knee Arthroplasty Affecting In Vivo Kinematics and Anterior Tibial Post Impingement During Gait. J Arthroplasty 2013;28:1722–7. https://doi.org/10.1016/J.ARTH.2012.09.006.

[155] Protopapadaki A, Drechsler WI, Cramp MC, Coutts FJ, Scott OM. Hip, knee, ankle kinematics and kinetics during stair ascent and descent in healthy young individuals. Clin Biomech 2007;22:203–10. https://doi.org/https://doi.org/10.1016/j.clinbiomech.2006.09.010.

[156] Harper NG, Wilken JM, Neptune RR. Muscle Function and Coordination of Stair Ascent. J Biomech Eng 2017;140. https://doi.org/10.1115/1.4037791.

[157] McClelland JA, Feller JA, Menz HB, Webster KE. Patterns in the knee flexion-extension moment profile during stair ascent and descent in patients with total knee arthroplasty. J Biomech 2014;47:1816–21. https://doi.org/https://doi.org/10.1016/j.jbiomech.2014.03.026.

[158] Stacoff A, Quervain IAK, Luder G, List R, Stüssi E. Ground reaction forces on stairs: Part II: Knee implant patients versus normals. Gait Posture 2007;26:48–58. https://doi.org/10.1016/J.GAITPOST.2006.07.015.

[159] Navacchia A, Rullkoetter PJ, Sch€ P, List RB, Fitzpatrick CK, Shelburne KB. Subject-specific modeling of muscle force and knee contact in total knee arthroplasty; Subject-specific modeling of muscle force and knee contact in total knee arthroplasty. J Orthop Res 2016;34:1576–87. https://doi.org/10.1002/jor.23171.

[160] Cheung AS, Gray H, Schache AG, Hoermann R, Lim Joon D, Zajac JD, et al. Androgen deprivation causes selective deficits in the biomechanical leg muscle function of men during walking: a prospective case–control study. J Cachexia Sarcopenia Muscle 2017;8:102–12. https://doi.org/10.1002/jcsm.12133.

[161] American Joint Replacement Registry. AJRR 2018 annual report n.d. http://www.ajrr.net/publications-data/annual-reports.

[162] American Joint Replacement Registry. AJRR 2019 annual Report 2019. http://www.ajrr.net/publications-data/annual-reports.

[163] Le DH, Goodman SB, Maloney WJ, Huddleston JI. Current modes of failure in TKA: Infection, instability, and stiffness predominate. Clin Orthop Relat Res 2014;472:2197–200. https://doi.org/10.1007/s11999-014-3540-y.

[164] Innocenti B, Pianigiani S, Labey L, Victor J, Bellemans J. Contact forces in several TKA designs during squatting: A numerical sensitivity analysis. J Biomech 2011;44:1573–81. https://doi.org/https://doi.org/10.1016/j.jbiomech.2011.02.081.

[165] Reilly DT, Martens M. Experimental Analysis of the Quadriceps Muscle Force and Patello-Femoral Joint Reaction Force for Various Activities. Acta Orthop Scand 1972;43:126–37. https://doi.org/10.3109/17453677208991251.

[166] Godest A-C, Simonis de Cloke C, Taylor M, Gregson PJ, Keane AJ, Sathasivan S, et al. A computational model for the prediction of total knee replacement kinematics in the sagittal plane. J Biomech 2000;33:435–42. https://doi.org/https://doi.org/10.1016/S0021-9290(99)00183-9.

[167] Smith SM, Cockburn RA, Hemmerich A, Li RM, Wyss UP. Tibiofemoral joint contact forces and knee kinematics during squatting. Gait Posture 2008;27:376–86. https://doi.org/https://doi.org/10.1016/j.gaitpost.2007.05.004.

[168] Bjerke J, Öhberg F, Nilsson KG, Foss OA, Stensdotter AK. Peak Knee Flexion Angles During Stair Descent in TKA Patients. J Arthroplasty 2014;29:707–11. https://doi.org/https://doi.org/10.1016/j.arth.2013.07.010.

[169] Petersen W, Rembitzki IV, Brüggemann G-P, Ellermann A, Best R, Koppenburg AG-, et al. Anterior knee pain after total knee arthroplasty: a narrative review. Int Orthop 2014;38:319–28. https://doi.org/10.1007/s00264-013-2081-4.

[170] D'Lima DD, Chen PC, Kester MA, Colwell CWJ. Impact of Patellofemoral Design on Patellofemoral Forces and Polyethylene Stresses. JBJS 2003;85.

[171] Churchill DL, Incavo SJ, Johnson CC, Beynnon BD. The influence of femoral rollback on patellofemoral contact loads in total knee arthroplasty. J Arthroplasty 2001;16:909–18. https://doi.org/https://doi.org/10.1054/arth.2001.24445.

[172] Shelburne KB, Pandy MG. A Dynamic Model of the Knee and Lower Limb for Simulating Rising Movements. Comput Methods Biomech Biomed Engin 2002;5:149–59. https://doi.org/10.1080/10255840290010265.

[173] Dahlkvist NJ, Mayo P, Seedhom BB. Forces during Squatting and Rising from a Deep Squat. Eng Med 1982;11:69–76. https://doi.org/10.1243/EMED_JOUR_1982_011_019_02.

[174] Kutzner I, Heinlein B, Graichen F, Bender A, Rohlmann A, Halder A, et al. Loading of the knee joint during activities of daily living measured in vivo in five subjects. J Biomech 2010;43:2164–73. https://doi.org/10.1016/J.JBIOMECH.2010.03.046.

[175] Zhao D, Banks SA, D'Lima DD, Colwell CW, Fregly BJ. In vivo medial and lateral tibial loads during dynamic and high flexion activities. J Orthop Res 2007;25:593–602. https://doi.org/10.1002/jor.20362.

[176] Kutzner I, Heinlein B, Graichen F, Bender A, Rohlmann A, Halder A, et al. Loading of the knee joint during activities of daily living measured in vivo in five subjects. J Biomech 2010;43:2164–73. https://doi.org/10.1016/j.jbiomech.2010.03.046.

[177] Brechter JH, Powers CM. Patellofemoral joint stress during stair ascent and descent in persons with and without patellofemoral pain. Gait Posture 2002;16:115–23. https://doi.org/https://doi.org/10.1016/S0966-6362(02)00090-5.

[178] Jevsevar DS, Riley PO, Hodge WA, Krebs DE. Knee Kinematics and Kinetics During Locomotor Activities of Daily Living in Subjects with Knee Arthroplasty and in Healthy Control Subjects. Phys Ther 1993;73:229–39. https://doi.org/10.1093/ptj/73.4.229.

[179] Bergmann G, Bender A, Graichen F, Dymke J, Rohlmann A, Trepczynski A, et al. Standardized Loads Acting in Knee Implants. PLoS One 2014;9:e86035.

[180] Kim KC, Choi JY, Kim JS, Chung HJ, Koo BS, Won SY. Influence of the posterior slope of the tibial component on the maximal flexion after total knee arthroplasty. J Korean Knee Soc 1998;10:13.

[181] Ahmad R, Patel A, Mandalia V, Toms A. Posterior Tibial Slope: Effect on, and Interaction with, Knee Kinematics. JBJS Rev 2016;4.

[182] Lee H-Y, Kim S-J, Kang K-T, Kim S-H, Park K-K. The effect of tibial posterior slope on contact force and ligaments stresses in posterior-stabilized total knee arthroplasty-explicit finite element analysis. Knee Surg Relat Res 2012;24:91–8. https://doi.org/10.5792/ksrr.2012.24.2.91.

[183] Bellemans J, Robijns F, Duerinckx J, Banks S, Vandenneucker H. The influence of tibial slope on maximal flexion after total knee arthroplasty. Knee Surgery, Sport Traumatol Arthrosc 2005;13:193–6. https://doi.org/10.1007/s00167-004-0557-x.

[184] Zelle J, Heesterbeek PJC, Malefijt MDW, Verdonschot N. Numerical analysis of variations in posterior cruciate ligament properties and balancing techniques on total knee arthroplasty loading. Med Eng Phys 2010;32:700–7. https://doi.org/10.1016/j.medengphy.2010.04.013.

[185] Kuriyama S, Ishikawa M, Nakamura S, Furu M, Ito H, Matsuda S. Posterior tibial slope and femoral sizing affect posterior cruciate ligament tension in posterior cruciate-retaining total knee arthroplasty. Clin Biomech 2015;30:676–81. https://doi.org/https://doi.org/10.1016/j.clinbiomech.2015.05.006.

[186] Kessler O, Patil S, Colwell CW, D'Lima DD. The effect of femoral component malrotation on patellar biomechanics. J Biomech 2008;41:3332–9. https://doi.org/https://doi.org/10.1016/j.jbiomech.2008.09.032.

[187] Blackburne JS, Peel TE. A new method of measuring patellar height. J Bone Joint Surg Br 1977;59-B:241–2. https://doi.org/10.1302/0301-620X.59B2.873986.

[188] Escamilla RF, Zheng N, Imamura R, MacLeod TD, Edwards WB, Hreljac A, et al. Cruciate Ligament Force during the Wall Squat and the One-Leg Squat. Med Sci Sport Exerc 2009;41. https://doi.org/10.1249/MSS.0b013e3181882c6d.

[189] Schwarzkopf R, Scott RD, Carlson EM, Currier JH. Does Increased Topside Conformity in Modular Total Knee Arthroplasty Lead to Increased Backside Wear? Clin Orthop Relat Res 2015;473:220–5. https://doi.org/10.1007/s11999-014-3648-0.

[190] Wimmer MA, Laurent MP, Haman JD, Jacobs JJ, Galante JO. Surface Damage Versus Tibial Polyethylene Insert Conformity: A Retrieval Study. Clin Orthop Relat Res 2012;470:1814–25. https://doi.org/10.1007/s11999-012-2274-y.

[191] D'Lima DD, Townsend CP, Arms SW, Morris BA, Colwell CW. An implantable telemetry device to measure intra-articular tibial forces. J Biomech 2005;38:299–304. https://doi.org/https://doi.org/10.1016/j.jbiomech.2004.02.011.

[192] D'Lima DD, Patil S, Steklov N, Slamin JE, Colwell CW. Tibial Forces Measured In Vivo After Total Knee Arthroplasty. J Arthroplasty 2006;21:255–62. https://doi.org/https://doi.org/10.1016/j.arth.2005.07.011.

[193] Miyazaki Y, Nakamura T, Kogame K, Saito M, Yamamoto K, Suguro T. Analysis of the Kinematics of Total Knee Prostheses With a Medial Pivot Design. J Arthroplasty 2011;26:1038–44. https://doi.org/https://doi.org/10.1016/j.arth.2010.08.015.

[194] Shimmin A, Martinez-Martos S, Owens J, Iorgulescu AD, Banks S. Fluoroscopic motion study confirming the stability of a medial pivot design total knee arthroplasty. Knee 2015;22:522–6. https://doi.org/https://doi.org/10.1016/j.knee.2014.11.011.

[195] Sakai N, Luo Z-P, Rand JA, An K-N. Quadriceps forces and patellar motion in the anatomical model of the patellofemoral joint. Knee 1996;3:1–7. https://doi.org/10.1016/0968-0160(96)00200-1.

[196] Zhang L-Q, Wang G, Nuber GW, Press JM, Koh JL. In vivo load sharing among the quadriceps components. J Orthop Res 2003;21:565–71. https://doi.org/10.1016/S0736-0266(02)00196-1.

[197] Farahmand F, Sejiavongse W, Amis AA. Quantitative study of the quadriceps muscles and trochlear groove geometry related to instability of the patellofemoral joint. J Orthop Res 1998;16:136–43. https://doi.org/10.1002/jor.1100160123.

[198] Elias JJ, Bratton DR, Weinstein DM, Cosgarea AJ. Comparing two estimations of the quadriceps force distribution for use during patellofemoral simulation. J Biomech 2006;39:865–72. https://doi.org/https://doi.org/10.1016/j.jbiomech.2005.01.030.

[199] Victor J, Labey L, Wong P, Innocenti B, Bellemans J. The influence of muscle load on tibiofemoral knee kinematics. J Orthop Res 2010;28:419–28. https://doi.org/10.1002/jor.21019.

VITA

Milad Khasian was born in Khorram Abad, Iran on September 23, 1987. Growing up, he inherited a love for science and mathematics from his father. His strong enthusiasm for mathematics and physics had continued to grow in high school and eventually, being at the top 0.2% among participants in the university entrance exam, Milad moved to Tehran to start his bachelor's degree in mechanical engineering in K. N. Toosi University of Technology in 2005. Milad graduated from KNTU in 2010 with a degree in mechanical engineering. He began his master's degree at the same university in mechanical engineering, specialized in dynamics and control systems. Milad implemented his knowledge to study the dynamics of high-speed railway vehicles and apply control theories to investigate the instability of railway vehicles.

In 2015, Milad decided to advance his career and knowledge by studying abroad. In 2016, He began his doctorate program in mechanical engineering at the University of Tennessee, specialized at the biomechanics of the human movement. Milad started to take courses in the field of biomechanics and quickly learned how to apply his knowledge in dynamics to study human joints. During his time at the Center for Musculoskeletal Research lab, Milad performed several fluoroscopic analyses of both the knee and the hip joints. Milad also developed a computation model to study the mechanics of the human knee joint. During his PhD, Milad published five peer-reviewed journal articles, wrote a book chapter, and presented his work in several international conferences.